

Geothermal exploration using the magnetotelluric method

Wouter Arian van Leeuwen

Urecht Studies in Earth Sciences 115

Utrecht 2016

Department of Earth Sciences
Faculty of Geosciences - Utrecht University

Local editors:

Prof.dr. Steven de Jong

Dr. Marjan Rossen

Prof.dr. Cor Langereis

Drs. Jan-Willem de Blok

ISBN 978-90-6266-438-2

Published by Faculty of Geosciences, the Netherlands, in:
Utrecht Studies in Earth Sciences (USES), ISSN 2211-4335

Printed in the Netherlands by Optima Grafische Communicatie, Rotterdam

Copyright © 2016 by Wouter van Leeuwen.

All rights reserved. No part of this publication may be reproduced in any form, by print or photo print, microfilm or any other means, without written permission by the publishers.

Geothermal exploration using the magnetotelluric method

Geothermische exploratie met de magnetotellurische methode

(met een samenvatting in het Nederlands)

Proefschrift

ter verkrijging van de graad van doctor aan de Universiteit Utrecht
op gezag van de rector magnificus, prof.dr. G.J. van der Zwaan,
ingevolge het besluit van het college voor promoties in het openbaar te
verdedigen op woensdag 26 oktober 2016 des middags te 12.45 uur

door

Wouter Arian van Leeuwen

geboren op 20 mei 1981 te Eindhoven

Promotor:

Prof. Dr. R.J. Schotting

Copromotor:

Dr. A. Raouf

"If you can't stand the heat, get out of the kitchen"
Harry S. Truman

Examination committee:

Prof. Dr. Michael Becken, University of Münster

Dr. Mark Muller, independent consultant

Prof. Dr. Bülent Tezkan, University of Cologne

Prof. Dr. Ir. Evert Slob, Delft University of Technology

Prof. Dr. Jan Diederik van Wees, Utrecht University

This work was financially supported by IF Technology bv, Arnhem

Contents

1	Introduction	1
1.1	Geothermal energy	2
1.2	Geothermal energy around the world	5
1.3	The magnetotelluric method in geothermal exploration	9
1.4	Projects	14
2	Geothermal plays and conceptual models	23
2.1	Introduction	24
2.2	Catalogue of geothermal plays	25
2.3	Exploration of geothermal systems	29
3	Theory of the magnetotelluric method	35
3.1	Introduction	36
3.2	Magnetotellurics in geothermal exploration	37
3.3	Electromagnetic theory	44
3.4	The magnetotelluric transfer function	46
3.5	Processing magnetotelluric data	51
3.6	Distortion of the magnetotelluric signal	54

3.7	Dimensionality	56
3.8	Cultural electromagnetic noise	58
3.9	Data acquisition	60
3.10	Inversion	63
4	Quality Index pre-sorting	71
4.1	Introduction	72
4.2	Magnetotelluric processing theory	74
4.3	Data evaluation	77
4.4	Quality Index pre-sorting	82
4.5	Reprocessing results	87
4.6	Comparison QI reprocessing and contractor-processed results	97
4.7	Discussion	100
4.8	Conclusions and future work	103
4.9	Acknowledgements	104
5	Comparison and interpretation of two 3-D inversion models	107
5.1	Introduction	108
5.2	Geology	110
5.3	Data acquisition, processing and evaluation	112
5.4	3-D inversion modelling	116
5.5	3-D modelling results quantitatively compared	122
5.6	Conclusions	130
6	The Montelago geothermal prospect	133
6.1	Introduction	134
6.2	A brief overview of the Montelago geothermal prospect	137
6.3	Geology of the geothermal prospect	141
6.4	Evaluation of the existing geophysical exploration data	145
6.5	Inversion of the resistivity data	157
6.6	Discussion on the various inversion results	174
6.7	Conclusions	191

7 Discussion and conclusions	195
7.1 Introduction	196
7.2 Noisy magnetotelluric data, field procedure or processing? . . .	198
7.3 Resistivity modelling of geothermal systems	203
7.4 Interpretation of resistivity models	206
7.5 Application of the magnetotelluric method in the Netherlands .	208
7.6 Conclusions	209
7.7 Future work	211
Bibliography	215
A Structural metrics	231
B Structural metrics of models in Chapter 5	239
Samenvatting	249
Summary	261
Acknowledgements	273
Curriculum Vitae	277

1

Introduction

1.1 Geothermal energy

The International Geothermal Association (IGA) defines geothermal energy as “that part of the Earth’s heat that can, or could be, recovered and exploited by man” [Dickson and Fanelli, 2004]. It is this definition that is used in this thesis when referring to geothermal energy.

Radiogenic heat production in the mantle and crust is the main source of Earth’s heat. Other sources contributing to the Earth’s surface heat flow are the Earth’s core and mantle cooling [Ledru and Guillou Frottier, 2010]. The Earth’s heat is conducted through the mantle to be stored in rocks and/or water in the crust. It is the utilization of this thermal energy, present in liquid water or as trapped steam within (porous) rocks and in the rocks itself, that is of interest for geothermal energy production.

A geothermal system is defined by Williams *et al.* [2011] as “any localized geological setting where portions of the Earth’s thermal energy may be extracted from natural or artificially induced circulating fluids transported to a point of use.” Geothermal systems are conventionally classified in terms of their temperature, leaving the geological setting, reservoir parameters such as porosity and permeability, as well as economic viability of the system, out of the classification.

A temperature-based classification of geothermal systems is an impractical approach when exploring for geothermal resources, even more so because no uniform temperature-based classification system is available. Although generally three classes, low temperature, medium temperature, and high temperature, are distinguished when classifying geothermal systems, the limits between the three temperature classes vary. This variation is illustrated in Figure 1.1.

Inspired by hydrocarbon exploration and considering the above, Moeck [2014] suggested categorizing geothermal systems by “play type”. The definition of a geothermal play is a model which comprises the geological factors controlling a technically and economically recoverable geothermal resource [Moeck, 2013]. These geological factors must describe the heat source, the reservoir, the heat or fluid pathways, the seal of the reservoir, the storage capacity

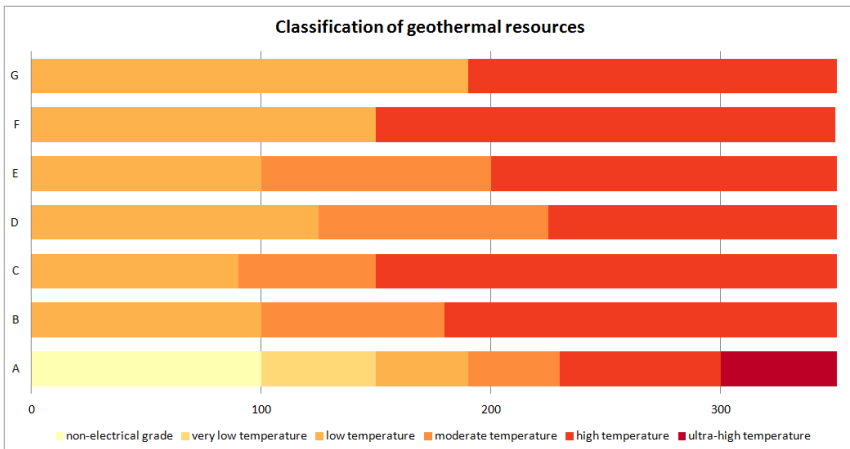


Figure 1.1: Different temperature-based classification schemes of geothermal systems. A) IFC [2013], B) Goldstein et al. [2011], C) to G) from Dickson and Fanelli [2004].

of the play, and the potential for economic recovery of the heat [MoECK, 2013, 2014]. Because most characteristics of a geothermal prospect are unknown at the early exploration stages of a geothermal prospect, categorizing a geothermal system following this classification scheme might initially introduce confusion. However, classifying geothermal systems following the categorization into geothermal play types, forces the utilization of all geological information while formulating the geothermal conceptual model.

Geothermal plays are divided into conduction-dominated type plays and convection-dominated type plays [MoECK, 2014]. Here, conduction and convection are related to the dominant mechanism of heat transfer providing the geothermal system's heat source. In a geothermal sense, conduction is the transfer of heat between geological formations that are in direct contact with each other. Or, in other words, the heat is transferred to the Earth's surface through solid rocks. Convection in a geothermal sense is the circulatory process of a hot liquid or gas rising towards the surface, after which a cooler liquid or gas takes its place and is heated again. Although heat conduction is also taking place in convective systems, the greatest amount of heat is transferred into the geothermal reservoir via liquids or gas.

Convection-dominated type plays are related to recent, i.e., less than roughly one million years old, volcanic activity found near plate boundaries such as subduction zones (the "Ring of Fire" in the Pacific), continental rifts (East African Rift), mid-ocean ridges and transform fault spreading centres, or at hot spot anomalies (Hawaii, Iceland). Conduction-dominated play types are, for example, found in areas with an increased heat flow in the continental crust, often generated by radioactive isotope decay, hot water percolating upward along fault zones, or deep seated intrusive bodies.

These regional differences in geothermal play types are very well recognized in a global surface heat flow map in which all the plate boundaries show an enhanced surface heat flow in comparison with the stable continental plates (see Figure 1.2). Depending on the local geological setting, both convective and conductive type geothermal plays can be divided into several sub-types which is further discussed in Chapter 2: "Geothermal plays and conceptual models".

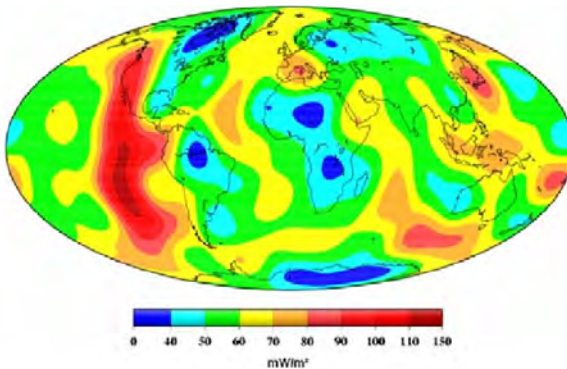


Figure 1.2: Global surface heat flow map, Figure from *Hamza et al.* [2008].

After drilling the first exploration well, geothermal plays are geologically described by their conceptual model. A conceptual model is defined as the geological model, both descriptive and graphic, containing the relevant structures and processes that characterize the geothermal reservoir and its response to exploitation [*Grant and Bixley*, 1982; *Axelsson*, 2013]. A more detailed discussion of conceptual models can be found in Chapter 2: "Geothermal plays and conceptual models".

Geothermal energy is utilized for electrical power generation or for direct heat applications. The advantages of electrical power generation from geothermal energy are apparent when connected to the electrical grid or on remote locations with insufficient power supply, including isolated islands, areas with a high energy demand (industrial processes, mining) or areas where other energy sources are scarce or expensive. Finally, it is one of the many sustainable energy alternatives alongside, e.g., wind, solar, and hydro. Geothermal energy can be utilized as direct heat for industrial purposes for those industrial processes needing high temperatures such as the paper industry or aluminium production. This type of exploitation of geothermal heat, without the use of ground source heat pumps, is referred to as direct heat. Direct heat is also applied for the heating of residential buildings and offices as well as utility buildings, often via a district heating system. Another known direct heat application is the heating of greenhouses by geothermal energy, although in those cases a ground source heat pump is generally installed and the term direct use is more appropriate.

1.2 Geothermal energy around the world

Geothermal energy has been utilized by mankind since at least Roman times, when natural hot springs were often used for bathing and medical use. The first known example of electricity production from geothermal energy is Larderello, Italy in 1904 [Dickson and Fanelli, 2004]. The utilization of geothermal energy by man is not only very old, it also offers a huge potential for sustainable energy production.

To illustrate this last point, the total energy stored in the Earth is estimated to be of the order of $12.6 \cdot 10^{12}$ EJ [Goldstein et al., 2011]. Only considering the upper 3 km of the crust, the heat stored in rocks is estimated to be roughly $43 \cdot 10^6$ EJ [Stefansson, 2005]. At a projected global energy consumption rate of 500 EJ per year [IEA, 2014] and assuming the geothermal heat recovered is not replenished with time, mankind could utilize this energy source for some 80,000 years. This is a conservative estimate since,

especially in conduction-dominated geothermal play type environments, the targeted depths are often considerably larger. When estimating the Earth's geothermal potential it must be considered that only roughly 30% of the Earth's surface is covered with land, making the remaining part of the Earth's surface virtually unusable for geothermal exploitation.

Generally said, it is at this moment technically challenging to drill geothermal wells directly into magma or into rock with temperatures above 500 °C or to depths greater than roughly 10 to 12 km below the Earth's surface. Although a successful very high temperature geothermal well was drilled into the Icelandic Krafla volcano, reaching temperatures of above 900 °C and producing at a temperature of 450 °C at a depth of about 2,100 m [*Fridleifsson et al.*], no commercial geothermal project under these conditions is currently operating. In other words, when estimating the true potential of geothermal energy, technical constraints should be taken into account. This is referred to as the technical potential [*Goldstein et al.*, 2011].

When considering geothermal systems from a utilization point of view, a division can be made between hydrothermal systems and engineered geothermal systems. Hydrothermal systems are liquid or steam dominated in which the fluids or gas transfer the geothermal heat. These systems are always convection-dominated play types. In engineered geothermal systems (EGS), located in conduction-dominated play type regions, the heat is stored in the rock itself and can only be exploited by artificially creating or increasing rock permeability. When estimating the world's geothermal potential, a separation between these two types of geothermal systems is made.

The geothermal technical potential of hydrothermal systems for direct heat of proven resources is estimated at 139 EJ/yr, or when including unproven resources, at about 1,000 EJ/yr [*Stefansson*, 2005]. Considering hydrothermal systems with a temperature suitable for electricity production, the geothermal technical potential is estimated by *Stefansson* [2005] at 6.3 EJ/yr or, including unproven resources, at 43 EJ/yr. Lacking a good reference in the form of a commercial project, estimating the geothermal technical potential for engineered geothermal systems is more complicated. In the overview given by *Goldstein et al.* [2011] of the different estimates available in literature, the technical po-

tential of engineered geothermal systems ranges from 89 EJ/yr for depths up to 3 km to 1,050 EJ/yr for depths up to 10 km. In Figure 1.3 these estimates, as well as their upper and lower boundaries, are summarized. In this graph, an energy conversion efficiency of 90% for power production and 30% for direct heat applications is applied to the estimated potentials.

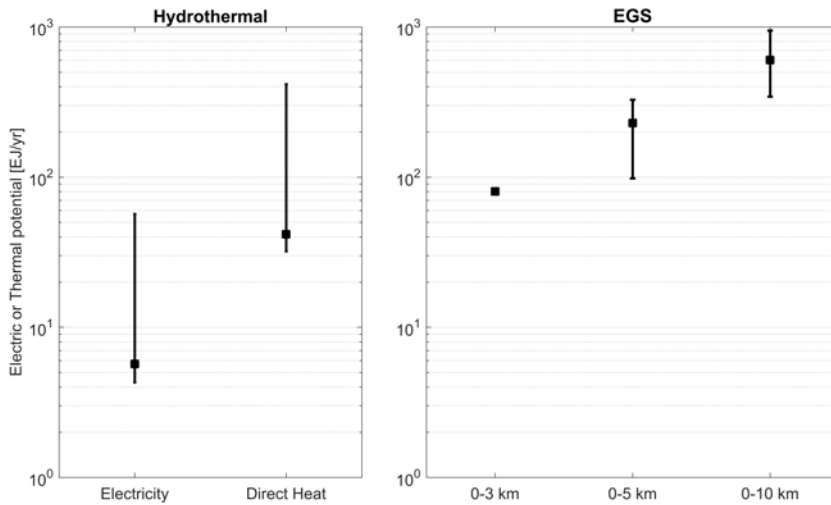


Figure 1.3: Geothermal technical potential with upper and lower bounds for hydrothermal geothermal systems and engineered or enhanced geothermal systems (EGS). Hydrothermal technical potential is expressed as either electric, in the case of electricity production, or thermal, in the case of direct heat utilization. EGS potential is plotted for technical potential estimates for electricity production of three different depth ranges. Modified from Goldstein *et al.* [2011] and Stefansson [2005].

As mentioned earlier, the first geothermal power plant was erected in Larderello in 1904. Until 1928, when Iceland started exploiting their geothermal resources for domestic heating, Larderello was the only place in Europe where geothermal energy was utilized for electricity production or heating [Dickson and Fanelli, 2004]. In 1959 geothermal power plants were also producing in Japan, the United States, New Zealand and Mexico [Dickson and Fanelli, 2004]. Since then the utilization of geothermal power generation has been

growing steadily with a current installed capacity of $12,635 \text{ MW}_e^1$ and a projected installed capacity in 2020 of $21,443 \text{ MW}_e$ [Bertani, 2015], see Figure 1.4.

Direct heat systems are generally much smaller than geothermal power plants producing electricity and, as they are most often privately owned, are often not reported. As the terminology is not consistently used from country to country, direct heat and ground source heat pump systems get mixed up and accurate estimates of the total installed capacity of direct heat applications are scarce. By grouping all geothermal applications utilizing geothermal heat, Sigússon and Uihlein [2015] estimate the installed capacity of direct heat geothermal applications at roughly 55 GW_{th}^2 including, or between 19 and 26 GW_{th} , excluding shallow geothermal systems.

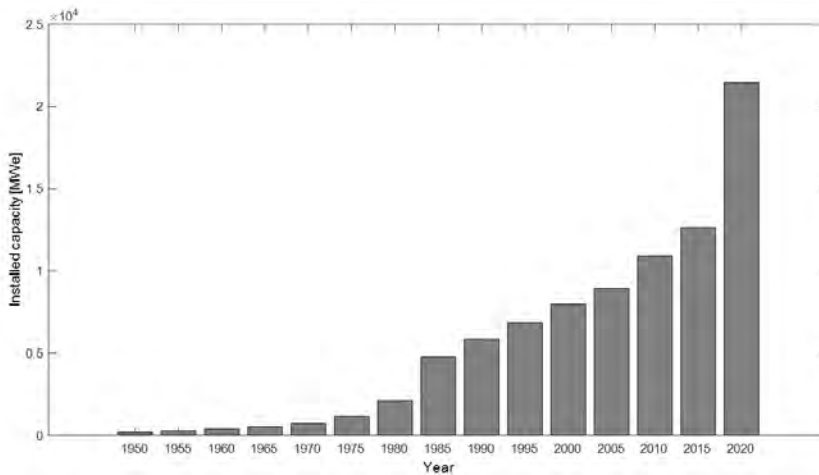


Figure 1.4: Worldwide installed geothermal electricity power capacity from 1950 up to end 2015 and short time forecasting until 2020. From Bertani [2015].

¹Electrical power in MegaWatts (J/s in SI-units)

²Thermal power in MegaWatts

1.3 The magnetotelluric method in geothermal exploration

Exploration work needs to be done before a conceptual model of a geothermal system can be made. The exploration data do not only serve as the basis of the conceptual model, they also provide the input to quantitatively estimate the economic viability of the geothermal prospect. This means that physical parameters such as temperature, depth, permeability and porosity, as well as the dimensions of the geothermal reservoir should be determined as accurately as possible. Independent of the type of geothermal system investigated, the surface exploration data for geothermal projects comprise geological, geochemical and geophysical data (see also Chapter 3: “Theory of the magnetotelluric method”). Of these three methods, geophysical surveying, and more specifically magnetotellurics, is the dominant exploration method discussed in this dissertation.

Geophysical exploration of the geothermal system is generally carried out to image the subsurface structure of the reservoir. Introducing constraints from borehole data or by combining different sources of geophysical data, geophysical prospecting can in some cases be used to determine reservoir properties such as temperature, porosity and permeability. Its main purpose is to determine the depth and dimensions of the reservoir as well as to identify the location of the heat source.

Magnetotellurics is a passive electromagnetic method measuring the time variations in the Earth’s electric and magnetic fields. These variations in the Earth’s electromagnetic fields are caused by the interaction of solar plasma with the ionosphere and magnetosphere and by global lightning activity [*Chave and Jones, 2012*]. As an electromagnetic field decays exponentially with depth [*Simpson and Bahr, 2005*], the penetration depth of the magnetotelluric method depends on the bulk electrical resistivity of the subsurface and the duration of a magnetotelluric recording, which determines the lowest frequency measured. Under the right conditions, sounding depths greater than 500 km can be achieved. The inferred linear relationship between the electric and magnetic

fields comprises the electrical resistivity structure of the Earth's subsurface. A detailed description of the principles and applications of the magnetotelluric method is given in Chapter 3: "Theory of the magnetotelluric method".

In the lithospheric mantle, the electrical resistivity of the subsurface is largely controlled by its thermal structure, however in the crust factors such as chemical and physical state, composition of rock and fluid, pressure, porosity and permeability are dominating the bulk electrical resistivity [Chave and Jones, 2012; Simpson and Bahr, 2005]. Natural geothermal reservoirs contain high temperatures in both rock and in fluids or vapour as well as good porosity and permeability. The geothermal reservoir is sealed with conductive clay minerals or impermeable rock. All these properties of a geothermal reservoir together generate a distinct resistivity response [Muñoz, 2014], making them a suitable prospect for magnetotelluric surveying.

The deployment of the magnetotelluric method during geothermal exploration in convection-dominated play types is widespread and common practice in the geothermal industry. The characteristic electrical resistivity response of volcanic geothermal systems with a very low electrically resistive clay cap of alteration clay minerals overlying a more electrically resistive geothermal reservoir, as shown in Figure 1.5, is an excellent setting for a magnetotelluric survey [Cumming, 2009; Pellerin *et al.*, 1996]. In reality, the resistivity response of a volcanic geothermal play type is not as straight-forward as in this theoretical example. A discourse on the factors influencing the resistivity response of volcanic geothermal play types is given in Chapter 3: "Theory of the magnetotelluric method".

Convection-dominated geothermal systems of different play types have been explored in, amongst others, New Zealand, Iceland, United States, Italy, Indonesia, and Japan [Muñoz, 2014; Arnason *et al.*, 2010; Cumming and Mackie, 2010; Newman *et al.*, 2008].

As the conceptual model of each geothermal system is unique, simply targeting the clay alteration - geothermal reservoir resistivity contrast when exploring a geothermal system is not without (financial) risks. This so-called anomaly hunting [Cumming, 2009; Muñoz, 2014; Younger, 2014] induces mis-

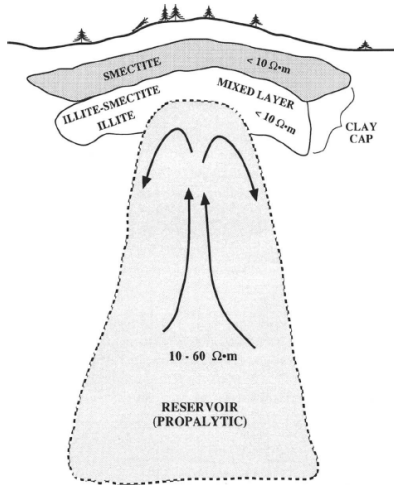


Figure 1.5: Generalized electrical resistivity structure of a volcanic geothermal system. Smectite and illite are clay alteration minerals. From *Pellerin et al.* [1996]. A discussion on how this particular geothermal system is imaged by magnetotellurics can be found in Chapter 3: “Theory of the magnetotelluric method”.

leading conceptual models and erroneous exploration well targets. This can, for example, be the case when investigating a retreating volcanic system leaving a resistivity imprint of remnant alteration mineralogy, creating a more complicated electrical resistivity structure. Here the geothermal reservoir might be located at greater depths, but the shallow low resistivity imprint of the old alteration minerals might lead to another conclusion.

Magnetotelluric geothermal exploration surveys have also been conducted on conduction-dominated geothermal play types. Instead of targeting an inferred clay-cap reservoir structure, these surveys were conducted to identify the hot fluids in the prospected geothermal reservoirs. For example *Muñoz et al.* [2010] resolve the main sedimentary layers at the Groß Schönebeck geothermal site using a combination of magnetotellurics and reflection seismics. More examples of magnetotelluric studies exploring low and medium enthalpy geothermal systems located in sedimentary basins can be found in, for example, India [*Abdul Azeez and Harinarayana*, 2007], Ireland [*Delhaye et al.*], Spain [*Arango et al.*, 2009], Poland [*Bujakowski et al.*, 2010], Brazil [*Pastana de Lugão et al.*, 2002], France [*Geiermann and Schill*, 2010], and Korea [*Uchida et al.*, 2005].

Although a proven method for geothermal surface exploration, the magnetotelluric method cannot be successfully deployed under all circumstances. In areas with high population density, heavy industry or intensive agricultural activity, the number of artificial electromagnetic signals, such as those from trains, cars, power lines, generators, buried cables and pumps, is high. When the signals of these man-made electromagnetic sources are measured during a magnetotelluric survey, they cause unwanted effects in the data, causing a low signal-to-noise ratio. This type of noise is often referred to as “cultural” or “man-made electromagnetic noise”. Logically, when the number of cultural electromagnetic sources is high or the signal of these sources is very irregular in time, it becomes harder to distinguish and eliminate the cultural electromagnetic noise from the data. This is especially relevant in areas where more than half of the recorded data consists of noisy measurements. Comprising the larger part of the recorded data, makes it difficult for the currently existing processing methods to automatically distinguish noise from data. Consequently, geothermal exploration in areas with high levels of cultural electromagnetic noise is a challenging task. With the globally increasing interest in geothermal energy, and the fact that a geothermal power station is ideally located near an area or facility with a high electricity demand, working with high levels of cultural noise is highly relevant in geothermal industry when exploring with magnetotellurics.

In Chapter 4: “Quality Index pre-sorting”, an additional, newly developed magnetotelluric processing approach, estimating the quality of the acquired signal, is introduced as a part of the re-processing of a magnetotelluric data set for geothermal exploration in Turkey. As demonstrated in this Chapter, the proposed approach is designed to efficiently identify any poor quality data points based on a quantitative measure of their quality.

Local effects such as topography, sea water, or regional geological structures, might cause distortion of the electromagnetic fields and induce a dimensional effect in the magnetotelluric data [Chave and Jones, 2012; Jiracek, 1990]. A well known example in geothermal exploration is the static shift effect which causes parallel shifts in the apparent resistivity curve of a magne-

totelluric sounding [Sternberg *et al.*, 1988; Jiracek, 1990; Arnason, 2015]. Besides static shift, also deeper resistivity contrasts caused by faults and fractures, lithological changes or other geological structures, can cause distortion and dimensional effects in the magnetotelluric data.

In geothermal exploration, the magnetotelluric data are inverted using a 1-D, 2-D or 3-D modelling approach. As demonstrated by, e.g., Ledo *et al.* [2002]; Ledo [2005]; Cumming and Mackie [2010], the results of the chosen modelling approach are strongly influenced by the dimensionality of the magnetotelluric data. This implies that the dimensionality of the (geological) structures in the subsurface should determine the dimensionality of the inversion applied to the magnetotelluric data.

Recently, more 3-D inversion codes have become available making 3-D inversion more commonplace in geothermal exploration. Since the 3-D inversion of a magnetotelluric data set is an under-determined problem, care must be taken when interpreting the 3-D modelling results. In Chapters 5: “Comparison and interpretation of two 3-D inversion models” and 6: “The Montelago geothermal prospect” the effects of different modelling strategies on the conceptual model are shown. Here the differences between two 3-D inversion models are assessed both qualitatively and quantitatively using a set of structural metrics. More importantly, it is illustrated how to use these structural metrics effectively with respect to the interpretation of the conceptual model and determining the locations of the exploration wells.

1.3.1 The application of magnetotellurics for geothermal exploration in the Netherlands

The application of geothermal energy in the Netherlands is currently limited to ground source heat pumps [van Heekeren and Bakema, 2015], but possibilities for power production are regularly investigated in commercial feasibility studies. Located in a sedimentary basin with an average geothermal gradient of 3 °C per kilometre [Bonté *et al.*, 2012], the geothermal reservoirs for power generation with temperatures above 120 °C can only be found at depths greater than 4,000 m. Although raw exploration data in the Netherlands are by law freely

accessible to the public and more than 6,000 hydrocarbon well logs as well as almost 6,000 seismic 2-D lines and more than 300 3-D seismic surveys are available, information about the geology below 4,000 m is still limited. Being a proven conventional geothermal exploration technique, capable of detecting electrical conductivity contrasts in the subsurface, magnetotelluric surveying of the deep geology of the Netherlands seems an attractive method to consider deploying.

However, some challenges are encountered when making magnetotelluric measurements in the Netherlands. Being a densely populated country, levels of cultural electromagnetic noise are high. Furthermore, the Netherlands has a direct current (DC³) railway network, which is known to heavily affect magnetotelluric signal-to-noise ratios [Szarka, 1988]. Another challenge can be found in the subsurface which consists of sedimentary geological formations. The electrical conductivity of these formations is expected to be very high, making the distinction between different geological structures difficult.

This research was initially started to investigate the possibilities of deploying magnetotellurics in the Netherlands for geothermal exploration purposes. However, as it was not possible to acquire magnetotelluric data in the Netherlands during the course of this thesis research, alternative (geothermal) magnetotelluric studies are investigated. While working on these studies, the original goal is not deserted. In Chapter 7: “Discussion and conclusions”, Section 7.5, the lessons learnt during this thesis research are translated to the possibilities and challenges met when deploying magnetotellurics for geothermal exploration in the Netherlands.

1.4 Projects

The relevant aspects of geothermal exploration using magnetotellurics, as discussed in Section 1.3, are all or partly validated in the geothermal projects investigated in this thesis. Research on two geothermal exploration projects was carried out. One project is located in Turkey and the other in the Philippines.

³Direct Current, the current travels only in one direction.

The geothermal projects in Turkey and the Philippines are both commercial projects currently being developed for electricity production. In the following, the background and current status of these two projects are briefly introduced, after which the main aspects of the magnetotelluric exploration are reviewed for each project.

1.4.1 Using magnetotellurics for the surface exploration of a geothermal field in Çanakkale, Turkey

Geothermal energy exploitation in Turkey is developing rapidly. In 2008, an installed electrical capacity of 33 MW_e and an installed thermal capacity of 165.4 MW_{th} for direct heat applications was reported by *Serpen et al.* [2009]. By 2015 these numbers have increased to 400 MW_e for power generation and 805 MW_{th} for direct heat applications. Another 165 MW_e from geothermal energy is currently under construction [*Mertoglu et al.*, 2015]. The geothermal potential for electricity production in Turkey is estimated at 4,500 MW_e [*Mertoglu et al.*, 2015].

All of the realized geothermal power plants are located in Western Anatolia [*Mertoglu et al.*, 2015]. The geothermal resource potential in Western Anatolia is related to Miocene volcanism and located in several graben systems formed during the Late Mesozoic in relation with the shrinking of the Tethys Ocean [*Serpen et al.*, 2009]. In Figure 1.6 the current status of the various geothermal fields in Turkey is shown. The general temperature regime of the, at least, 28 geothermal systems identified in this area [*Mertoglu et al.*, 2015], is in the medium to high temperature range [*Serpen et al.*, 2009; *Erdogdu*, 2009].

The magnetotelluric data acquired during the geothermal exploration in 2013 from one of the geothermal fields in this area was made available for further research by the developers of the geothermal field. This specific magnetotelluric data set was acquired in the Çanakkale province in 2013. This magnetotelluric data set was processed by a local contractor and inverted to a 3-D resistivity model by another, globally operating, contractor. The magnetotelluric data were acquired using acquisition units built by two different instrument manufacturers and processed using two different processing codes.



Figure 1.6: Current status of geothermal development for power generation in Western Anatolia. Modified from *Mertoglu et al.* [2015]. The number of the the power plants correspond to the following geothermal fields: 1. Denizli-Kızıldere, 2. Aydın-Salavatlı, 3. Aydın-Germencik, 4. Çanakkale-Tuzla, 5. Aydın-Hıdırbeyli, 6. Aydın-Gümüşköy, 7. Denizli-Geralı, 8. Manisa-Alaşehir 9. Kütahya-Simav, 10. Aydın-Germencik, 11. Denizli-Kızıldere, 12. Manisa-Alaşehir-Alkan, 13. Manisa-Alaşehir-Kavaklıdere, 14. Aydın-Sultanhisar, 15. Aydın-Yılmazköy 16. İzmir-Seferihisar, 17. İzmir-Balçova, 18. Manisa-Salihli-Caferbeyli, 19. Balıkesir-Sındırgı, 20. Aydın, 21. Kütahya-Şaphane, 22. Aydın-Nazili, 23. Aydın-Umurlu, 24. Aydın-Buharkent, 25. Aydın-Atça.

In Chapter 4: “Quality Index pre-sorting”, it is shown that the magnetotelluric data set as it is currently processed, has some inconsistencies and needs re-processing. The entire magnetotelluric data set is therefore reprocessed using a processing code written in Matlab which is loosely based on

the processing approach of *Egbert and Booker* [1986]. In this Chapter, an additional processing tool based on a pre-sorting approach and conveniently called “Quality Index pre-sorting” is introduced. Quality Index pre-sorting estimates the relative quality of a data point in the frequency domain and can be used to efficiently enhance the quality of the final station responses. It is demonstrated that re-processing using Quality Index pre-sorting produces a set of better quality processed magnetotelluric data.

In Chapter 5: “Comparison and interpretation of two 3-D inversion models”, a new 3-D resistivity inversion model is created using ModEM [*Egbert and Kelbert*, 2012] with the reprocessed data. This new inversion demonstrates the quality of the re-processed magnetotelluric data. The differences between this new 3-D inversion model and the 3-D inversion model provided by the contractor, are qualitatively and, using structural metrics, quantitatively assessed, as are the consequences for the conceptual model. It is concluded that both inversion models support a roughly similar geological interpretation, confirming the conceptual model. However, small scale resistivity differences are such that it is impossible to determine a location for an exploration well solely on basis of a single 3-D resistivity model and other information sources should be consulted as well.

As the exploration wells drilled in 2015 validated the presence of the geothermal reservoir, this geothermal prospect is currently being developed for electricity production. The geothermal reservoir is situated in a porous limestone beneath an ophiolite complex, both having a resistive signature in the 3-D inversion models.

1.4.2 Philippines, the Montelago geothermal prospect

Being the world’s second largest producer of geothermal power with approximately 1,850 MW_e [*Bertani*, 2015; *Fronza et al.*, 2015] and planning another 1,500 MW_e to be installed by 2030 [*Fronza et al.*, 2015], the Philippines is a significant player in the world geothermal market. The Philippine archipelago is situated at the edge of the “Ring of Fire” with more than 7,000 islands. These islands are often of volcanic origin and are regularly poorly connected to the

national power grid. As a result numerous islands are suffering from power shortages or high electricity prices. These topographic and economic ingredients form good conditions for the realization of the ambitious geothermal goals of the Philippine government.

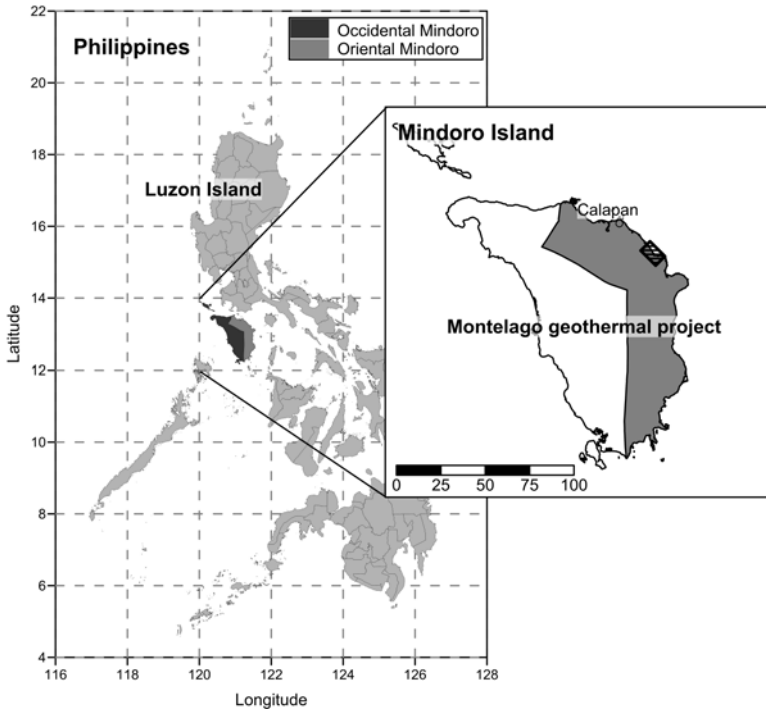


Figure 1.7: Location of the Montelago geothermal prospect on Mindoro Island within the Philippine archipelago. Scale bar in kilometres.

The Montelago geothermal prospect discussed in Chapter 6: “The Montelago geothermal prospect” is a good example of a geothermal project with these ingredients. The Montelago geothermal prospect is located on the island of Mindoro which suffers on a regular basis from power black-outs and additionally has a high price for electricity. Although not originated as a result of volcanism, volcano’s are present on the island. Mindoro is located directly

south of Philippines main island, Luzon, and is the seventh-largest island of the country, see Figure 1.7.

The Montelago Geothermal prospect has already been explored for several decades. As a consequence of this long time span and the ownership of the license by different developers, many exploration studies were carried out [Clemente, 1979; Apuada *et al.*, 1989; Leynes and Rosell, 1997; Clemente, 1982; PNOC EDC, 1989a; Ramos, 1989; Delfin and Zaide-Delfin, 1989; PNOC EDC, 1989b; Leynes and Sanchez, 1998; Maneja *et al.*, 2000; Lovelock and Lafrades, 2011; Tolentino *et al.*, 2011, 2012; Heijnen *et al.*, 2013; Hersir *et al.*, 2014; Árnason and Hersir, 2014]. Furthermore, the quality of the reports written and the fieldwork carried out is variable. In an effort to get an accurate estimate of the potential of the geothermal prospect, all the research carried out was summarized and evaluated by Benavente *et al.* [2014]. Five of the exploration studies carried out are resistivity surveys:

- A Vertical Electrical Sounding (VES) survey [Apuada *et al.*, 1989]. This study is poorly documented and is not used in this thesis research as the original data are unavailable.
- A 27 station magnetotelluric survey [Maneja *et al.*, 2000]. This study maps the resistivity of the survey area by interpolating 1-D inversions of the measured station responses.
- A 112 station controlled-source magnetotelluric (CSMT) survey Tolentino *et al.* [2012]. This study maps the resistivity of the survey area by interpolating 1-D inversions of the measured station responses.
- A combined 54 station transient electromagnetic-magnetotelluric (TEM-MT) survey Hersir *et al.* [2014]. The transient electromagnetic soundings are used to correct for the static shift effect in the magnetotelluric data. The resistivity of the survey area is mapped by interpolating 1-D inversions of the static shift corrected magnetotelluric data.
- A 3-D inversion of the static shift corrected magnetotelluric data mentioned above [Árnason and Hersir, 2014].

It is shown in Chapter 6: “The Montelago geothermal prospect” that in the CSMT study [Tolentino *et al.*, 2012] the resistivity data are misinterpreted, while the first magnetotelluric study [Maneja *et al.*, 2000] “under-modelled” the collected data leading to either erroneous or oversimplified resistivity models of the geothermal prospect. To create a subsurface resistivity model on the basis of these two electromagnetic data sets from 2000 and 2012, the data are re-processed and re-modelled. It is shown that where the 2000 magnetotelluric data can be recycled into a comprehensive resistivity model, the resistivity models based on the CSMT data lack sufficient penetration depths for a meaningful interpretation.

Combined with the results of the 2014 resistivity surveys [Hersir *et al.*, 2014; Árnason and Hersir, 2014], the new resistivity model of the 2000 magnetotelluric data creates the opportunity to evaluate the quality and quantity of electromagnetic exploration data necessary during the different exploration stages of a geothermal prospect.

To investigate the consequences for the conceptual model and the locations of the exploration wells when using different 3-D inversion codes on the same magnetotelluric data, the 3-D resistivity model as produced by Hersir *et al.* [2014] is qualitatively and quantitatively compared to the 3-D inversion model as produced by using the ModEM algorithm on the same data. To this end, a set of structural metric is used. As in the case of the Turkish geothermal project (see Section 1.4.1), the 3-D inversion models assessed in this Chapter reveal that both inversion algorithms resolve similar large scale resistivity structures, while the small resistivity variations vary between the two algorithms.

In 2015 two slim exploration wells were drilled to validate the presence of the geothermal prospect. Hydrothermal clay alteration mineralogy recovered in these two wells validated the imaged resistivity structure of the subsurface, while the temperatures measured indicated a fossil geothermal system. Furthermore do temperatures decrease at greater depths, indicating an inflow of cooler water from elsewhere.

1.4.3 The common thread

In order to develop geothermal energy into an energy source that contributes significantly to the global power supply, three themes regarding geothermal surface exploration using the magnetotelluric method need to be addressed.

- 1 Performing successful magnetotelluric surveys in areas with high levels of cultural electromagnetic noise.
- 2 Conducting a meaningful magnetotelluric survey in sedimentary basins with little conductivity contrasts.
- 3 Interpreting the resistivity response of geothermal systems which do not match the generally applied volcanic play type conceptual models based on clay alteration minerals and an upflow zone.

In Chapter 7: “Discussion and conclusions” the evidence gathered and the experience gained during the course of this research are combined with respect to these three main themes.

2

Geothermal plays and conceptual models

2.1 Introduction

As previously discussed in Chapter 1: “Introduction”, the common categorization of geothermal systems by their reservoir temperature is impractical as it overlooks the geological properties of the geothermal system as well as its economic viability. A categorization based on temperatures makes it difficult to identify analogous geothermal systems for comparison. In this dissertation the suggestion of *Moeck* [2014] to categorize geothermal systems by their play type, which is a commonly used concept in hydrocarbon exploration, is followed.

A geothermal play is defined as the model which comprises the geological factors controlling a technically and economically recoverable geothermal resource [*Moeck*, 2013]. These geological factors must provide the heat source, the reservoir, the heat or fluid pathways, the seal of the reservoir, the storage capacity of the play, and the potential for economic recovery of the heat [*Moeck*, 2013, 2014]. In Section 2.2 the catalogue of geothermal plays as proposed by *Moeck* [2014] is discussed.

A geological description of a geothermal system is its conceptual model as introduced in Chapter 1: “Introduction”. In a conceptual model the data from several geoscientific disciplines are integrated into a single comprehensive model which serves as the starting point for well targeting and resource assessment. The initial conceptual model of a geothermal resource, which is updated by reservoir engineers as soon as exploration wells are drilled, is formulated using the data collected by exploration geoscientists and is often presented in the form of a cross section. The set of exploratory geoscientific data generally contains geological, geophysical and geochemical data. Although often bearing some similarities, the conceptual model of each geothermal system is unique and depends fully on the geology of the area.

The conceptual model of each geothermal play type is defined by a number of geological factors which need to be known before the geothermal system can be developed. The exploration plan of a geothermal play should be designed to determine these factors as accurately as possible. Depending on the

geology of the geothermal system considered, different exploration techniques might be necessary. Although the characteristics of the various geothermal play types are different, they consist of the same elements together defining its conceptual model:

- **The heat source**, (continuously) providing the system with geothermal energy.
- **The geothermal reservoir**, containing the recoverable geothermal energy of the system.
- **The seal or cap rock**, trapping the geothermal energy (or its agent) in the reservoir.

The way in which these three geological factors have developed throughout geological history and their relationships are a key part of the conceptual model. In addition to these geological factors, the temperatures, permeability, depth and dimensions of (the liquid or gas in) the geothermal reservoir are required to estimate the total amount of energy it contains as well as its economic viability.

Because they initially appear to be much alike, it might be confusing to distinguish between a geothermal play type and a conceptual model. However, where the geothermal play type should be determined at the start of the exploration of a geothermal project and is qualitative, the conceptual model is not defined before most of the exploration work is carried out and is more quantitative. Additionally, the geothermal play type is a powerful tool to determine an optimal exploration strategy as well as to force the full integration of all geological information with the geophysical and geochemical data. Using the geothermal play type categorization prevents bias in the interpretation of geophysical models and might help with defining the conceptual model.

2.2 Catalogue of geothermal plays

Two major classes of geothermal plays can be recognized; conduction-dominated geothermal type plays and convection-dominated type plays [Moeck, 2013]. This separation is made on the basis of the dominating type of heat transfer in the geothermal system, i.e. conduction or convection.

Convection-dominated geothermal play types are related to shallow, i.e. less than 3,000 m deep, high temperature or enthalpy geothermal systems. They occur in regions that are tectonically active, have active volcanism, are lying adjacent to plate tectonic margins, or have young plutonism [Moeck, 2013].

The conduction-dominated geothermal play types can be found in passive tectonic plate settings without any significant recent volcanism [Moeck, 2013]. Because passive tectonic plate settings are geologically relatively stable, temperatures are generally increasing with depth. Consequently, conductive plays which are commercially viable are often located at greater depths, i.e., deeper than 2,000 m.

Both convection-dominated and conduction-dominated type geothermal plays can be subdivided into three sub-types, see Table 2.1. The former in volcanic, plutonic and extensional domain type plays, and the latter in intracratonic basins, orogenic belt and basement type plays. In the following a short description of the six play types is given, for a more detailed discussion about geothermal plays, see Moeck [2014].

Table 2.1: Overview of the geothermal play types and their characteristics, modified from Moeck [2014].

Convection-dominated geothermal plays		
<i>Play type</i>	<i>Geological setting</i>	<i>Heat source</i>
Volcanic	Magmatic arcs, mid ocean ridges and hotspots	Magma chamber and intrusion
Plutonic	Young orogens, post-orogenic phase	Young intrusion and extension
Extensional domain	Metamorphic core complexes, back-arc extension, pull-apart basins and intracontinental rifts	Elevated heat flow due to thinned crust
Conduction-dominated geothermal plays		
<i>Play type</i>	<i>Geological setting</i>	<i>Heat source</i>
Intracratonic basin	Rift basins and passive margin basins	Sedimentary aquifers and porosity/permeability with depth
Orogenic belt	Fold-and-thrust belts and foreland basins	Sedimentary aquifers, porosity/permeability with depth and fault and fracture zones
Basement	Intrusion in flat terrain and highly radiogenic rocks	Hot intrusive rock, low porosity/low permeability and fault and fracture zones

Volcanic type geothermal plays, as illustrated in Figure 2.1(a), can be characterized by a shallow heat source, generally a magma chamber. Examples can be found in areas with active volcanism such as Indonesia and Iceland, see also Table 2.1. In these type of plays, the geothermal fluid flows vertically to the surface via an upflow zone. The upflow zone is also the typical primary reservoir target for development. Since structural controls such as geological layering, faults and fractures, as well as topography influence the fluid pathways, lateral flow causes the fluids to reach the surface at outflow zones [Grant and Bixley, 1982]. Outflow zones, which are sometimes targeted as secondary reservoirs, can be geothermal manifestations such as hot springs and geysers, and can be located at very large distances from the upflow zone. As fluids leave the system at the outflow zone, an area where surface fluids can enter the geothermal system is necessary to maintain continuous circulation of fluids within the geothermal system. Volcanic type geothermal systems are regularly recharged by surface water flowing down into the reservoir through natural faults and fractures.

Plutonic type geothermal plays are typically heated by laterally large, slowly cooling plutons, often controlled by the age of its magmatism [Moeck, 2014]. Active magmatism is characterized by shallower, smaller and hotter plutons in comparison to extinct or inactive magmatism. Geothermal plays such as these are related to continent-continent convergent or transform margins with recent magmatism. Conceptually, plutonic type geothermal plays have the same elements as volcanic type plays, as illustrated in Figure 2.1(c).

Extensional domain type geothermal plays are found in regions where the mantle is locally elevated and the crust is thinned as a result of crustal extension. In this setting, the heat source is formed by the elevated mantle which causes a steep geothermal gradient. An extensional domain system is fault-controlled, where convection or a combination of convection and conduction occurs along the faults [Moeck, 2014]. The conceptual model of this play type is shown in Figure 2.1(e).

Intracratonic basin type geothermal plays are sedimentary basins located in stable continental crust without active igneous or tectonic activity. An ex-

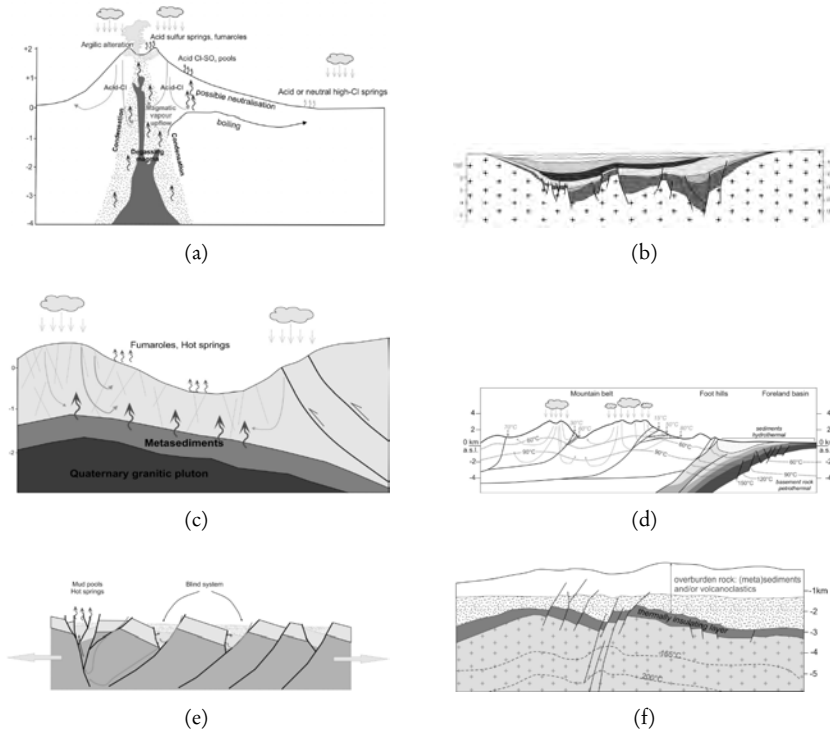


Figure 2.1: Generalized conceptual models of (a) a volcanic type geothermal play, (c) a plutonic type geothermal play, (e) an extensional-domain type geothermal play, (b) an intracratonic basin type geothermal play, (d) an orogenic belt type geothermal play, and (f) a basement type geothermal play. From *Moeck* [2014].

tensional graben system is an example of this type of play. In sedimentary basins, the heat source is the natural geothermal gradient of the region, while the reservoir is formed by a geological formation with high porosity and permeability. Suitable formations typically are sandstones and limestones, whose properties are controlled by faults, stress field and basin evolution. Economically viable formations for geothermal projects are often located at great depths, i.e. > 3,000 m. In Figure 2.1(b) a generic conceptual model of an intracratonic basin type geothermal play is shown.

Orogenic belt type geothermal plays can be found in orogenic belts and their foreland basins with little or no tectonic activity. These kinds of systems are often heated by deep fluid circulation systems through major crustal faults *Moock* [2013]. The weight of the orogenic belt and the loading of erosional products cause crustal subsidence in the foreland basin of an orogen. As a result, local extensional regions within a compressional setting are present, the associated downbending of the lithosphere may enhance increased geothermal gradients through faults or folded permeable layers. Similar to intracratonic basin type plays, sedimentary formations are targeted as the geothermal reservoir, but depending on the local geology, faults might also serve as a geothermal reservoir. A typical orogenic belt type geothermal play is shown in Figure 2.1(d).

Basement type geothermal plays occur in areas with little or no natural porosity and permeability, but store vast amounts of heat. Often, the host rock is a faulted or fractured granite, see Figure 2.1(f). These systems are very abundant but need to be artificially stimulated to be productive, resulting in so-called Enhanced Geothermal Systems (EGS). The local stress field is the most important technical parameter determining the feasibility of the development of an EGS project.

2.3 Exploration of geothermal systems

Surveys from three disciplines in Earth sciences can be distinguished for the exploration of a geothermal system; geology, geochemistry and geophysics. As a full discussion of all details of the various methods from these disciplines used during a geothermal exploration project is beyond the scope of this dissertation, a short overview of the combined aims of geological, geochemical and geophysical surveys is given.

The properties of a geothermal system targeted by a geological, geochemical or geophysical survey are listed below. The properties addressed in this overview all serve to define the heat source, the reservoir or the seal of the geothermal system as mentioned in Section 2.1.

The temperature in the reservoir. This is a key parameter for the feasibility of a geothermal prospect as it determines the suitability of the reservoir for electricity production or direct heat applications. Reservoir temperature is often interpreted using geothermometry applied to water or gas samples collected at geothermal manifestations around the resource. The interpretation of the results of the geochemistry is simultaneously used to define characteristics such as temperature, depth and age, of the heat source. Other information used to reconstruct reservoir temperature can include electrical resistivity and petrological data, as well as borehole logs or heat flow data [*Spichak and Zakharova, 2015*].

The permeability and porosity of the reservoir rock. For a geothermal reservoir to be productive, it is necessary that the geothermal fluid can flow through the system. Porosity and permeability can be determined on basis of petrological information interpreted from, for example, sonic or gamma ray combined with resistivity or density well logs, neutron porosity well logs or laboratory analysis of rock samples. Another regularly applied method to determine porosity and permeability values, is to estimate them on basis of resistivity data using empirical relations.

The geology as well as the geological evolution of the geothermal system, comprising heat source, reservoir and seal. Knowledge of the lithology, geological history, rock properties and petrology of the geothermal system helps to formulate its conceptual model as well as to make an initial estimation of the geothermal reservoir properties. Similarly, knowledge about orientation, location, and history, of faults and fractures and their stress field, indicate if they serve as barriers or path-ways for reservoir fluids and heat. The geological history, structural geology and lithology of a geothermal system are determined by studying the available literature and conducting geological mapping and structural fieldwork in the research area, simultaneously collecting rock samples for laboratory analysis to study the petrology and geochemistry of the rocks. Faults and fractures and other significant geological structures can

sometimes be identified using geophysical methods such as gravity, magnetics and/or magnetotellurics.

The reservoir pressure. When sufficiently over-pressured the geothermal fluid will rise towards the surface and there is no need for a pump at the production well, making pressure an important parameter for the energetic and economical balance of a geothermal project. Reservoir pressure can be determined using density well logs and well tests.

The fluid phase within the reservoir, two-phase, liquid or steam. For the design of the wells and surface installations, it is important to know which fluid phases are present in the reservoir. This can be determined by using the temperature and pressure data of the reservoir.

The chemical composition of the reservoir fluid. As scaling and corrosion are likely to occur during geothermal production, knowledge about the chemical composition of the reservoir fluid is essential for a sound design of geothermal wells and surface installations. The chemical composition can be determined by analysing fluid samples in the laboratory. Health and safety issues in relation to the minerals present in the reservoir fluid can be assessed simultaneously.

The hydrothermal alteration and/or cap rock description. As discussed in Section 2.1, a geothermal reservoir needs a seal and this can be formed by hydrothermal alteration minerals, sedimentary clays and/or sealing faults. Knowledge about this seal can be interpreted from the geological fieldwork or from subsurface models based on surface measurements acquired during a geophysical exploration survey. Depending on the local geological setting the geophysical exploration survey could for example be a magnetotelluric or a seismic survey,

The depth and dimensions of the geothermal reservoir and, if possible, the location of the heat source. As these are subsurface properties of the geother-

mal system, they are generally determined using geophysical measurements at the Earth's surface. Which geophysical technique is applied depends on the characteristics of the rocks to be measured. Generally applied techniques are magnetotellurics or seismic.

The locations of geothermal surface manifestations. These locations can for example be efficiently mapped during a geochemical water sampling campaign. They deliver useful information to localize the outflow area of the geothermal system under investigation and the formulation of the conceptual model.

3

Theory of the magnetotelluric method

3.1 Introduction

Magnetotellurics is a non-invasive geophysical technique which utilizes the time-variations of the Earth's electromagnetic fields to image the electrical resistivity structure of the subsurface. Magnetotellurics is utilized for research purposes and commercial activities such as deep crustal studies and mining exploration. Besides these applications, magnetotellurics has a long track record in the exploration of convection-dominated play type geothermal systems. This is especially the case for volcanic type geothermal systems, which have a clear resistivity pattern [Spichak, 2009; Manzella et al., 2006].

When it comes to the exploration of volcanic type geothermal systems, the surveyed areas are often located in remote areas. Furthermore, these geothermal systems are often characterized by a sharp resistivity contrast at a relatively shallow depth indicating the top of the geothermal reservoir [Newman et al., 2008; Layugan et al., 2005].

Some typical examples of regions where magnetotellurics is used for geothermal exploration are the Philippines [Layugan et al., 2005; Del Rosario Jr. et al., 2005], Korea [Uchida et al., 2005], the United States [Newman et al., 2008; Wannamaker, 1997; Wannamaker et al., 2005], as well as several countries in Europe [Muñoz et al., 2010; Bujakowski et al., 2010; Manzella et al., 2006; Gianni Volpi et al., 2003]. Review papers discussing the application of magnetotellurics in geothermal based on case studies were published by Spichak [2009] and Muñoz et al. [2010].

When applying magnetotellurics for the exploration of geothermal systems of the conduction-dominated geothermal play type or for geothermal systems located in densely populated regions, both the measurement and the subsurface conditions can be challenging. In densely populated areas cultural electromagnetic noise is always in the vicinity of a magnetotelluric sounding and decreases the quality of the acquired data. In areas where conduction-dominated geothermal geothermal play types are present, the subsurface generally consists of layered sedimentary basins of thick conductive sequences like sandstones, claystones and limestones. When imaging potential geothermal re-

sources in these regions, the resistivity contrasts in the subsurface are expected to be very small and difficult to detect.

In order to understand the contribution of subsurface resistivity models to geothermal surface exploration, the factors effecting resistivity and the geothermal interpretation of resistivity models is discussed in Section 3.2: “Magnetotellurics in geothermal exploration”. A summary of the theoretical principles of the magnetotelluric method are given in Section 3.3: “Electromagnetic theory”, while in Section 3.5: “Processing magnetotelluric data” the common approaches used for magnetotelluric data processing are discussed. Following, in Section 3.6: “Distortion of the magnetotelluric signal”, the in geothermal exploration regularly appearing galvanic distortion is introduced as are its mitigation measures. The effects of the dimensionality of subsurface structures on the magnetotelluric signal are discussed in Section 3.7: “Dimensionality”. In Section 3.8: “Cultural electromagnetic noise”, the effects of man-made influences on magnetotelluric signals are discussed as are the available options for the mitigation of these noise effects. A description of the strategies followed in data acquisition is given in Section 3.9: “Data acquisition”. Finally, the inversion of the processed magnetotelluric data to subsurface resistivity models is discussed in Sections 3.10: “Inversion”.

3.2 Magnetotellurics in geothermal exploration

As discussed in Chapter 2: “Geothermal plays and conceptual models”, a catalogue of geothermal systems can be formulated based on heat transport type and geological setting. Each of the different geothermal system play types defined in this catalogue has a distinct electromagnetic response. The electrical resistivity of the subsurface of a geothermal system depends on its temperature, porosity and permeability, fluid salinity, and alteration mineralogy [*Spichak, 2009; Chave and Jones, 2012; Muñoz et al., 2010; Muñoz, 2014*].

3.2.1 Factors affecting resistivity

The hot fluids flowing upwards from the contact between the groundwater and magma influence the resistivity of the geothermal system. At temperatures above 800 °C magma itself has a very low intrinsic resistivity. The resistivity of the melt is greatly dependent on the melt composition, the fraction of partial melt and the presence of water in the melt. Several empirical relations to predict the bulk resistivity of the solid phase based on temperature were derived in the laboratory [*Spichak, 2009*].

Another factor affecting the resistivity of rock is the porosity and permeability. The dependency between electrical resistivity and porosity is given in empirical relations such as *Archie [1942]*. At typical exploration depths the electric resistivity decreases as a function of temperature and pressure, while porosity and permeability are not only dependent on temperature and pressure but also on the geological history of the geological formations considered.

As the fluids present in the rocks can contain varying concentrations of dissolved salts, the fluid salinity also plays a role in the electrical resistivity response of the subsurface. Fluids with a higher concentration of dissolved salts generally have a higher conductivity.

The last factor affecting the electrical resistivity of a geothermal system is its hydrothermal clay alteration mineralogy. Hydrothermal clay alteration occurs when the fluid composition in the geothermal system comprises a volcanic component. As illustrated in Figure 3.1, in which a depth-resistivity profile of a basaltic geothermal system is shown, specific clay alteration minerals are formed at different temperature regimes in the subsurface. The clay alteration minerals often form an impermeable clay cap covering the geothermal reservoir. If the present day temperature is lower than the temperature regime at which the clay alteration minerals were initially formed, the alteration mineralogy is a reflection of the maximum temperature experienced by the rocks [*Arnason et al., 2010*].

As shown in Figure 3.1, an extra conduction pathway through the interface of clay minerals and water is formed in the presence of clay alteration [*Spichak, 2009*].

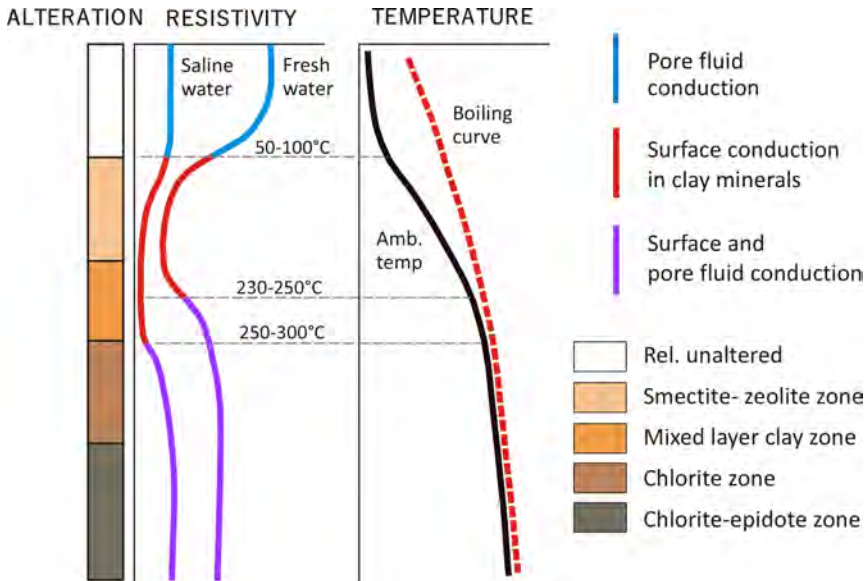


Figure 3.1: Generalized resistivity structure of a basaltic geothermal system. From Flóvenz *et al.* [2005]. Plotted as a function of depth are from left to right, the clay alteration, the electrical resistivity of saline and fresh water and the ambient and boiling temperatures. In the resistivity curves, the type of conduction, either pore fluid or mineral, is indicated. At temperatures up to 70 °C these minerals are smectite and zeolites having a high electrical conductivity. At temperatures between 180 °C and 220-240 °C a mixture of these clay minerals with illite, in acidic regimes, and/or chlorite, in basaltic regimes, are found. These newly formed clay alteration minerals tend to reduce the conductivity. Above 240 °C the smectite and illite have completely disappeared and a pure chlorite or illite zone is formed and bulk conductivity is increasing again. At even higher temperatures epidote is added to the alteration mineralogy.

Given the factors influencing the electrical resistivity of the subsurface, relations are being investigated to predict rock temperature, porosity and permeability or clay alteration mineralogy directly or indirectly from resistivity measurements. Where the approximation of porosity and permeability from electrical conductivity is still a work in progress, it is possible to estimate regional geotherms on basis of resistivity measurements [Spichak, 2009]. Further developed is the determination of the temperature of a geothermal system on basis of the clay alteration mineralogy. Besides predicting the temperature, the alteration mineralogy is often utilized for the interpretation of geothermal systems [Pellerin *et al.*, 1996; Cumming, 2009].

3.2.2 Magnetotelluric exploration of geothermal plays

In the previous Section the factors affecting the bulk electrical resistivity of the subsurface and more specifically geothermal systems are listed. Utilizing this knowledge, the resistivity characteristics for geothermal exploration of the various geothermal play types as previously discussed in Chapter 2: “Geothermal plays and conceptual models” can be illustrated on the basis of a selection of case studies. Two review papers, discussing the application of the magnetotelluric method in geothermal exploration based on case studies were published by *Spichak* [2009] and *Muñoz et al.* [2010].

Convection-dominated geothermal play types

As described in Chapter 2, a volcanic type geothermal system consists of a upflow area overlain by a clay-cap. As discussed in Section 3.2.1, this clay-cap is formed by clay alteration minerals such as smectite and illite. The electrical resistivity structure of a highly conductive layer above an *up-doming* zone with a lower conductivity is a characteristic electrical response for a volcanic type geothermal system. The upflow area is caused by thermal buoyancy through the permeable reservoir and is characterized by an up-doming pattern of isotherms simultaneously reflecting the pattern of fluid flow [*Cumming*, 2009]. This generalized concept of the electrical resistivity structure of a volcanic type geothermal play is illustrated in Figure 3.2. It is inferred that the base of the clay-cap coincides with the temperature contour of the geothermal reservoir. Since the geothermal fluids flow laterally away from the upflow zone, the clay-cap may thicken in the outflow zone.

Application of the magnetotelluric method for the exploration of these types of geothermal systems is common and often successful. Especially when the volcanic system is active, the generalized resistivity model described above can be applied to the survey results. A characteristic example of the successful application of this resistivity model of a volcanic geothermal play type is the Taupo Volcanic zone in New Zealand [*Bibby et al.*, 1995; *Heise et al.*, 2008] as well as the Hengill area in Iceland [*Arnason et al.*, 2010].

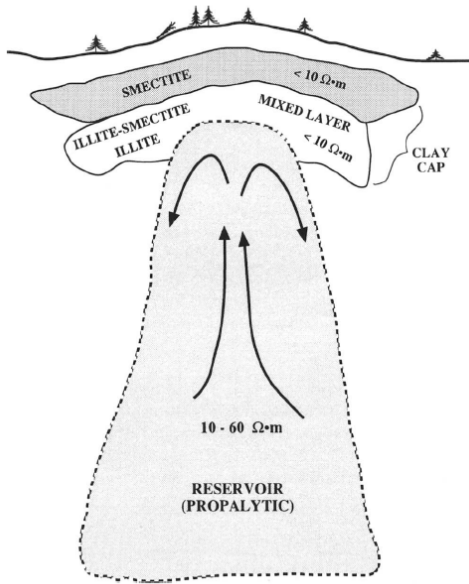


Figure 3.2: Generalized electrical resistivity model of a volcanic type geothermal system with a reservoir temperature of above 200 °C. Given are the clay cap with a low resistivity and the geothermal reservoir with a increased resistivity. Due to the moderate resistivity contrasts and relatively high bulk conductivity in the resistivity model as sketched this Figure, it is likely that the geothermal system having this particular resistivity structure, is poorly resolved by a magnetotelluric survey. From *Pellerin et al.* [1996].

In contrast to the Hengill area, the Krýsuvík geothermal system, which is also located in Iceland, has no central volcano and the retrieved 3-D resistivity model can not be interpreted similarly. Although the system is characterized by the typical resistivity-depth profile related to hydrothermal alteration found in Iceland [*Flóvenz et al.*, 2005], its deep conductor is not related to an upflow zone, but probably the result of inflation due to the emission of gas [*Hersir et al.*, 2013]. Here, recovered temperatures are lower than clay alteration mineralogy suggests, indicating that cooling has taken place.

In fact, also plutonic type and extensional-domain type geothermal plays can, due to their high temperature regimes, often be characterized by the same generalized resistivity model as discussed above. In these cases the depth and extend of the heat source as well as the presence of faults and fractures acting as fluid pathways or barriers will complicate the interpretation of the resistivity model.

An example of the geothermal exploration of a plutonic type geothermal play is given by the case of the Travale geothermal system situated in Tuscany, Italy. The Travale geothermal system is heated by a deep-seated pluton, while the fluid flow is fault controlled. Low resistivity zones in the inversion model of the geothermal system are coincident with high permeability and porosity and possibly also hydrothermal alteration. This geothermal system has two producing reservoirs, a shallow fractured metamorphic formation and a deeper porous limestone formation, both characterized by reduced resistivities [Manzella *et al.*, 2006].

The Coso geothermal field in the western United States is an example of a geothermal system fitting an extensional-domain play type. The geothermal field is characterized by a magma reservoir which is slowly moving upwards. The intrusions in the basement rocks beneath the geothermal reservoir are related to this magma reservoir. The geothermal reservoir permeability is fracture controlled [Wannamaker *et al.*, 2005]. The 3-D resistivity model of the Coso geothermal field shows a steeply dipping low resistivity zone which is related to the fluid flow in the main fault in the field. This leads to the conclusion that this geothermal system is both temperature and porosity and permeability controlled. The shallow resistivity layers of this system are also characterized the typical resistivities related to hydrothermal alteration [Newman *et al.*, 2008].

Summarizing, it can be concluded that, due to their high temperatures, all geothermal play types in the convection-dominated geothermal systems have a resistivity imprint from hydrothermal alteration mineralogy. However, when geothermal systems are fracture or porosity and permeability controlled, low resistivity anomalies are often related to the relating geological structures instead of to alteration mineralogy.

Conduction-dominated geothermal play types

For conduction-dominated type geothermal systems, the applicable resistivity is often dominated by the porosity and permeability of the geological structures, although temperature and alteration mineralogy might play a role as well. These systems are generally located in stable tectonic regions with thick

sedimentary sequences. In many of these cases resistivity imaging as sole geophysical method does not sufficiently distinguish the layered sediments and geophysical methods such as seismics, which do not detect permeability and porosity or temperature, are often utilized as well.

Examples of this can be found at Groß-Schönebeck in Germany and at Skier-niewice in Poland, both located in an intracratonic basin type geothermal play. In Groß-Schönebeck a joint interpretation of magnetotelluric and seismic data was carried out to accurately interpret the geology of the site. The targeted reservoir formations are deep sandstones and volcanic strata, hosting aquifers and heated by a granitic intrusive body. Low resistivity structures in this study are related to fracture anhydrites, resulting in enhanced permeability [Muñoz *et al.*, 2010; Muñoz, 2014]. The geology of the geothermal system at Skierniewice is purely sedimentary and consists of at least 8 kilometre of sedimentary geological formation. Using a combination of magnetotelluric and seismic data Bujakowski *et al.* [2010] were able to identify permeable structures coinciding with fractured zones in the subsurface.

As geothermal systems in an orogenic belt play type setting are generally located in small sedimentary basins, similar exploration strategies as for intracratonic basin type plays are utilized. The Lluçmajor aquifer system is an example of such a system. Here magnetotellurics is used to identify two resistive aquifers, a shallow unconfined and a deeper confined, as well as a conductive aquitard separating the two aquifers in the geothermal system. This system is conceptualized by a lower reservoir containing the thermal waters and a fault allowing the vertical flow of waters where the aquitard is thinnest [Arango *et al.*, 2009].

Finally, as basement geothermal play types tend to target very high temperatures, volcanic influences are often present and alteration mineralogy can play a role in the resistivity models of these systems. This can be seen at the geothermal test site of Souz-sous-Forêts, France, targeting a hot granite. Here a resistivity model was made reconstructing the graben including the faults in which the test site is located. The low resistivities in this model are attributed to either clay alteration minerals or pore-space [Geiermann and Schill, 2010].

Another example of a basement play type geothermal system is the Habanero Geothermal EGS Project where a 2-D resistivity model was made. Situated in a stable craton this model is summarized by a three layer model with low resistivities up to 2 kilometre depth for unconsolidated sediments, intermediate resistivities for consolidated sediments between 2 and 4 kilometre depth and high resistivities for the granitic basement at depths greater than 4 kilometre [Didana *et al.*]

3.3 Electromagnetic theory

During a magnetotelluric experiment the time-variations of the electromagnetic fields of the Earth are measured to determine the electrical resistivity structure of the subsurface. The principles of magnetotellurics were first published by *Rikitake* [1948], *Tikhonov* [1950] and *Cagniard* [1953]. They realized that the electric response of the Earth's subsurface could be obtained from large depths by extending the measuring (or sounding) period during a magnetotelluric experiment. This principle is described in the electromagnetic skin depth relation, which is in a simplified form [Spies, 1989; Simpson and Bahr, 2005]:

$$p(T) \approx 500\sqrt{T\rho_a}. \quad (3.1)$$

Here $p(T)$ is the electromagnetic skin depth in metre (m), T is the magnetotelluric sounding period in seconds (s) and ρ_a is the apparent resistivity in Ohm-metre (Ωm).

Bulk electrical resistivity of Earth's materials present in the crust and upper mantle are ranging from 10^{-1} to $10^5 \Omega\text{m}$. Magnetotelluric experiments are typically conducted in the frequency range from 10^{-4} to 10^5 s [Chave and Jones, 2012]. Taking this into account, the skin depth of a magnetotelluric experiment ranges from several tens of meters to several hundreds of kilometres, or in other words from the near-surface deep into the Earth's mantle.

The variations of the Earth's electromagnetic fields measured during a magnetotelluric sounding are initiated by lightning discharges or interactions

between solar plasma and the ionosphere and magnetosphere. Here the former is causing high frequency (≥ 10 Hz) time variations and the latter is causing low frequency (≤ 10 Hz) time variations [*Simpson and Babr, 2005*]. A more detailed description of the sources inducing the time-variations in the electromagnetic fields can for example be found in *Chave and Jones [2012]*.

The relationship between electrical and magnetic fields in a medium is described by the Maxwell equations:

$$\nabla \times \mathbf{E} = -\frac{\partial \mathbf{B}}{\partial t} \quad (3.2)$$

$$\nabla \times \mathbf{H} = \mathbf{j}_f + \frac{\partial \mathbf{D}}{\partial t} \quad (3.3)$$

$$\nabla \cdot \mathbf{B} = 0 \quad (3.4)$$

$$\nabla \cdot \mathbf{D} = \eta_f \quad (3.5)$$

where \mathbf{E} is the electric field in volt per metre (Vm^{-1}), \mathbf{B} is the magnetic induction in tesla (T), \mathbf{H} is the magnetic intensity in ampere per metre (Am^{-1}), \mathbf{D} is the electric displacement in coulomb per square metre (Cm^{-2}), \mathbf{j}_f is the electric current density in ampere per square metre (Am^{-2}), and η_f the electric charge density in coulomb per cubic metre (Cm^{-3}).

Assuming linear constitutive relationships in the material properties of the medium and considering that time-varying displacement currents are negligible, electric and magnetic fields can be related through the constitutive equations:

$$\mathbf{j}_f = \sigma \mathbf{E} \quad (3.6)$$

$$\mathbf{D} = \varepsilon \mathbf{E} \quad (3.7)$$

$$\mathbf{B} = \mu \mathbf{H} \quad (3.8)$$

where σ is the electrical conductivity in siemens per metre (Sm^{-1}), ε is the electrical permittivity in farads per metre (Fm^{-1}), and μ is the magnetic permeability in henries per metre (Hm^{-1}).

Furthermore, considering an isotropic medium, i.e. electric permittivity ε and electrical conductivity σ are all scalars, as well as assuming a free space magnetic permeability μ_0 , a set of Maxwell equations becomes available which can be used for a wide range of geophysical problems including magnetotellurics [*Chave and Jones, 2012*].

3.4 The magnetotelluric transfer function

Assuming a time-varying quasi-uniform horizontal magnetic field above the surface of the Earth, inducing an electric field within the Earth, the relation between the electric and magnetic fields at the surface of the Earth can be described by the “magnetotelluric transfer function” \bar{Z}

$$E_h = \bar{Z} \cdot B_h \quad (3.9)$$

where E_h and B_h are the horizontal electric and magnetic fields in the spectral domain. The magnetotelluric transfer function is the ultimate target during a magnetotelluric survey. It is estimated from the measured horizontal electric and magnetic fields.

A similar relationship between the horizontal and vertical magnetic fields can be formulated as

$$B_z = T \cdot B_h \quad (3.10)$$

where B_z is the vertical magnetic field and T is the vertical magnetic transfer function, or Tipper.

Taking the Maxwell equations describing the behaviour of electromagnetic fields in a polarisable, magnetisable medium as well as the constitutive equations, as given in Equations 3.2 to 3.8, the magnetotelluric transfer function can be derived.

For magnetotellurics it can be assumed that the Earth is isotropic, and that variations in the magnetic permeabilities μ and the electrical permittivities ε of the rocks are negligible compared to the variations in electrical resis-

tivity [Simpson and Babr, 2005]. Following these assumptions, the Equations 3.2 to 3.5 can be reformulated to

$$\nabla \times \mathbf{B} = \mu_0 \sigma \mathbf{E} \quad (3.11)$$

$$\nabla \cdot \mathbf{E} = \eta_f / \varepsilon_0 \quad (3.12)$$

where μ_0 and ε_0 are respectively the free-space values of the magnetic permeability ($\mu_0 = 1.2566 \times 10^{-6} \text{ Hm}^{-1}$) and the electrical permittivity ($\varepsilon_0 = 8.85 \times 10^{12} \text{ Fm}^{-1}$). Furthermore, as displacement currents are negligible with respect to typical magnetotelluric sounding periods, the left hand side of Equation 3.11 can be set to zero. Assuming a homogeneous half-space and that no current sources exist within the Earth, Equation 3.12 can be set to zero as well.

According to Faraday's law (Equation 3.2) a time-varying primary magnetic field induces a circulating electric field. The axis of the induced electric field is directed in the same orientation as the primary magnetic field. This electrical field will, following Ampere's law (Equation 3.3), in turn induce a circulating secondary magnetic field, with its axis directed perpendicular to the primary magnetic field. Assuming a plane wave, e.g. the incident magnetic field is planar, the electric and magnetic fields can be expressed as diffusive harmonic waves through the Earth. Since diffusion is a three-dimensional process, magnetotelluric soundings are in fact measuring volumetric averages of the Earth's material properties.

Using the assumptions discussed before and considering a layered Earth, $\nabla \cdot \mathbf{E} = 0$. This implies that only horizontal electric fields are induced. Taking the curl of Equation 3.2 and applying this model yields

$$\nabla^2 \mathbf{E} = \mu_0 \sigma \frac{\partial \mathbf{E}}{\partial t} = i\omega \mu_0 \sigma \mathbf{E}. \quad (3.13)$$

To arrive at the magnetotelluric transfer function an insulating uniform half-space at $z = 0$ is considered and Equation 3.2 for the x -component reduces to

$$\frac{\partial E_x}{\partial z} = -k E_x = -\frac{\partial B_y}{\partial t} = -i\omega B_y \quad (3.14)$$

in which $k^2 = i\omega\mu_0\sigma$. Equation 3.14 linearly relates the horizontal magnetic to the horizontal electric fields. This leads to the formulation of the magnetotelluric transfer function for the horizontal electric field in the x -direction and the horizontal magnetic field in the y -direction:

$$Z_{xy} = \frac{E_x}{B_y}. \tag{3.15}$$

Similarly, equations can be derived for the relations between all horizontal electromagnetic field directions which leads to the definition of the magnetotelluric transfer function:

$$\begin{pmatrix} E_x \\ E_y \end{pmatrix} = \begin{pmatrix} Z_{xx} & Z_{xy} \\ Z_{yx} & Z_{yy} \end{pmatrix} \cdot \begin{pmatrix} B_x \\ B_y \end{pmatrix}. \tag{3.16}$$

Since in a 2-D case $Z_{xx} = Z_{yy} = 0$ and considering Equations 3.14 to 3.16, the horizontal electric and magnetic fields for a uniform half-space can be related as

$$C = \frac{1}{k} = \frac{E_x}{i\omega B_y} = -\frac{E_y}{i\omega B_x}. \tag{3.17}$$

Here C is also known as the Smucker-Weidelt C -response. Knowing that the conductivity is the reciprocal of resistivity, the apparent resistivity ρ_a , as a function of frequency, can now be directly calculated from Equation 3.17

$$\rho_a = \frac{1}{\sigma} = \mu_0\omega|C|^2. \tag{3.18}$$

3.4.1 Properties of the magnetotelluric transfer function

Besides resistivity and phase the magnetotelluric transfer function is known to have other properties containing information about the subsurface. Examples can be found in the transverse magnetic mode (TM-mode) and transverse electric mode (TE-mode), the rotational invariants, as well as in the induction arrows.

TM-mode and TE-mode

The TM-mode and TE-mode can be described by considering a discontinuity in a 2-D Earth, for example a infinite vertically orientated dyke as illustrated in Figure 3.3. Since the current should be conserved across a discontinuity, the incident electric field E_x should also be discontinuous. All other fields are continuous and because there are no along-strike variations in the conductivity, the TM-mode (Equation 3.19) and TE-mode (Equation 3.20) are:

$$\left. \begin{aligned} \frac{\partial B_x}{\partial y} &= \mu_0 \sigma E_z \\ -\frac{\partial B_x}{\partial z} &= \mu_0 \sigma E_y \\ \frac{\partial E_z}{\partial y} - \frac{\partial E_y}{\partial z} &= i\omega B_x \end{aligned} \right\} \text{TM-mode.} \quad (3.19)$$

$$\left. \begin{aligned} \frac{\partial E_x}{\partial y} &= \frac{\partial B_z}{\partial t} = i\omega B_z \\ \frac{\partial E_x}{\partial z} &= \frac{\partial B_y}{\partial t} = -i\omega B_y \\ \frac{\partial B_z}{\partial y} - \frac{\partial B_y}{\partial z} &= \mu_0 \sigma E_x \end{aligned} \right\} \text{TE-mode.} \quad (3.20)$$

In the example with a vertical dyke of infinite length as shown in Figure 3.3, the TM-mode, describing currents flowing perpendicular to the strike, is discontinuous at the conductive discontinuity. Since the conductivity is not varying along the discontinuity the TE-mode, describing currents flowing parallel to the strike, is continuous.

Rotational invariants

The magnetotelluric transfer function \bar{Z} maps B_h onto E_h without defining a horizontal coordinate system. However, when individual tensor elements, such as Z_{xy} or Z_{yx} , are considered, the definition of a coordinate system is required. Consequently, the coordinate representation of \bar{Z} depends on the orientation of the coordinate system used.

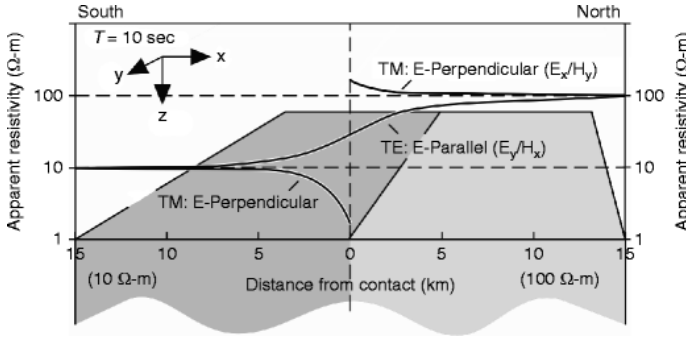


Figure 3.3: Apparent resistivity response of the TM-mode and TE-mode versus distance from a infinite vertical conductivity discontinuity [Simpson and Bahr, 2005].

Equation 3.16 represents the magnetotelluric transfer function orientated according to the coordinate system x, y . The magnetotelluric transfer function orientated in a x', y' coordinate system rotated clockwise through an angle α is then represented by

$$\bar{Z}'(\alpha) = \bar{R}(\alpha) \cdot \bar{Z}(\alpha) \cdot \bar{R}(-\alpha) \tag{3.21}$$

where $\bar{R}(\alpha)$ is the rotation matrix

$$\bar{R}(\alpha) = \begin{pmatrix} \cos\alpha & \sin\alpha \\ -\sin\alpha & \cos\alpha \end{pmatrix}. \tag{3.22}$$

Equation 3.21 can be written out explicitly for the individual components of the magnetotelluric transfer function, for example for the Z_{xy} or Z_{yx} components Equation 3.21 becomes

$$Z'_{xy}(\alpha) = Z_{xy} \cos^2\alpha - (Z_{xx} - Z_{yy}) \sin\alpha \cos\alpha - Z_{yx} \sin^2\alpha \tag{3.23}$$

$$Z'_{yx}(\alpha) = Z_{yx} \cos^2\alpha - (Z_{xx} - Z_{yy}) \sin\alpha \cos\alpha - Z_{xy} \sin^2\alpha. \tag{3.24}$$

The magnetotelluric transfer function has a number of properties, or so-called rotational invariants, that hold for any orientation of the horizontal

coordinate system. These rotational invariants can for example be used as dimensionality indicators or as a first guess for the resistivity structure of the subsurface. A simple example of such a rotational invariant can be deduced from Equation 3.23

$$Z'_{xy}(\alpha) - Z'_{yx}(\alpha) = Z_{xy} - Z_{yx} \quad (3.25)$$

which shows that the off-diagonal elements of \bar{Z} are invariant under rotation.

Induction arrows

The vector representation of the ratios of the real and imaginary parts of the vertical to horizontal magnetic field components is called the induction arrow. Induction arrows are commonly used to assess if there are lateral variations in conductivity.

3.5 Processing magnetotelluric data

To recover the resistivity of the subsurface in the spectral domain, \bar{Z} has to be estimated from Equations 3.9 or 3.16. In the case of actual magnetotelluric measurements, \mathbf{E} and \mathbf{B} contain noise and not only \bar{Z} but also its uncertainty $\delta\bar{Z}$ has to be estimated. Similarly, the uncertainty for the vertical magnetic transfer function should be estimated.

The magnetotelluric transfer function (Equation 3.9) and the vertical magnetic transfer function (Equation 3.10) can in the spectral domain be generalized using the expression:

$$X = Z_1 \cdot Y_1 + Z_2 \cdot Y_2 \quad (3.26)$$

where X is the predicted channel associated with either E_x , E_y or B_z and Y_1 and Y_2 being the predicting channels B_x and B_y . Z_1 and Z_2 are the magnetotelluric transfer functions of a linear system of equations, e.g. Z_{xx} and Z_{xy}

associated with E_x , B_x , and B_y . The magnetotelluric transfer function can be estimated following:

$$\bar{Z} = (E \otimes B^*) \cdot (B \otimes B^*)^{-1} \tag{3.27}$$

where \otimes is the outer product and $*$ denotes the complex conjugate.

At this point it is necessary to mention that in magnetotelluric data processing the raw time-dependent magnetotelluric data is transformed to the frequency domain. To fully utilize all measured frequencies, the time-series are decimated¹, creating a number of time-dependent magnetotelluric data sets with decreasing sampling rates. Depending on the sampling rate and the number of samples present, each decimation level spans a number of frequencies. Following, the individual samples are stacked along pre-defined overlapping time-windows. The magnetotelluric data is smoothed by applying for example a running average filter to the stacked time windows. Finally, the stacked time-windows are transformed to the frequency domain using a direct or fast Fourier transform. Consequently the auto- and cross-spectra in Equation 3.27 comprise a number of stacked and smoothed Fourier coefficients of the magnetotelluric data. It is important to realize that the decimation scheme, window length, type of smoothing filter are all choices affecting the final processing result (see Chapter 4).

If cultural electromagnetic noise (see Section 3.8) is included in the measurements, Equation 3.26 becomes

$$Z = \frac{(Y_0 + n_Y)}{(X_0 + n_X)} \tag{3.28}$$

where X_0 and Y_0 are the predicted respectively predicting channels without noise, and n_X and n_Y are the recorded noise in these channels.

As solving this system of equations using the least-squares principle often delivers unreliable results when applied to real magnetotelluric data, it is hardly used in practice [Chave and Jones, 2012]. Robust processing approaches, such as introduced by Egbert and Booker [1986]; Chave and Thomson [1989, 2004];

¹The process of reducing the sampling rate of the measured signal is called *decimation*.

Larsen et al. [1996], are used instead to estimate the magnetotelluric transfer function. These approaches utilize unbiased statistical estimators and data-adaptive weighting-schemes for the calculation of the magnetotelluric transfer function. In robust processing approaches the norm of the errors ε in $X = (Z_1 \cdot Y_1 + Z_2 \cdot Y_2) + \varepsilon$ is minimized without letting the extreme outliers dominate the result [*Chave and Jones*, 2012]. A generalization of the robust processing approaches is described in the following:

- 1 The least-squares estimate of the magnetotelluric transfer function is computed.
- 2 The residual r and the residual sum of squares are calculated for each channel: $r = X - (Z_1 \cdot Y_1 + Z_2 \cdot Y_2)$. Here, Z_1 and Z_2 are the least-squares estimate of the magnetotelluric transfer function. At this point a scale factor to make r independent of the size of the input data, is calculated as well.
- 3 The weights and the chosen estimate, e.g. M-estimate [*Chave and Thomson*, 1989] or bounded influence estimate [*Chave and Thomson*, 2004], are computed.
- 4 Steps 1 to 3 are repeated until the change in the residual sum of squares is below 1%
- 5 The data points with zero weight are eliminated from the data.
- 6 Again, steps 1 to 3 are repeated until the change in the residual sum of squares is below 1%, but this time with a fixed scale factor.
- 7 The data fit of this final estimate of the magnetotelluric transfer function to the measured magnetotelluric data is evaluated and the confidence bands are calculated.

To optimize the estimated magnetotelluric transfer function several processing methods are available which can be applied in addition to or instead of the robust processing approaches. Most important and used in almost every magnetotelluric survey is the remote reference method [*Gamble et al.*, 1979]. The remote reference method utilizes the plane wave assumption by simultaneously measuring the horizontal magnetic field (\mathbf{B}_R) at a remote station.

Assuming uncorrelated magnetic noise between the local and the remote magnetotelluric station, the noise in the local station can be eliminated by substituting the remotely recorded magnetic field in Equation 3.27

$$\bar{Z} = (E \otimes \mathbf{B}_R^*) \cdot (\mathbf{B} \otimes \mathbf{B}_R^*)^{-1}. \quad (3.29)$$

As it is assumed that the magnetic noise recorded at the local and remote stations is uncorrelated, $\mathbf{n}_B \cdot \mathbf{n}_{B_R} = 0$, and the noise term disappears in Equation 3.29.

Coherence-sorting is incorporated into most commercial processing software packages to distinguish signal from noise. Coherence-sorting is an easy to implement approach that evaluates the coherence between input and output channels by utilizing the linear relationship of Equation 3.26, and is applied before the estimation of the magnetotelluric transfer function. Consequently, high coherences indicate good quality data, while a poor quality data has a low coherence. During processing one can for example decide to remove all samples with a coherence below 0.9 from the magnetotelluric data set. Although practical, this method is not always effective [Jones *et al.*, 1989].

3.6 Distortion of the magnetotelluric signal

It is known that small near-surface conductive inhomogeneities and topography can cause distortion of the electromagnetic signal [Jiracek, 1990; Sternberg *et al.*, 1988]. Additionally large scale regional structures, like the coastline, a large mountain range in the vicinity of the survey area or the dominant strike direction of geological structures, can cause a less well understood distortion of the electromagnetic fields [Chave and Jones, 2012].

3.6.1 Galvanic distortion

A well known example of galvanic distortion, induced by amongst others near-surface inhomogeneities or topography, is the *static shift effect* [Sternberg *et al.*, 1988; Árnason, 2015]. Its effect on the magnetotelluric data can best be de-

scribed by a relative upward or downward shift in the resistivity amplitude of the magnetotelluric transfer function from station to station, while the shape of the station's responses remains comparable (see Figure 3.4). As the static shift effect affects the resistivity model resulting from the measured magnetotelluric data, mitigation measures are necessary.

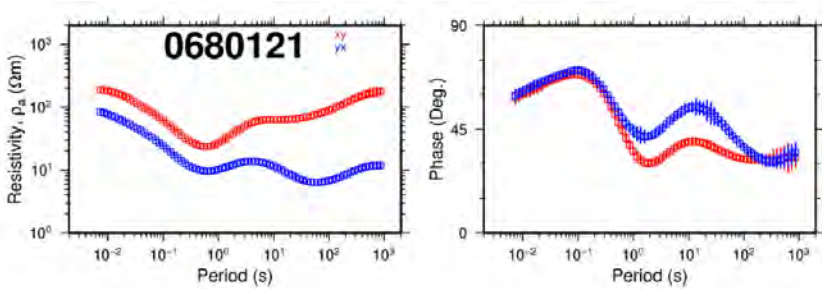


Figure 3.4: Static shift effect in a magnetotelluric sounding. Here recognized in the large separation of the XY and YX resistivity curves at periods below 1 s. [Árnason *et al.*, 2010].

Several approaches are available to correct for the static shift. Árnason *et al.* [2010] for example, uses 1-D TEM² measurements to iteratively shift the invariant³ of the magnetotelluric data towards the TEM response under the assumption that the TEM response reflects the true 1-D resistivity of the shallow subsurface. In other cases the magnetotelluric response is corrected by mapping the TEM apparent resistivity versus time to the magnetotelluric apparent resistivity versus period [Sternberg *et al.*, 1988]. Another approach is to correct for the static shift effect by smooth regularized joint inversion of the magnetotelluric data and static shifts [deGroot Hedlin, 1991; Sasaki and Meju, 2006]. Ultimately, the last strategy to mitigate for the static shift effect is by incorporating the topography into the model mesh, under the condition of suf-

²Transient Electromagnetics (TEM) is a controlled-source electromagnetic method which measures a 1-D apparent resistivity versus time response of the shallow subsurface.

³Here, the invariant of the magnetotelluric data is the average of the Z_{xy} and the Z_{yx} components of the magnetotelluric transfer response. Generally computed by taking the geometric mean of the apparent resistivities ρ_{xy} and ρ_{yx} and the arithmetic mean of the phases of the two. The magnetotelluric response is assumed to be 2-D and rotated to its principal axis, e.g. $Z_{xx} = Z_{yy} = 0$

ficiently high resolution, and assuming that the 3-D inversion accommodates the correction.

Since several methods for static shift correction are available, it is often debated in geothermal industry which method is “best”. On the basis of synthetic data it is concluded by *Ledo et al.* [2002] that static shift effects should be removed from the data prior to inversion. On the other hand *Cumming and Mackie* [2010] advocate that by incorporating the topography into the model mesh, under the condition of a sufficiently high resolution, the 3-D inversion accommodates this correction. It is worthwhile mentioning that although effective in many cases, not all available methods can be applied under all circumstances.

3.7 Dimensionality

Dimensionality distortions in the electromagnetic signal are caused by 2-D or 3-D structures in the subsurface and will be reflected in the chosen survey design and modelling strategy. As discussed by *Ledo et al.* [2002]; *Ledo* [2005], and *Cumming and Mackie* [2010] care should be taken when the dimensionality of the structures in the subsurface is different from the dimensionality of the modelling code used. In those instances, inaccurate resistivity structures might be resolved by the modelling, leading to an erroneous geological interpretation of the inversion model. The dimensionality of a magnetotelluric data set can be assessed using tools such as induction arrows, rotational invariants, dimensionality indicators and Groom and Bailey distortion parameters [*Ledo et al.*, 2002].

Independent of the dimensionality of the data, the main resistivity structures resolved by either 1-D, 2-D and 3-D inversions are all credible [*Ledo et al.*, 2002]. To illustrate this, a resistivity cross-section resulting from 1-D, 2-D and 3-D inversions of magnetotelluric data acquired in the Glass Mountain geothermal field in the USA is shown in Figure 3.5. In Figure 3.5 it can be observed that although the main resistivity structures are resolved by all three models, the differences between the models are significant. Differences in depth and

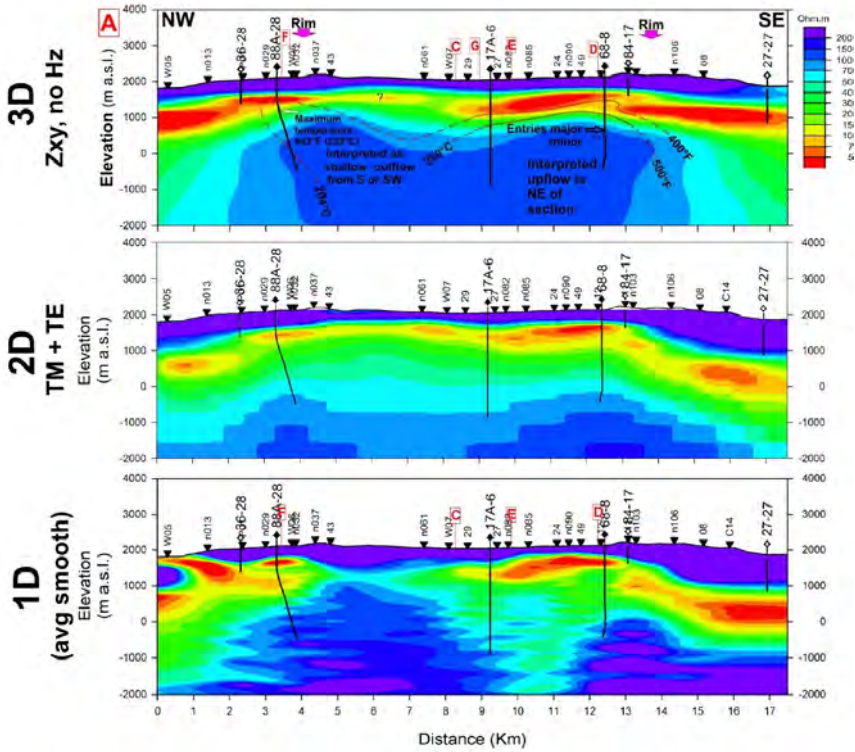


Figure 3.5: Cross-section with 1-D, 2-D and 3-D resistivity inversions of the Glass Mountain geothermal field. Wells, isotherms and magnetotelluric stations are given. Note the differences in shape and depth of the conductive clay cap and resistive geothermal reservoir between the inversion. For details see *Cumming and Mackie* [2010].

shape of the conductive clay cap and the resistive geothermal reservoir are apparent. The elongated structures in the 1-D resistivity cross-section are caused by the dimensionality of the magnetotelluric data.

A regularly applied strategy in geothermal exploration to determine the reliability of a 2-D or 3-D inversion is to compare the resistivity model with a resistivity model of stitched 1-D inversions [*Cumming and Mackie*, 2010]. With respect to geothermal exploration *Cumming and Mackie* [2010] point out that for accurate well targeting a full assessment of at least 1-D and 2-D in-

version models, but preferably 1-D and 3-D inversion models should be carried out. Care should be taken when utilizing this strategy, as the inverted component(s) of the magnetotelluric transfer function are likely to influence the result. Additionally, *van Leeuwen et al.* [2016] suggest to run at least two 3-D inversions using different inversion codes for accurate well targeting.

3.8 Cultural electromagnetic noise

A magnetotelluric sounding can also be distorted by man-made noise, often referred to as “cultural electromagnetic noise”. This electromagnetic noise can be caused by for example power lines, subsurface pumps, anti-corrosion systems in buried pipelines, wind turbines, electric trains, electric fences, and mining areas. As the population and the electrification of the Earth are growing, the effects of cultural electromagnetic noise on magnetotelluric surveys will increase as well. There are already many areas where it is virtually impossible to carry out a magnetotelluric survey.

Cultural electromagnetic noise can be divided into *passive* and *active* electromagnetic noise [*Szarka*, 1988]. Besides these two types, a third type of cultural noise can be recognized, caused by for example passing vehicles or other artificial vibrations of the subsurface, this is often referred to as motional noise [*Szarka*, 1988]. Logically, in densely populated areas the amount of cultural noise sources will be greater than in quiet areas. It is also likely that in densely populated areas the amplitudes of the electromagnetic cultural noise will be larger, sometimes exceeding the amplitude of the natural electromagnetic signal [*Junge*, 1996].

Passive noise sources such as roads, ditches, power lines, and pipelines, are redistributing the electromagnetic source field. Depending on the size of their local electromagnetic field, the influence of passive noise sources on the measurements can be avoided or minimized by placing the magnetotelluric stations a considerable distance away. Some of these structures can also serve as an active noise source when inducing an electromagnetic (secondary) field into the subsurface.

To illustrate this, a power line serves as a primary source, potentially generating passive noise, and the transmitted electrical power via this power line will generate active noise as it induces a secondary electromagnetic field. To put it more simply, all power consuming devices are potentially active noise sources [Junge, 1996]. Examples of active noise sources are Direct Current (DC) railways, electric power transmission lines, subsurface pumping stations, and anti-corrosion systems in buried pipelines. Active noise will heavily disturb the measured electromagnetic spectra. When measuring far away enough from the noise source, its effect will be decreased, as illustrated in Figure 3.6.

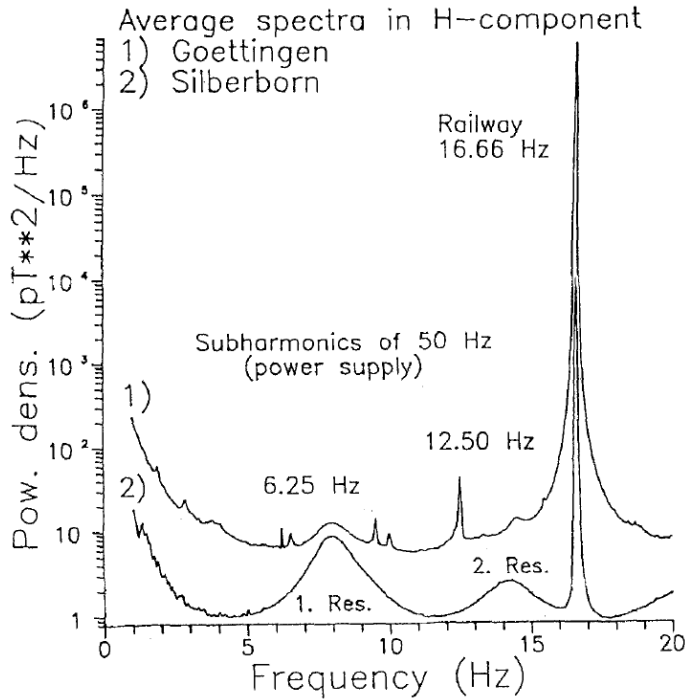


Figure 3.6: Electromagnetic noise spectra from two locations in Germany [Junge, 1996].

In Figure 3.6 the spectra of two locations 30 km apart are shown. At site 1, located close to an industrial region, the railway, the (sub)harmonics of the power lines generating an electromagnetic signal at 50 Hz as well as several minor peaks are easy to recognize and have a very large amplitude, while at site 2, which is far away from any industrial activity, only the railway is observed in the spectra [Junge, 1996].

As it is not always possible to avoid all sources of cultural electromagnetic noise during a magnetotelluric field survey, cultural electromagnetic and other noise effects must be eliminated from the magnetotelluric data during processing to obtain an accurate resistivity model of the subsurface.

When the amplitude of the recorded noise is larger than the electromagnetic signal, it is difficult to reconstruct the magnetotelluric signal. In cases where the wavelengths of the noise in the magnetic fields at the local and the remote site are correlated, the contribution of the noise to the estimated magnetotelluric transfer function will be significant (see Equation 3.27). Noise effects in magnetotelluric data are generally removed or down-weighted using a selection of processing techniques ranging from the time-consuming process of the visual inspection and cleaning of the raw time-series data, the (automatic) evaluation of statistical parameters in the frequency domain, and the remote reference method, to robust processing methods as described in Section 3.5.

3.9 Data acquisition

Magnetotelluric surveys are conducted using data loggers measuring the five, B_x , B_y , B_z , E_x , and E_y , electromagnetic fields. The electric field is measured using electrodes set up as two perpendicular dipoles, often orientated North-East and South-West. The electrodes are buried to account for day-night temperature variations in the upper few tens of centimetres of the subsurface. Magnetic coils measure the three components of the magnetic field. Two of the magnetic coils are positioned horizontal with a perpendicular orientation, measuring the horizontal magnetic fields, while a third magnetic coil is positioned vertical, measuring the vertical magnetic field. Since accurate and stable positioning

of the coils is important, the coils are buried in shallow holes to prevent any external disturbances. The general layout of a magnetotelluric station is shown in Figure 3.7. A GPS-receiver is connected to the data logger for time synchronization with the remote reference station. To power the data logger while measuring, a battery is also part of the setup of a magnetotelluric station.

During a magnetotelluric survey a remote station is often recording at an electromagnetically quiet location measuring simultaneously with the local magnetotelluric stations, see Section 3.5. Finding a good, quiet location for the remote reference station is always worth the effort for a successful magnetotelluric field campaign.

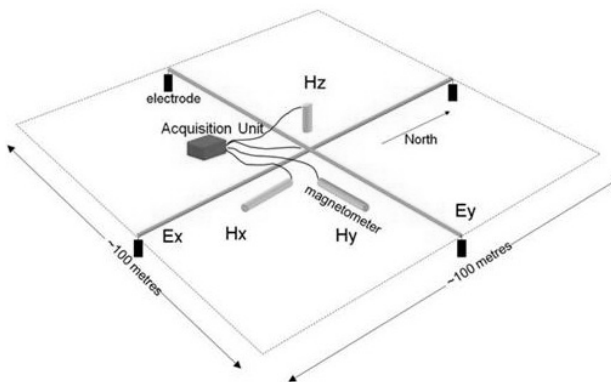


Figure 3.7: Generalized layout of a magnetotelluric station showing electric dipoles, magnetic coils, data logger, battery and GPS-receiver.

Depending on the depth of the target of the magnetotelluric survey and the local bulk electrical resistivity of the Earth, the magnetotelluric sounding period varies from a few hours to several days, months or years. A possibility is to use Equation 3.1 (see Section 3.3) to estimate the desired magnetotelluric sounding period for a survey. A more sophisticated strategy is to determine the desired period range of the survey and adjust the magnetotelluric sounding period accordingly. The period T can be determined using

$$T = \mu_0 \sigma \pi p^2. \quad (3.30)$$

Equation 3.30 is a reformulation of the inverse of Equation 3.18 to compute the bulk apparent resistivity. Here σ is the bulk electrical conductivity of the subsurface in Sm^{-1} . To explore a geothermal reservoir from 0.5 to 5 km depth with an average bulk resistivity of $1 \Omega\text{m}$, a period $T = 1$ to 100 s is necessary. In practice the resistivity of the surface is not homogeneous and this simple computation becomes more complex. For geothermal exploration purposes it is common to record magnetotelluric data for roughly 18 to 24 hours. This sounding period corresponds, depending on the bulk resistivity of the Earth, with penetration depths up to several kilometres.

The survey grid layout is determined by the local topography, size of the survey area, the available budget and time, and the expected dimensionality of the local geological structures. In geothermal exploration practice a few profile lines or a semi-regular grid layout with a site spacing of a half to two kilometres is the norm.

One factor influencing the magnetotelluric data quality is the accuracy of the station layout in the field. The easiest way to acquire good data is to work accurately and assure that the field crew is working precisely. Regularly sites are set up too close to possible (cultural) electromagnetic noise sources and with an inaccurate positioning of the coils or electrodes. Another straightforward mitigation procedure for distortion of the electrical field is ensuring good conductance between the electrodes and the Earth. Preparing strategies to tackle the possible difficulties of the terrain in the survey area and scouting the station locations prior to the field work or station occupation often increases the average data quality of the magnetotelluric survey.

Finally, the strength of the magnetic field is influenced by the space weather. For the magnetic field this is forecasted and reported online as the Kp-index. The higher the Kp-index at a location, the stronger the local magnetic field strength, and the more likely the acquired magnetotelluric data is of good quality. Consequently, if possible, a magnetotelluric survey should be carried out during a period of forecasted high Kp-indices. The altitude at which the magnetotelluric survey is conducted also influences the magnetic field strength.

At high altitudes, the magnetic field strength is generally weaker. This should be accounted for by adjusting the recording settings of the data logger in the field.

3.10 Inversion

To estimate the subsurface resistivity distribution in the Earth's subsurface, the observed magnetotelluric data needs to be inverted. The process of inversion is iterative and is aimed at finding one or more resistivity models whose predicted response matches the observed data as good as possible. Depending on the properties of the magnetotelluric response and the dimensionality of the local geology the inversion can be done in 1-D, 2-D or 3-D. The resulting inversion model is non-unique, i.e. the responses of several resistivity models fit the observed magnetotelluric data equally well. Consequently the inversion of magnetotelluric data is inherently unstable, or ill-posed, and the solution estimated must be constrained using other sources of information.

Although an extensive discourse on inversion theory is beyond the scope of this dissertation, a condensed formulation of the inverse problem is given. Following, three different 3-D inversion codes are considered: 1) *Egbert and Kelbert* [2012], 2) *Siripunvaraporn et al.* [2005], and 3) *Mackie and Watts* [2012].

The inverse problem can be formulated as

$$\mathbf{d} = F(\mathbf{m}) + \mathbf{e} \quad (3.31)$$

where \mathbf{d} is the data space, a vector containing the observed data, e.g. the magnetotelluric transfer function, the apparent resistivity and phase, or the conductivity. The vector \mathbf{e} contains the data errors of \mathbf{d} . The model space \mathbf{m} represents the real resistivity values of the Earth, while F is a forward function predicting the theoretical values of the data for a hypothetical (model) representation of the Earth. In the theoretical case $\mathbf{e} = 0$, the solution to Equation 3.31 becomes $\mathbf{m} = F^{-1}(\mathbf{d})$, hence the term inverse problem.

As finding F^{-1} is not considered realistic, the challenge becomes to find the best estimate of \mathbf{m}

$$\tilde{\mathbf{m}} = G(\mathbf{d}). \quad (3.32)$$

Here G is a meaningful substitute of F^{-1} .

Although in electromagnetics the solution to the inverse problem is not linear, it is illustrative to discuss it here. For finite-dimensional model spaces, the forward function is a linear transformation and can be expressed as

$$F(\mathbf{m}) = \mathbf{A}\mathbf{m} \quad (3.33)$$

where \mathbf{A} is a $N \times M$ matrix with the vectors of the function a_i^T as its rows. The linear operations carried out by F are defined by the right-hand side of Equation 3.33.

An approach to solve the non-linear inverse problem is to linearize it. This is done by expanding the linear Equation 3.33 around a reference model \mathbf{m}_* [Chave and Jones, 2012]. A first-order approximation of the forward function will then be

$$\bar{F}(\mathbf{m}) = F(\mathbf{m}_*) + \mathbf{A}_{m_*}(\mathbf{m} - \mathbf{m}_*). \quad (3.34)$$

In Equation 3.34 \mathbf{A} is the Fréchet derivative of F , where F is a linear transformation. In geophysical inversion theory it contains the partial derivatives of the forward functions F_i and is referred to as the *Jacobian* matrix [Chave and Jones, 2012].

The basis for much geophysical inverse theory is the least-squares estimation [Chave and Jones, 2012]. A least-squared solution is defined as finding the minimum solution of a fitting function, estimating the goodness of the fit between the model and the observed data. This data misfit can be expressed by a penalty function

$$\Phi(\mathbf{m}) = (\mathbf{d} - F(\mathbf{m}))^T \bar{\mathbf{W}} (\mathbf{d} - F(\mathbf{m})) \quad (3.35)$$

where \bar{W} is the weight matrix containing pre-assigned weights, or the data covariance matrix [Siripunvaraporn, 2012; Egbert and Kelbert, 2012], and $\mathbf{r} = \mathbf{d} - F(\mathbf{m})$ is the residual vector. Minimizing $\Phi(\mathbf{m})$ is done by starting from some initial model and iteratively solving the inverse problem until a pre-defined data misfit is reached.

The above holds for problems which are mixed-determined, meaning that some parts of the solution are constrained by the observed data, while others are not. In practice most electromagnetic inversion problems are under-determined. In an under-determined problem the number of unknown parameters is larger than the number of observations $N > M$. An approach to define a well-posed problem⁴ is the damped least-squares estimate [Chave and Jones, 2012].

$$\Omega(\mathbf{m}) \leq \mu \quad (3.36)$$

in which $\mu \neq 0$ and Ω is the positive-valued *stabilizing functional*. This functional is designed to penalize undesired properties of \mathbf{m} . Regularization of the solution of the inverse problem comprises finding the minimum solution of $\Omega(\mathbf{m})$ subject to Equation 3.36 [Chave and Jones, 2012].

$$\Psi(\mathbf{m}) = \Phi(\mathbf{m}) + \lambda\Omega(\mathbf{m}) \quad (3.37)$$

where $\lambda > 0$ is the *regularization parameter* which is determined by μ .

Finally, the stabilizing functional $\Omega(\mathbf{m})$, which is a measure of the spatial roughness of a model, is defined as [Chave and Jones, 2012]

$$\Omega(\mathbf{m}) = (\mathbf{m} - \mathbf{m}_0)^T \bar{K} (\mathbf{m} - \mathbf{m}_0) \quad (3.38)$$

where \mathbf{m}_0 is an initial or starting model and \bar{K} is a positive semi-definite matrix, also referred to as the model covariance matrix [Siripunvaraporn, 2012; Egbert and Kelbert, 2012]. The structure of penalty \bar{K} can be interpreted as an inverse a priori model covariance matrix.

⁴A well-posed problem is when the solution to the problem exists, is unique, and is stable [Hadamard, 1902].

By substituting Equations 3.35 and 3.38 into Equation 3.37, the damped least-squares functional becomes

$$\Psi(m) = (d - F(m))^T \bar{W} (d - F(m)) + \lambda (m - m_0)^T \bar{K} (m - m_0). \quad (3.39)$$

By utilizing different approaches and techniques, the majority of the electromagnetic inversion algorithms try to minimize the damped least-squares functional of Equation 3.39 efficiently.

3.10.1 The three 3-D inversion algorithms

Although they use different approaches, minimizing the functional in Equation 3.39 efficiently is the central aim of the three inversion algorithms considered in this dissertation. The three inversion algorithms discussed are all frequently used in electromagnetic induction studies and are among the current state of the art algorithms available.

The WSINV3DMT inversion algorithm uses a data space Occam approach [Siripunvaraporn, 2012; Siripunvaraporn et al., 2005]. Modelling in the data space has the advantage over modelling in the model space that the matrix to be inverted is of size $N \times N$ instead of a larger matrix of size $M \times M$. Nevertheless, the matrix \bar{J} of size $M \times N$ still has to be solved. Solving this smaller matrix of size $N \times N$ comes with computational advantages [Siripunvaraporn, 2012]. When utilizing the Occam approach the stationary point in

$$\Psi(m, \lambda) = \{(d - F(m))^T \bar{W} (d - F(m)) - \chi^2\} + \lambda (m - m_0)^T \bar{K} (m - m_0) \quad (3.40)$$

is computed in two steps using Equation 3.39. In Equation 3.40 χ^2 is the desired level of misfit.

First, the root-mean-square (rms) misfit⁵ is brought down to the level of χ^2 by varying λ . By doing this, the first term on the right hand side in

⁵The root-mean-square or rms misfit is a measure of the fit of the model with respect to the observed data.

Equation 3.40 becomes zero. Second, the model norm is minimized by varying λ while keeping the in the first step computed rms misfit constant. Now the minimum of the second term in the right hand side of Equation 3.39 can be determined and the best fitting resistivity model is computed.

Both ModEM [Egbert and Kelbert, 2012] and the inversion algorithm, “Mackie3D”, developed by Mackie and Watts [2012] and based on Rodi and Mackie [2001], utilize the Non-Linear Conjugate Gradient (NLCG) approach. The difference with conjugate gradient approaches is that the NLCG approach can be directly applied to Equation 3.39 [Siripunvaraporn, 2012; Egbert and Kelbert, 2012; Rodi and Mackie, 2001]. The model is iteratively updated following

$$\mathbf{m}_{k+1} = \mathbf{m}_k + \alpha_k \mathbf{u}_k \quad (3.41)$$

where $k = 1, 2, \dots, n$ is the iteration number and \mathbf{u}_k is the product of a system pre-conditioner $\overline{\mathbf{M}}$ and the gradient of the damped least-squares functional (Equation 3.39) $-\nabla \Psi(\mathbf{m}_k)$. The model is updated when an α is found such that the penalty function $\Psi(\mathbf{m}_k + \alpha_k \mathbf{u}_k)$ is minimized. The NLCG approach is gaining popularity in the 3-D inversion of magnetotelluric data as there is no need to compute large matrices and its consequently computational efficiency [Siripunvaraporn, 2012].

Additionally, the inversion algorithm Mackie3D utilizes Finite Integration Technique (FIT) which reformulates the Maxwell equations in their integral form. This strategy defines the electric fields along model cell edges and the magnetic fields normal across model cell faces on a dual orthogonal staggered grid [Mackie and Watts, 2012]. In fact, finite difference is a subset of FIT. Mackie3D solves for the unknown electric grid voltage $\tilde{\mathbf{e}}$

$$\tilde{\mathbf{C}} \overline{\mathbf{M}}_v \overline{\mathbf{C}} \hat{\mathbf{e}} = i\omega m \overline{\mathbf{M}}_\sigma \hat{\mathbf{e}} \quad (3.42)$$

where $\tilde{\mathbf{C}}$ is discrete analogue to the curl operator on the secondary grid, $\overline{\mathbf{M}}_v$ is the material matrix for the inverse of the magnetic permeability, $\overline{\mathbf{M}}_\sigma$ is the material matrix for the conductivity, and $\overline{\mathbf{C}}$ is discrete analogue to the curl

operator on the primary grid [*Mackie and Watts, 2012*]. Equation 3.42 can be expanded of the grid complex and, after adjusting for boundary conditions and the source term, a system of linear equations is achieved.

Assuming a current-free half space and ignoring displacement currents, the right hand side of Equation 3.42 becomes zero. The discretization of a $-\nabla^2$ operator for a homogeneous model is applied to be able to uniquely determine the electric fields in the air [*Mackie and Watts, 2012*].

Where WSINV3DMT and ModEM use the same format for data input and output, Mackie3D uses the WinGLink formats [*GEOSYSTEM SRL, 2008*]. However, as all formats are ASCII, the resistivity models are interchangeable. The version of WSINV3DMT used here cannot include topography into the model, where ModEM and Mackie3D can. In comparison to WSINV3DMT, ModEM is computationally faster. No information is available on Mackie3D as this algorithm is not freely accessible.

4

Quality Index pre-sorting

4.1 Introduction

In 2013, a magnetotelluric survey was carried out to determine the dimensions and depth of a geothermal reservoir for a geothermal project in Çannakale, Western Turkey. The resistivity survey was carried out using both Metronix ADU-07 and Phoenix MTU5A instruments. All stations were measured simultaneously with a remote reference station, and recording took place for approximately 16 hours per station. The reference station was located about 10 km away from the survey area. Initially 51 stations were recorded, while an additional 3 stations were recorded a year later, bringing the total of recorded stations for this survey to 54. A local contractor processed the acquired data using two different processing codes.

Agricultural activity as well as several scattered villages can be found in the survey area. As a consequence, the area is cut through with small roads and power lines. Several wind turbines are also present. These cultural electromagnetic noise sources negatively influenced the quality of the data recorded at several of the magnetotelluric soundings. Tracking the consistency of the field acquisition procedure of the magnetotelluric data set is difficult as instruments of two different makes and two different processing codes were used. Furthermore, the vertical magnetic transfer functions recorded at sites using Phoenix equipment, are of a poor data quality.

To get an uniform data quality for the entire survey, the magnetotelluric data set is reprocessed using a new robust processing routine. This processing routine is written in Matlab and loosely based on the processing routine developed by *Egbert and Booker* [1986]. Without any data editing, the cultural electromagnetic noise in the region is clearly visible in most of the resulting magnetotelluric transfer function estimations, indicating the necessity of additional processing steps. In order to do so, alternative approaches were tested. Amongst these were wavelet processing as proposed by *Garcia and Jones* [2008], the cross-power editing approach as implemented in the proprietary Phoenix software as well as the frequency domain selection scheme described by *Weckmann et al.* [2005]. Although the empirical mode decomposition to process

magnetotelluric data, as described by *Chen et al.* [2012], was considered, a working algorithm was not available and consequently not implemented. As it turned out, the tested approaches were not sufficiently efficient or effective on this particular set of magnetotelluric data. For example, the wavelet processing is very inefficient in Matlab and the Metronix proprietary time-series format is not compatible with the Phoenix proprietary processing software. Of the tested approaches, the frequency domain selection scheme shows the largest potential, but is time-consuming and does not promote a consistent treatment of every individual station.

To be able to process the magnetotelluric data set up to the desired quality efficiently and effectively, a new pre-sorting processing approach was developed. This approach was developed with the frequency selection scheme of *Weckmann et al.* [2005] in mind. During the development, two objectives were formulated: 1) Create a semi-automatic methodology, allowing fast processing. 2) Eliminate those outliers which are not eliminated or sufficiently down-weighted in robust processing methods such as developed by *Egbert and Booker* [1986] and *Chave and Thomson* [2004], to produce practical magnetotelluric transfer function estimations. Ultimately, this approach should allow us to process magnetotelluric data acquired in areas with high levels of cultural electromagnetic noise.

The outline of this Chapter is as follows. In Section 4.2 a brief overview of the theory of robust processing is generalized as is the frequency selection scheme. Following, in Section 4.3 the quality of the magnetotelluric data set is evaluated. The Quality Index Pre-sorting processing approach is introduced in Section 4.4. The results of the Quality Index Pre-sorting reprocessed magnetotelluric data set are presented in Section 4.5 and compared to the commercially processed magnetotelluric data set in Section 4.6. Finally, the Quality Index Pre-sorting reprocessed results are discussed in Section 4.7 after which conclusions about the effectiveness of Quality Index Pre-sorting processing are drawn in Section 4.8.

4.2 Magnetotelluric processing theory

The time variations of the orthogonal components of the electric and magnetic fields can be captured at the surface of the Earth. The response of the Earth to electromagnetic induction can be described by the magnetotelluric transfer function \bar{Z} , which comprises the resistivity structure of the Earth. It is assumed that the horizontal electric and magnetic fields are linearly related by the impedance tensor when observed in the frequency domain.

In the absence of cultural electromagnetic noise the magnetotelluric transfer function in the frequency domain, \bar{Z} is

$$\begin{pmatrix} E_x \\ E_y \end{pmatrix} = \begin{pmatrix} Z_{xx} & Z_{xy} \\ Z_{yx} & Z_{yy} \end{pmatrix} \cdot \begin{pmatrix} B_x \\ B_y \end{pmatrix} \quad (4.1)$$

where E is the electric field in $\text{mV} \cdot \text{km}^{-1}$, B the magnetic field in nT, and Z_{ij} ($i, j = x, y$) the components of the magnetotelluric transfer function \bar{Z} in ms^{-1} . In Equation 4.1 the magnetic field predicts the electric field via \bar{Z} . A typical magnetotelluric data logger has separate channels to measure the individual components of the electromagnetic fields. Therefore, the magnetic field components B are often referred to as the predicting channels while the electric fields E are referred to as the predicted channels.

Similarly to Equation 4.1, the vertical magnetic transfer functions, T_x and T_y , relate the vertical magnetic field to the horizontal magnetic fields

$$B_z = \begin{pmatrix} T_x & T_y \end{pmatrix} \cdot \begin{pmatrix} B_x \\ B_y \end{pmatrix}. \quad (4.2)$$

Equations 4.1 and 4.2 can be generalized using the expression

$$X = Z_1 \cdot Y_1 + Z_2 \cdot Y_2 \quad (4.3)$$

where X is the predicted channel associated with either E_x , E_y or B_z and Y_1 and Y_2 being the predicting channels B_x and B_y . Z_1 and Z_2 are the magnetotelluric

transfer functions of a linear equation system, e.g., Z_{xx} and Z_{xy} , associated with E_x , B_x , and B_y . When E and B are real measurements, noise is measured as well and consequently not only \bar{Z} but also its uncertainty $\delta\bar{Z}$ should be estimated.

The above implies that processing magnetotelluric data is the estimation of the magnetotelluric transfer function \bar{Z} on basis of the measured values of the predicted and predicting channels. The estimation of the magnetotelluric transfer function in the frequency domain is

$$\bar{Z} = (E \otimes B^*) \cdot (B \otimes B^*)^{-1}, \quad (4.4)$$

where \otimes is the outer product and $*$ denotes the complex conjugate.

The easiest way to solve this system of equations is by application of the least-squares principle. The results of least-squares estimation of the magnetotelluric transfer function are, even when applied to noise-free data, often unpredictable [Chave and Jones, 2012]. Therefore the least-squares principle is hardly used in practice and alternative processing approaches have been introduced to estimate the magnetotelluric transfer function as accurately as possible [Gamble *et al.*, 1979; Jones *et al.*, 1989; Larsen *et al.*, 1996; Chave and Thomson, 2004].

The remote reference method was introduced by Gamble *et al.* [1979] and is nowadays used in almost every magnetotelluric survey. This method utilizes the plane wave assumption by simultaneously measuring the magnetic field at a remote station located at a considerable distance away from the local station. It is assumed that both the local and remote magnetic signals are similar and that the recorded electromagnetic noise is uncorrelated between the stations. Following, the electromagnetic noise can be eliminated by substituting the remotely recorded magnetic fields in place of the complex conjugates of the local magnetic fields in Equation 4.4.

Another strategy often applied to distinguish signal from noise is coherence-sorting. This is a pre-sorting strategy applied before the estimation of the magnetotelluric transfer function on basis of the coherence between input and

output channels. Although practical, this method is not always useful [Jones *et al.*, 1989].

Robust processing routines as developed by *Egbert and Booker* [1986], *Chave and Thomson* [1989], *Chave and Thomson* [2004], and *Larsen et al.* [1996] utilize unbiased statistical estimators and data-adaptive weighting-schemes for the calculation of the magnetotelluric transfer function. It was shown by *Jones et al.* [1989] that these robust processing schemes outperformed the other processing approaches available at the time. The robust processing methods operate on the data by minimizing the norm of the measured errors, ε , without letting the extreme outliers dominate the result [Chave and Jones, 2012]. A generalization of the robust processing approaches is described in the following:

- 1 The least-squares estimate of the magnetotelluric transfer function is computed.
- 2 The residual r and the residual sum of squares are calculated for each channel: $r = X - (Z_1 \cdot Y_1 + Z_2 \cdot Y_2)$. Here, Z_1 and Z_2 are the least-squares estimate of the magnetotelluric transfer function. At this point a scale factor to make r independent of the size of the input data, is calculated as well.
- 3 The weights and the chosen estimate, e.g. M-estimate [Chave and Thomson, 1989] or bounded influence estimate [Chave and Thomson, 2004], are computed.
- 4 Steps 1 to 3 are repeated until the change in the residual sum of squares is below 1%
- 5 The data points with zero weight are eliminated from the data.
- 6 Again, steps 1 to 3 are repeated until the change in the residual sum of squares is below 1%, but this time with a fixed scale.
- 7 The data fit of this final estimate of the magnetotelluric transfer function to the measured magnetotelluric data is evaluated and the confidence bounds are calculated.

To optimize the results of the robust processing routine, the processed magnetotelluric data can be pre-sorted. Pre-sorting is a method which can be

applied to magnetotelluric data in the frequency domain, before the estimation of the magnetotelluric transfer function. A well-known example of pre-sorting is to eliminate those Fourier coefficients where the coherence between orthogonal electric and magnetic fields is low. Other properties can be used as well to select poor quality data points. *Weckmann et al.* [2005] utilize statistical properties to pre-sort the magnetotelluric data for single site applications. These properties are:

- the spectral power density,
- the bivariate and partial coherences,
- the polarization directions of the electric and magnetic fields,
- the least-square estimate of the magnetotelluric transfer function, and
- the estimated error of the least-square estimate of the magnetotelluric transfer function.

When plotted as a function of time, the variations in these statistical properties reveal information on the basis of which inconsistent data points can be eliminated to improve the estimate of the magnetotelluric transfer function. This approach requires the independent assessment of all Fourier Coefficients of each frequency of a single magnetotelluric station.

4.3 Data evaluation

As an explanation for the development of the pre-sorting processing approach introduced in this Chapter, the magnetotelluric data set used is briefly evaluated.

Table 4.1: Acquisition parameters of the magnetotelluric survey

Gear	Metronix stations	Phoenix stations
Sampling rates	128 Hz, 512 Hz, 65,536 Hz	15 Hz, 150 Hz, 2400 Hz
Frequency range measured	16,384 Hz - 512 s	600 Hz - 273 s
Magnetotellurics stations	20	34
Remote reference stations	yes	yes
Acquisition time	~16 hours	~16 hours

In Table 4.1 the acquisition parameters of the magnetotelluric survey are listed for both the Phoenix and Metronix measured stations. The sampling rates of the three frequency bands measured by each type of instrument differ, with the Phoenix equipment measuring at lower sampling rates in comparison to the Metronix equipment. This difference in the sampling rates leads to differences in the frequency ranges covered during this survey.

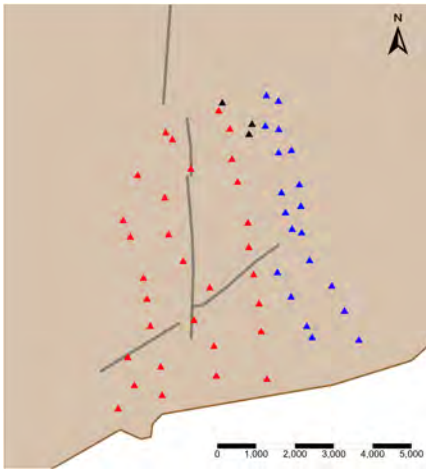


Figure 4.1: Station layout of the 54-station resistivity survey. Red stations are measured using Metronix equipment and blue stations using Phoenix equipment. The black stations were acquired using Phoenix equipment, approximately a year after the main survey. The main faults in the area (grey) and the coast line (brown) are also given.

The stations measured with the Metronix equipment were all located in the eastern part of the survey area and are acquired during the first part of the survey, while the Phoenix equipment recorded data at stations located in the western part of the area during the second part of the survey. The survey layout is illustrated in Figure 4.1. The stations were placed in an irregular grid with an interstation spacing varying from about 250 to 1,200 m. As mentioned, a remote station was recording simultaneously during data acquisition. Consequently, remote reference processing was applied on all stations by the contractor.

The remote reference station of this survey is located at roughly 8.5 kilometres west of the centre of the survey area. The in 2013 recorded remote magnetotelluric data have a relatively good data quality and are suited for remote reference processing. Despite being recorded at the same location, the remote

reference data recorded in 2014 are of insufficient data quality. Consequently the 2015 magnetotelluric stations are processed using the local magnetic fields.

Despite the differences in survey dates, hardware and software used for the two parts of the survey, the apparent resistivity and phase responses are predominantly consistent for all measured stations. The consistency between the Metronix and Phoenix recorded stations is checked by applying the Rho+ algorithm [Parker and Booker, 1996] to the acquired data. A Rho+ [Parker and Whaler, 1981] or the D+ [Parker and Booker, 1996] test is an effective means of testing the consistency between apparent resistivity and phase of 1-D and 2-D magnetotelluric data. Applying the D+ algorithm to the magnetotelluric data showed that in general the phases and resistivities are consistent with each other, see Figure 4.2. In this Figure the station responses and the result of the D+ consistency check of magnetotelluric transfer functions of station P001 measured with Phoenix equipment and station M001 measured with Metronix equipment are compared with each other.

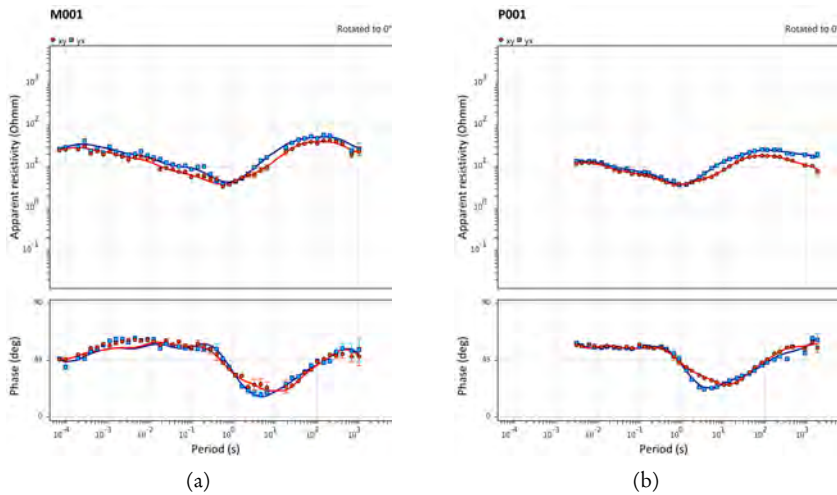


Figure 4.2: Station apparent resistivity and phase responses of Z_{xy} (red dots) and Z_{yx} (blue squares) for a station measured with Metronix equipment ((a) M001) and a station measured with Phoenix equipment ((b) P001). Subsequent Rho+ curves (solid lines) are plotted as well for both stations. These two sites are located about 2,000 m apart from each other. Note the differences in frequency ranges recorded by the two stations.

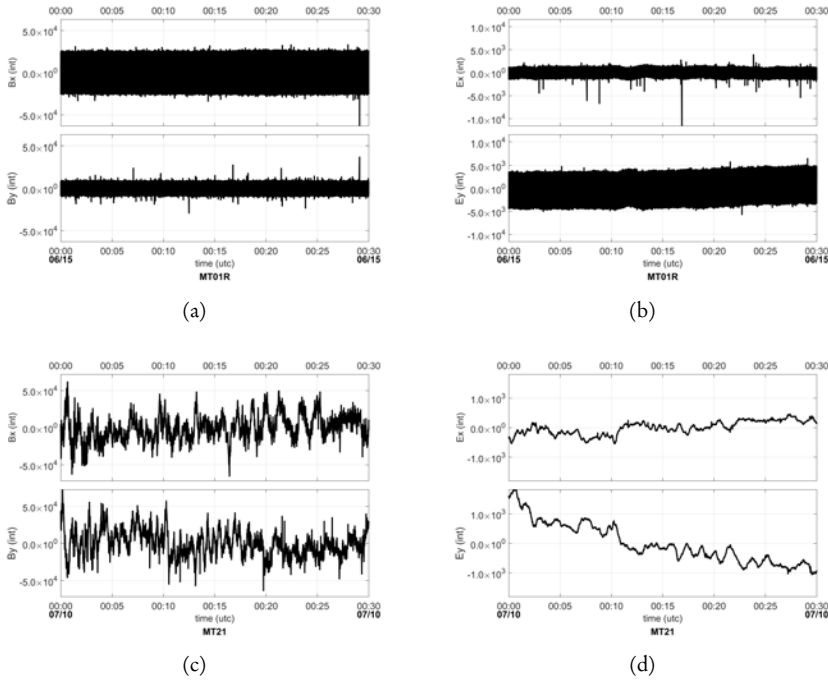


Figure 4.3: 30 minutes of raw time series magnetotelluric data in digital units as measured at a station occupied with Metronix equipment acquiring data at 128 Hz ((a) and (b), station M001) and a station measured with Phoenix equipment acquiring data at 15 Hz ((c) and (d), P001). 0:00 UTC-time is two hours past midnight local time.

In Figure 4.3, 30 minutes of the raw time series data for both stations are plotted. The effect of the different sampling rates used at the two stations is noticed at once. There is almost a factor of ten difference in the number of samples measured in 30 minutes. Due to the higher sampling rate at station M001 it is difficult to assess the data quality based on the raw time series. For station P001 the horizontal electric and magnetic fields are of a reasonable quality, although some high frequency electromagnetic noise is present in the magnetic fields.

There is, however, an inconsistency in the magnetic data between the two - Metronix and Phoenix - data sets when looking at the vertical magnetic

transfer functions. The data measured with Metronix instruments and coils show consistent, clean tipper responses as illustrated in Figure 4.4 at station M001. In contrast, the vertical magnetic transfer function derived from the Phoenix measured stations is questionable at frequencies below 1 Hz, as illustrated at station P001, also plotted in Figure 4.4. The shape of the vertical magnetic transfer function at station M001, characterised by larger amplitudes at longer periods, is also consistent with the presence of the conductive Mediterranean Sea present at the southern side of the survey area. The characteristics of the Phoenix vertical magnetic transfer function are probably noisy between 8 and 0.5 Hz, and therefore masked in Figure 4.4, with a near-zero response below 0.01 Hz. This may be the result of recording the Hz component with an audiomagnetotelluric (AMT¹) coil rather than with a magnetotelluric coil, as used for the horizontal components. Reprocessing of the vertical magnetic data could provide a double-check if the different frequency responses of the different coils are accounted for and will assess whether the Phoenix tipper characteristics result from the rapid drop-off in the amplitude response of the AMT coils at frequencies below 1 Hz.

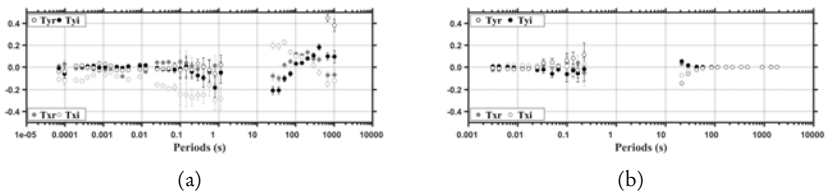


Figure 4.4: Vertical magnetic transfer function (tipper) of stations M001 ((a) a Metronix instrument site) and P001 ((b) a Phoenix instrument site). T_{zx} : magenta (real) and green (imaginary); T_{zy} : red (real) and blue (imaginary). Responses shown were processed by a commercial contractor. Phoenix data between 8 and 0.5 Hz (0.125 and 20 s) were masked by the contractor. Presumably because of high noise levels.

In the magnetotelluric response data, as delivered by the contractor, some frequencies are masked out, probably those data points with low quality and/or high noise levels. By reprocessing the magnetotelluric data, it might be possible

¹Audiomagnetotelluric coils utilize a higher frequency band than a regular magnetotelluric coil.

to recover and evaluate the currently missing frequencies. Another motivation to reprocess the data is to create a consistent magnetotelluric data set, processed by a single processing routine so the quality of the field acquisition can be assessed as well.

4.4 Quality Index pre-sorting

The magnetotelluric data set is reprocessed using a pre-sorting approach. Pre-sorting is carried out after the raw magnetotelluric data time series are transformed to the frequency domain.

To fully utilize all measured frequencies, a standard processing approach is followed. First, the time-series are decimated², creating a number of magnetotelluric data sets with decreasing sampling rates. Depending on the sampling rate and the number of samples present, each decimation level spans a number of frequencies. Following, the individual samples are stacked along pre-defined time-windows, overlapping each other. By applying a running average filter to the stacked time windows, the data are smoothed. Finally, the stacked time-windows are transformed to the frequency domain.

The approach introduced here is developed aiming at those outliers that are not eliminated or sufficiently down-weighted by robust processing approaches. Instead of evaluating every frequency individually, a strategy is developed that evaluates each decimation level separately. This strategy is chosen to speed up the pre-sorting process. To increase the efficiency of the pre-sorting, three statistical parameters are combined to estimate the relative quality of a data point, instead of evaluating each parameter separately. The three parameters used are defined as follows:

²The process of reducing the sampling rate of the measured signal is called *decimation*.

- **The bivariate coherence** r_b^2 , which is the ratio of predicted to measured signal energy between input channels and output channel

$$r_b^2 = \frac{Z_1 \cdot [Y_1 X^*] + Z_2 \cdot [Y_2 X^*]}{[X X^*]} \quad (4.5)$$

where the brackets denote the smoothed and stacked auto or cross spectra. In Equation 4.4, a linear relationship between input channels and output channel is assumed. When electromagnetic data are noisy, Equation 4.4 should not only be solved for \bar{Z} but also for its error $\delta\bar{Z}$.

- **The least-squares estimate** of the magnetotelluric transfer functions

$$Z_1 = \frac{[X Y_1^*] [Y_2 Y_2^*] - [Y_2 Y_1^*] [X Y_2^*]}{[Y_1 Y_1^*] [Y_2 Y_2^*] - |[Y_1 Y_2^*]|^2}, \quad (4.6)$$

and

$$Z_2 = \frac{[Y_1 Y_1^*] [X Y_2^*] - [Y_1 Y_2^*] [X Y_1^*]}{[Y_1 Y_1^*] [Y_2 Y_2^*] - |[Y_1 Y_2^*]|^2}. \quad (4.7)$$

- **The statistical error estimate** of the least-square estimate of the magnetotelluric transfer functions:

$$|\delta Z_1|^2 = \frac{(1 - r_b^2) \cdot - [X X^*] [Y_2 Y_2^*]}{[Y_1 Y_1^*] [Y_2 Y_2^*] - |[Y_1 Y_2^*]|^2} \cdot \frac{4}{\nu - 4} \cdot F_{4, \nu - 4, 1 - \alpha}, \quad (4.8)$$

and

$$|\delta Z_2|^2 = \frac{(1 - r_b^2) \cdot - [X X^*] [Y_1 Y_1^*]}{[Y_1 Y_1^*] [Y_2 Y_2^*] - |[Y_1 Y_2^*]|^2} \cdot \frac{4}{\nu - 4} \cdot F_{4, \nu - 4, 1 - \alpha}, \quad (4.9)$$

where ν is the number of degrees of freedom and $F_{4, \nu - 4, 1 - \alpha}$ is the Fisher F distribution. Here α is a chosen probability set at 68%³ [Weckmann *et al.*, 2005].

³The Fisher F distribution is a continuous statistical distribution to compare the similarity of the variance of the population of the estimators Y_1 and Y_2 . By choosing a probability of 68%, the influence of large outliers is minimized.

Where the bivariate coherence is a non-dimensional number between zero and one, the estimate of the least-squares estimate of the magnetotelluric transfer function (Equations 4.6 and 4.7) and their error estimates (Equations 4.8 and 4.9) are normalized to be able to make a meaningful combination of the three parameters.

Being complex, the noise-free least-squares estimates of the magnetotelluric transfer function of all time-windows at a certain frequency plots as a point in the complex plane. As, in reality, the magnetotelluric transfer function estimates of each time window differ, estimates plot as a cloud around a central point. The farther away a data point (time-window) is from the central point, the lower the signal-to-noise ratio of this particular data point. According to this reasoning, the normalized distance to the central point of a data point, or *offset*, is a measure for the quality of this particular data point

$$\widehat{Z}_{\text{off}} = 1 - \frac{|Z - Z_c|}{\|Z\|_{\infty}} \quad (4.10)$$

where \widehat{Z}_{off} is the normalized vector of the least-squares estimates of the magnetotelluric transfer function and Z_c is its the central point. The central point is calculated by taking the trimmed mean of Z excluding the 5% largest outliers. The double bars with subscript infinity is the infinity norm, $\max(|Z_i|)$ with $i = 1 \dots n$.

The normalized error estimate of the least-squares estimate of the magnetotelluric transfer function is then

$$\delta\widehat{Z} = 1 - \frac{\delta Z}{\|\delta Z\|_{\infty}} \quad (4.11)$$

where $\delta\widehat{Z}$ is the normalized vector of the error estimates of the least-squares estimate of the magnetotelluric transfer function $|\delta Z|^2$.

Now all three parameters have values in the range $[0 - 1]$ with values closer to zero representing data samples with a relative low coherence, large offset and large error estimate, and with values closer to one vice versa. The “Quality Index”, or QI, indicating the relative quality of the magnetotelluric data is defined as

$$QI = \frac{1 - \frac{a}{\sum a}}{2} \cdot \mathbf{P}_{\text{stat}} \quad (4.12)$$

where \mathbf{P}_{stat} is a vector comprising the three statistical parameters discussed before, and the weighting factor a is

$$a = \left(\begin{array}{c} r_b^2 \\ \left(\langle \widehat{Z}_{1,\text{off}} \rangle + \langle \widehat{Z}_{2,\text{off}} \rangle \right) / 2 \\ \left(\delta \langle \widehat{Z}_1 \rangle + \delta \langle \widehat{Z}_2 \rangle \right) / 2 \end{array} \right) \quad (4.13)$$

where $\langle \rangle$ denotes the mean. By defining a in this way, the resulting Quality Index is always in the range $[0 - 1]$.

When a data sample has a low QI value, its data quality is relatively low, while a high QI value indicates a relatively good quality data sample. The Quality Index is defined such that it gives a quantitative indication of the spread in the data quality within the data samples considered. Consequently, a data set with large differences in data quality will show both very good, close to 1, and very bad, close to 0, QI values. This results in a polarized QI plot with extreme values, but without much detail. On the other hand, a more homogeneous data set will have, independent of the data quality, intermediate QI values which results in a more detailed QI plot.

During processing, the Quality Index is plotted for a certain decimation level as shown in Figure 4.5. The Quality Index for a certain output channel E_x , E_y or B_z is plotted in the lower part of Figure 4.5 with the frequency band evaluated covering the decimation level considered on the y -axis, and the Fourier coefficients in time on the x -axis. The lower the frequency, the fewer time windows evaluated and the coarser the Quality Index will appear. The upper row in Figure 4.5 shows from left to right, the bivariate coherence,

the normalized offset of the estimated magnetotelluric transfer functions and their normalized error estimates for the channels evaluated. Since a conventional magnetotelluric station measures two predicting (input) fields, and three predicted (output) fields three of these plots are made for each decimation level.

At this moment, the remote reference station is not implemented into the Quality Index pre-sorting. The future implementation of the remote reference station into the approach described here, would be done by expanding Equations 4.12 and 4.13 with the remote reference magnetic channels. In its present form, Quality Index pre-sorting can only be applied to the local station. However, the time windows of the local station masked out based on their QI values, are simultaneously masked out for the remote reference station.

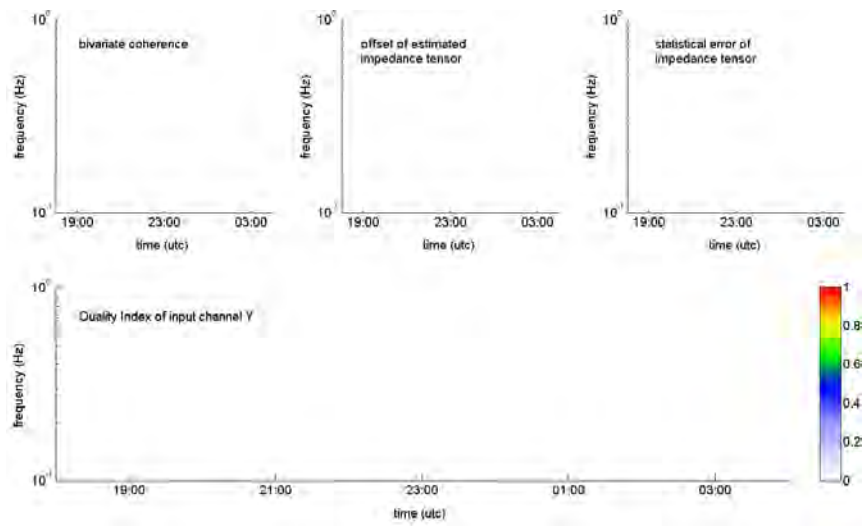


Figure 4.5: Empty Quality Index plot for a certain decimation level of a magnetotelluric station data set for predicting fields Y_1 and Y_2 and predicted field X , with clockwise starting in the upper left corner, the bivariate coherence for the fields considered, the normalized offset of the estimated magnetotelluric transfer function for these fields, the normalized statistical error of this estimated magnetotelluric transfer function, and the Quality Index. On all plots, the y -axis shows the frequency band covering the decimation level considered and the x -axis shows evaluated Fourier coefficients in time.

4.5 Reprocessing results

The magnetotelluric data set is reprocessed using Quality Index pre-sorting of the frequency data applying the following routine:

- 1 Without any pre-sorting in the frequency domain, the magnetotelluric transfer function is estimated using the developed robust processing algorithm mentioned in Section 4.1. Besides the use of the remote reference stations, at this stage no additional processing methods are applied. In the following, these responses are referred to as the “initial station response”.
- 2 Based on the results of the initial station response, those decimation levels with corresponding frequencies showing noisy behaviour are selected for Quality Index pre-sorting.
- 3 After the selected frequencies are Quality Index pre-sorted, the magnetotelluric transfer function is estimated again to assess the reprocessed results.

In this Section some typical examples of station responses on which Quality Index pre-sorting is applied, are analysed. Both Metronix and Phoenix sites and different frequency bands are discussed separately.

Figure 4.6(a) shows the initial station response of the Z_{xy} and Z_{yx} components at frequencies (or periods) from 16,384 Hz to 512 s of magnetotelluric station M05. Albeit being a very good response, it is clear that at very high frequencies, at periods around the “electromagnetic dead band”⁴ at 10 s and at longer periods, the station responses are not well resolved. Through decimation, the apparent resistivities and phases above 100 s period are estimated using a 32 s sampling rate. With an acquisition time of 14 hours and a time window of 128 samples, only 16 Fourier coefficients are available to estimate the magnetotelluric transfer function at these frequencies. Logically, this results in a less accurate estimate of the magnetotelluric transfer function.

⁴The electromagnetic dead band, or simply dead band, covers the frequency range around 0.1 Hz where the electromagnetic signal is known to be weak.

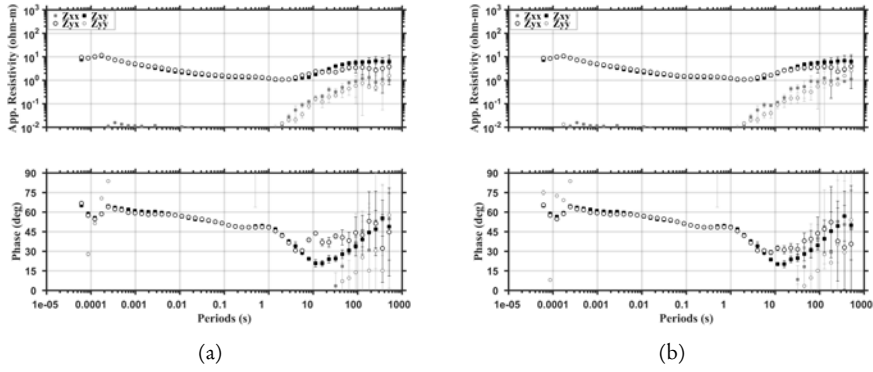


Figure 4.6: (a) Initial (i.e. no pre-sorting) station response of magnetotelluric station M05 and corresponding errors. (b) Quality Index pre-sorting reprocessed station response of magnetotelluric station M05 and corresponding errors.

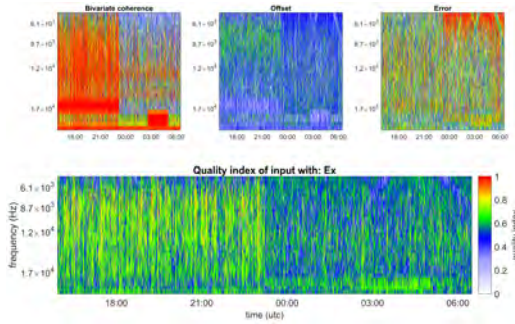


Figure 4.7: Quality Index of station M05 for frequencies measured with a sampling rate of 65,536 Hz for output channel E_x . The frequencies shown contain the magnetotelluric data in first decimation level of this sampling rate spanning the four plotted central frequencies.

Figure 4.7 shows the E_x Quality Index of station M05 of the data measured with a sampling rate of 65,536 Hz. This data set contains the first four periods as shown in Figure 4.6. The bivariate coherence for both the E_x and the E_y (not shown) output channels indicates that the quality of the data acquired

before 0:00 hours UTC⁵ is higher than of the data acquired afterwards. Both the normalized offset and the normalized error estimate are relatively homogeneous of character and don't show this trend. These observations are reflected in the Quality Index which is around 0.75 before UTC 0:00 and around 0.5 after. By visual inspection it is estimated that more than half of the data points have a QI value greater than 0.75. Consequently, the pre-sorting is based on this observation by masking samples with a Quality Index below 0.75.

The QI value threshold is independently decided for each decimation band for every individual magnetotelluric station. Initially, poor quality data points are identified in the QI plot. Following, the corresponding threshold QI value is estimated, tested and, if necessary, adjusted to obtain the best magnetotelluric transfer function estimate.

An analysis of the quality of the measurements in the magnetotelluric dead band is made based on the QI plot as shown in Figures 4.8(a) and 4.8(b) in which the corresponding decimation levels, containing the magnetotelluric data between 10 s and 100 s period, for the E_x -channel of station M05 are given. In Figure 4.8(a), showing the higher frequencies, the later part of the data seems to have the best quality, which can also be noticed in the bivariate coherence and error estimate as well, to a lesser extend, in the offset. Overall the Quality Index at this decimation level appears to be better during the first and the last hours of the acquisition time. When considering the lower frequencies in Figure 4.8(b), an excellent bivariate coherence is observed, while the offset is relatively homogeneous. The normalized error estimate is higher (i.e. the error estimate is quantitatively small) during the measurements taken in the early morning hours.

One possible strategy when evaluating the robust estimate of a magnetotelluric transfer function is assessing the distribution of its residuals *Chave* [2014]. Although robust processing approaches assume a Gaussian core, the residuals are typically long tailed and well represented by a Rayleigh distribution *Chave et al.* [1987]. In Figure 4.9, histograms of the residuals of the robust estimate of the MT transfer function and their fit to a Rayleigh distribution

⁵Local time is +2 UTC

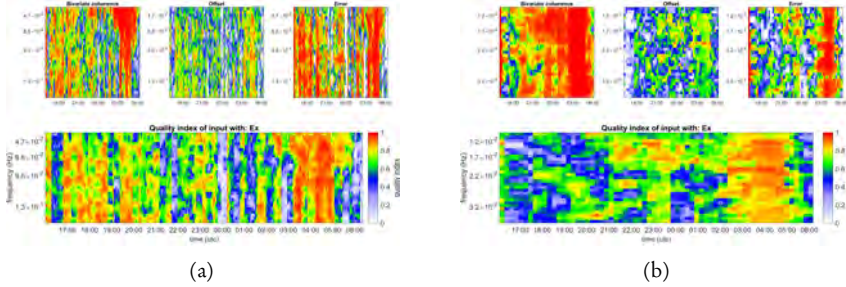


Figure 4.8: Quality Index of station M05 for frequencies measured at roughly (a) 0.1 Hz (central frequency is 0.13 Hz (7.7 s)) and at roughly (b) 0.01 Hz (central frequency is 0.012 Hz (83.3 s)) for output channel E_x .

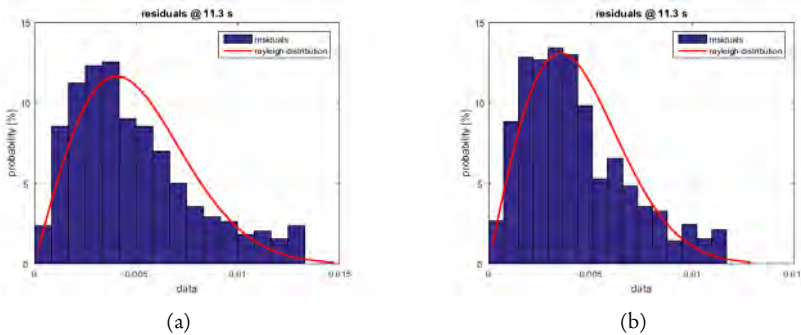


Figure 4.9: Histogram and its fit to the Rayleigh distribution of the residuals of the robust estimate of the magnetotelluric transfer function before ((a)) and after ((b)) Quality Index pre-sorting of station M05 for a period of 11.3 s (0.09 Hz) for output channel E_x .

before and after Quality Index pre-sorting is given for a period of 11.3 s. From this Figure it can be concluded that Quality Index pre-sorting removes the outliers in the tail of the distribution which are not accounted for by the robust processing algorithm used.

Considering the periods above 100 s, with a limited number of Fourier coefficients available, an example of the E_x channel is given in Figure 4.10. In this case masking all coefficients with a Quality Index below 0.7 leaves insufficient coefficients for a meaningful estimation of the magnetotelluric transfer function. Nevertheless, masking was applied based on Quality Index results at

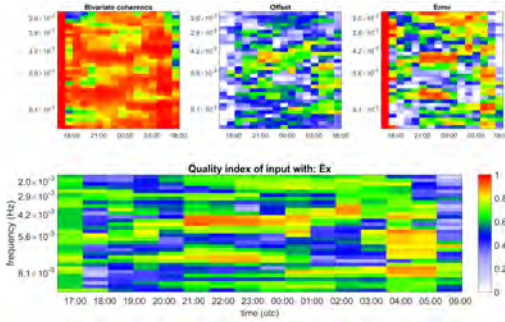


Figure 4.10: Quality Index of station M05 for frequencies measured below 0.01 Hz (central frequency $8.1 \cdot 10^{-5}$ Hz (123 s)) for output channel E_x .

this decimation level to investigate its effects on the estimate of the magnetotelluric transfer function.

After Quality Index pre-sorting, using thresholds between 0.7 and 0.8, is applied to all low quality data points of station M05, the final magnetotelluric transfer function is estimated. The resulting apparent resistivity and phases of the Z_{xy} and Z_{yx} components of the magnetotelluric transfer function are plotted in Figure 4.6(b). When this plot is compared to initial station response, see Figure 4.6(a), it can be observed that the Quality Index Pre-sorting changed the response at very high frequencies and, as expected, at very low frequencies. In the period range from 10 s to 100 s the effects of Quality Index Pre-sorting are especially visible in the Z_{yx} component, which now has a much smoother character. Except for the extreme periods, the overall station response is now significantly cleaner than before Quality Index Pre-sorting was applied.

Stations M02 and M16, see Figures 4.11(a) and 4.13(a), are in comparison to the relatively noise-free station M05, of poorer data quality. Station M02 is very noisy at periods above 5 s, while in station M16 the Z_{yx} component comprises noisy data points. Quality Index pre-sorting processing is applied to these stations following the same strategy as for station M05.

Figure 4.12 shows the Quality Index for station M02 for the decimation level containing the periods around 10 s (0.1 Hz). The low values of the bivari-

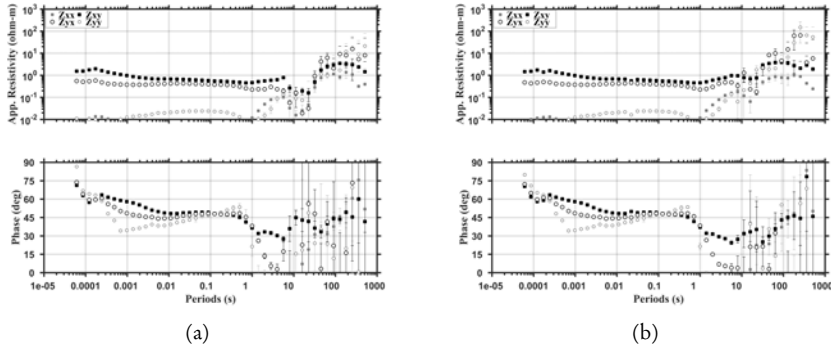


Figure 4.11: (a) Initial station response of magnetotelluric station M02 and corresponding errors. (b) Quality Index pre-sorting reprocessed station response of magnetotelluric station M02 and corresponding errors.

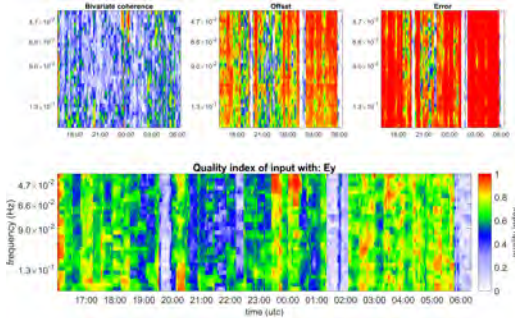


Figure 4.12: Quality Index of station M02 for frequencies measured around 0.1 Hz (10 s) for output channel E_y . The frequencies shown contains the magnetotelluric data in the assessed decimation level of the specific sampling rate spanning the central frequencies.

ate coherence already indicate a noisy data set. From the relatively homogeneous offset and error estimates, it can be concluded that the magnetotelluric transfer function estimation will only be marginally improved by pre-sorting strategies. Figure 4.11(b) shows the station response after Quality Index pre-sorting. The Quality Index pre-sorted processed station response shows reliable results up to periods of about 10 s and for periods above 22 s for the Z_{xy} component. Despite some exceptions, the Z_{yx} component shows good results

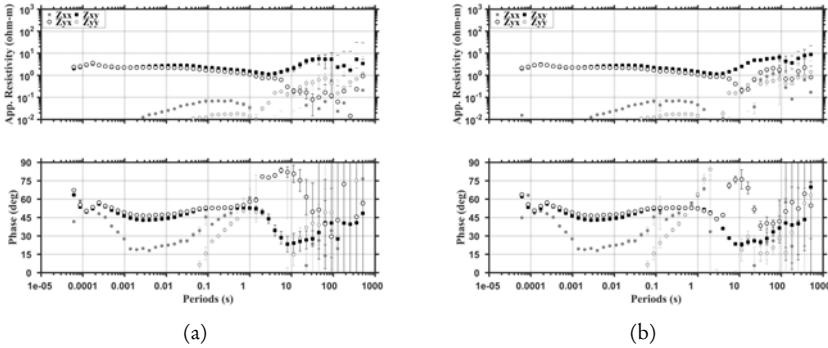


Figure 4.13: (a) Initial station response of magnetotelluric station M16 and corresponding errors. (b) Quality Index pre-sorting reprocessed station response of magnetotelluric station M16 and corresponding errors.

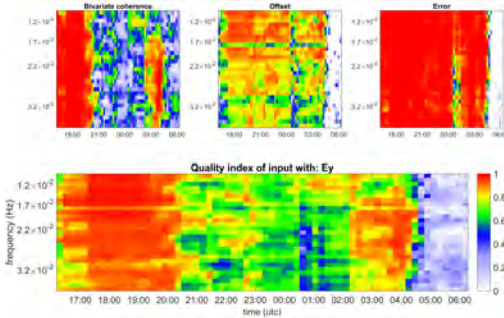


Figure 4.14: Quality Index of station M16 for frequencies measured between 0.032 Hz (31 s) and 0.012 Hz (83 s) for output channel E_y . The frequency shown contains the magnetotelluric data in the assessed decimation level of the specific sampling rate spanning the central frequencies.

up to periods of 10 s. Above periods of 22 s the results of the Z_{yx} component could not be improved. Despite the expected poor improvement in the periods above 100 s, good results for the Z_{xy} component are achieved up to periods of 256 s.

The initial station response of M16, see Figure 4.13(a), shows reasonable results for the Z_{xy} component up to periods of about 100 s and good results for the Z_{yx} component up to periods of 1.4 s. In Figure 4.14 the Quality Index

of the E_y channel for the central periods between 32 s (0.032 Hz) and 83 s (0.012 Hz) is shown. As a result of a relatively homogeneous error estimate and a strongly varying bivariate coherence, the Quality Index indicates good quality data during the first hours of the acquisition period as well as during the early morning hours of the acquisition. In contrast, the data acquired during the last two hours are of a poorer quality. After applying Quality Index pre-sorting based on these observations, the resulting magnetotelluric transfer function is plotted in Figure 4.13(b). Similar results as for station M02 are achieved here, good results for the Z_{yx} components up to periods of 256 s while the Z_{yx} components show good results up to periods of 6 s and reasonable results between periods of 32 s and 90 s.

Stations M02, M05 and M16 were all acquired using Metronix equipment. In Figure 4.15 the initial and Quality Index pre-sorting reprocessed station responses of magnetotelluric station P04 measured using Phoenix instruments are shown. The initially estimated apparent resistivity is quite good, while the phases above periods of 10 s are inconsistent. After Quality Index pre-sorting is applied on the phases above periods of 10 s, see Figure 4.16 for the QI plot of these periods of the E_x channel, are consistent up to periods of 100 s, simultaneously maintaining the apparent resistivity response.

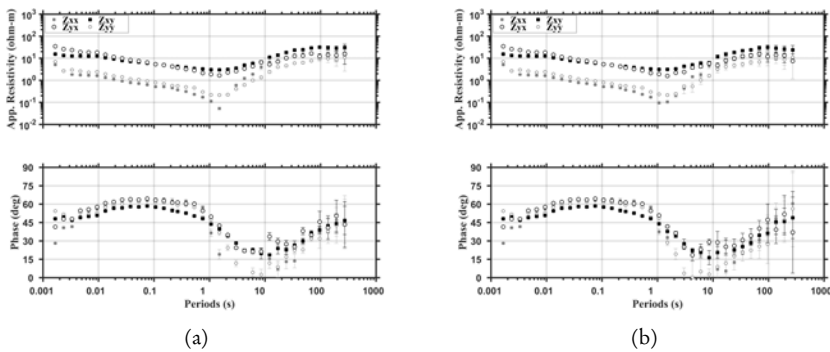


Figure 4.15: (a) Initial station response of magnetotelluric station P04 and corresponding errors. (b) Quality Index pre-sorted reprocessed station response of magnetotelluric station P04 and corresponding errors.

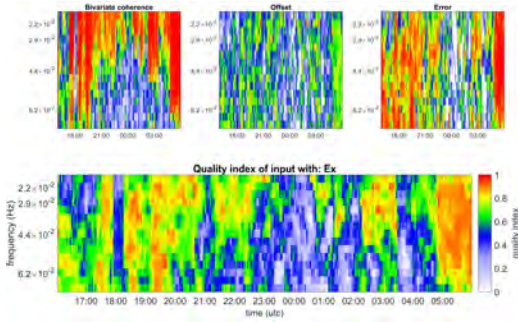


Figure 4.16: Quality Index of station P04 for data spanning the central frequencies between 0.062 Hz (16.1 s) and 0.022 Hz (45.5 s) for output channel E_x . Overall E_x has good quality data, expect for two short periods of low quality data around roughly 22:00 UTC and 3:00 UTC.

Another example is station P26 of which the initial station response is given in Figure 4.17(a). This station has a good response for the Z_{xy} component while the Z_{yx} component apparent resistivities and phases show several outliers, notably in the high frequencies and in the electromagnetic dead band. When studying the frequencies of the Z_{yx} component around the electromagnetic dead band in Figure 4.18, two patterns can be noticed in the Quality Index. First, the Quality Index is higher during the last half of the recording time of the station. Second, at a period of 16.1 s, covered 0.062 Hz central frequency, considerably lower Quality Index values compared to the other frequencies are observed. When masking data at a QI value threshold of 0.7, it can be predicted that the final station response can be enhanced, expect for the data measured at a period of 16.1 s.

This is indeed illustrated in the Quality Index pre-sorted reprocessed magnetotelluric transfer function of station P26 as shown in Figure 4.17(b). In general the phases of the Z_{yx} component around the electromagnetic dead-band are smoother compared to the initial station response phases. However, as predicted by the Quality Index, the quality of the 16.1 s (0.062 Hz) period of the magnetotelluric transfer function is poor. Additionally, the first four data points of this station were edited according to the Quality Index, but no convincing improvements were made.

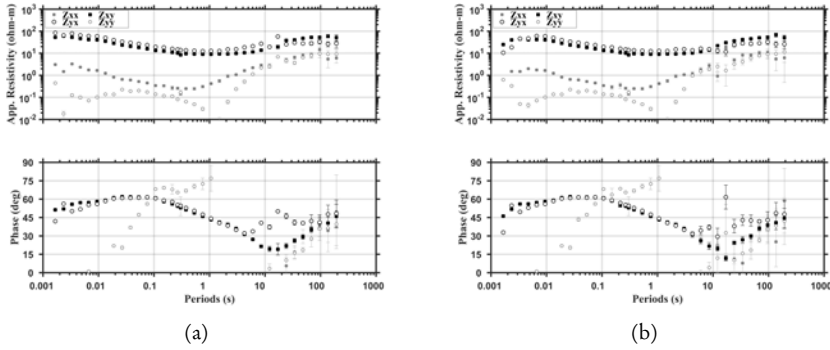


Figure 4.17: (a) Initial station response of magnetotelluric station P26 and corresponding errors. (b) Quality Index pre-sorted reprocessed station response of magnetotelluric station P26 and corresponding errors.

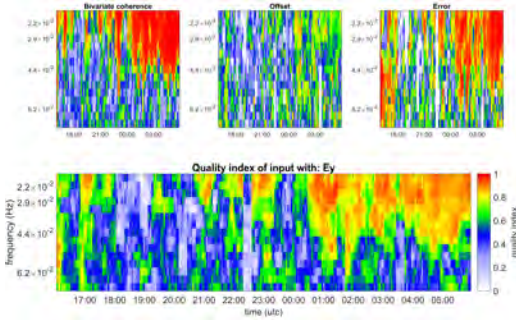


Figure 4.18: Quality Index of station P26 for the data spanning the central frequencies between 0.062 Hz (16.1 s) and 0.022 Hz (45.5 s) for output channel E_y .

Overall less pre-sorting was required for Phoenix recorded stations P01 to P34, while Metronix recorded stations MT01 to MT20 regularly needed more rigorous reprocessing. This might be explained by differences in the field procedures followed or the data acquisition settings of the instruments when measuring the Metronix (M01-M20) and the Phoenix (P01-P34) stations. Unfortunately, these details were not reported by the contractor recording the data.

Stations P32, P33 and P34 were measured roughly one year after the other stations. The remote reference station for these additional three stations was located at the same location as the 2013 remote reference station. Unfortunately, the magnetotelluric data acquired at the remote reference station measuring simultaneously during data acquisition of these three stations is of a low quality. As a consequence, these three stations are processed as single stations using locally recorded magnetic fields. A fourth station (P35) is completely discarded from the survey due to a lack of local data quality. Although the response of the Z_{xy} component could be sufficiently restored using Quality Index pre-sorting, the quality of the Z_{yx} component is such that it was decided not to use this particular station.

Of the 54 stations reprocessed, 46 stations were processed using Quality Index pre-sorting. All stations measured with Metronix equipment are reprocessed using Quality Index pre-sorting, while for 76% of the stations measured with Phoenix instruments Quality Index pre-sorting is applied.

4.6 Comparison between Quality Index pre-sorting reprocessed results and the contractor-processed responses

To validate the Quality Index pre-sorting reprocessed results, they are compared with the processing results delivered by the local contractor. In Figures 4.19 to 4.21, both the contractor-processed responses and some of the reprocessed responses of the stations discussed in Section 4.5 are plotted. As only EDI-files with masked out frequencies (i.e. the data at these frequencies are missing) are available of the contractor-processed responses, it is impossible to compare the contractor-processed and Quality Index pre-sorting reprocessed results at the masked out frequencies.

When the station responses in Figure 4.19 are compared, it is clear that the main trends of the apparent resistivity and phases are comparable. However, a few differences can be noticed. Besides the masked out data points, the first four and last five periods in Figure 4.19(b) are notably different. These first four periods are located in the so-called "AMT dead band" between 0.0002

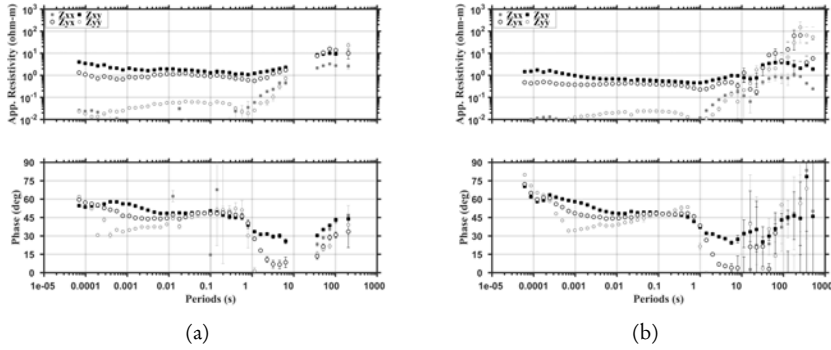


Figure 4.19: (a) Contractor-processed station response of magnetotelluric station M02 and corresponding errors. (b) Quality Index pre-sorting reprocessed station response of magnetotelluric station M02 and corresponding errors.

and 0.001 s, while the last five periods are based only on a limited number of samples. Another difference can be found in the amplitude of the apparent resistivity, which is a higher for the results delivered by the contractor. Generally, the two station responses show a similar behaviour between periods of roughly 0.0002 and 10 s.

Interesting in Figure 4.20(a) is the large data gap around the electromagnetic dead band. In Figure 4.20(b) the Z_{xy} components are good while the Z_{yx} around 10 s are not well resolved and will be masked out for modelling.

The Quality Index reprocessed and contractor-processed station responses of station P04 as shown in Figure 4.21 are, except for the first few periods, similar up to approximately 1 s periods. At longer periods, the commercial processing result appears to have more problems resolving the magnetotelluric transfer function compared to Quality Index pre-sorting processing results. It cannot be left unnoticed that the phases of the Z_{yx} components above 1 s period are slightly higher than the phases of the Z_{xy} components in the similar period range in Figure 4.21(a), where they have similar values in Figure 4.21(b). The same holds for the apparent resistivities above 1 s, in Figure 4.21(a) the apparent resistivities of the Z_{yx} component are higher than those of the Z_{xy} component, while this situation is the opposite in Figure 4.21(b).

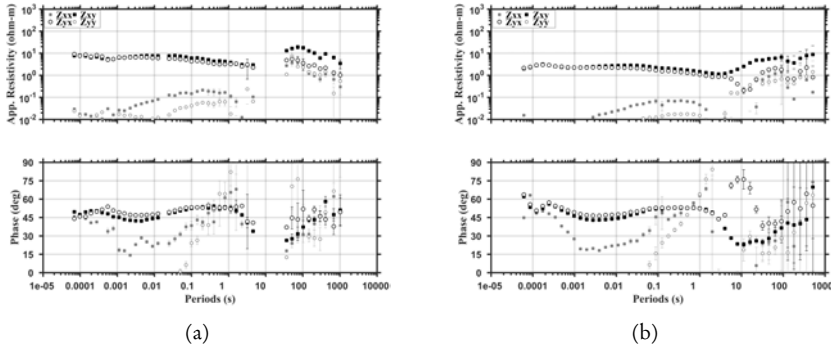


Figure 4.20: (a) Contractor-processed station response of magnetotelluric station M16 and corresponding errors. (b) Quality Index pre-sorting reprocessed station response of magnetotelluric station M16 and corresponding errors.

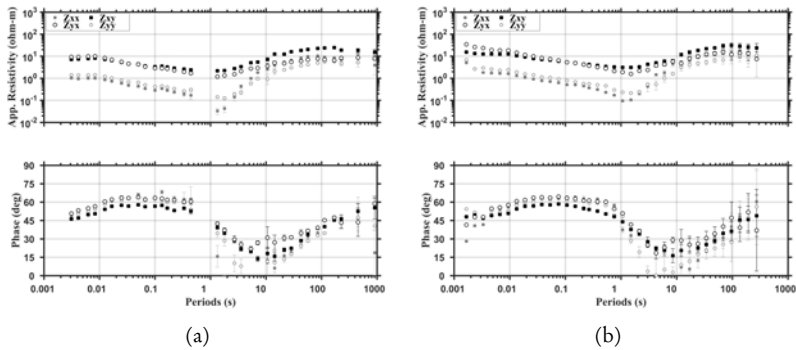


Figure 4.21: (a) Contractor-processed station response using Phoenix proprietary software magnetotelluric station P04 and corresponding errors. (b) Quality Index pre-sorting reprocessed station response of magnetotelluric station P04 and corresponding errors.

As visible in Figure 4.22(b), reprocessing of the magnetotelluric data is an effective measure for repairing the vertical magnetic transfer function of the stations recorded with Phoenix instruments up to 1 s period. Above a 1 s period, the vertical magnetic transfer function response appears to be noisy. Quality Index pre-sorting processing is applied to the vertical magnetic transfer

function of all stations in similar fashion as for the magnetotelluric transfer functions. For illustration, the vertical magnetic transfer functions as delivered by the contractor and resulting from the reprocessing of Metronix recorded station M02 is shown in Figure 4.23.

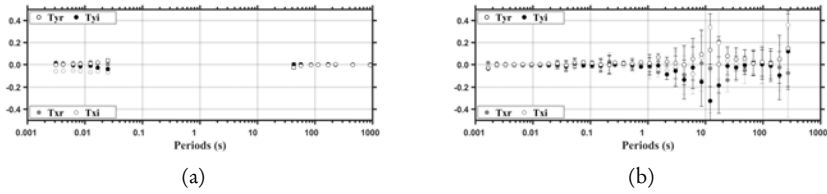


Figure 4.22: (a) Contractor-processed vertical magnetic transfer function of station P04. (b) Quality Index pre-sorted reprocessed vertical magnetic transfer function of station P04.

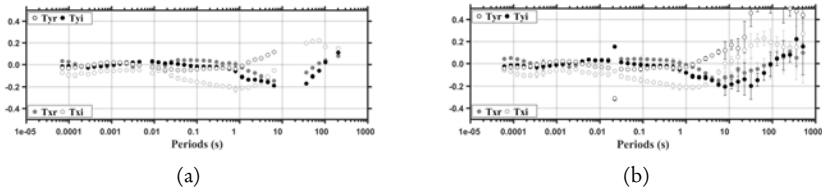


Figure 4.23: (a) Contractor-processed vertical magnetic transfer function of station M02. (b) Quality Index pre-sorted reprocessed vertical magnetic transfer function of station M02.

4.7 Discussion

The proposed pre-sorting processing method described in Section 4.4 is able to consistently and quantitatively eliminate bad data points from magnetotelluric data as an intermediate step in the frequency domain before robust processing is carried out. The Quality Index pre-sorting processing approach is quick and effective and works the same on every magnetotelluric station evaluated. This approach gives consistent results, even when handling data acquired with instruments built by different manufacturers.

From the examples given in Section 4.5 it is clear that a substantial set of good data is necessary to get coherent magnetotelluric responses across all frequencies. In most cases, the magnetotelluric response function estimated based on unedited Fourier coefficients is significantly improved after Quality Index pre-sorting. Since the Quality Index displays the relative quality of the magnetotelluric data, magnetotelluric data with homogeneous, average to good, quality data is likely to have Quality Index values above 0.5 within a relatively small range. Magnetotelluric data comprising both very noisy data and very good data will show large variations in the Quality Index, while a set of consistently noisy magnetotelluric data will show Quality Index values below 0.5 within a relatively small range. However, very noisy data points will, due to the influence of the error estimate, always show consistently low Quality Index values.

The Quality Index pre-sorting processing appears to be more effective when applied to Metronix data than when applied to Phoenix recorded magnetotelluric data. This can be explained by the sampling frequencies utilized by the two instruments and the decimation schemes and window lengths chosen for the Fourier transform.

The Metronix recorded magnetotelluric data set discussed here is decimated with a factor 4 after each iteration and uses a window length of 128 samples with an overlap of 32 samples. Since a frequency band should contain at least 16 Fourier coefficients, at a typical Metronix sampling rate of 128 Hz, a maximum of seven decimation levels can be derived from one set of the magnetotelluric time series processed here. The seven decimation levels are sampled at 128 Hz, 32Hz, 8Hz, 2Hz, 2s, 8s and 32s. With 16 hours of acquisition time, the first decimation level consists of 57,600 seconds of data and of 7,372,800 samples in the time domain. With stacked windows in the frequency domain, this leads to 65,828 Fourier coefficients. Similarly, the seventh decimation level has 16 Fourier coefficients.

In comparison, from a Phoenix recorded magnetotelluric station measuring data for 16 hours at 15 Hz, processed using the same decimation scheme and window length, five decimation levels can be derived. The five decimation

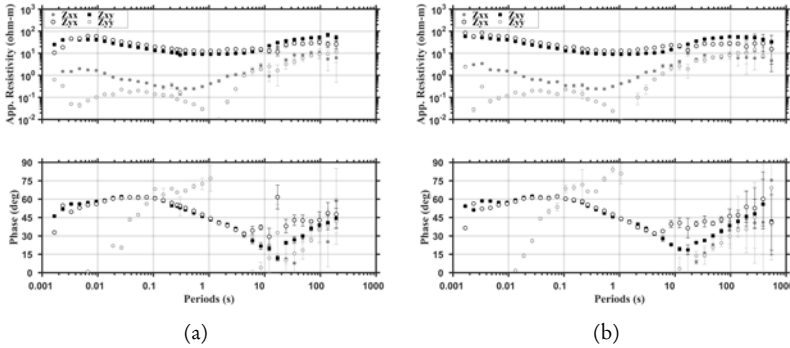


Figure 4.24: Quality Index pre-sorting reprocessed magnetotelluric response functions of station P26 processed with a window length of 128 (a) and 64 (b) samples respectively.

levels are sampled at 15 Hz, 3.75 Hz, 1.067 s, 4.267 s and 17.067 s. The first level has 7,714 Fourier coefficients while the fifth decimation level contains 30 Fourier coefficients. A window length of 64 samples with an overlap of 16 samples, applied to this same magnetotelluric time series data set results in six decimation levels with 15,750 Fourier coefficients for the first decimation level at 15 Hz and 16 Fourier coefficients for the sixth decimation level with a sampling rate of 68.267 s. The shorter window length of 64 samples rather than 128 samples provides more detail in the Quality Index plots.

Quality Index pre-sorting processing of this particular set of magnetotelluric data acquired with Phoenix instruments might be more effective when using a shorter window length and overlap. In Figure 4.24 the Quality Index pre-sorted reprocessed magnetotelluric transfer functions of station P26 are displayed for processing window lengths of 128 and 64 samples. The number of frequencies evaluated increases for the data recorded at a 15 Hz sampling rate when using the 64 samples windows, adding two frequencies at the low frequency end of the spectrum. Considering the limited number of samples, the reliability of these two magnetotelluric transfer function estimates can be debated. As a result of the shorter window length, more Fourier coefficients are evaluated when Quality Index pre-sorting reprocessing and/or estimating

the magnetotelluric transfer function at a certain frequency. As a result, the data can be evaluated more thoroughly, in this case resulting in a better estimation of the transfer function around the “dead band”. In this example the other problematic frequencies which are located at the high frequency end of the transfer function are improved in comparison with the processing with the 128 sample window length (see Figure 4.24(b)). Although clearly present in the case of magnetotelluric station P26, using a shorter window length didn’t lead to a similar improvement for all Phoenix recorded magnetotelluric stations. Consequently, the initially chosen window length of 128 samples was maintained while reprocessing the data.

4.8 Conclusions and future work

A magnetotelluric data set for geothermal exploration in Western Turkey, acquired with both Metronix and Phoenix instruments, was reprocessed using the Quality Index pre-sorting processing approach and a robust processing code developed in Matlab. The Quality Index pre-sorting approach estimates the relative quality of a magnetotelluric data point in the frequency domain based on a combination of the bivariate coherence, the normalized offset of the central point of the least-squares estimate of the magnetotelluric transfer function and the normalized error estimate of this estimate.

With the Quality Index pre-sorting reprocessing, several inconsistencies in the magnetotelluric data could be efficiently and effectively reconstructed. As the result still depends on the quality of the data, Quality Index pre-sorting won’t produce much positive effects on the final result when data quality is very poor. However, isolated outliers could be effectively reduced to acceptable values.

The inconsistent vertical magnetic transfer functions reported for the Phoenix recorded transfer functions could be reconstructed by reprocessing the magnetotelluric time series.

The choice of the window length for stacking and overlap, before the Fourier transform, can be of significant influence on the quality of the estimate

of the magnetotelluric response function. However this is a parameter choice which needs further investigation with respect to its implementation in the robust processing code as discussed before. Additionally, the high frequencies of the magnetotelluric transfer function are regularly not well resolved. The estimation of the magnetotelluric transfer functions at these frequencies needs to be improved. An approach to achieve this improvement is to let the window length for stacking depend on the sampling rate of the recorded magnetotelluric time series, instead of using a uniform window length for all recorded time series at a single station. It is expected that this strategy will improve the transfer function estimates at both high and low frequencies.

Quality Index pre-sorting is currently only implemented for a local station. In the future, the effectiveness of Quality Index pre-sorting when applied to a remote reference site and/or magnetic channels measured at a nearby station will have to be investigated.

4.9 Acknowledgements

The author would like to thank Transmark Renewables for making their exploration magnetotelluric data available for this research.

5

**Comparison and
interpretation of
two 3-D inversion
models**

5.1 Introduction

Geothermal energy resources in Turkey are related to the tectonic processes and structures associated with the geological development of the Menderes Metamorphic Massif (MMM) which is bounded by the İzmir-Ankara mountain range at its western and north-western boundaries. Recent north-south oriented extensional tectonics, related to the northward movement of the Afro-Arabian Plate and the westward movement of the Anatolian Sub-plate, created several major east-west oriented grabens in south-eastern Anatolia. The faults bounding these structures are open as a result of the extensional stress regime and allow for the deep circulation and heating of meteoric waters. The Northern Anatolian Fault Zone along the northern boundary of the Anatolian Sub-plate provides deep permeable flow channels for geothermal waters. The high heat flow and associated geothermal systems throughout western Anatolia and along the Aegean Coastal Belt are related to this tectonic regime [Serpén *et al.*, 2009], see Figure 5.1.

The geothermal field discussed in this Chapter is situated on the Biga Peninsula in Çanakkale province in north-western Turkey. It is one of several similar, low-to-medium temperature, geothermal fields, generally grouped within the Aegean Coastal Belt as indicated with an A in Figure 5.1. Having all the characteristics of this play type, the geothermal systems within the Aegean Coastal Belt are classified as of the extensional domain geothermal play type (see Chapter 2: “Geothermal plays and conceptual models”). More details of the exact location of this geothermal field cannot be disclosed due to the confident nature of the data discussed in this Chapter.

The geothermal energy potential in this area has been extensively studied [Serpén *et al.*, 2009] and a number of geothermal projects have recently been developed or are currently being developed. Numerous exploration licenses have been granted in the region. The exploration resistivity survey that forms the focus of this Chapter was conducted in June 2013 by a third party with the aim of defining the dimensions and depth of the geothermal reservoir. During the resistivity survey, 51 combined audiomagnetotelluric (AMT) and magne-

telluric (MT) sites were occupied, each magnetotelluric station recording for about 16 hours duration, with a remote-reference station operating simultaneously at a quiet location approximately 10 kilometres away. The number of magnetotelluric stations measured was increased to 54 in 2014, when another three stations were measured. The data acquisition and processing are discussed in Section 5.3

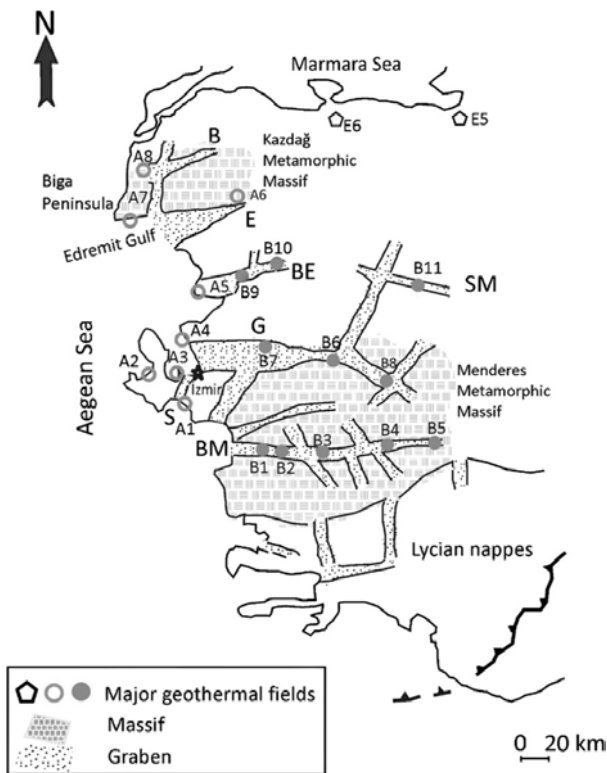


Figure 5.1: Geothermal fields in the Aegean Coastal Belt of western Anatolia and schematic overview of the geology of the region illustrating the main structural grabens: B = Bayramiç, E = Edremit, BE = Bergama, SM = Simav, G = Gediz, S= Seferihisar and BM = Büyük Menderes. The known major geothermal fields in this area are indicated with either A (located in the Aegean Coastal Belt), B (located in the Western Anatolian grabens) or E (located in the North Anatolian Fault Zone). The symbols of the geothermal fields (shape, fill) correspond to their location, e.g. A, B or E. Çanakkale province is located in the north-west of this map, bounded in the South by Edremit Gulf and in the North by the Marmara Sea, in the East it is roughly bounded by the Kazdağ Metamorphic Massif [Serpen *et al.*, 2009].

A qualitative assessment between two different inversion models using these magnetotelluric data recently revealed that the resistivity models created by two different inversion codes produce comparable resistive structures [*van Leeuwen et al.*, 2015]. Applying a set of structural metrics makes it possible to compare the two resistivity models quantitatively as well.

As a first step after data processing, the acquired (A)MT data were inverted in 1-D to create an initial 1-D model of the reservoir. Following, 3-D inversion models are created using two different inversion codes, one of them being ModEM [*Egbert and Kelbert*, 2012] and the other being the proprietary CGG 3-D inversion code developed by *Mackie and Watts* [2012]. The qualitative differences and similarities between the model results of these two 3-D inversion codes are discussed in Section 5.4.

To identify the resistivity structures resolved using both inversion codes, the two inversion models are quantitatively compared using a set of structural metrics. The results are presented in Section 5.5. In the same Section the consequences of this comparison for the geological interpretation are discussed. Finally, in Section 5.6, the most important conclusions from the work presented in this Chapter are summarized.

5.2 Geology

The geology of the Biga Peninsula is characterized by the volcanic rocks of plutonic origin related to the Tertiary transition from a collisional to an extensional regime. Below the volcanic rocks, the area is dominated by two main geological units. These are the Denizgören ophiolite and the underlying sedimentary Enzine Group [*Beccaletto and Jenny*, 2004]. Besides these two dominant formations, two other units are recognized in the area. The Karakaya complex, consisting of Triassic subduction-accretion complexes, in the East and the accretion related Mid-Cretaceous Çetmi mélange. High-grade metamorphic rocks are present at the base of these four units [*Beccaletto and Jenny*, 2004].

The Enzine Group consists of Middle-to-Late Permian to Middle-Triassic limestones and can reach a thickness of 3,500 m. This indicates a long period of subsidence in which little erosion occurred. The sedimentary sequences are interpreted by *Beccaletto and Jenny* [2004] as related to a syn-rift environment, and at later stages, to a post-rift environment. Low-grade metamorphism related to the an Upper Oligocene- Lower Miocene intrusion is recognized in the Enzine Group. The development of the geothermal field investigated here is associated with this Miocene volcanism.

The Denizgören Ophiolite is of oceanic origin and consists mainly of partially serpentinized harzburgite, while crustal components of a typical ophiolitic suite, such as gabbros, sheeted dikes, and basalts, are absent.

The Biga Peninsula is furthermore shaped by intersecting fracture systems, responsible for the graben-like system present in the project area. The geothermal waters circulate in the deep rooted faults related to the fracture systems related to the volcanism [*Serpen et al.*, 2009]. In Figure 5.2 a schematic model of the conceptual model of the studied geothermal system is given, while the main faults present in the survey area are shown in Figure 5.3.

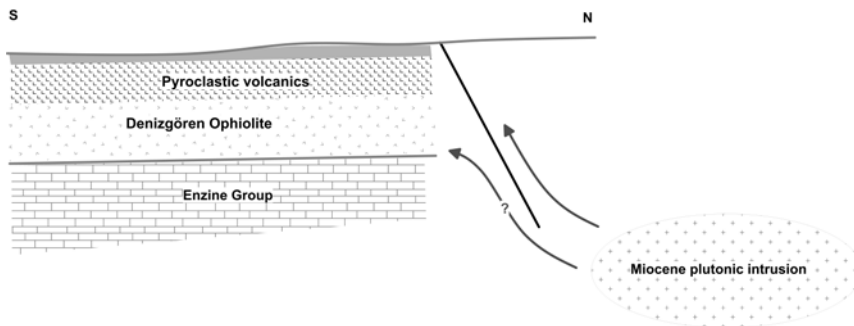


Figure 5.2: Simplified North-South orientated cross-section of the conceptual model of the geothermal system studied. The potential geothermal reservoir are the limestones of the Enzine Group. The upper units in this cross-section are alluvium and a layer of pyroclastic volcanic rocks. These units are overlying the main geological units, the Denizgören ophiolite and the Enzine Group. The pluton of miocene age is heating the geothermal system, while thermal waters are circulating upward through deep rooted faults (black) and fractures. The arrows indicate the possible fluid pathways.

Given the geological setting of the investigated geothermal prospect, it is expected that the electrical resistivity response of the subsurface is mainly controlled by porosity and permeability of faults and fractures and geological formations as well as by clay alteration mineralogy.

5.3 Data acquisition, processing and evaluation

In Chapter 4: “Quality Index pre-sorting” an extensive description of the data acquisition and processing of the magnetotelluric data set used here is given. For completeness and readability the main points of this Chapter are repeated in this Section.

5.3.1 Acquisition

A 51 (A)MT station resistivity survey was carried out in June and July 2013. Additionally a three station survey was carried out to fill a gap in the data coverage in July 2014. During the magnetotelluric recordings, a magnetotelluric remote station was operating simultaneously at a distance of approximately 10 km from the survey area. For the AMT data recordings no remote station was used. To be able to eliminate effects of local electromagnetic noise sources using the remote reference method (see Chapter 3: "Theory of the magnetotelluric method"), the AMT data were processed using the local magnetic field of another simultaneously recorded AMT station as the remote magnetic field. The main part of the resistivity data was collected during two periods in June and July 2013.

Both Phoenix MTU5A and Metronix ADU-07 instruments were used as data loggers during the resistivity survey. The sites occupied with Metronix instruments were all located in the eastern part of the survey area and were acquired during the first part of the survey, while the Phoenix instruments recorded data at sites located in the western part of the area during the second part of the survey. The survey layout, designed with an irregular grid, is illustrated in Figure 5.3. The station spacing varies from roughly 250 to 1,200 m. Sites occupied with Phoenix instruments were recorded using both

AMT (AMTC-30) and MT (MTC-50H) coils, with an AMT coil deployed as vertical magnetic sensor H_z for all measurements. At sites occupied with Metronix instruments, only one type of magnetic coil was deployed (MFS-06e). Data were acquired in the frequency range from 0.001 Hz to either 320 Hz, using the Phoenix MT coils, or to 10,000 Hz, using the Metronix and Phoenix AMT coils. In all instances magnetotelluric data were collected for 16 hours per site.

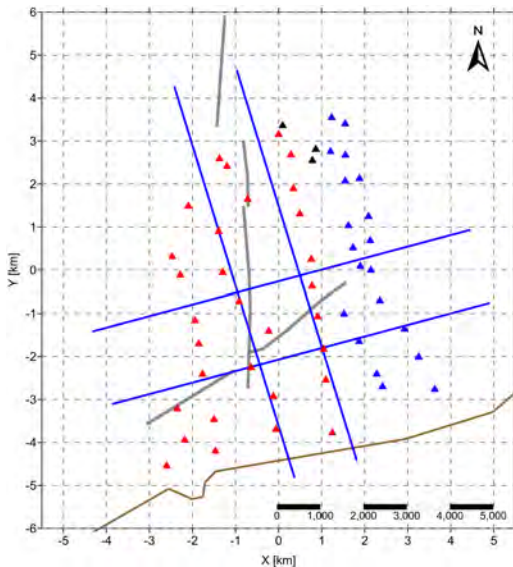


Figure 5.3: Station layout of the 54-station resistivity survey. Red stations were measured using Metronix instrumentation and blue stations using Phoenix instrumentation, while the black stations were acquired a year after the main survey using Phoenix instruments as well. In this Figure the coastline is indicated by the dark brown line and the main faults in the area by the grey lines. The blue lines indicate the locations of the resistivity cross-sections discussed in Sections 5.4 and 5.5.

5.3.2 Data evaluation and reprocessing

All the acquired resistivity data were initially processed by the contractor using existing data processing software. This implies that the raw time series data recorded using Metronix instruments were processed using the EMTF code developed by *Egbert and Booker* [1986], while the raw time series data acquired with Phoenix instruments were processed using proprietary Phoenix software [*Phoenix Geophysics*, 2005]. Each of the two different processing software codes perform differently depending on the electromagnetic noise measured [*Jones et al.*, 1989]. Consequently, it is difficult to conduct an objective assessment of

the data quality of the recorded time series data independently of the processing code used.

A Rho+ test [Parker and Booker, 1996] applied on the magnetotelluric data to check its consistency showed that the apparent resistivity and phase of the magnetotelluric data are in general consistent with each other. There is, however, an inconsistency in the magnetic data between the two magnetotelluric data sets when looking at the vertical magnetic transfer functions (see Chapter 4: “Quality Index pre-sorting” for details).

Relatively small static shift effects in the apparent resistivities can be recognized in about 15% of the measured stations. No static shift correction was applied before inverting the data.

In the magnetotelluric data, as delivered by the contractor, some frequencies are masked out. These frequencies are probably those data points of low quality and/or noisy data. By reprocessing the magnetotelluric data, it might be possible to repair and evaluate the currently missing frequencies. Another motivation to reprocess the data is to create a consistent magnetotelluric data set, processed by a single processing routine such that the quality of the field acquisition can be assessed as well.

This reprocessing is conducted using a robust processing routine loosely based on EMTF [Egbert and Booker, 1986] and developed in Matlab. As an extra processing step a pre-sorting approach is applied. This approach is called Quality Index pre-sorting and is described in detail in Chapter 4: “Quality Index pre-sorting”. Although an extensive discussion on the results of the reprocessed magnetotelluric data is given in the same chapter, the results are summarized below.

In Figures 5.4 and 5.5 the Quality Index pre-sorting reprocessed results are compared to the results as delivered by the contractor. Since only EDI-files with masked out frequencies are available (i.e. the data at these frequencies are deleted), it is impossible to compare the results at the masked out frequencies.

When the two station responses plotted in Figure 5.4 are compared, it is clear that the main trends of the apparent resistivity and phases are comparable. However, a few differences can be noticed. Besides the masked out data

points, the first four and last five periods in Figure 5.4(b) are notably different. These first four periods are located in the AMT dead band between 0.0002 and 0.001 s, while the last five periods are based on a limited number of samples only. The difference at short periods between the two processing results are probably caused by the difference in window length, see also Chapter 4. Another difference can be observed in the amplitude of the apparent resistivity, which is higher for the results as delivered by the contractor. Generally, the two station responses show a similar behaviour between periods of roughly 0.0002 and 10 s.

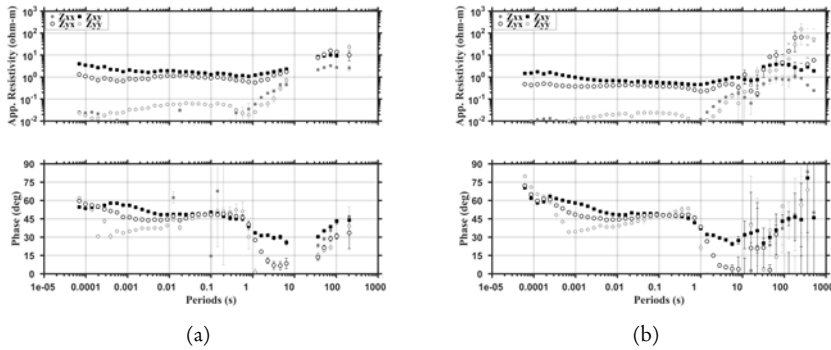


Figure 5.4: (a) Third party processed station response of the four components of the magnetotelluric transfer function of magnetotelluric station M02 and their errors. (b) Quality Index pre-sorting reprocessed station response of the four components of the magnetotelluric transfer function of magnetotelluric station M02 and their errors.

The station responses of station P04 as shown in Figure 5.5 are, except for the first few periods, very similar up to approximately 1 s. At longer periods, the commercial processing result appears to have more problems resolving the magnetotelluric transfer function as compared to Quality Index pre-sorting processing results. It cannot be left unnoticed that the apparent resistivities of the Z_{yx} components above a 1 s period are slightly higher than the apparent resistivities of the Z_{xy} components in the similar period range in Figure 5.5(a), while this situation is the opposite in Figure 5.5(b). Finally, the station responses produced by the Quality Index pre-sorting processing are smoother in comparison to the responses as delivered by the contractor.

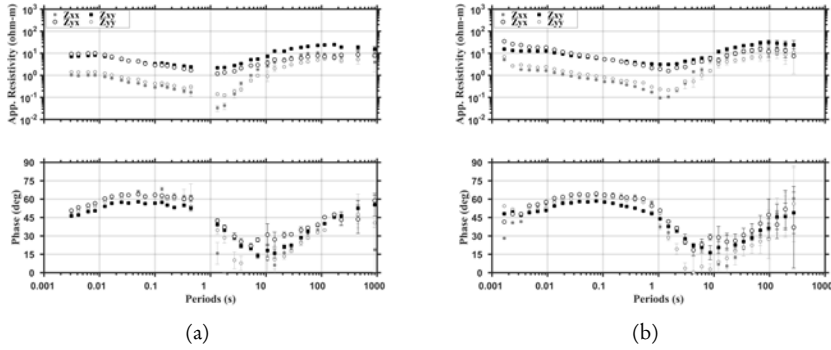


Figure 5.5: (a) By the contractor processed station response using Phoenix proprietary software of the four components of the magnetotelluric transfer function of magnetotelluric station P04 and their errors. (b) Quality Index pre-sorting reprocessed station response of the four components of the magnetotelluric transfer function of magnetotelluric station P04 and their errors.

5.4 3-D inversion modelling

As indicated previously, two different codes were used to create a 3-D inversion model of the survey area. Both codes use a finite difference approach, while the differences between the two codes can be found in the solvers applied to the system of linear equations, the model grid and the boundary conditions applied. The two codes used are ModEM [Egbert and Kelbert, 2012] and the 3-D inversion code of CGG [Mackie and Watts, 2012], here conveniently called 'Mackie3D'. A detailed description of the similarities and differences between the inversion strategies used by ModEM and Mackie3D is outside the scope of this Chapter. However, a summary is given in Chapter 3: "Theory of the magnetotelluric method" and a more detailed discourse on inversion theory can for example be found in Siripunvaraporn [2012] and Chave and Jones [2012].

For the inversion with Mackie3D, carried out by a commercial contractor, the by the contractor processed data was used, while the ModEM inversion model, created for this research, is based on the Quality Index pre-sorted processed data. The inversion using the Mackie3D algorithm has a minimum cell size of 125 x 125 x 10 m. The layer thickness increases logarithmically with

increasing depth of investigation until a maximum layer thickness of 100 m is reached at 1.6 km and stays constant thereafter. The maximum depth of the model is 5.3 km. In addition to the topography, the bathymetry is also included in the model grid. The modelling is carried out over a frequency range from 0.0056 to 320 Hz, using four frequencies per decade. The model grid has dimensions of 73 x 68 x 103 cells. Spurious data points were masked before running the inversion. An initial model with a homogeneous resistivity of 10 Ωm was used. To be able to make a meaningful comparison between the inversion results of the two codes, a similar model mesh is used for the inversion with ModEM, while other inversion parameters are chosen as similar as possible. As can be seen in Table 5.1 the differences between the input data of the two inversions can be found in the number and the range of frequencies inverted.

Table 5.1: Model parameters for the 3-D inversion of the MT data using either Mackie3D or ModEM.

	Mackie3D	ModEM
Approach	<i>Mackie and Watts [2012]</i>	ModEM [<i>Egbert and Kelbert, 2012</i>]
Dimensions	73 x 68 x 103 cells	73 x 68 x 103 cells
Minimum cell size	125 x 125 x 10 meter	125 x 125 x 10 meter
Frequency range	0.0056-320 Hz	0.0032-316 Hz
Number of frequencies	20	24
Frequencies per decade	4	5
Initial model	10 Ωm	10 Ωm
Data inverted	Full tensor complex impedances	Full tensor complex impedances
Spurious data points masked	Yes	Yes
Topography	Yes	Yes
Batymetry	Yes	Yes
resistivity of sea water	0.33 Ωm	0.33 Ωm
Root-Mean-Square misfit ¹	1.53	1.99
Number of iterations	56	95

5.4.1 Inversion results

By calculating the root-mean-square (rms) misfit² per station, the differences in the data fit of the inversion of the two models are analysed. In Figure 5.6 the rms misfits of the stations for the two inversion results, “Mack-10-Tur” for the

²The rms misfit is calculated using $RMS = \sqrt{\frac{1}{N} \sum \left(\frac{OBS - MOD}{\epsilon} \right)^2}$, where OBS is the observed and MOD the predicted data, while N is the number of data points and ϵ is the error of the data.

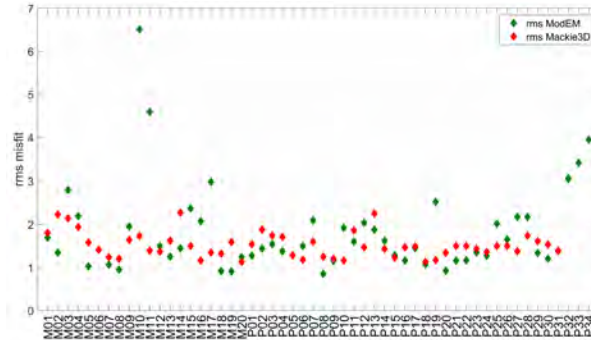


Figure 5.6: Rms misfit per station for all frequencies of the inversion of the two models, indicated in green (ModEM-10-Tur) and red (Mack-10-Tur).

results of the Mackie3D inversion, and “ModEM-10-Tur” for the results of the ModEM inversion, are plotted.

First of all it must be noticed that the three new (2014) stations (P32, P33 and P34) included in ModEM-10-Tur have a large rms misfit. This is somewhat expected since the data quality of these three stations is relatively poor. Furthermore stations M10 and M11 in this model show high rms misfits. These high rms misfits can be explained by a poor fit in the long periods for M10 and poor data quality in the short periods for M11. In general, the rms misfit per station is roughly between 1 and 2.5, where the misfits of the Mack-10-Tur model show a slightly smaller variation between stations in comparison with the ModEM-10-Tur model.

To illustrate this, the observed and modelled responses of both inversion models for stations M16, P02 and P09 are plotted in Figure 5.7. As can be observed in Figures 5.6 and 5.7(a) for station M16 the model fit of Mack-10-Tur is better than the fit of ModEM-10-Tur. The observed difference in model fit can be explained by the exclusion of a number of the long period data points in Mack-10-Tur, which is not the case in ModEM-10-Tur. Station P09 as plotted in Figure 5.7(b) shows a better fit for ModEM-10-Tur compared to Mack-10-Tur. This good model fit is a result of the reprocessing of the magnetotelluric data (see Section 5.3.2), of which the effects are especially visible in the long

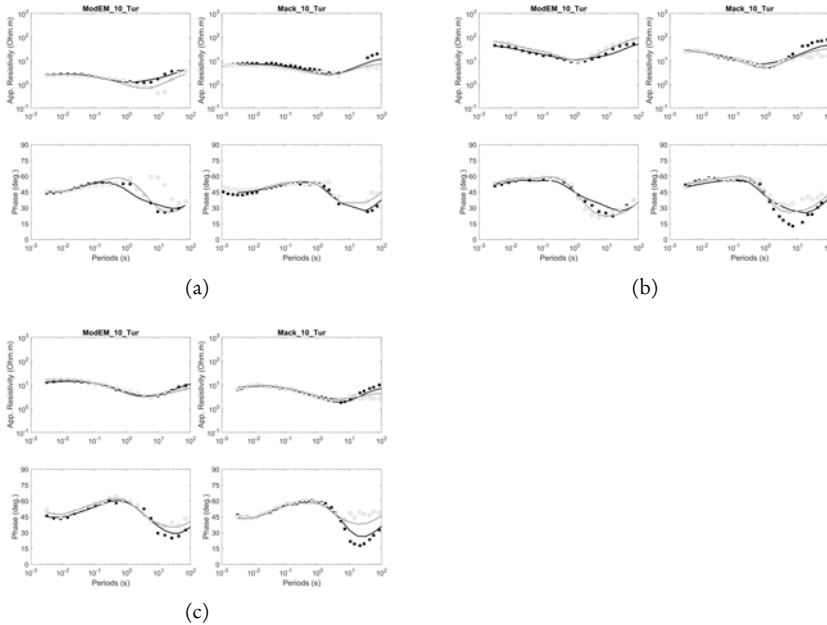


Figure 5.7: Observed (dots) and modelled (lines) station responses of the XY (grey) and YX (black) components for stations M16 (a), P02 (b) and P09 (c) for ModEM-10-Tur and Mack-10-Tur inversion models. Note that the Mack-10-Tur inversion model is based on re-sampled resistivity data rather than the observed data as plotted here.

periods. Finally, station P09 as shown in Figure 5.7(c) shows a very good fit for both models of this station. During the 3-D inversion, neither algorithm corrected the static shift effects present in about 10% of the magnetotelluric stations.

Resistivity maps at constant elevation derived from the inversion results of the two models are plotted in Figure 5.8, at elevations of -500, -1,000 and -1,500 m above mean sea level (amsl.). As can be seen in Figures 5.8(a) and 5.8(b), both models have a high conductivity and appear to be relatively homogeneous at a depth of 500 m below sea level (bsl.). At this depth, ModEM-10-Tur shows some relatively resistive structures in the south-east of the model. At a depth of 1,000 m bsl., both models have a low resistivity in the south-east

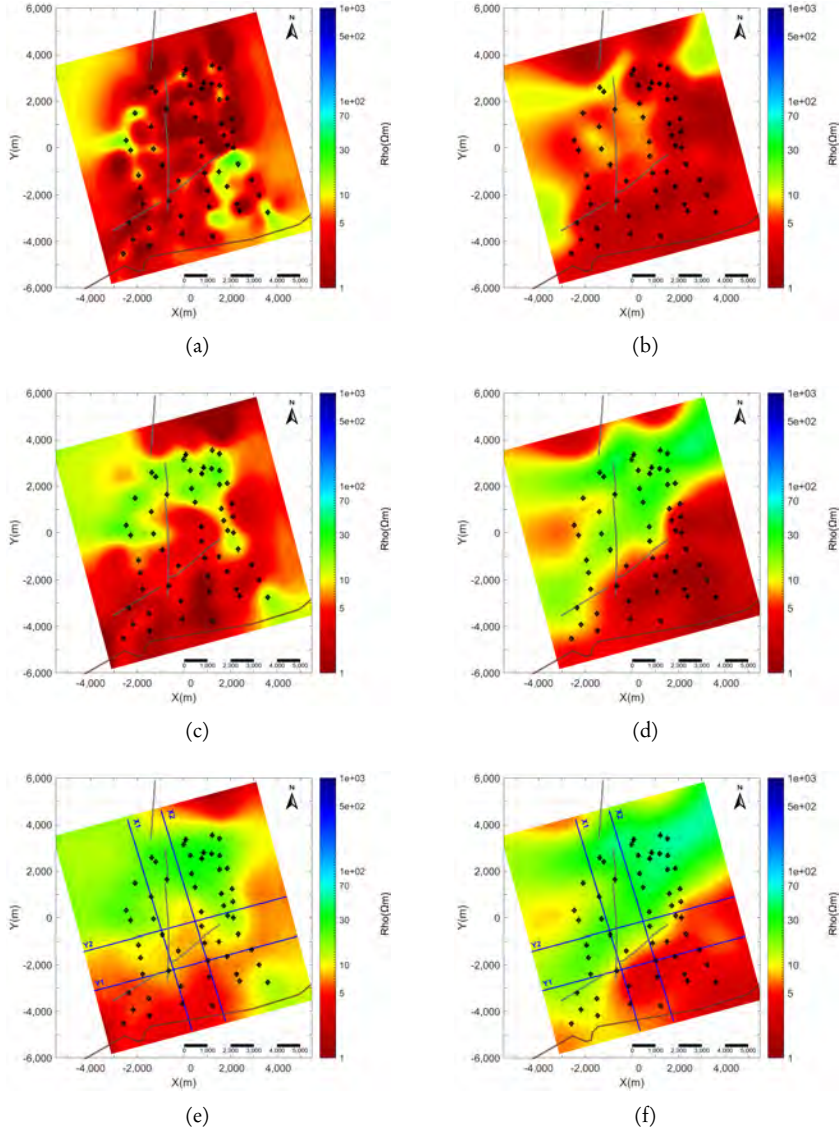


Figure 5.8: Resistivity maps at constant elevation from the two inversion models. Resistivity at -500 m amsl. from (a) ModEM-10-Tur and (b) Mack-10-Tur. Resistivity at -1,000 m amsl from (c) ModEM-10-Tur and (d) Mack-10-Tur. Resistivity at -1,500 m amsl from (e) ModEM-10-Tur and (f) Mack-10-Tur, in these two maps, the locations of the profiles of the resistivity cross-sections shown in Figure 5.9 are given. Magnetotelluric stations (diamonds), main faults (grey solid lines) and the coast line (brown solid line) are shown as well in all maps. Resistivity in Ωm .

and a relatively high resistivity in the north-west, the boundary of which is roughly coinciding with the east-west striking faults, see Figures 5.8(c) and 5.8(d). This trend is more pronounced in Mack-10-Tur compared to ModEM-10-Tur and continues at greater depths as illustrated in Figures 5.8(e) and 5.8(f).

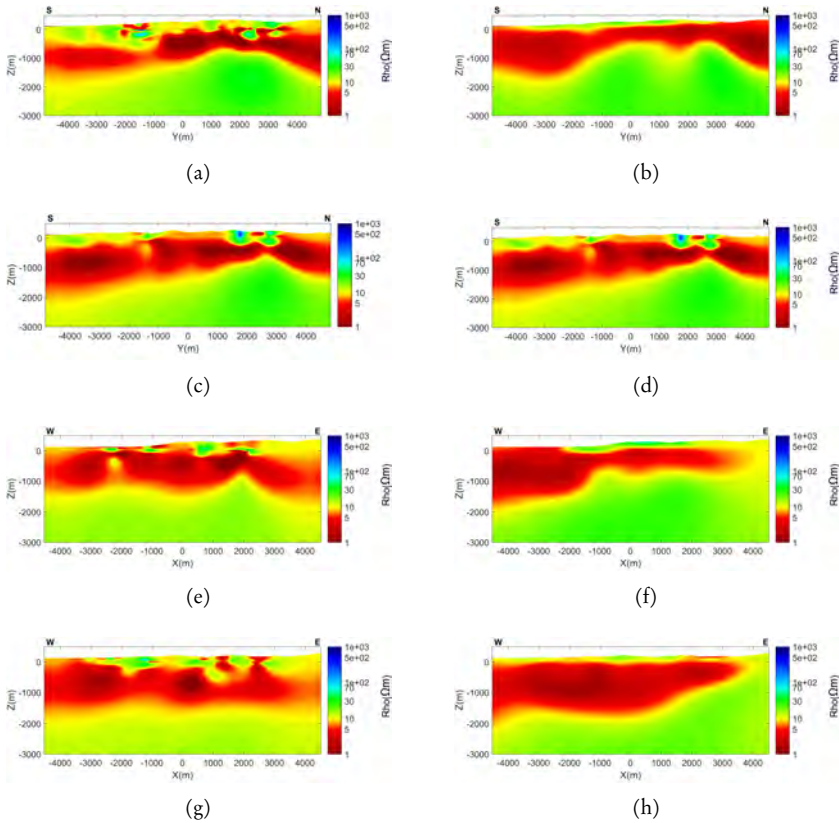


Figure 5.9: Resistivity cross-sections from the two inversion models. Cross-section of profile X1 at $X = -1,187.5$ m from (a) ModEM-10-Tur and (b) Mack-10-Tur. Cross-section of profile X2 at $X = 312.5$ m from (c) ModEM-10-Tur and (d) Mack-10-Tur. Cross-section of profile Y2 at $Y = -500.0$ m from (e) ModEM-10-Tur and (f) Mack-10-Tur. Cross-section of profile Y1 at $Y = -2,000$ m from (g) ModEM-10-Tur and (h) Mack-10-Tur. Resistivity in Ωm . The surface locations of the cross-sections are given in Figures 5.3, 5.8(e), and 5.8(f).

Resistivity cross-sections named X1, X2, Y1 and Y2, as shown in Figures 5.3, 5.8(e), and 5.8(f), are plotted perpendicular to the model X- and the model Y-direction. All resistivity cross-sections from both models, as plotted in Figure 5.9, show a conductive layer overlying a more resistive basement. However, where Mack-10-Tur shows a thin resistive layer on top of this conductive layer, ModEM-10-Tur is more heterogeneous at shallow depths. In the XZ-orientated cross-sections more differences between Mack-10-Tur and ModEM-10-Tur can be observed. Whereas in ModEM-10-Tur the conductive layer spans the entire model, this layer is discontinuous and significantly thinner towards the east of the model in Mack-10-Tur as can be seen in see Figures 5.9(e) and 5.9(g).

5.5 3-D modelling results quantitatively compared

The bulk of the resistivity structures in the two 3-D inversion models presented in Section 5.4.1 are related to geological structures, particularly those anomalies consistent between both models. However, some of the features may be artefacts introduced by the inversions. To make a quantitative comparison between the two models, a set of structural metrics used to identify those resistivity structures which are required by the model, is computed. Those required or robust resistivity structures represent geological structures and are suitable for the geothermal interpretation of the resistivity models.

5.5.1 Structural metrics

The structural metrics used in this Section are normally applied to compare different geophysical models before joint inversion and are described in, for example, the review article by *Gallardo and Meju* [2011]. Some of these metrics are also used in a slightly modified version proposed by *Rosenkjaer et al.* [2015] to compare electromagnetic inversion models resulting from different inversion codes. The metrics described below are based on the gradient, cross product and Laplace operators. The structural metrics used to verify the resistivity structures in the model are:

- 1 The magnitude (or norm) of the model gradient $\|\nabla m\|$.
- 2 The difference between the normalized model gradients of the two resistivity models, the gradient difference, $\delta\bar{\varphi} = \frac{\nabla\bar{m}_1}{\|\nabla m_1\|} - \frac{\nabla\bar{m}_2}{\|\nabla m_2\|}$.
- 3 The norm of the cross product of the two model gradients, the cross gradient, $\bar{\tau} = \nabla m_1 \times \nabla m_2$.

Here \bar{m} is the three-dimensional model matrix of the inversion model. The details of these metrics are described in Appendix A.

Synthetic model

The structural metrics of synthetic resistivity data were computed to guide the interpretation of the structural metrics of the resistivity models. All synthetic models considered are given in Appendix A. In Figure 5.10 a generalized model of the dominant resistivity structures present in the inversion models presented in Section 5.4 are given, as are the structural metrics of these resistivity patterns. Similarly to the real resistivity models, the two synthetic resistivity models consist of several resistive layers. The models differ in the position of the boundary between high and low resistivity, see Figures 5.10(a) and 5.10(b).

The magnitude (or norm) of the model gradients of the two synthetic models are shown in Figures 5.10(c) and 5.10(d). In the regions where the resistivity of the model is not changing, the normalized model gradients are small (blue), while in the regions where there are differences in the resistivity of the model, the normalized model gradients are large (red). Although the two synthetic models are not significantly different, the cross gradient of the two synthetic models, as given in Figure 5.10(e), highlights the outer margins of the region where both models are subject to a resistivity change. This in contrast to Figure 5.10(f) in which the difference between the normalized model gradients is given. In this Figure, the inner margins of the region where the two synthetic models are subject to resistivity change are relatively similar between both models. In this case, the boundary between the intermediate and high

resistive layers can be found in between the limits of the highlighted regions of the cross gradient and gradient difference metrics. The boundary between the intermediate and the low resistive layers is only present in the gradient difference metric.

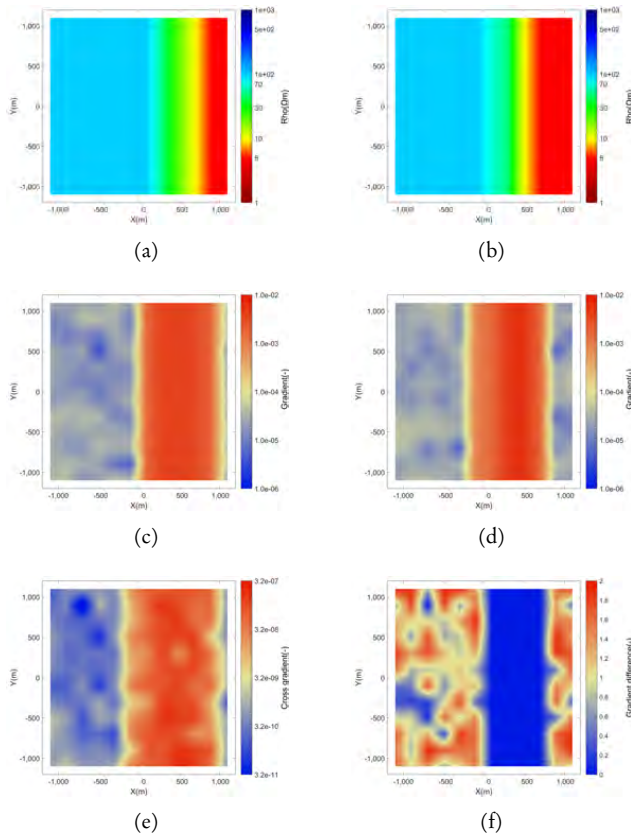


Figure 5.10: Synthetic resistivity model of two slightly different three-layer models, model 1 5.10(a) and model 2 5.10(b), as well as the structural metrics of these two models. Resistivities are given in Ωm . Norm of the model gradient of 5.10(c) model 1 and respectively of 5.10(d) model 2. Here, red colors indicate a change in resistivity, while blue colors indicate regions with a *stable* resistivity structure. 5.10(e) shows the norm of the cross product of the two synthetic models. 5.10(f) shows the difference between the normalized model gradients of the two synthetic models.

From this analysis it is concluded that the cross gradient is sensitive for the location of a resistivity structure and picks up similarities and differences between resistivity values of two models. On the other hand, the difference between model gradients is sensitive for similarities between model gradients, and indicates large differences for areas with a very low model gradient.

Resistivity models

In Appendix B, the structural metrics of all the elevation maps and cross-sections discussed in Section 5.4.1 are presented. A selection of these elevation maps and cross-sections are presented here in the Chapter text as well. In Figure 5.11 the elevation maps at -1,000 m of the gradient, the cross gradient and the gradient difference of the resistivity models are shown, while in Figures 5.12 and 5.13 the cross-sections of these structural metrics for profiles X1 and Y2 are presented.

At an elevation of -1,000 m, see Figures 5.11(c) and 5.11(d), the gradient maps of both models show pronounced changes in resistivity. The gradient of the resistivity model shows regions in which ModEM-10-Tur has less resistivity changes, see Figure 5.11(c). Those regions are especially present in the south and along the eastern and western edges of the model. Similarly, despite appearing at different locations, regions with a stable resistivity are present in Mack-10-Tur in the south-east and along the western edge of the model. The region in the south is bounded by the east-west striking fault in the area. This observation is confirmed in Figure 5.11(e) in which the cross gradient of the models is given. In the dominantly blue areas the models are relatively similar, while in the red areas the differences in the locations of the resistivity boundaries are highlighted. Also in Figure 5.11(f), the southern region of the project area is dominated by a stable resistivity, as high values generally indicate low model gradients in both models, see Section 5.5.1, while in the North the resistivity gradients of the two models are relatively similar and at roughly coinciding locations.

The cross-sections of the model gradient, as shown in Figures 5.12(c), 5.12(d), 5.13(c), and 5.13(d) for the two resistivity models, are relatively similar. At shallow depths, ModEM-10-Tur appears to be more heterogeneous,

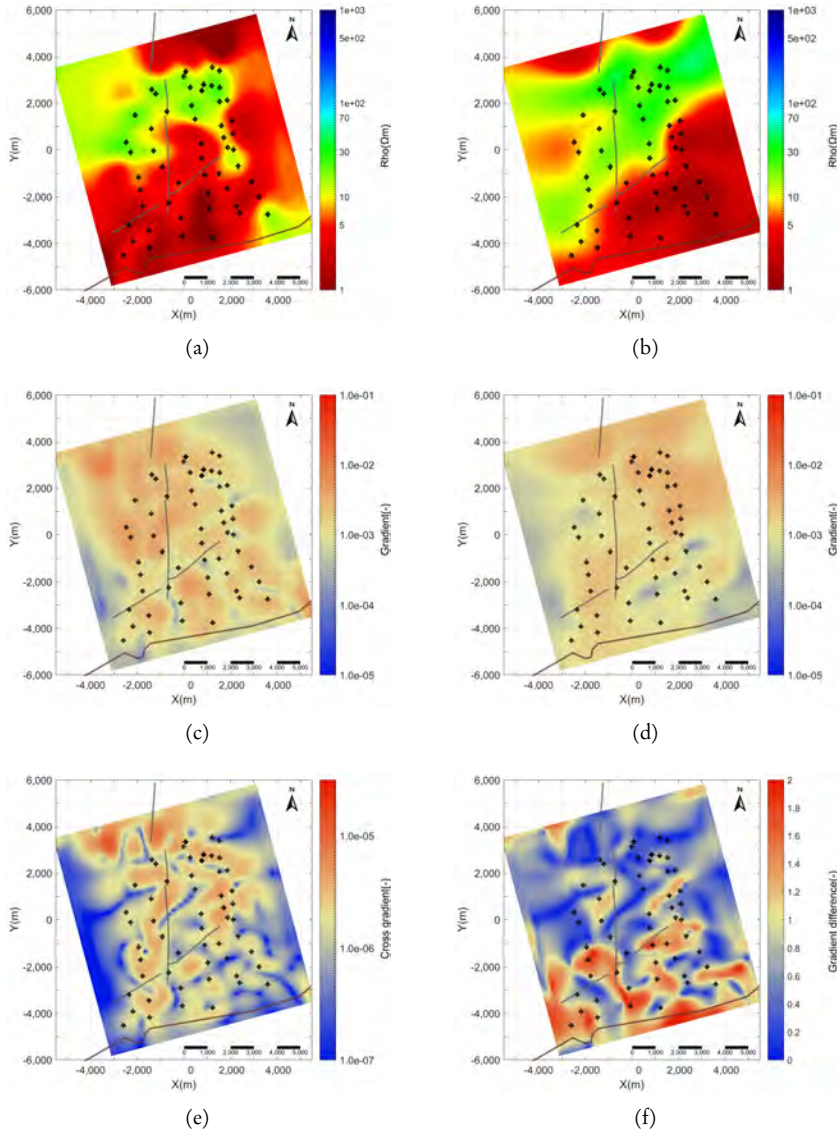


Figure 5.11: Resistivity maps at -1,000 m elevation from (a) ModEM-10-Tur and (b) Mack-10-Tur. Norm of the resistivity gradient at -1,000 m elevation from (c) ModEM-10-Tur and (d) Mack-10-Tur. (e) The cross gradient of the two resistivity models at -1,000 m elevation. (f) Normalized difference of the difference between the model gradients. Magnetotelluric stations (diamonds), main faults (grey solid lines) and the coast line (brown solid line) are shown as well in all maps. Resistivity in Ωm .

although a certain layering is recognizable, while Mack-10-Tur clearly shows a layered structure. Where these layers are continuous in the X-direction, Figure 5.12, they are discontinuous in the Y-direction, Figure 5.13. Cross-sections of the norm of the cross product of the gradients are presented in Figures 5.12(e) and 5.13(e), while in Figures 5.12(f) and 5.13(f) the differences between the two gradients is plotted. As expected, the differences between the models at shallow depth are larger in comparison with those at larger depths. A small gradient difference, induced by a minor difference between the model gradients, is present in the north and east of the models. The maximum depth of base of the low resistivity layer in the inversion models is interpreted to be around a depth of

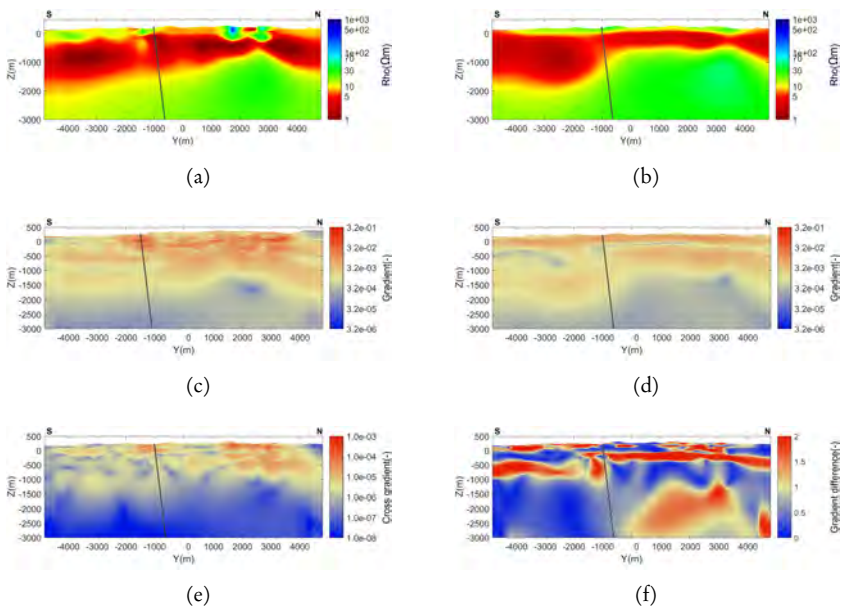


Figure 5.12: Resistivity cross-sections of the two models of profile X2 at model coordinate $X = 312.5$ m and its structural metrics. (a) Resistivity cross-section of ModEM-10-Tur. (b) Resistivity cross-section of Mack-10-Tur. (c) Model gradient of ModEM-10-Tur. (d) Model gradient of Mack-10-Tur. (e) The cross gradient of the two resistivity models for cross-section X2. (f) Normalized difference of the difference between the model gradients. Main fault (grey line) is shown in all cross-sections. Resistivity in Ωm .

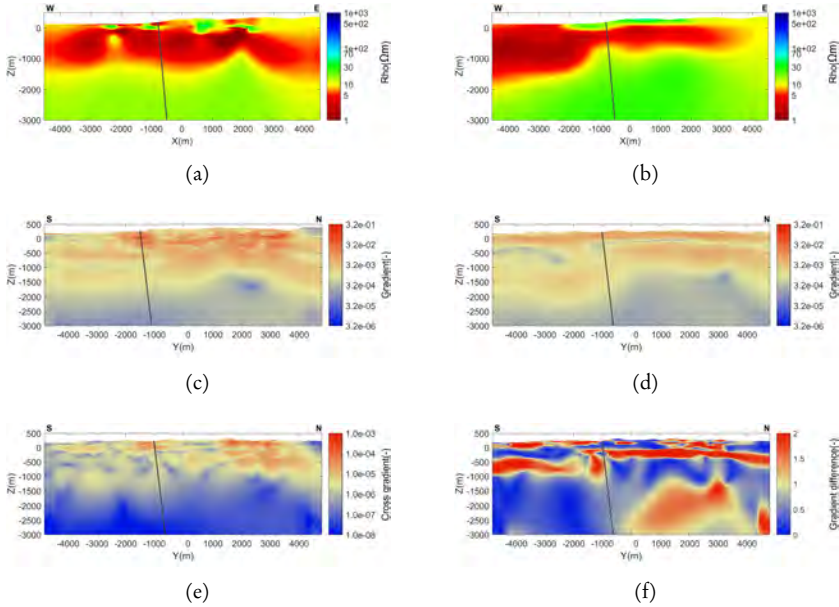


Figure 5.13: Resistivity cross-sections of the two models of profile Y2 at model coordinate $Y = -500$ m and its structural metrics. (a) Resistivity cross-section of ModEM-10-Tur. (b) Resistivity cross-section of Mack-10-Tur. (c) Model gradient of ModEM-10-Tur. (d) Model gradient of Mack-10-Tur. (e) The cross gradient of the two resistivity models for cross-section Y2. (f) Normalized difference of the difference between the model gradients. Main fault (grey line) is shown in all cross-sections. Resistivity in Ωm .

1,500 m in both cross-sections of the norm of the cross gradient as shown in Figures 5.12(e) and 5.13(e). The minimum depth of the base of this layer can be found at a depth of approximately 1,000 m in the cross-sections of the gradient difference of both models (Figures 5.12(f) and 5.13(f)). The location of the fault in the cross-section is only supported by resistivity cross-section of the Mackie_10_Tur model and not by the ModEM-10-Tur model or the structural metrics.

Based on the resistivity maps and cross-sections and the corresponding structural metrics, the resistivity models are in accordance with the local geological situation. Where the low resistivity structure is interpreted as corre-

sponding with a conductive weathered pyroclastic volcanic rocks overlying a more resistive basement formation, possibly an ophiolite complex overlying a limestone sequence. This limestone formation is the inferred geothermal reservoir [Serpen *et al.*, 2009]. The south-west north-east striking trend in the -1,000 and -1,500 m elevation maps coinciding with the parallel faults, is interpreted as the boundary of a graben-like system, see Figure 5.8.

The low resistivity observed in the south of the survey area appears to be related to the presence of Pliocene sediments and Quaternary alluvium. Low resistivities near the seashore in the south are likely the combined effect of the conductive sea water and water saturated sediments. This effect of the conductive sea is especially visible in Mack-10-Tur (see Figures 5.11(b), 5.12(b) and 5.13(b)).

The interpretation can be summarized as a layered model consisting of a resistive basement of ophiolite overlying limestones below a conductive layer of volcanic rocks, see Section 5.2. Following the description of other geothermal systems in the area, it is expected that this resistive basement is a limestone and serves as the geothermal reservoir. Two wells drilled in the prospect in 2015 penetrated the limestones at 2,300 m and 2,550 m respectively. The two wells were drilled slightly to the east of profile X2 and positioned around Y = 3,000 m. Consequently, the limestone sequence was penetrated after drilling through roughly 1,000 m of ophiolite.

As discussed in this section, the top of the resistive basement can be imaged by precisely mapping the features of the cross gradient and gradient difference indicating this boundary. This is of great added value when having to determine well targets. Another application of the structural metrics is the identification of faults in the subsurface. In this case the east-west striking fault could be identified on basis of the resistivity maps and was validated by the structural metrics. This same fault is identified in the resistivity cross-sections of the Mackie_10_Tur model, but not in the structural metrics when comparing both models.

5.6 Conclusions

The magnetotelluric data modelled and interpreted in this research is of average quality, but is difficult to assess since the data were acquired and processed in two parts, using different instruments and processing codes. Therefore, all data have been reprocessed from the time series data, using a single processing routine.

Two 3-D inversion models using two different codes, ModEM and Mack-3D, were derived from the magnetotelluric data. The former using the reprocessed and the latter using the original magnetotelluric data. Both models have identical model meshes, while other input parameters such as the number and extend of inverted frequencies, were chosen to be as similar as possible.

The inversion results of the two models are not only qualitatively compared based on their resistivity, but also quantitatively compared using a set of structural metrics. These structural metrics indicate that similar large scale resistivity structures are supported by both models, while this is not the case for the small scale resistivity anomalies. It is furthermore reassuring that the absolute resistivity values show comparable values.

The application of the structural metrics to 3-D inversion models is not straight forward. Not every metric is well suited to compare the structural similarities and differences between the two models. Here the difference between the model gradients is most sensitive for differences in the rate of resistivity change between two models and consequently highlights those regions in the model where these rates similar. As a result, the gradient difference detects the minimum boundaries of a resistivity structure present in two models. On the other hand, the cross gradient identifies the maximum boundaries of resistivity structures present in two models.

Being more smooth, the Mack-10-Tur model is more straightforward to interpret geologically, when compared to ModEM-10-Tur. Since the quantitative analysis revealed that both inversion models resolve the same subsurface resistivity structures, neither of them is more true. Both resistivity models are a good representation of the observed magnetotelluric data.

To eliminate the effect of the difference in smoothness between the two models, another ModEM inversion should be carried out using identical (or more similar) regularization parameters as the Mack3D inversion used for these magnetotelluric data. Since the available computational resources were depleted, this inversion run could not be carried out within this research.

The results of the two models validate the known geological structure of the survey area, with conductive volcanic rocks overlying a resistive base layer, consisting of ophiolite on top of a limestone sequence. It is expected that this limestone is the geothermal reservoir. This interpretation has been recently validated by two wells drilled into the geothermal prospect.

Furthermore, one edge of a graben-like system filled with sediments can be recognized in the inversion models and validated by the east-west striking faults in the area. These faults are recognized in the resistivity cross-sections of Mack-10-Tur, but not in the resistivity cross-sections of ModEM-10-Tur or in the structural metrics of these cross-sections. The conductive sea is also well resolved in the models.

6

The Montelago geothermal prospect

6.1 Introduction

The Montelago geothermal prospect on Mindoro Island, Philippines (see Figure 6.1), has been the target of development studies over a period spanning several decades. As a result, the volume of exploration studies carried out is high and is inconsistent in both time and focus (e.g. *Clemente [1979]; Apuada et al. [1989]; Leynes and Rosell [1997]; Clemente [1982]; PNOC EDC [1989a]; Ramos [1989]; Delfin and Zaide-Delfin [1989]; PNOC EDC [1989b]; Leynes and Sanchez [1998]; Maneja et al. [2000]; Lovelock and Lafrades [2011]; Tolentino et al. [2011, 2012]; Heijnen et al. [2013]; Hersir et al. [2014]; Árnason and Hersir [2014]*). Furthermore, the quality of the reports written and the fieldwork carried out is variable.

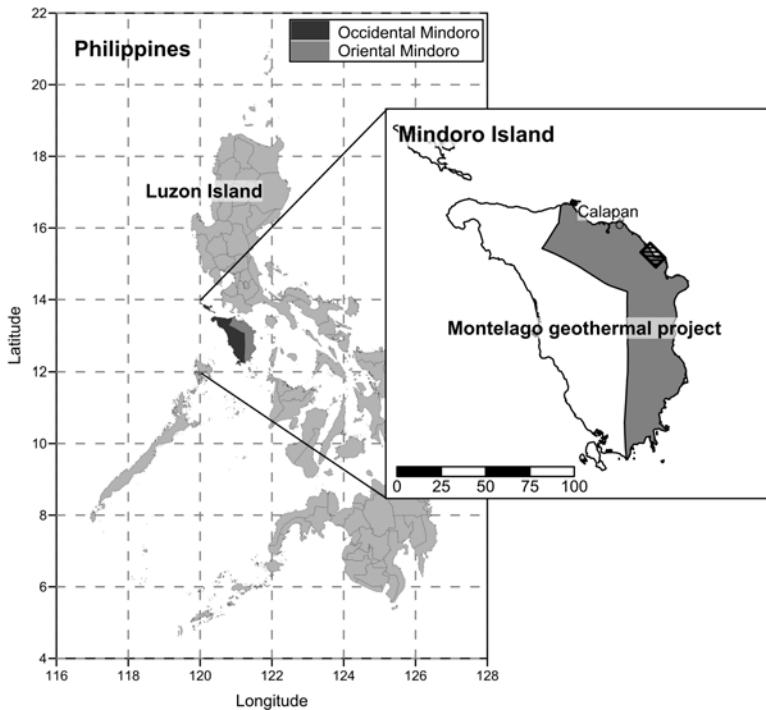


Figure 6.1: Location of the Montelago geothermal prospect on Mindoro Island within the Philippine archipelago. Scale bar in kilometres.

To get an accurate estimate of the potential of the geothermal prospect, all the research work carried out was summarized and evaluated by *Benavente et al.* [2014]. In this report it is concluded that the geothermal prospect has a temperature of at least 200 °C. A possible upflow zone is present below the Pungao area in the south-west of the project area. The geological and geochemical surveys indicated that the resource is fault-controlled with the most active upflow located roughly in the center of the project area. The size of the reservoir is estimated by *Benavente et al.* [2014] to be about 1.3 km² with a maximum resource capacity of 25 MW_e.

One of the most prominent components of the geothermal exploration work carried out for the Montelago geothermal prospect is the resistivity survey carried out in 2014 [*Hersir et al.*, 2014; *Árnason and Hersir*, 2014]. Resistivity surveying is a commonly applied exploration method for evaluating the technical potential of geothermal prospects (see Chapter 3). This is reflected in the high number of resistivity exploration studies carried out for the Montelago geothermal prospect. Since 1989 five different resistivity surveys were carried out:

- A study in which vertical electrical soundings were made using the Schlumberger method was carried out by *Apuada et al.* [1989]. The report of this study does not contain much detail and as the original data are not available, this survey does not carry added value for the current exploration of the geothermal prospect. Consequently, this survey is not used in this Chapter.
- A magnetotelluric survey was carried out by *Maneja et al.* [2000]. As this magnetotelluric data set might contain more information than reported, the magnetotelluric data are evaluated in this work in Section 6.4.1.
- A Controlled-Source Magnetotelluric (CSMT) study was carried out by *Tolentino et al.* [2012]. Both the raw data and the report of this survey are available and are discussed in Section 6.4.2.

- A combined TEM¹-MT resistivity survey was carried out by *Hersir et al.* [2014]. The data of this survey are evaluated in Section 6.4.3.
- A 3-D inversion of the static shift corrected magnetotelluric data mentioned above was carried out by [*Árnason and Hersir, 2014*], the 3-D inversion models of this study are discussed in Section 6.5.3.

In Section 6.2 a brief overview of the historical development of the Montelago geothermal prospect is given. Here, the history and the of the geothermal prospect is introduced as well. Following, in Section 6.3 the geology of the area and the conceptual model of the geothermal prospect are discussed. In Section 6.4 the quality of the data and the modelling work carried out with the respective electromagnetic data sets is assessed. It is shown that in some of the older studies the resistivity data is misinterpreted [*Tolentino et al., 2012*] or 'under-modelled' [*Maneja et al., 2000*], leading to erroneous or oversimplified models of the geothermal prospect. In the same Section, several measures, such as reprocessing and modelling are proposed to improve the current results. Hereafter, the proposed steps are carried out in Section 6.5. Together with the results of the recent resistivity survey [*Hersir et al., 2014; Árnason and Hersir, 2014*], the new resistivity models created in Sections 6.5.2 and 6.5.3 offer the opportunity to evaluate the different inversion models. The differences between the 3-D resistivity models as well as the quality and quantity of the resistivity exploration data necessary during the different development stages of a geothermal prospect are discussed in Section 6.6. Finally the main conclusions of this work are summarized in Section 6.7.

The objectives of this research are to *a)* summarize and evaluate the geophysical exploration research carried out for the Montelago geothermal prospect and interpret its impact on the current conceptual model, *b)* to evaluate, reprocess, remodel and interpret the electromagnetic data collected by *Maneja et al.* [2000] and *Tolentino et al.* [2012], *c)* to analyse the structural differences between the resistivity models of a single magnetotelluric data set created by two different inversion codes, and *d)* to assess the quality and quantity of the

¹Time-domain electromagnetic

geophysical data necessary to determine the optimal locations for geothermal exploration drilling and the subsequent stages of field development.

6.2 A brief overview of the Montelago geothermal prospect

The Montelago geothermal prospect is situated on Mindoro Island, the seventh-largest island of the Philippines and situated directly south of the main island of the country, Luzon, see Figure 6.1.

The project area is situated in Oriental Mindoro Province along the east coast of Mindoro Island and lies south of its main port, Calapan, situated in the north-east of the island. Despite the main mountain range being situated along the north-western shoreline of Mindoro Island, the topography of the project area is nevertheless locally very rugged. The project is named after the local dormant volcano Mount Montelago, situated within the project area (see Figure 6.2). The project area is about 2 km wide and 3 km long striking in a north-west south-east direction. In the north-east, the project area is bounded by Tablas Strait and in the south-west it is adjacent to the Lake Naujan nature reserve.

An insufficient number of oil-fired generators are currently the main power source for Mindoro Island, leading to a permanent power shortage with regular black-outs. This situation has created a high kWh-price, slowing down the economical development of the island, especially with respect to agriculture and tourism. As a result, an interest in alternative energy sources, with geothermal energy being one of them, has emerged. This combination of factors motivated Emerging Power Inc. (EPI) to acquire the geothermal license when it was made available for bidding by the Philippine government in 2009.

6.2.1 History of the geothermal prospect

Motivated by black-outs caused by the undercapacity of the national electrical grid, the state owned Philippine National Oil Company - Energy Development Corporation (PNOC-EDC) started a nationwide geothermal exploration survey in the late 1970's to identify the geothermal systems with exploitation

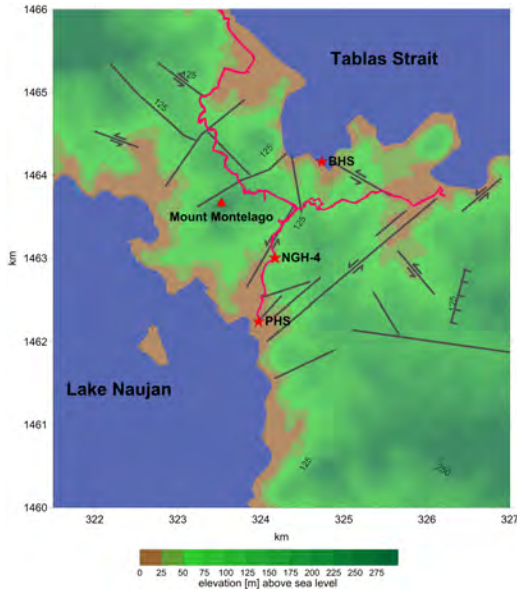


Figure 6.2: The project area of the Montelago geothermal prospect, with Mount Montelago and Lake Naujan. Indicated on the map are a gradient temperature well (NGH-4) which revealed a temperature of 94 °C at a depth of 305 m, Mount Montelago and the locations of the Pungao (PHS) and Buloc-Buloc (BHS) hot springs. Also the faults (grey) in the prospect area as well as the main road (purple) are given. Contours show topographic elevation. Coordinates of this and all following maps in this Chapter are, unless specifically mentioned otherwise, projected in UTM zone 51N using the WGS-84 datum.

capacity and to estimate the country's potential [Clemente, 1979, 1982]. The Montelago geothermal prospect was one of the projects identified as having sufficient geothermal potential to justify further exploration studies.

Thereafter, several geothermal exploration studies were completed by the end of 1980's, comprising amongst others a resistivity survey [Apuada *et al.*, 1989], a geochemical study [Ramos, 1989], a geological study [Delfin and Zaide-Delfin, 1989], thermal gradient drilling results [PNOC EDC, 1989b] and a report summarizing the different surveys carried out [PNOC EDC, 1989a]. From these early exploration studies it was concluded that while the geothermal prospect was considered to have adequate potential for further exploration, at the time it was not sufficient to pursue further development. Despite this conclusion, several new geophysical studies were carried out several years before the separation and privatization of EDC in 2007 [Leynes and Rosell, 1997; Maneja *et al.*, 2000].

The fully privatized company Energy Development Corporation (EDC) did not acquire all the geothermal licenses it had investigated in the past. Sev-

eral geothermal licenses were made available for bidding in 2008 and 2009. In the 2009 bidding round, EPI managed to acquire the Montelago license, considering geothermal a feasible economical solution for the power shortage on Mindoro Island.

EPI directly revived the project by performing a new study based on the available exploration reports up to 2011, estimating the geothermal potential by a so-called volumetric assessment [Lovelock and Lafrades, 2011]. In this study the potential of the Montelago geothermal prospect and the power grid and electricity market of Mindoro Island are both analyzed. It is concluded that the power situation at Mindoro Island is such that there is an ample market for a power operator to exploit a geothermal power plant.

In terms of geothermal potential, a reservoir temperature of 180-200 °C, spanning an area of 3-5 km² about 1.5 km thick is estimated. This leads to a geothermal resource potential in the region of 20 to 30 MW_e. This capacity will be more than sufficient to provide the base load for the whole of Mindoro Island. The artesian waters sampled in 1989 [Ramos, 1989; Lovelock and Lafrades, 2011] indicate a geothermal resource with temperatures above 200 °C. It was advised by Lovelock and Lafrades [2011] that the existence of this geothermal resource be verified by conducting a magnetotelluric survey and by reinterpreting the existing magnetotelluric data as acquired and reported on by Maneja *et al.* [2000].

Simultaneously another summary of the existing exploration studies was reported by Tolentino *et al.* [2011]. Where Lovelock and Lafrades [2011] focus on the geothermal and economical potential of the geothermal resource, the Tolentino *et al.* [2011] report is more technical and attempts to define the geothermal conceptual model of the Montelago prospect. Tolentino *et al.* [2011] assume a volcanic play type geothermal system, interpreting the existing information in line with this model. It is speculated that the geothermal system is heated by a series of volcanic dykes and that the hydrothermal waters are of a meteoric origin, circulating to the surface through open fractures. This study predicts a reservoir temperature of 190 to 200 °C, with a resource potential of 20 to 40 MW_e.

Instead of following the recommendation of *Lovelock and Lafrades* [2011], to re-interpret the existing magnetotelluric data and carry out a new magnetotelluric survey, the Controlled-Source Magnetotelluric (CSMT) survey, as suggested by *Tolentino et al.* [2011], was carried out [*Tolentino et al.*, 2012]. The acquired CSMT data is reprocessed and re-modelled in Sections 6.4 and 6.5 in 1-D and 2-D to obtain a more realistic resistivity model of the subsurface on the basis of the CSMT data.

In 2013 yet another summarizing study was carried out by *Heijnen et al.* [2013], this time the reports produced in 2011 [*Lovelock and Lafrades*, 2011; *Tolentino et al.*, 2011] and 2012 [*Tolentino et al.*, 2012] are included as well. By including a thermal infra-red study, as well as several geoscientific papers considering the geology and/or geothermal properties of Mindoro Island and its nearest surroundings, the amount of information reviewed was increased significantly in comparison to the earlier reviews of *Lovelock and Lafrades* [2011] and *Tolentino et al.* [2011]. The main conclusions from this 2013 report are that the Montelago geothermal prospect is located in an area with paleovolcanism, where faulting is probably still active, although the structural geological setting is poorly understood. Therefore it was recommended to carry out a structural geological fieldwork study.

The re-analysis of the geochemistry data of the area indicates a similar temperature range as reported by *Lovelock and Lafrades* [2011]. Since the water sampling was carried out 15 years earlier and the sampling procedure is poorly documented, the uncertainty of the predicted temperature range is high and a new water sampling expedition is strongly advised by *Heijnen et al.* [2013]. The re-interpretation of the CMST data, being a part of this study, suggests at least four areas of interest in the Montelago area, covering roughly 50% of the research area. To be able to be more precise, *Heijnen et al.* [2013] recommended a new resistivity survey be carried out. A conceptual model consisting of a deep seated cooling pluton which transports its heat through hydraulically conductive faults, is considered to be the most plausible explanation for the heat source. As the volcanic system is probably cooling, the geothermal system is likely of a medium enthalpy type. Finally, a geothermal potential of

40 MW_e, with a reservoir thickness of 1.5 km and reservoir area of 3 to 7 km², is estimated [Heijnen *et al.*, 2013].

Most of the recommendations made by Heijnen *et al.* [2013] were indeed followed up by EPI and a structural geological mapping fieldwork was carried out late 2013 and early 2014, as was a geochemical sampling expedition at around the same time [Regandara, 2014; Asnin, 2014]. Additionally magnetic and gravimetric surveys were carried out [Wibobo, 2014a,b]. Finally, a new combined TEM-MT, or resistivity, survey was carried out by Hersir *et al.* [2014].

Two successful exploration wells, SH-1 and SH-2 (see Figure 6.3), were drilled to a depth of approximately 1,200 m in the first quarter of 2015. The geothermal resource was confirmed and its potential is estimated at 35 to 40 MW_e [Rojas, 2015]. It is important to note that this depth is considerably deeper than the initially estimated depth of 300 m of the top of the geothermal reservoir. The next step in the development of the geothermal prospect will be the erection of a geothermal power plant.

6.3 Geology of the geothermal prospect

The results of these new exploration studies and especially their added value for the understanding of the Montelago geothermal system are summarized by PT LAPI ITB [2014] and van Leeuwen *et al.* [2016].

The volcanism present in the prospect area is part of a narrow north-west trending volcanic chain of Pleistocene-Quaternary age. Locally, this volcanic range overlies Tertiary sediments as well as the Paleozoic-Mesozoic basement consisting of meta-sediments and amphibolites. There are currently no active volcanoes present on Mindoro Island, where the latest volcanic activity is dated between 1.6 and 0.8 Ma. Within the prospect area, the volcanic centers are eroded.

The dominant tectonic setting of the prospect area has a north-west south-east striking direction. This orientation controls the structural geology on the island, which is dominated by strike-slip faulting. In the prospect

area, geological structures are dominated by north-east and north-west trending faults. Since the locations of the geothermal manifestations at the surface coincide with north-east trending faults, it is believed that these faults act as fluid pathways for geothermal flow to the surface.

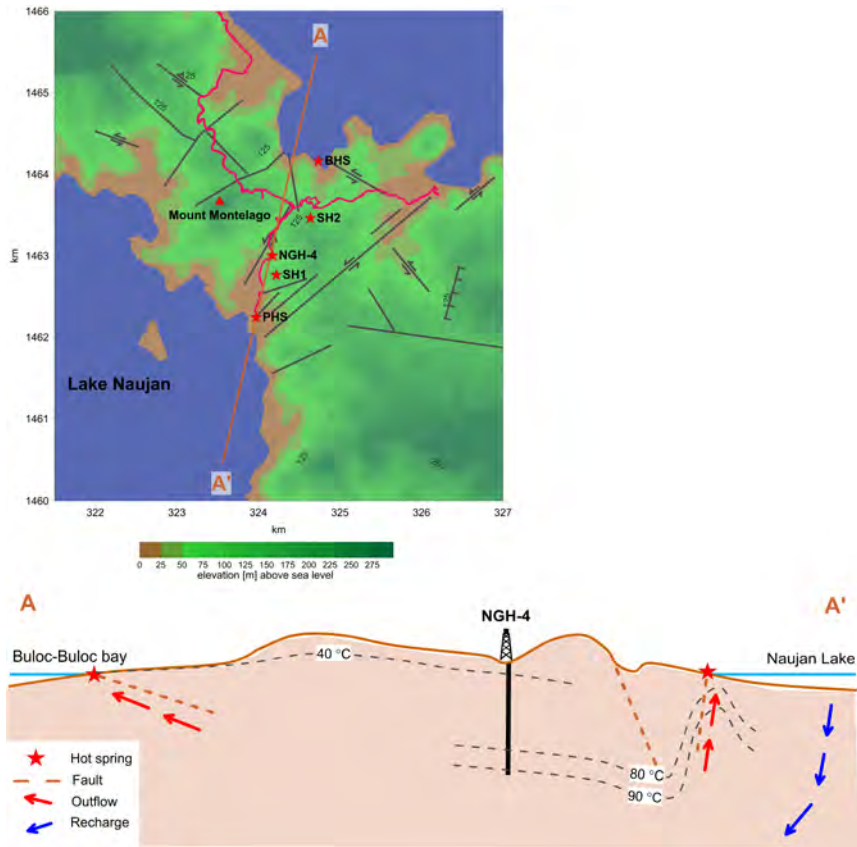


Figure 6.3: Map of the prospect area of the Montelago geothermal prospect (upper) and a not to scale cross-section of the geothermal prospect (lower). Indicated on the map are a gradient temperature well (NGH-4) which revealed a temperature of 94 °C at a depth of 305 m, Mount Montelago, the locations of well SH-01 and SH-02, and the location of the cross-section. Also the location of the Pungao (PHS) and Buloc-Buloc (BHS) hot springs are given, as well as the faults in the prospect area. BHS is located in the Buloc-Buloc bay. The main roads in the area are shown in purple. The cross-section indicates inferred outflow areas, faults and recharge of the geothermal system. Inferred isotherms are also given in the cross-section.

Hydrothermal clay alteration mineralogy present at the surface in the prospect area comprises interlayered illite-smectite as well as quartz-epidote-calcite minerals. The former is formed at temperatures of at least 150 °C and is typically found at depths greater than 50 m. The latter is formed at much higher temperature (> 240 °C). The occurrence of these two alteration minerals at the surface suggests that either erosion has occurred or that the materials are brought to the surface.

The geochemical analysis of sampled waters from the hot springs indicates that the system is water dominated. Furthermore, the magmatic component in the thermal water is very small, which implies that the geothermal system is not related to shallow magma or recent volcanic activity.

On basis of the findings summarized above, a conceptual model of the geothermal reservoir was defined [*PT LAPI ITB*, 2014]. The elements of the conceptual model are shown as a north-south orientated cross-section of the geothermal system in Figure 6.3. The Buloc-Buloc bay hot springs with a temperature of 40 °C are possibly originating from another geothermal reservoir. Recharge of the geothermal system is believed to be from Lake Naujan, located south-west of the prospect area. Thermal gradient well NGH-4 measured a temperature of 94 °C at a depth of 305 m. As the thermal gradient in this well is linear, the drilled formation is impermeable, possibly a clay cap.

It is inferred that the heat source of the system is a very deep cooling pluton. Consequently, the Montelago geothermal prospect is categorized as a plutonic play type geothermal system (see Chapter 2). Reservoir temperatures are estimated to be at least 200 °C.

Two slim holes down to 1,200 m depth below the surface were drilled to test the conceptual model of the Montelago geothermal prospect, see Figures 6.3 and 6.4. Both wells were fully cored and the drill cuttings were described using hand lens and microscope. Methylene Blue (MeB) analysis was carried out on the cores and the cuttings of both wells to identify the clay type and identify the top of the geothermal reservoir when drilled into.

Determination of the clay type can be carried out following a simplified relation between MeB-index and clay type. This relation states that a small

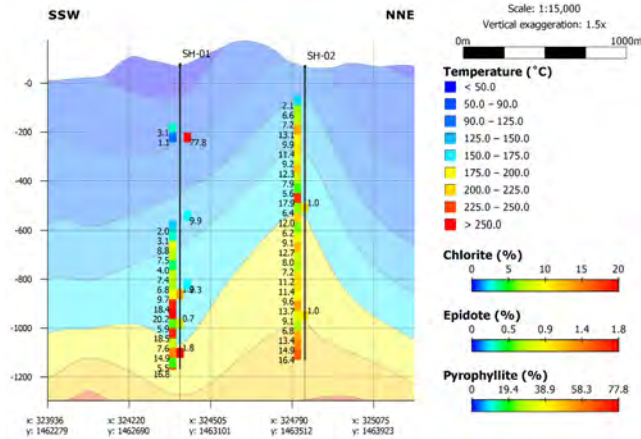


Figure 6.4: Illustration of chlorite (left of well line), pyrophyllite (right of well line) and epidote (center of well line) in slim well SH-01 and SH-02 with rock temperature. The location of the wells is given in Figure 6.3.

MeB index value (< 10) corresponds to illite or kaolinite clay minerals, while a high MeB index value (> 10) indicates smectite, interlayered illite-smectite or interlayered chlorite-smectite clay minerals.

Based on core and cutting description, high temperature alteration clay minerals such as epidote occur in well SH-1 at 900-1,200 m below surface and between 600-1,000 m below surface in well SH-2. The temperature at the depth interval in which epidote is found is below 200 °C [Sigurgeirsson *et al.*, 2015]. In contrast to the well temperature as shown in Figure 6.4, epidote is formed at temperatures above 230 °C. This suggests that the present day temperature is lower than the paleo temperature. In other words, the alteration mineralogy found in the present day geothermal system is the remnant of a former geothermal system.

The results of the MeB analysis suggests that at a depth of 500 m below surface the clay alteration type in the geothermal system is changing from interlayered illite-smectite (or smectite) to illite (or kaolinite). Interlayered illite-smectite usually is an indication of clay alteration above the geothermal reservoir, while illite is commonly related to clay minerals formed at higher temperatures near the top of the geothermal reservoir.

6.4 Evaluation of the existing geophysical exploration data

Although more geophysical surveys were carried out to explore the Montelago geothermal prospect, currently only three of them are considered to be relevant. The studies considered irrelevant are either very old, very poorly reported, or both. The three currently relevant surveys are the 2000 magnetotelluric survey conducted by *Maneja et al.* [2000], the 2012 CSMT survey carried out by *Tolentino et al.* [2012], and finally the 2014 combined TEM-MT survey carried out by *Hersir et al.* [2014].

In this Section the data acquired, as well as the models resulting from the inversion of these data sets, are evaluated. Measures to improve the resistivity models are proposed in this Section and carried out in Section 6.5.

6.4.1 The 2000 magnetotelluric study

The magnetotelluric data acquired by *Maneja et al.* [2000] consists of 27 magnetotelluric sites measured with a Phoenix V5 magnetotelluric system acquiring data at frequencies ranging from 384 Hz ($2.6e^{-3}$ s) to $5.5e^{-4}$ Hz (1,818 s). The stations were measured in a 3-D grid with a spacing of about 500 m, see Figure 6.5. A remote-reference station was set up at about 12 km away from the survey area. Magnetotelluric data were recorded for a minimum of 10 hours per station. The penetration depth of this survey will likely be limited, as 10 hours is a relatively short recording time for this kind of measurements. The data were processed using the proprietary Phoenix software [*Phoenix Geophysics*, 2005]. Unfortunately the digital data are not available, so only the reported Z_{xy} and Z_{yx} components of the magnetotelluric transfer function are available for further modelling.

Overall the data quality is intermediate (see Figure 6.6), good enough to support the reported 1-D models [*Maneja et al.*, 2000], and also adequate to support further 2-D or 3-D modelling. For some stations an explanation for the poor quality data can be found in the location of the station, e.g. close to a power line, road or houses, in most cases however, this is not possible. For example, station NAU-015A in Figure 6.6 is located near a settlement which is

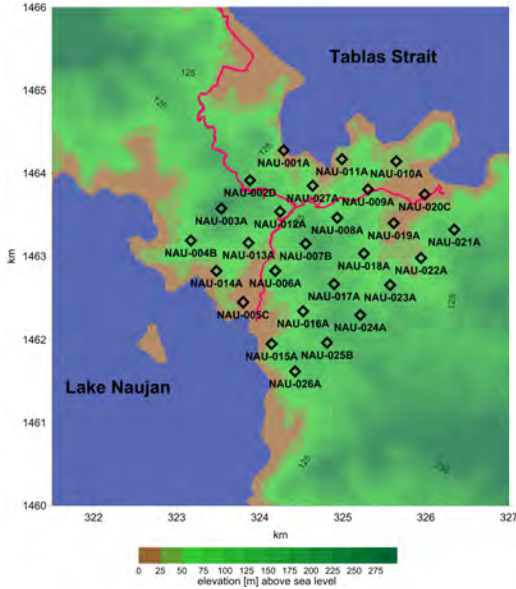


Figure 6.5: Magnetotelluric grid layout in Montelago as measured during the 2000 magnetotelluric campaign conducted by PNO-EDC [Maneja *et al.*, 2000].

connected to the electrical grid, probably explaining the poor data quality at long periods.

In the original modelling of these magnetotelluric data in 2000, each station was independently rotated to the local electrical strike direction (or principal axis) and was static shift corrected [Maneja *et al.*, 2000]. Following, although it is more common to model the invariant², the TM-mode was modelled in 1-D. There is no reason given for this choice, but it is speculated that Maneja *et al.* [2000] follow the inversion strategy of Wannamaker *et al.* [1984]. This strategy assumes that TE-mode modelling suffers from a bias towards shallow and low resistivities when 2-D and 3-D electrical structures are present, while using the TM-mode provides more accurate subsurface resistivity models. In fact, the authors have chosen to present three pseudo 2-D cross-sections created by interpolating the 1-D models of the TM-mode of the stations on the

²Here, the invariant of the magnetotelluric data is the average of the Z_{xy} and the Z_{yx} components of the magnetotelluric transfer response. Generally computed by taking the geometric mean of the apparent resistivities ρ_{xy} and ρ_{yx} and the arithmetic mean of the phases of the two. The magnetotelluric response is assumed to be 2-D and rotated to its principal axis, e.g. $Z_{xx} = Z_{yy} = 0$

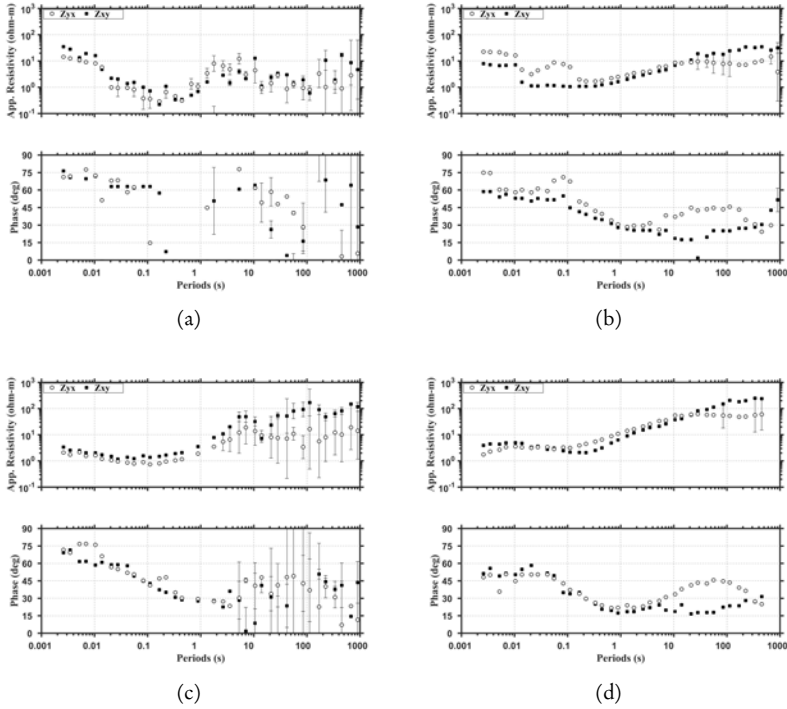


Figure 6.6: The responses of stations NAU-003A, NAU-008A, NAU-015A, and NAU-025B from the 2000 magnetotelluric survey [Maneja *et al.*, 2000], which represent typical responses observed throughout the survey. (a) Station NAU-003A shows poor quality data at all periods, typical of about 15% of the stations.; (b) Station NAU-008A shows poor quality data at the short periods, typical of about 45% of the stations; (c) Station NAU-015A shows poor quality data at long periods, typical of about 40% of the stations; and, (d) Station NAU-025B shows good quality data at all periods, typical of about 30% of the stations. Note that as there are stations showing poor quality data at both long and short periods, the sum of the percentages is more than 100%

profiles. In addition to the cross-sections, a set of iso-resistivity maps is presented. Both the cross-sections and the iso-resistivity maps show an up-doming high resistivity structure at a depth of 500-550 m below the surface. The center of this structure is located close to station NAU-007B. The authors interpret this dome as a possible geothermal heat source and propose that the best tar-

gets for drilling are the steep resistivity gradients surrounding it, which are coincident with the mapped faults in the area as known in 2000, see Figure 6.7.

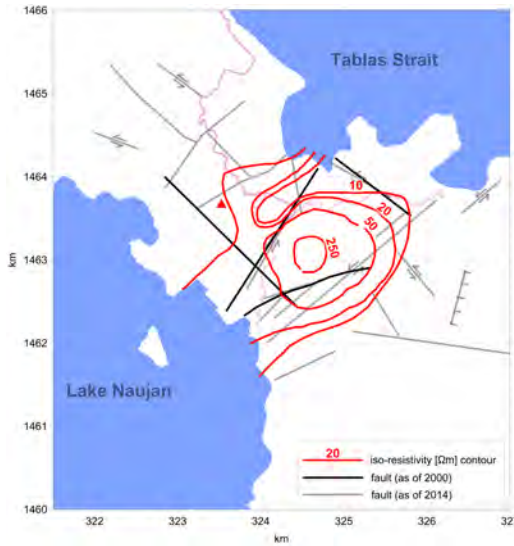


Figure 6.7: Iso-resistivity map at -1,000 m elevation as presented by *Maneja et al.* [2000]. The up-doming resistivity structure is located near station NAU-007B (see Figure 6.5 with steep resistivity gradients coinciding with faults mapped as of 2000 and 2014 [Maneja et al., 2000; Regandara, 2014]. The main roads (light purple) and the location of Mount Montelago (red triangle) are given on this map as well.

6.4.2 The 2012 CSMT study

In 2012, FEDS Energy Resources and Development Services Inc. (FEDS) conducted a CSMT survey in the Montelago geothermal prospect area. The CSMT data were acquired between 21 April and 3 June 2012. The area covered by the CSMT survey is approximately 8 km² and the survey was designed to reoccupy the 27 magnetotelluric stations of *Maneja et al.* [2000]. The survey delivered a total of 112 CSMT sites with a site spacing of approximately 250 m along 12 profiles orientated 45° East of North, see Figure 6.8. The locations of the CSMT stations were measured using a hand-held GPS unit.

The CSMT equipment has four channels, one channel for the magnetic field and three channels for the electric fields, measuring at 14 frequencies between 0.625 and 5,120 Hz. The instrument does not record the time series, instead it stores the internally calculated magnetotelluric transfer function. At

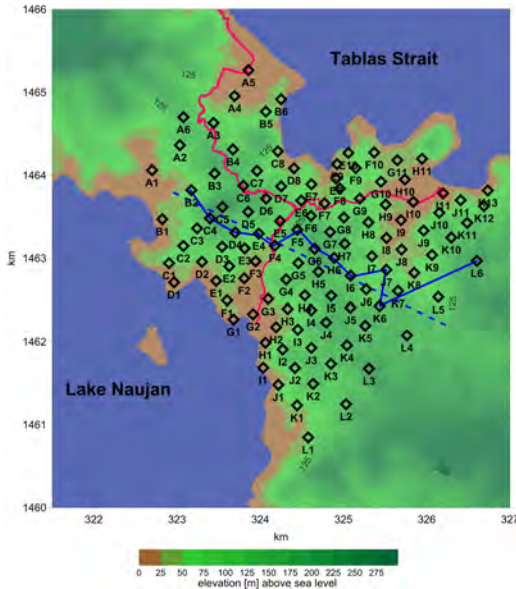


Figure 6.8: Locations of the CSMT stations measured by FEDS in May 2012 [Tolentino *et al.*, 2012]. The location of the resistivity cross-section P-1 of Figure 6.9 is shown as the blue dotted line, while the choice of the stations presented in this cross-section is given by the blue solid line. The main roads (purple) are also shown on this map.

each frequency, a number of repeat measurements is carried out and averaged for resistivity and phase. These averaged values are stored as the final result.

Tolentino *et al.* [2012] produced a 1-D model of each CSMT station and compiled three cross-sections made up of a stitched series of 1-D CSMT models along the profiles. One of these cross-sections is shown in Figure 6.9. Visible in this profile is the three layer approach FEDS used when modelling. The lateral electrical resistivity structure suggests a low resistivity layer, interpreted by Tolentino *et al.* [2012] as a conductive clay-cap consisting of clay alteration minerals smectite and illite and overlaying a more resistive geothermal reservoir. The top of this conductive layer varies between surface and -500 m elevation, while the bottom of the conductive layer varies between -1,000 and -1,500 m elevation. The interpretation of this resistivity model by Tolentino *et al.* [2012] is in line with the classic resistivity model of a volcanic type geothermal system as described by, for example, Cumming [2009] and Pellerin *et al.* [1996].

It is common to measure a single off-diagonal component, such as Z_{xy} or Z_{yx} , of the horizontal magnetotelluric transfer function during a CSMT

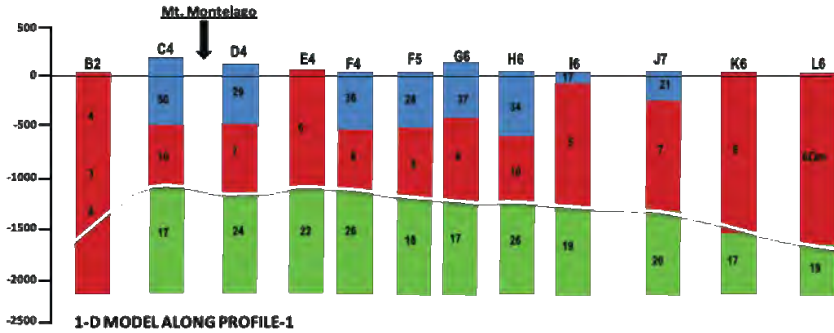


Figure 6.9: Cross-section along profile P-1 consisting of stitched 1-D CSMT layered models (from *Tolentino et al. [2012]*). The location of the profile is shown in Figure 6.8. Resistivities values of the layers of the individual 1-D CSMT models are shown in the 1-D model columns. The three layers are visualized by the colors blue (high resistivity), red (low resistivity) and green (intermediate resistivity).

survey. In the case of the CSMT survey in Montelago the electric field was measured parallel to the profile direction (45° E of N), while the magnetic field was measured perpendicular to the profile direction. Consequently the survey was conducted in the TM-mode, the YX-component of the magnetotelluric transfer function with respect to the profile direction. To measure in the TM-mode it is assumed that the profile is oriented perpendicular to an electrical strike direction of -45° E of N. A likely argument for the chosen electrical strike direction of -45° E of N is the orientation of the survey area and the coast line. This choice is however not supported by the dominant geological strike direction in the area (see Section 6.3) and does probably not adequately represent the actual electrical strike direction.

For the evaluation of the data collected during the 2012 CSMT survey, the data recorded at site G4 are used as an example to represent the properties of the CSMT data set. The repeat measurements for each frequency and phase are shown in Figure 6.10(a). Where the resistivity values are consistent for the repeat measurements, the phases show a large variability between repeats at all frequencies. Physically the phases for the TM-mode should lie between

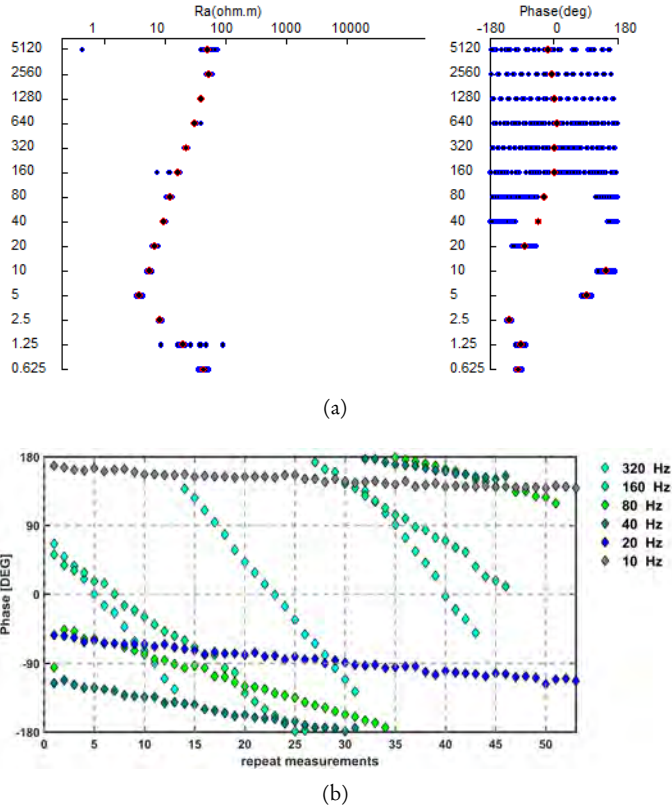


Figure 6.10: (a) Apparent resistivity and phase response for each frequency of CSMT station G4 as presented in *Tolentino et al.* [2012]. Repeat measurements at each frequency are shown in blue and the averages of the entire measurement are shown in red. Note that the apparent resistivity of the three lowest frequencies have a 45 °slope. (b) Phase repeat measurements for frequencies between 10 and 320 Hz of CSMT station G4.

-90 ° and -180 °, but they do not. In fact, the recorded phases systematically decrease for each repeat measurement, as is illustrated in Figure 6.10(b) for the phases recorded between 10 and 320 Hz.

Since the reason for the instability of the phases and their systematic decrease is unknown³, the phase measurements are assessed as being not usable. To this end a D+ approach [Parker, 1980; Parker and Whaler, 1981] is used to predict reasonable phase responses based on the good quality apparent resistivity measurements. The D+ model can best be described as an 1-D inverse problem approach for electromagnetic induction data. Here the D+ approach is utilized to construct a fitting mathematical model, containing both electrical resistivities and phases, to the measured CSMT data. The predicted phases are consistent with the resistivity data and can thus be used for further inversion modelling, replacing the original observed phases.

The three lowest frequencies showing an abrupt increase in apparent resistivity in Figure 6.10(a) are likely to be characteristic of a “near-field” response. To satisfy the plane wave assumption during a CSMT survey, it is crucial that the transmitter dipole is placed at a sufficient distance from the survey area. When the transmitter dipole is placed too close to the survey area, the plane wave assumption does not hold and near-field effects may be recorded. A D+ consistency check on the data revealed that in about 90% of the CSMT stations responses, near-field effects are indeed present at low frequencies. Consequently, a spurious resistor beneath the overlying conductor will be introduced when modelling these low-frequency data when using a plane wave field approach. The base of this conductor will also be entirely spurious. The consequences of the near-field effect on the results of the 1-D inversion modelling for a plane wave assumption, are illustrated in Figure 6.11. Both Occam and layered 1-D models of site G4 are made: in the left panel the results excluding the near-field data are shown, while in the right panel the inversion results including the low-frequency near-field data are shown. It is clear in the right panel that a deep resistive layer is introduced by the low-frequency near-field data. This deep resistive layer is modelled by Tolentino *et al.* [2012] as can be observed in Figure 6.9. Excluding the near-field data from the 1-D inversion strongly decreases the penetration depth of the CSMT survey as demonstrated in Figure 6.11.

³This was the case when this research was conducted in 2013. After meeting both the FEDS geophysicist responsible for the survey and an ex-employee from the Department of Energy, it was learned that the system used here is known to have problems with clock synchronisation. This was already known at the time of the survey.

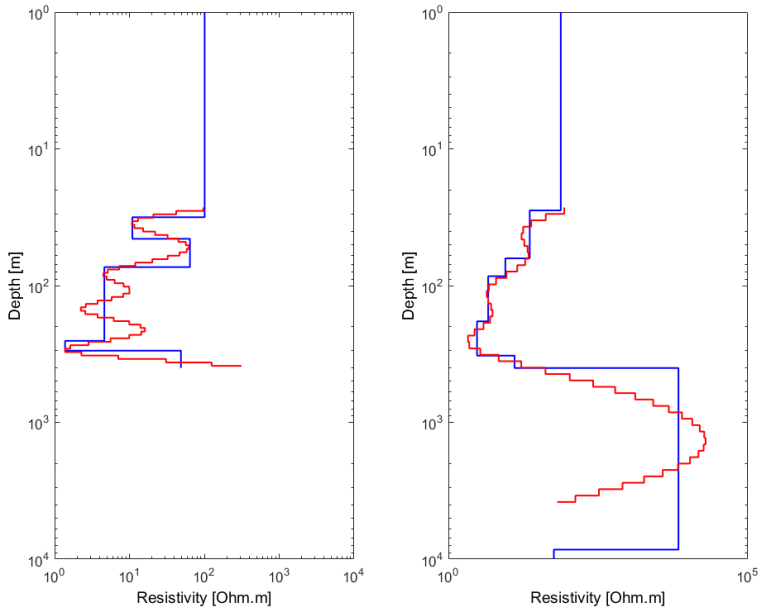


Figure 6.11: Layered (blue) and Occam (red) 1-D models of site G4 using only the far-field data (left) and both the far-field and the near-field data (right). The spurious resistor at depth is visible in the 1-D model on the right, which includes the near-field data. The Occam and layered 1-D modelling algorithms assume a plane-wave source field.

Based on the observations in this Section, it is concluded that the 2012 CSMT survey was not processed properly and, consequently, a resistivity inversion model, imaging an unrealistic subsurface, was created.

6.4.3 The 2014 magnetotelluric study

To obtain an accurate and complete magnetotelluric data set, a new 54 station TEM-MT study was carried out by Iceland GeoSurvey (ISOR) in early 2014. The recorded stations are shown in Figure 6.12. In this study time-domain electromagnetics (TEM) was used to mitigate the expected static shift effect in the magnetotelluric data [Sternberg *et al.*, 1988; Cumming and Mackie, 2010; Ármason, 2015]. The magnetotelluric data were collected using a set of four Phoenix MTU-5A data-loggers and the TEM soundings were acquired using a PROTEM digital receiver and a TEM-57 transmitter from Geonics Ltd.

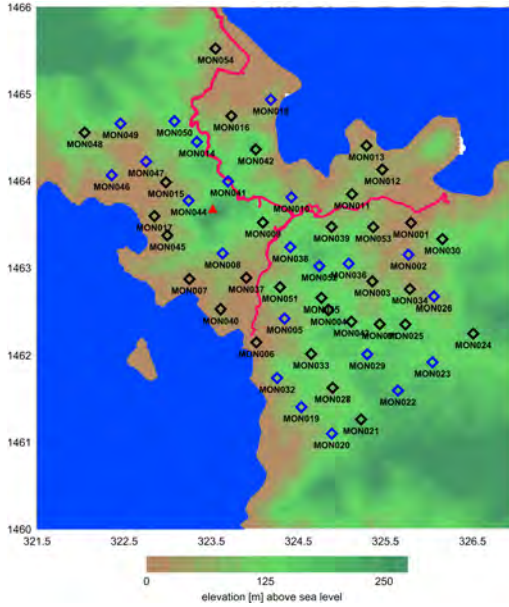


Figure 6.12: Map of the Montelago geothermal prospect area showing the measuring grid of the TEM-MT survey. Black stations are full tensor magnetotelluric stations and blue stations are telluric stations. Mount Montelago and the main roads are also shown.

For the magnetotelluric data a remote reference station was installed about 40 km away from the survey area. Each magnetotelluric station collected data for approximately 20 hours. A quality check of the data was performed before each station was cleared from the site and moved to a new location. Despite the presence of elevated power lines and several villages in the survey area, as well as the rugged topography, the data quality is assessed as fairly good [Hersir *et al.*, 2014]. The survey layout is a semi-grid with an interstation spacing of approximately 500 m.

During data acquisition every third station was a telluric station⁴. Measuring telluric stations in-between full tensor magnetotelluric stations is a common approach during magnetotelluric exploration surveys. Care should be taken when recording the telluric stations to ensure the maximum distance between simultaneously recorded telluric and magnetotelluric stations does not exceed the interstation spacing of 500 m.

⁴A telluric station only records the electric field. To calculate the magnetotelluric transfer function of a telluric station, the horizontal magnetic field of the nearest, simultaneously recorded magnetotelluric station is used.

To obtain maximal data quality in the difficult terrain in which the survey was conducted, the TEM field layout was tested for two days. The steep hills and dense vegetation made working with 200 m x 200 m or even 150 m x 150 m transmitter loops too difficult. After the test soundings showed that the data quality was sufficient using a 100 m x 100 m transmitter loop recording at a frequency of 30 Hz utilizing 20 time gates between 0.08813 ms and 6.978 ms, it was decided to use this layout during the TEM survey [Hersir *et al.*, 2014]. These time gates probe the same depth interval as the short periods of a magnetotelluric sounding. Quality control of the TEM recording is done while measuring, which effectively means that the recording is not stopped until the best possible quality data are recorded.

The magnetotelluric data were measured in a range from 320 Hz to approximately $8.4e^{-4}$ Hz (1,190 s) and were processed using the proprietary Phoenix processing software [Phoenix Geophysics, 2005]. The processing was done using either a common robust processing technique [Egbert and Booker, 1986; Chave and Thomson, 2004] or, when introducing spurious resistivity layers into the data, a non-robust processing technique [Jones *et al.*, 1989]. A total of 22 stations were recorded as telluric stations and consequently solely the four components of the horizontal magnetotelluric transfer function were measured here. The remaining 32 magnetotelluric stations also recorded the vertical magnetic transfer function.

The data quality of the acquired magnetotelluric responses is fairly good, although almost all stations show some problems around the magnetotelluric dead-band, where 15 (28%) stations are of a poor quality and 18 (33%) stations are of a good quality. Some typical responses are shown in Figure 6.13.

To correct for the static shift, the determinant invariant (see Chapter 3: “Theory of the magnetotelluric method”) of each magnetotelluric response is shifted iteratively towards the TEM response of the coincident TEM station following the procedure described in Árnason [1989]. Simultaneously with the static shift correction, smooth Occam 1-D inversions of the determinant invariant of the station responses are made. Based on the resulting 1-D models, a series of interpolated resistivity maps and interpolated resistivity cross-sections is

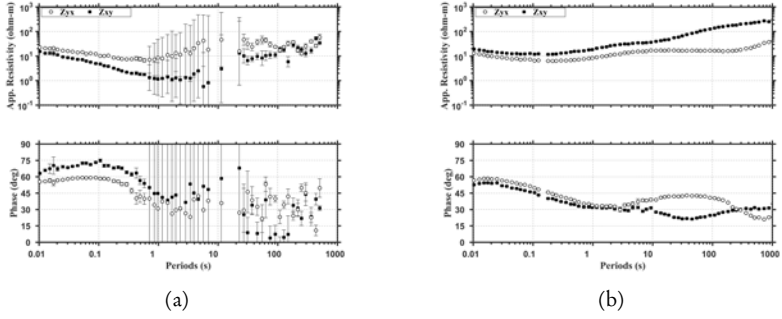


Figure 6.13: The responses of stations MON014 and MON021 from the 2014 magnetotelluric survey [Hersir et al., 2014], which represent examples of a very good quality and a very bad quality station response. (a) Station NAU-003A shows poor quality data at intermediate and long periods, typical of about 28% of the stations. (b) Station NAU-008A shows good quality data at all periods, typical of about 33% of the stations.

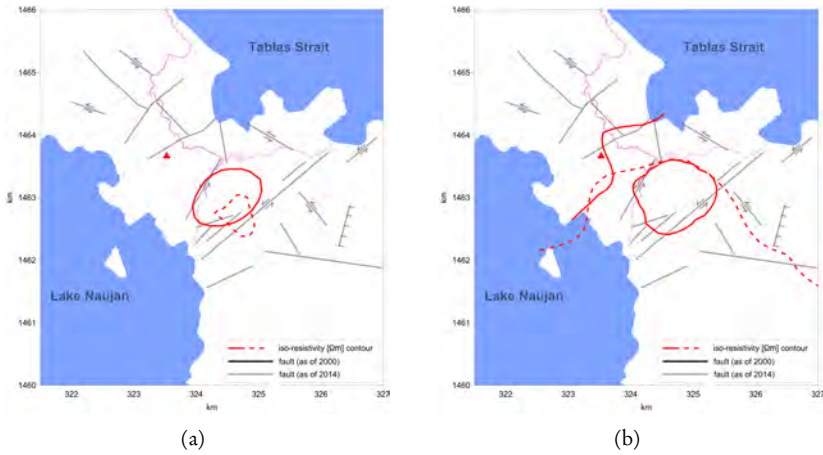


Figure 6.14: 10 and 50 Ωm iso-resistivity contours of the interpolated 1-D resistivity models of the 2000 PNOG [Maneja et al., 2000] and (solid contours) 2014 ISOR magnetotelluric data [Hersir et al., 2014] (dotted contours) at elevations of (a) -250 m amsl. and (b) -1,000 m amsl. respectively.

constructed. The resistivity structure of the subsurface of Montelago based on these interpolated 1-D models, as shown in Figure 6.14, indicates the presence of a resistive anomaly partly coinciding with the resistive anomaly interpreted by *Maneja et al.* [2000] and discussed in Section 6.4.1.

6.5 Inversion of the resistivity data

In this Section the available resistivity data collected for the exploration of the Montelago geothermal prospect are inverted using 1-D, 2-D and 3-D algorithms. In Section 6.5.1, the CSMT data discussed in Section 6.4 are inverted with Winglink software using different 1-D and 2-D inversion strategies. As the results of these inversion are not very useful for interpretation purposes, a summary is presented in Section 6.5.1.

In Section 6.5.2 and Section 6.5.3 the results of three different 3-D inversions studies are presented and qualitatively compared to each other. These are a.) a 3-D inversion based on the 2014 magnetotelluric survey conducted and carried out by ISOR as presented in [*Árnason and Hersir, 2014*], b.) a 3-D inversion using ModEM [*Egbert and Kelbert, 2012*] with the same 2014 magnetotelluric data set, and c.) a 3-D inversion using ModEM with the digitized 2000 magnetotelluric data as discussed in Section 6.4.1.

6.5.1 Inversion of the CSMT data

For the 1-D modelling approach, WingLink software is used that is capable of conventional 1-D magnetotelluric modelling using an ordinary plane-wave assumption. As a consequence only the far-field magnetotelluric data can be modelled. As the 1-D inversions are carried out with maximum periods between 0.1 and 0.5 seconds, the inversion results have a limited penetration depth. Furthermore, the inverted resistivity is too heterogeneous to be geologically interpretable. Consequently, the 1-D modelling results of the CSMT data are not presented here.

Two sets of 2-D models are created. One using TM-mode assumptions, i.e., the profiles are orientated perpendicular to an electrical strike direction

of -45° E of N and profiles oriented 45° E of N. It is, however, unknown if this assumption of an electrical strike direction holds true. Since the electrical strike direction cannot be directly determined from the single-component dataset available, the reliability of the features imaged in the TM-mode inversion is tested by carrying out a second comparative TE-mode 2-D inversion, using the same dataset with an equally valid assumption of an electrical strike direction oriented 45° E of N and profiles oriented -45° E of N. The difference between the two assumptions is illustrated in Figure 6.15. In general, TM-mode inversions are more sensitive to, and effective in, recovering the lateral resistivity variation in the subsurface, while TE-mode inversions are more sensitive to recovering absolute resistivities.

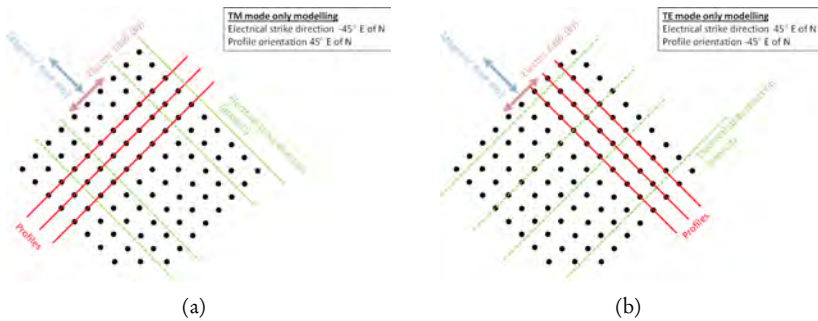


Figure 6.15: Schematic representation of the CSMT survey geometry of *Tolentino et al.* [2012] showing the two possible 2-D magnetotelluric modelling geometries: (a) TM-mode (B-polarization), and (b) TE-mode (E-polarization). The orientation of the assumed electrical strike is marked in green and the magnetic and electric fields are blue and purple, respectively. The CSMT recording sites are shown as black dots. The modelled profiles are shown as red lines.

To run the inversion for the TM-mode, twelve profile lines orientated exactly 45° E of N were constructed from 110 CSMT stations, two stations were rejected because of insufficient data quality,. Similarly, to run the inversion for the TE-mode 9 profile lines orientated exactly -45° E of N were created using a total of 87 CSMT stations. For each individual profile, a subsurface grid mesh is generated which accommodates the rugged topography and allows for sufficient detail in the vertical direction. For each profile mesh, inversion pa-

parameters were tested applying a forward run of the model to calculate the initial model root-mean-square (rms) misfit. The rms misfit is a measure of the fit of the model with respect to the observed data. When model mesh and inversion parameters are accepted, a 99 iteration run is applied over all profiles in either TM- or TE-mode. After inversion, a rms misfit of 1.5 or less, indicating a good fit between modelled and observed data, is an acceptable value for the misfit of the inversion model.

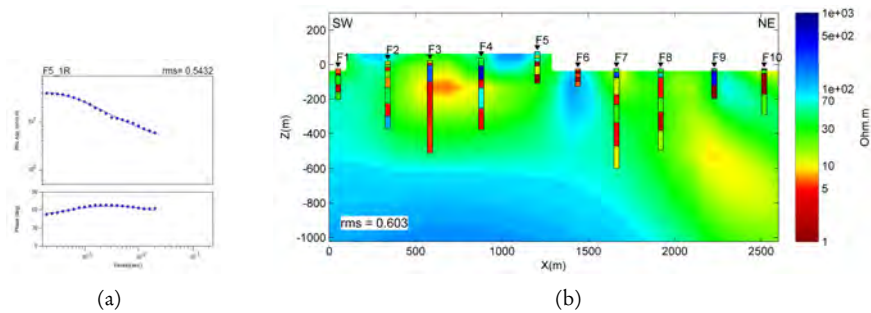


Figure 6.16: (a) Observed (dotted) and modelled (line) station responses for station F5 on profile F of the CSMT survey. (b) 2-D TM-mode inversion result for profile F. The 1-D layered model results of the CSMT stations are projected onto the resistivity cross-section as well. Note the mismatch between the elevation of the individual stations as measured with GPS and the used digital elevation map (DEM) of the survey area. This is caused by the coarse resolution of the DEM available. See Figure 6.17 for the location of profile F.

Results 2-D inversion of the CSMT data

All but two of the CSMT stations were used in the TM-mode 2-D inversion modelling, which was performed on profiles corresponding to the 2012 CSMT data acquisition profiles labelled A to L [Tolentino *et al.*, 2012]. Here station F5, as shown in Figure 6.16(a), is used to illustrate station responses of the 2-D inversion modelling in the TM-mode. For this particular station the rms misfit is 0.54. The 2-D inversion results of profile F, which comprises station F5, are shown in Figure 6.16(b). The overall rms misfit of profile F is 0.603. The resistive structures of the 2-D TM-mode inversion models are distinctively

different compared to the interpolated results of the 1-D inversion. Where the pseud0 2-D cross-sections constructed using the 1-D resistivity models reveal a highly heterogeneous subsurface, the 2-D TM-mode modelling results are less heterogeneous and reveal high resistivity structures at shallow depths.

For the deeper subsurface, a few distinct resistive features can be recognized. Each cross-section shows an “up-doming” resistive structure located in the south western part of the survey area. This resistive structure, although not always positioned at the same lateral position or depth, can be tracked from profile to profile. This is illustrated using resistivity maps at constant elevation as, for example, shown in Figure 6.17(a) for an elevation of -250 m amsl.

In the TE-mode 2-D inversion modelling, 9 profiles, named P-1 to P-9 as shown in Figure 6.17(b), were constructed using 87 CSMT stations. In this case, station F6 as shown in Figure 6.18(a) is used to illustrate the station responses of the 2-D inversion modelling in the TE-mode. For station F6 the rms misfit is 0.41. The 2-D inversion results of profile P-5, which comprises station F6, are shown in Figure 6.18(b). The overall rms misfit of profile P-5 is 0.776. Also apparent here are the differences between the 1-D inversion results and the 2-D TE-mode inversion. The resistivity of the TE-mode inversion at an elevation of -250 m amsl is plotted in Figure 6.17(b).

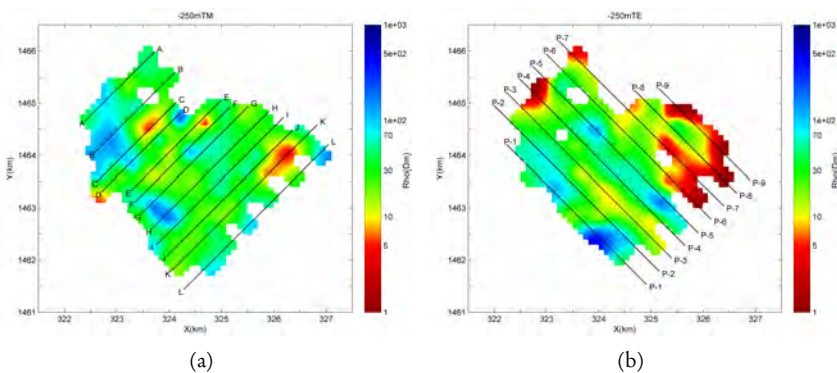


Figure 6.17: (a) Resistivity map of the survey area at a constant elevation of -250 m amsl. as constructed from the 12 cross-sections resulting from the 2-D TM-mode inversion. Resistivities are plotted in Ωm . (b) Resistivity map of the survey area at a constant elevation of -250 m amsl. as constructed from the 9 cross-sections resulting from the 2-D TE-mode inversion.

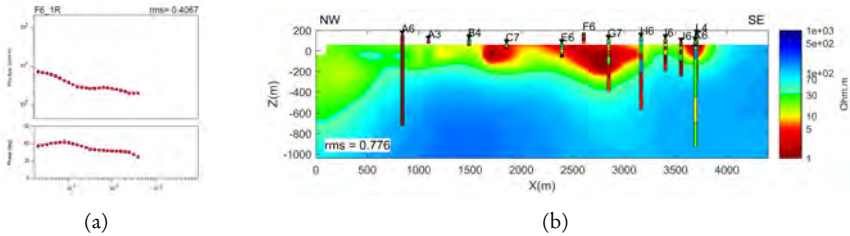


Figure 6.18: (a) Observed (dotted) and modelled (line) station responses for station F6 on profile P-5 of the CSMT survey. (b) 2-D TE-mode inversion result for profile P-5. The 1-D layered model results of the CSMT stations are projected onto the resistivity cross-section as well. Note the mismatch between the elevation of the individual stations as measured with GPS and the used digital elevation map (DEM) of the survey area. This is caused by the coarse resolution of the DEM available. See Figure 6.17 for the locality of profile P-5.

Where there is little similarity between the 1-D inversion results, the TM-mode 2-D inversion results and the TE-mode 2-D inversion results, the correlation between TM and TE-mode inversion results is clear. In Figure 6.17 the dominant resistivity structures can be recognized in both models. As a general trend higher resistivity values are present in the southern part of the survey area while lower resistivity values are found in the northern part. An especially pronounced stripiness can be noticed in the TE-mode inversion results. This is the effect of a cross-section with a deviated average resistivity with respect to the resistivity values of the other cross-sections.

6.5.2 Inversion of the 2000 MT data

To investigate if it is possible to use the magnetotelluric data set from *Maneja et al.* [2000] to create a 3-D resistivity image of the Montelago geothermal prospect, the responses of the 27 station magnetotelluric survey are inverted using ModEM [Egbert and Kelbert, 2012]. As digital data are unavailable, the necessary digitizing of the responses, as shown in Figure 6.6, introduce inaccuracies into the magnetotelluric data. As only the two off-diagonal, Z_{xy} and Z_{yx} , out of six possible components of the magnetotelluric transfer function and vertical magnetic function are available, the accuracy of the modelling results is affected.

After digitizing, the magnetotelluric responses are re-sampled to 32 pe-

riods to create a series of magnetotelluric responses measured at the same frequencies. The consistency of the responses is then checked by applying the Rho+-algorithm [Parker and Booker, 1996] to the data. The results are used to mask spurious data points before running the inversion. Except for station NAU-003A, which has insufficient data quality, the Rho+ results of the same stations as shown in Figure 6.6, are shown in Figure 6.19. In this Figure, the data points masked for inversion purposes are omitted from the plots. The data

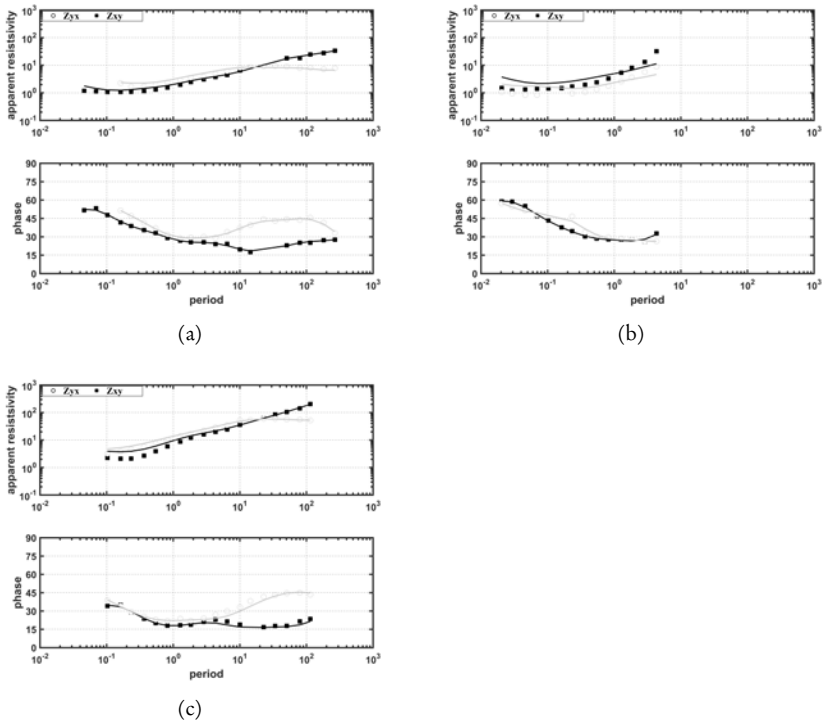


Figure 6.19: The measured and digitized responses (dots) and Rho+-model (lines) of stations NAU-008A, NAU-015 A, and NAU-025B from the 2000 MT survey. Masked data points are omitted from the station responses before 3-D inversion. (a) Station NAU-008A shows a good fit between phases and resistivities for the data points used. (b) Station NAU-015A shows a reasonable fit between phases and resistivities for the data points used. (c) Station NAU-025B shows good fit for long periods, but a relatively poor fit at short periods.

quality of magnetotelluric stations NAU-003A, NAU-011A, and NAU-21A is insufficient to be used in the 3-D inversion. The longest two and the shortest five periods of all stations show an inconsistent relation between apparent resistivity and phase and are therefore masked at all stations, leaving 25 periods ranging from 0.02 s (50 Hz) to 400 s (0.0025 Hz). Without considering the three omitted stations, 30% of 1,200 resistivity-phase data pairs within these 25 frequencies are masked before 3-D inversion.

Because only the two off-diagonal components of the magnetotelluric transfer function are available for inversion, no data rotation to another coordinate system is possible. Consequently, it is assumed that all stations are oriented to the magnetic North and the model is oriented accordingly. A model mesh is designed with an internal grid spacing of 250 m in both the model X- and the model Y-direction. The model cell sizes of the horizontal axes are logarithmically increasing from the model center towards the model boundaries. In the Z-direction, the topography, bathymetry and five air layers are taken into account. Between the highest elevation and sea level, the layer thickness is 20 m, below this the layer thickness is increasing logarithmically. The maximum depth of the model is designed based on the anticipated depth of penetration in the model. The maximum penetration depth in the model was determined by estimating the skin depth based on the maximum period in the magnetotelluric responses, given an apparent resistivity of 100 Ωm . To avoid edge effects this depth is multiplied by at least a factor 1.5. This leads to a model mesh with dimensions 32 x 32 x 83 cells (x, y, z) which extends over a horizontal distance range of 115.4 km x 115.4 km with an elevation ranging from 480 m above to 185 km below sea level. In Figure 6.20 the central area of the model mesh as well as the magnetotelluric stations are plotted. The model mesh is given a homogeneous initial resistivity, commonly either 10 or 100 Ωm , the first a likely underestimation of the average electrical resistivity and the second a likely overestimation of the average electrical resistivity of the studied area. Bathymetry and topography are included into the model mesh by assigning characteristic resistivity values for seawater-filled (0.3 Ωm) and air-filled (10^{10} Ωm) model cells.

As mentioned previously, the 3-D inversion is carried out using a paral-

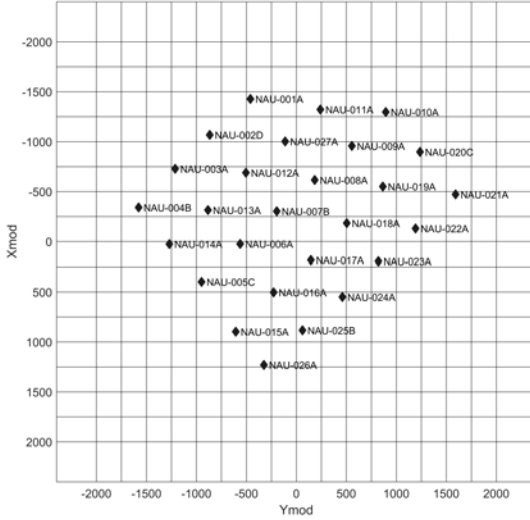


Figure 6.20: XY-view of the central area of the model mesh used for the 3-D inversion of the 2000 magnetotelluric data.

lel version of ModEM [Egbert and Kelbert, 2012]. Two inversions were carried out, the first with a homogeneous starting model of 10 Ωm, probably highlighting the resistive features in the model, the second with a homogeneous starting model of 100 Ωm, highlighting the conductive subsurface structures. The resulting rms misfit as reported by ModEM for the 10 Ωm starting model is 2.84 and is 3.03 for the 100 Ωm starting model.

In the following, the inversion results of the 10 Ωm starting model, “PNOC-10-mod”, are presented as they show slightly better results in comparison to the results of the 100 Ωm starting model.

The overall rms misfit⁵ is a general measure of the goodness of fit of the inverted model with respect to the observed data. Because of the nature of the inverted data, using this overall rms misfit might be misleading and therefore the rms misfit per station for all frequencies and per frequency for all stations are calculated as well. The rms misfit for PNOC-10-mod is shown in Figure 6.21. For longer periods an increasing rms misfit per frequency for all stations is observed, which implies that resolution decreases with depth. Con-

⁵The rms misfit is calculated using $RMS = \sqrt{\frac{1}{N} \sum \left(\frac{OBS - MOD}{\epsilon} \right)^2}$, where OBS is the observed and MOD the predicted data, while N is the number of data points and ε is the error of the data.

sequently, care should be taken when interpreting the inverted model at greater depths. The rms misfit of each station for all frequencies lies roughly between 0.4 and 1.0, with the majority of the stations to be found around 0.7. Stations NAU-001, NAU-002, NAU-004, and NAU-005 have a considerably larger misfit compared to the other stations. It is the misfits of these stations that mainly contribute to the relatively high general rms misfit of 2.84. Apart from their location at the western edge of the survey area, no significant differences between the quality and shape of the magnetotelluric responses of the four high rms misfit stations and the remaining inverted magnetotelluric stations are observed.

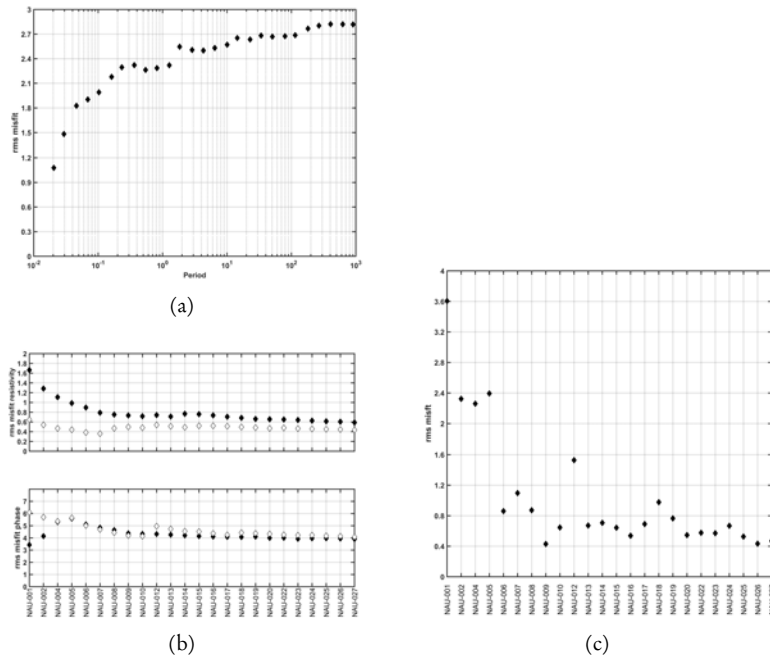


Figure 6.21: (a) Rms misfit per inverted frequency for all stations. (b) Rms misfit per station for apparent resistivity and phases separately for all frequencies. (c) Rms misfit per station for all frequencies, note station NAU-001 with a rms misfit of around 3.6. Filled diamonds indicate the XY and open diamonds the YX components of the magnetotelluric transfer function.

It is also possible to take a look at the rms misfit per component of resistivity and phase per station. In Figure 6.21(b) the rms misfits of the Z_{xy} and the Z_{yx} phase components are relatively high, but near to identical, while this is not the case for the rms misfits of the resistivities. This is illustrated in Figure 6.22, in which the modelled and observed station responses of the same stations as discussed earlier are plotted. The misfit in resistivity is often an over- or underestimation with respect to the observed resistivity data. Based on this observation, it can be speculated that this “static shift” is the effect of the topography and that, consequently, the static shift correction carried out by *Maneja et al.* [2000] was not conducted properly.

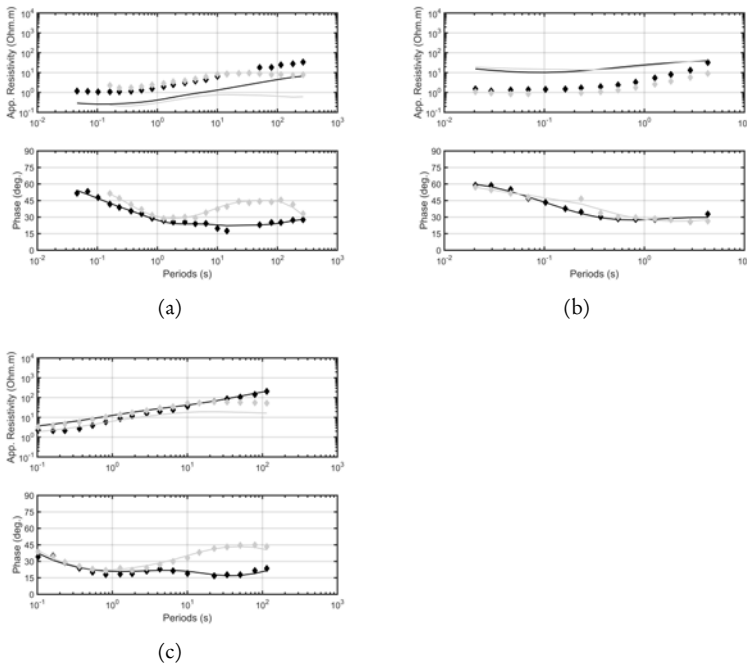


Figure 6.22: The observed responses (dots) and model responses (lines) of stations NAU-008A, NAU-015 A and NAU-025B from the 3-D inversion of the 2000 magnetotelluric data. Masked data points are omitted from the stations. Horizontal axis shows period in seconds, vertical axis shows apparent resistivity in Ωm (upper plot) and phases (lower plot) in degrees. (a) Station NAU-008A shows a good fit between phases, but an underestimation of the modelled resistivities. (b) Station NAU-015A shows a reasonable fit between phases and overestimation of the modelled resistivities. (c) Station NAU-025B shows good fit between phases, and a reasonable fit between resistivities.

The raw model results of PNOC-10-mod at an elevation of -260 m and -1,042 m amsl. are shown in Figure 6.23. Figure 6.24 shows the model results for the cross-section along the Y-axis of the model at $Y = 125$ m, i.e. the cross-section X-Z at $Y = 125$ m. In the upper parts of these two Figures, the raw inversion results are shown by plotting the modelled resistivity in each individual model cell. A more intuitive and common way of presenting the inversion results is to contour the results using the center of each grid cell, which are shown in the lower plots in these three Figures.

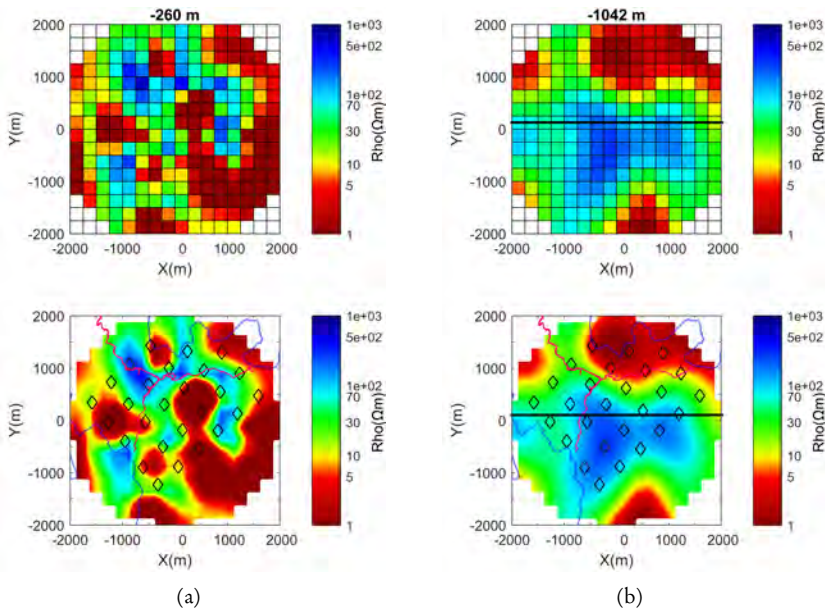


Figure 6.23: (a) Horizontal slices of the raw (upper) and smoothed (lower) model results of PNOC-10-mod at an elevation of -260 m amsl. (b) Horizontal slices of the raw (upper) and smoothed (lower) model results of the 3-D inversion modelling of the 2000 magnetotelluric data at an elevation of -1,042 m amsl. In black the location of the resistivity cross-section of Figure 6.24. The main roads in the area (purple) and the coast lines (blue) are given as well. Diamonds are magnetotelluric stations. Resistivity values in Ωm .

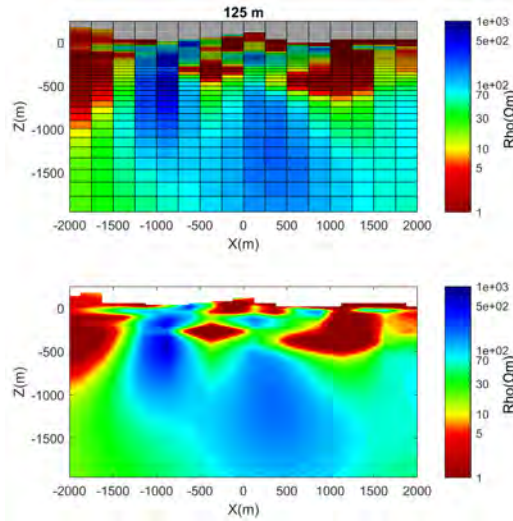


Figure 6.24: Cross-sections of the raw (upper) and smoothed (lower) model results of PNOC-10-mod along the model Y-axis at $Y = 125$ m. Resistivity values in Ωm . See Figure 6.23(b) for the location of the cross-section.

The resistivity model has a heterogeneous high conductivity dominated shallow structure. The high conductivity structures that are located along the edges of the model center and, consequently, away from the control of the magnetotelluric sites are probably model artefacts. Beneath these high conductivity structures and slightly south-west of the model center, a high resistivity structure extending to a depth of approximately 2,500 m is present. This resistive structure is laterally bounded by lower resistivities.

6.5.3 Inversion of the 2014 MT data

The magnetotelluric data acquired by ISOR in 2014 (see Section 6.4.3) are inverted using two different 3-D inversion codes. The first code used, WSINV3DMT, is developed by *Siripunvaraporn et al.* [2005]. The results of this inversion, which was carried out by ISOR, are presented in *Árnason and Hersir* [2014] and are referred to as “WSINV-10-mod”. The second code used is ModEM, developed by *Egbert and Kelbert* [2012]. The results of this inversion, carried out here, are presented in this Section and are referred to as “ModEM-10-mod”.

To make a meaningful comparison, inversion mesh and inverted frequencies are chosen to be as similar as possible. As the magnetotelluric data are already corrected for static shift (see Section 6.4.3), it is assumed by *Árnason et al.* [2010] that inverting the model without topography, but including bathymetry, and applying a post-inversion correction for topography, will deliver the most reliable resistivity model. To produce comparable models, the same inversion strategy was chosen for the ModEM inversion of the 2014 magnetotelluric data (ModEM-10-mod).

The model mesh used for both models consists of $52 \times 48 \times 32$ cells (x, y, z) with total dimensions of approximately $94 \text{ km} \times 94 \text{ km} \times 110 \text{ km}$. The strike analysis carried out by *Hersir et al.* [2014] suggests that the electrical strike direction of the survey area is roughly parallel to the coast line. Accordingly, the model mesh and the magnetotelluric coordinate system are rotated -46° , i.e. to 46° West of North. In Figure 6.25 the central area of the model mesh is shown, as well as the locations of the recorded magnetotelluric stations within the mesh. The central area of the model mesh is 5.7 by 4.5 km. The cell size of the central area of the mesh is $200 \text{ m} \times 200 \text{ m}$. The horizontal cell size increases semi-logarithmically towards the model boundaries. The smallest vertical cell size is 2 meters increasing semi-logarithmically with depth, to a maximum vertical cell size of $36,709 \text{ m}$ at the base of the mesh.

The 2014 magnetotelluric data are resampled to 31 periods with six values per decade covering 0.01 s to 1000 s for the inversion using WSINV3DMT. The inversion using the ModEM code uses magnetotelluric data resampled to 28 periods with five values per decade covering the same range of periods.

In their 3-D inversion *Hersir et al.* [2014] run three models using different initial models: a) a homogeneous half-space of $10 \Omega\text{m}$, b) a homogeneous half-space of $100 \Omega\text{m}$, and c) the resistivity model compiled from joint 1-D inversion of individual TEM and MT sounding pairs. It is concluded by *Árnason and Hersir* [2014] that the resistivity model resulting from the $10 \Omega\text{m}$ shows the best fit to the data and gives the most realistic image of the resistivity structure of the subsurface. Therefore, for the inversion of this magnetotelluric data

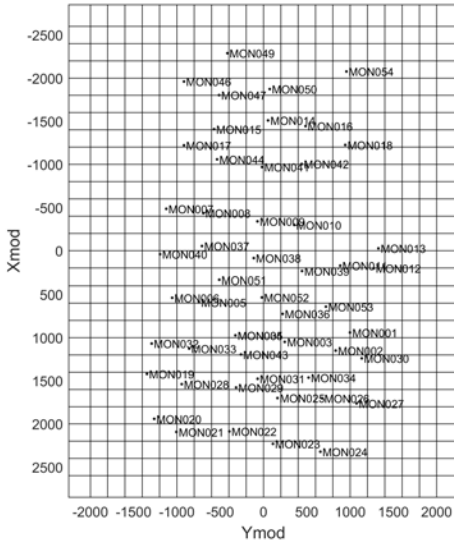


Figure 6.25: XY-view of the central area of the model mesh used for the 3-D inversion of the 2014 magnetotelluric data with WSINV3DMT and ModEM.

set using ModEM, an initial model of a homogeneous 10 Ωm half-space is used as well. Where the final rms misfit of WSINV-10-mod is 1.74, the final rms misfit of ModEM-10-mod is 1.92.

The inversion results of the two different inversions are shown in Figure 6.26 in which the iso-resistivity elevation maps at -200 m, -500 m and -1,000 m amsl. are plotted. As visible in Figures 6.26(a) and 6.26(b), both models show strongly heterogeneous conductivities at a depth of 200 m with a high conductivity at the boundaries of the survey area and some high resistivity anomalies in the center. The resistivity contrasts at this depth are more pronounced in WSINV-10-mod compared to ModEM-10-mod. At a depth of 500 m, as shown in Figures 6.26(c) and 6.26(d), the large scale resistivity structure between the two inversion models appears to be quite similar. However, while the resistive anomaly in the south of the survey area seems to be coincident in the two models, WSINV-10-mod also shows a resistive anomaly in the west of the survey area that is not present in ModEM-10-mod. This resistive anomaly is still visible at a depth of 1,000 m, as observed in Figure 6.26(e). At this depth, the

resistivity maps of the two inversion models are in rough agreement with each other, as shown in Figure 6.26(f). However, while the resistive anomaly in ModEM-10-mod is apparent as a single coherent anomaly, in WSINV-10-mod this resistive anomaly consists of three discrete parts.

To consider these observations further, the two resistivity cross-sections perpendicular to the model X- and Y-directions as shown in Figures 6.26(e) and 6.26(f) are plotted in Figure 6.27. In Figures 6.27(a) and 6.27(c) the similarities between the two models at $Y = -700$ m are clear. Both inversion models show a resistive layer with its maximum resistivity around approximately 2,000 m bsl. and with its top surface variable between about 500 m to 1,000 m depth. Several strong conductive anomalies between the surface and roughly 500 m depth can be identified. In WSINV-10-mod however, the resistive layer clearly rises towards the surface at two locations, while this is less pronounced in ModEM-10-mod. In the resistivity cross-section at $X = 300$ m, this difference in character of the resistive anomaly is more pronounced as shown in Figures 6.27(b) and 6.27(d). Although both models require a conductive layer at shallow depth, the deep resistive anomaly is significantly smaller in ModEM-10-mod compared to WSINV-10-mod.

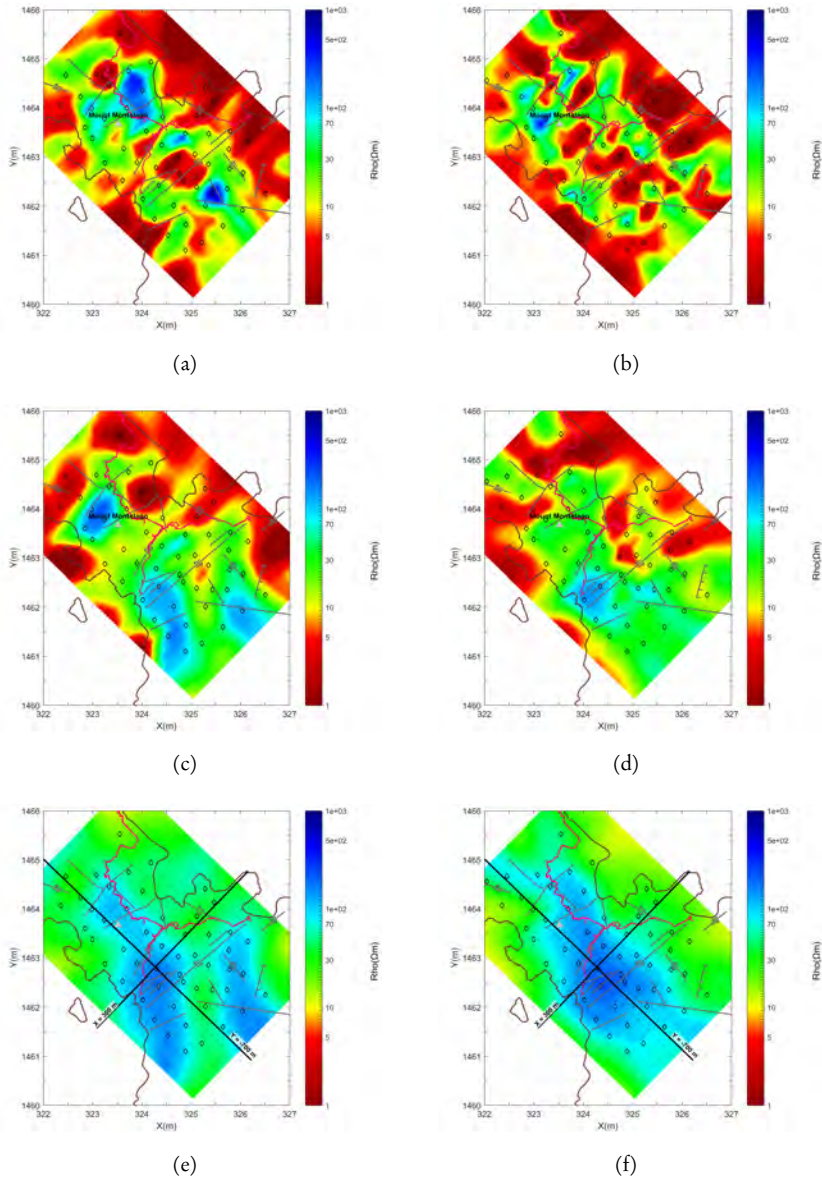


Figure 6.26: See next page for the caption of this Figure.

Figure 6.26: Inversion results of the 2014 magnetotelluric data acquired by *Hersir et al.* [2014] presented as resistivity plots at a constant elevation. Resistivity values in Ωm . Main roads (purple) and coast line (dark brown), as well as the locations of the faults (grey) and Mount Montelago (grey triangle) are also given. Diamonds are magnetotelluric stations. (a) WSINV-10-mod at an elevation of -250 m. (b) ModEM-10-mod at an elevation of -250 m. (c) WSINV-10-mod at an elevation of -500 m. (d) ModEM-10-mod at an elevation of -500 m. (e) WSINV-10-mod at an elevation of -1,000 m. (f) ModEM-10-mod at an elevation of -1,000 m.

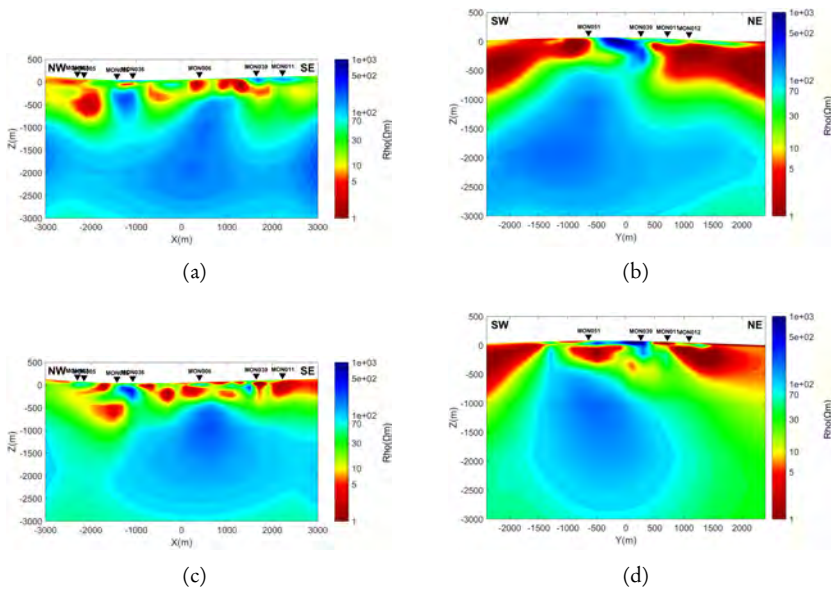


Figure 6.27: Inversion results of the 2014 magnetotelluric data acquired by *Hersir et al.* [2014] presented as resistivity cross-sections perpendicular to the model X- and Y-direction. See Figure 6.26 for the locations of the cross-sections. Inverted triangles are magnetotelluric stations and resistivity values are in Ωm . (a) Resistivity cross-section WSINV-10-mod at $Y = -700$ m. (b) Resistivity cross-section of WSINV-10-mod at $X = 300$ m. (c) Resistivity cross-section of ModEM-10-mod at $Y = -700$ m. (d) Resistivity cross-section of ModEM-10-mod at $X = 300$ m.

6.6 Discussion on the various inversion results

In Section 6.5 the inversion results of the different electromagnetic data sets from the Montelago geothermal prospect are presented. In this Section, the robustness of the resistive anomalies in the inversion results is discussed, as is the interpretation of the inversion models with respect to the geothermal reservoir.

As the in the Section 6.5.1 presented 1-D and 2-D inversion results of the different modelling strategies used for modelling the CSMT data show large differences, the interpretation of these resistivity models is complicated. The shallow penetration depth of the CSMT survey especially affected the 1-D inversion results. The TM-mode 2-D inversion results appear to deliver more realistic results of the resistivity structure in the project area. An example of the difference between the 3-D inversion result of ModEM-10-mod and 2-D TM-mode inversion of the CSMT data is given in Figure 6.28. The top of the resistive anomaly at depth is resolved by both inversions, while the resistivity structures above a depth of approximately 500 m are notably different. Consequently, as both TM-mode and TE-mode models confirm the presence of an up-doming resistive structure in the south-west of the research area, this is considered to be robust and a reasonable expression of the geology of the geothermal prospect. Contrastingly, the shallow resistivity structures as resolved by the inversion of the CSMT data are not in accordance with the inversion results of the magnetotelluric data. For this reason, the inversion results of the CSMT data are no longer taken into consideration.

6.6.1 Analysis of the 3-D inversion model of the 2000 MT data

To be able to assess the 3-D inversion results of PNOC-10-mod, as presented in Section 6.5.2, the inversion results are qualitatively compared with the inversion results of WSINV-10-mod *Árnason and Hersir* [2014]. To this end, resistivity maps at a similar elevation are shown in Figure 6.29.

When comparing these two models, it must be noted that the former resistivity model, PNOC-10-mod, is based on 27 stations using two compo-

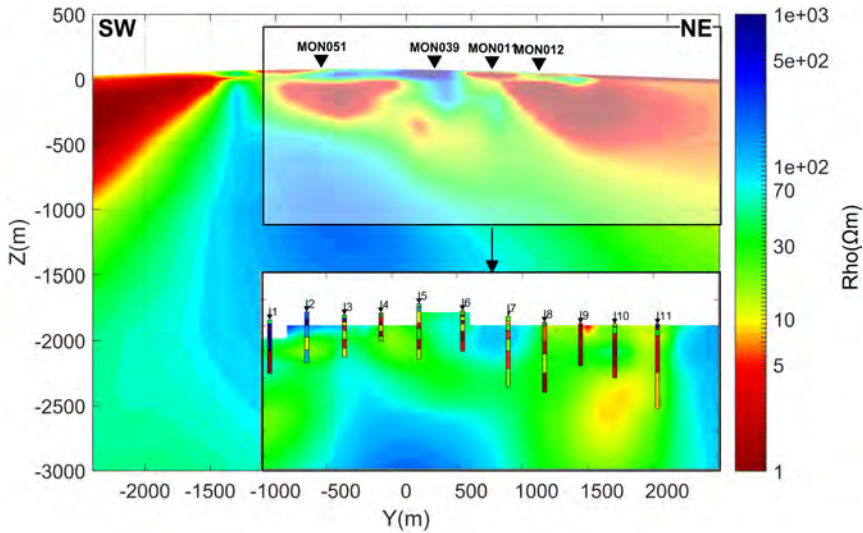


Figure 6.28: Inversion results of the 2014 magnetotelluric data acquired by *Hersiv et al.* [2014] and inverted using ModEM presented as a resistivity cross-section at $X = 300$ m and inversion results of the 2012 CSMT data acquired by *Tolentino et al.* [2012] and inverted in the TM-mode for the coinciding profile *I* (see Figure 6.17(a)). See Figure 6.26 for the location of the cross-section. Inverted triangles are magnetotelluric stations and resistivity values are in Ωm . The resistivity cross-section of profile F resulting from the TM-mode inversion of the CSMT data is plotted on top of the resistivity cross-section resulting from ModEM-10-mod, using an equal scale. Its actual location is indicated by the black rectangle. The 1-D layered model results of the CSMT stations are projected onto the resistivity cross-section.

nents of the magnetotelluric transfer function, while for the latter resistivity model, WSINV-10-mod, 53 stations with four components each are used. In both models the vertical magnetic transfer function is not inverted. More data spread over a larger area was available for this newer 3-D inversion. Nevertheless, a basic comparison can be made.

From Figure 6.29(a) it can be concluded that at shallow depths both models have a heterogeneous resistivity structure, although the general trend is that of a relatively high conductivity at the model edges, probably the effect of the sea to the east and Lake Naujan to the west. In both models, the boundaries of the surveyed area show a high conductivity, with the difference being that in the -46° rotated WSINV-10-mod the high conductivity is aligned with the

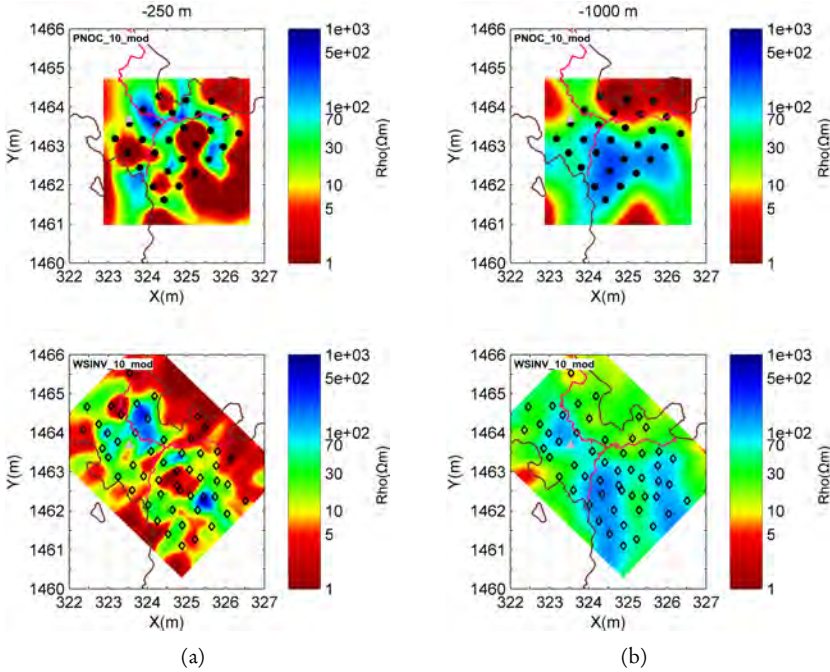


Figure 6.29: 3-D inversion results of the 2000 magnetotelluric data of [Maneja et al., 2000] (upper, PNOC-10-mod) and the 2014 magnetotelluric data acquired by Hersir et al. [2014] (lower, WSINV_10_mod) presented as resistivity elevation maps at an elevation of (a) -250 m and (b) -1,000 m amsl. Resistivity values in Ωm . Coastlines (dark brown) and roads (purple) are also given.

orientation of the coast line in the survey area. The resistivity contrasts in PNOC-10-mod at this elevation are also larger than those in WSINV-10-mod. However, the main character of the central area seems to be similar.

At an elevation of -1,000 m amsl. as shown in Figure 6.29(b), the differences between the two 3-D inversions are smaller. PNOC-10-mod shows a central resistivity structure while at this elevation WSINV-10-mod is more smooth with some resistive structures at roughly the same location as the central resistivity structure in PNOC-10-mod. However, resistivity contrasts in PNOC-10-mod are larger in comparison with those in WSINV-10-mod. At the model edges of PNOC-10-mod low resistivity anomalies are observed, three of these anomalies are model artefacts induced by the limited data coverage of the

survey area, while the conductive structure in the east is constrained by the magnetotelluric data.

As the orientation of the two inversion models is different, it is impossible to make cross-sections with a similar orientation from the two models without manipulating the data. Instead, the cross-sections parallel to the model grid of both models crossing the central area are presented in Figure 6.30, assumed to be constrained by the largest possible amount of magnetotelluric data.

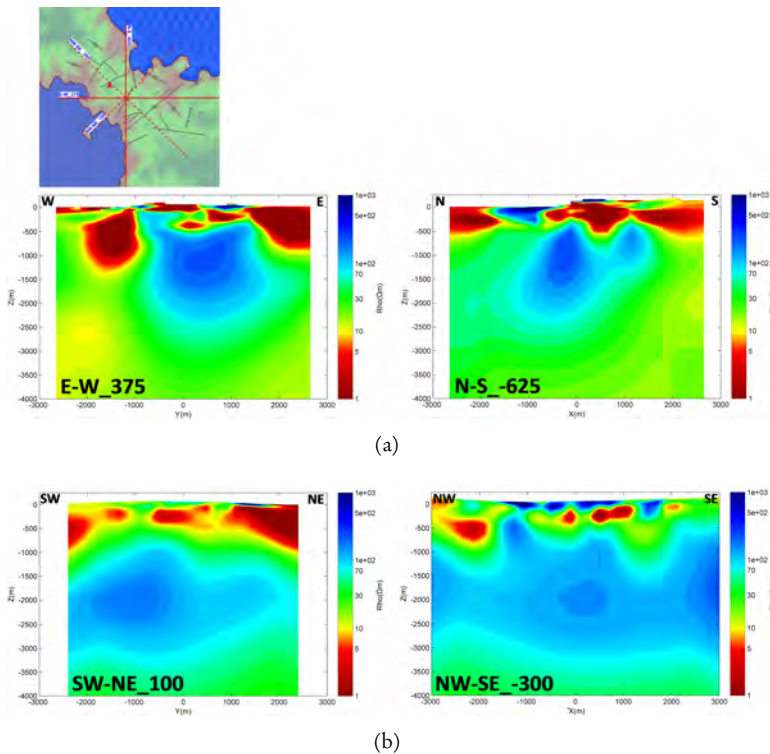


Figure 6.30: Resistivity cross-sections and their locations from (a) PNO-10-mod and (b) WS-INV-10-mod. Resistivity values in Ωm and the locations of the cross-sections are plotted as solid lines on the corresponding map view. Mount Montelago is indicated as a red triangle.

From Figure 6.30 it can be concluded that both models consist of a shallow conductive layer overlying a more resistive structure. In PNOC-10-mod, this resistive structure is isolated and is not present below a depth of approximately 2,500 m. WSINV-10-mod shows a more layered conductive structure up to depths of about 3,000 m. The character of the conductive top layer shows differences between the two models. This seems to be more heterogeneous in WSINV-10-mod when compared to PNOC-10-mod.

6.6.2 Comparison between the two 3-D inversion models of the 2014 MT data

The bulk of the resistivity structures of the two 3-D inversion models presented in Section 6.5.3 are likely related to geological structures, particularly those anomalies consistent between both models. However, some of the features may be artefacts introduced by the inversions. To make a quantitative comparison between the two models, a set of structural metrics, considered to identify those resistivity structures which are required by the model, is computed. These robust and required resistivity structures might then be regarded as suitable for the geothermal interpretation of the resistivity models.

The structural metrics used in this Section have been introduced previously in Chapter 5: “Comparison and interpretation of two 3-D inversion models” and are introduced in detail in Appendix A. The metrics described below are based on the gradient, cross product and Laplace operators. The structural metrics used to verify the resistivity structures in the model are:

- 1 The magnitude (or norm) of the model gradient $\|\nabla m\|$.
- 2 The difference between the normalized model gradients of the two resistivity models, the gradient difference, $\delta\bar{\varphi} = \frac{\nabla\bar{m}_1}{\|\nabla m_1\|} - \frac{\nabla\bar{m}_2}{\|\nabla m_2\|}$.
- 3 The norm of the cross product of the two model gradients, the cross gradient, $\bar{\tau} = \nabla m_1 \times \nabla m_2$.

Here \bar{m} is the three-dimensional model matrix of the inversion model. The details of these metrics are described in Appendix A.

Synthetic model

The structural metrics of synthetic resistivity data were computed to guide the interpretation of the structural metrics of the resistivity models. All synthetic models considered are given in Appendix A. The structural metrics of two slightly different layered synthetic resistivity models have been discussed in Chapter 5 “Comparison and interpretation of two 3-D inversion models”. As in the resistivity models presented in this Chapter spherically shaped resistivity structures are present, the structural metrics of slightly different synthetic models with spherically shaped resistivity structures are discussed. The models differ in the position of the spherically shaped resistivity structures, see Figures 6.31(a) and 6.31(b).

The magnitude (or norm) of the model gradients of the two synthetic models are shown in Figures 6.31(c) and 6.31(d). In the regions where the resistivity of the model is not changing, the normalized model gradients are small (blue), while in the regions where there are differences in the resistivity of the model, the normalized model gradients are large (red). Although the two synthetic models are not significantly different, the cross gradient of the two synthetic models, as given in Figure 6.31(e), highlights the outer margins of the region where both models are subject to a resistivity change in red. Similarly in Figure 6.31(f), in which the difference between the normalized model gradients is given, the outer margins of the region where the two synthetic models are subject to resistivity change are highlighted in blue. This is in contrast to the synthetic layered model as discussed previously in Chapter 5. Here, the locations of the spheres can be found roughly at the edges of the highlighted areas in the the cross gradient and gradient difference metrics plots, although the cross gradient produces more accurate results.

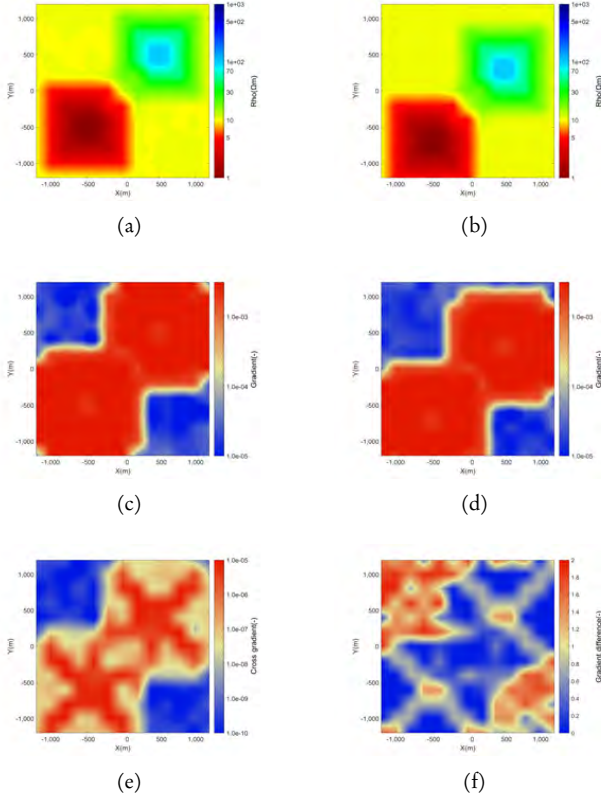


Figure 6.31: Synthetic resistivity model of two slightly different resistivity models, model 1 6.31(a) and model 2 6.31(b), as well as the structural metrics of these two models. Resistivities are given in Ωm . Norm of the model gradient of 6.31(c) model 1 and respectively of 6.31(d) model 2. Here, red colors indicate a change in resistivity, while blue colors indicate regions with a stable resistivity structure. 6.31(e) shows the norm of the cross product of the two synthetic models. 6.31(f) shows the difference between the normalized model gradients of the two synthetic models.

From this analysis it is concluded that the cross gradient is sensitive for the location of a resistivity structure and picks up similarities and differences between resistivity values of two models. On the other hand, the difference between model gradients is sensitive for similarities between model gradients, and indicates large differences for areas with a very low model gradient.

Resistivity models

Structural metrics are calculated for the WSINV-10-mod and ModEM_10_mod models. Only a selection of the structural metrics is given in this Section. The two resistivity models at an elevation of -500 m amsl. and -1,000 m amsl. as well as their corresponding structural metrics are shown in Figures 6.32 and 6.33.

The normalized model gradients at an elevation of -500 m amsl. as shown in Figures 6.32(a) and 6.32(b) are different along the northern boundaries of the survey area and in the south of the survey area, as well as below Mount Montelago. In the area of the SW-NE striking strike-slip fault, the model gradients show roughly similar values and shapes. The differences between the model gradients are expressed in Figure 6.32(f) showing the gradient difference at an elevation of -500 m amsl. This Figure especially highlights the similarities between the models in the central area and at the location of the ocean. The gradient difference is large along the boundaries of the survey area and around the coast line, stressing the variation in shape of the conductive anomalies. Based on the experiments with the synthetic data it can be inferred that the conductive anomalies around the survey are required by both models, while the shape and location of the resistivity structure in the central area remain inconclusive. At an elevation of -500 m amsl., the cross gradient is supporting the resistivity structures south of Mount Montelago, at the southern end of the SW-NE striking strike-slip fault and along the south-eastern boundary. At an elevation of -1,000 m amsl. as shown in Figures 6.33(c) and 6.33(d), both models show small model gradient values, highlighting the locations of the resistive anomalies. The gradient difference as shown in Figure 6.33(f) shows high values at the edges of the resistive anomalies, indicating the minimum extend of these anomalies. The cross gradient on the other hand shows the maximum extend of the resistive anomalies in deep blue, see Figure 6.33(e). In these two Figures the location of exploration wells SH-1 and SH-2 are also given, see Section 6.3, SH-1 targeting the resistive anomaly, and SH-2 targeting a fault.

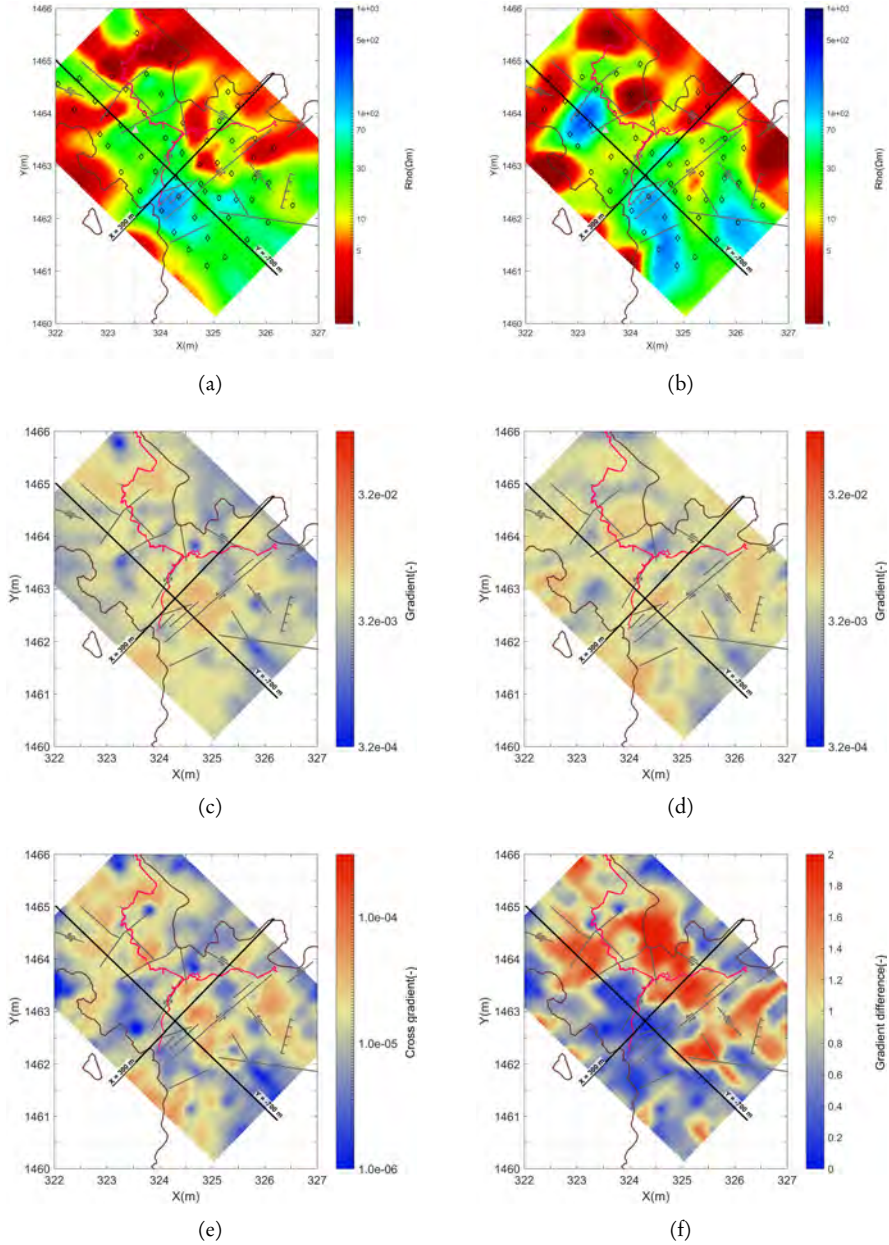


Figure 6.32: See next page for the caption of this Figure.

Figure 6.32: Resistivity maps at -500 m elevation amsl. from (a) ModEM-10-mod and (b) WSINV-10-mod. Norm of the resistivity gradient at -500 m elevation amsl. from (c) ModEM-10-mod and (d) WSINV-10-mod. (e) The cross gradient of the two resistivity models at -500 m elevation amsl. (f) Normalized difference between the model gradients at -500 m elevation amsl. Magnetotelluric stations (diamonds), main roads (purple), main faults (grey solid lines), the coast line (brown solid line) and Mount Montelago (grey triangle) are shown as well. Resistivity in Ωm . The locations of the two profiles at $X = 300$ m and $Y = -700$ m are also given.

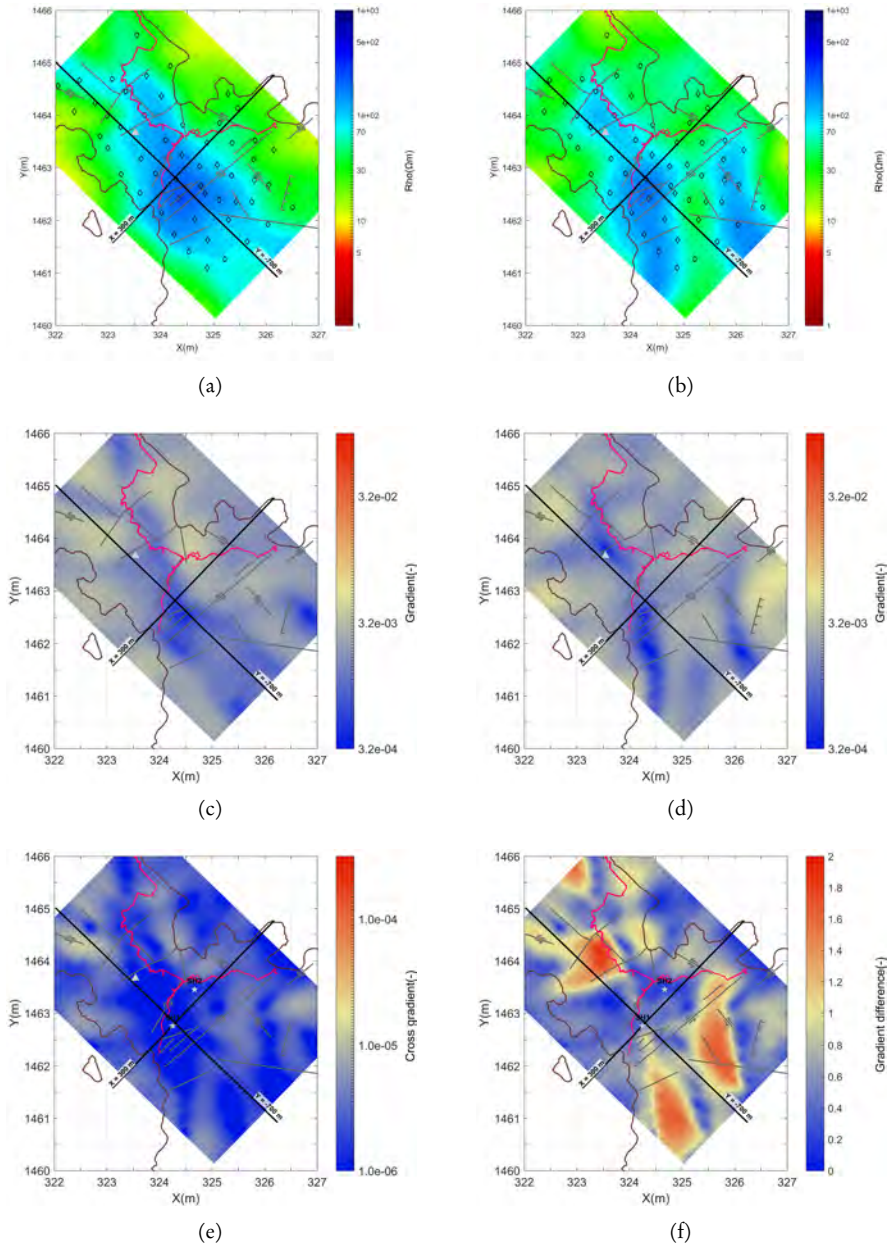


Figure 6.33: See next page for the caption of this Figure.

Figure 6.33: Resistivity maps at -1,000 m elevation amsl. from (a) ModEM-10-mod and (b) WSINV-10-mod. Norm of the resistivity gradient at -1,000 m elevation amsl. from (c) ModEM-10-mod and (d) WSINV-10-mod. (e) The cross gradient of the two resistivity models at -1,000 m elevation amsl. (f) Normalized difference between the model gradients at -1,000 m elevation amsl. Magnetotelluric stations (diamonds), main roads (purple), main faults (grey solid lines), the coast line (brown solid line) and Mount Montelago (grey triangle) are shown as well. Resistivity in Ωm . The locations of the two profiles at $X = 300$ m and $Y = -700$ m are also given as are the locations of wells SH-1 and SH-2.

To further assess the observations made on basis of the constant elevation metric maps presented above, the structural metrics of the inversion models are plotted in Figure 6.34 for the cross-section at $X = 300$ m, see Figure 6.33 for the location of the cross-section. The changes in resistivity are relatively similar for both models in the upper 3,000 meters. Where WSINV-10-mod in Figure 6.34(d) shows a layered structure with a slightly faster changing model gradient with more variations, ModEM-10-mod in Figure 6.34(c) shows a more steady change in resistivity throughout the model. In general, all cross-sections show a layered structure with a thin shallow layer near the surface where the resistivity is increasing overlaying a layer with decreasing resistivity. Below this second layer another layer with a relatively constant resistivity is completing the model. Evidence of an “up-doming” structure is present in both models around $Y = -500$ m. In Figure 6.34(f) the gradient difference structural metric is plotted in which the largest depth of the resistive anomaly at $Y = 500$ m is indicated by a large gradient difference. The cross gradient on the other hand indicates the shallowest depth of the resistive anomaly around $Y = 500$ m, see Figure 6.34(e). The low cross gradient values below a 1,000 m depth indicate that both models agree on the resistive structures at this depth. The resistive heterogeneity at shallower depth is reflected in the high cross gradient values.

Considering the locations of wells SH-1 and SH-2 as given in these Figures, based on the structural metrics, well SH-1 will drill into the resistive anomaly, while SH-2 will most likely not penetrate this anomaly.

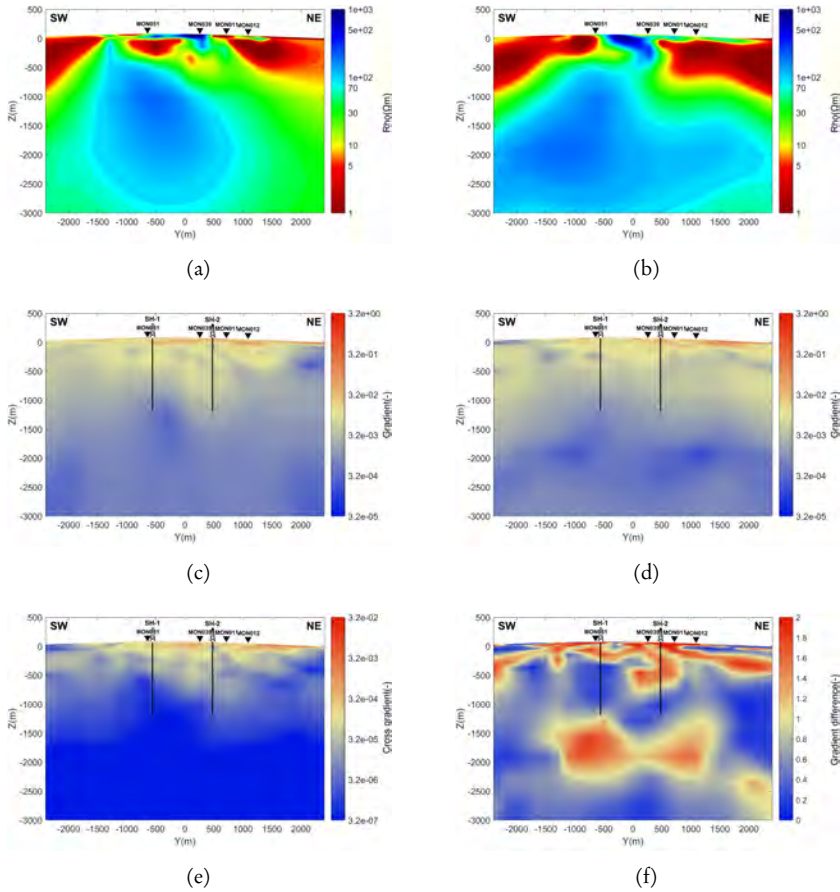


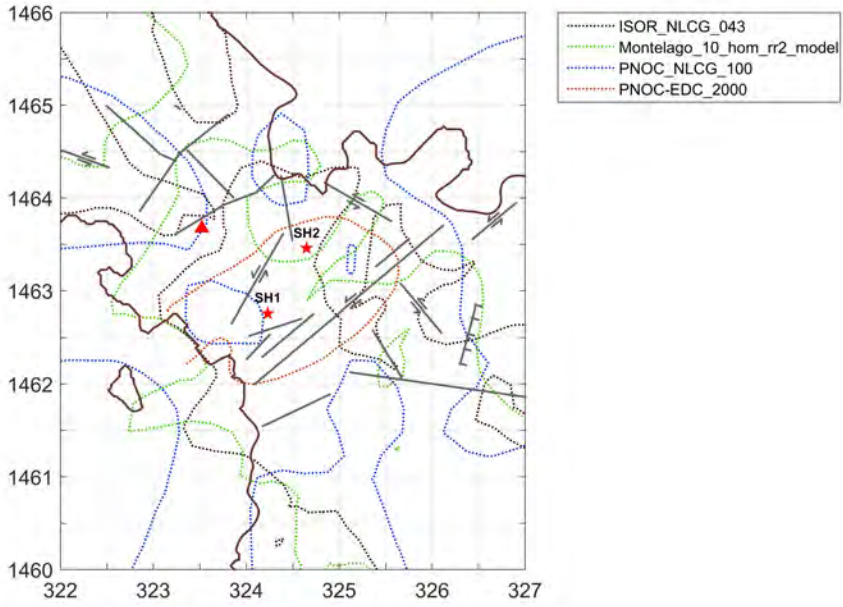
Figure 6.34: Resistivity cross-sections at $X = 300$ m from (a) ModEM-10-mod and (b) WSINV-10-mod. cross-sections of the norm of the resistivity gradient at $X = 300$ m from (c) ModEM-10-mod and (d) WSINV-10-mod. (e) cross-section of the cross gradient of the two resistivity models at $X = 300$ m. (f) cross-section of the normalized difference between the model gradients at $X = 300$ m. Magnetotelluric stations (inverted triangles) and wells SH-1 and SH-2 are given as well.

On basis of the comparison between the two inversion models of the 2014 magnetotelluric data, it can be concluded that a three layer model is the best representation of the geological situation of the survey area of the Montelago geothermal prospect. The resistive anomaly located slightly south of the center of the project area and up-doming towards the surface seems to be real, as it is visible in both models and supported by the analyses of structural metrics. When locating a well target it is this structure that should be targeted. Determining the dimensions of the reservoir solely on basis of the resistivity model is not possible here. Geological and geochemical information should be included as well.

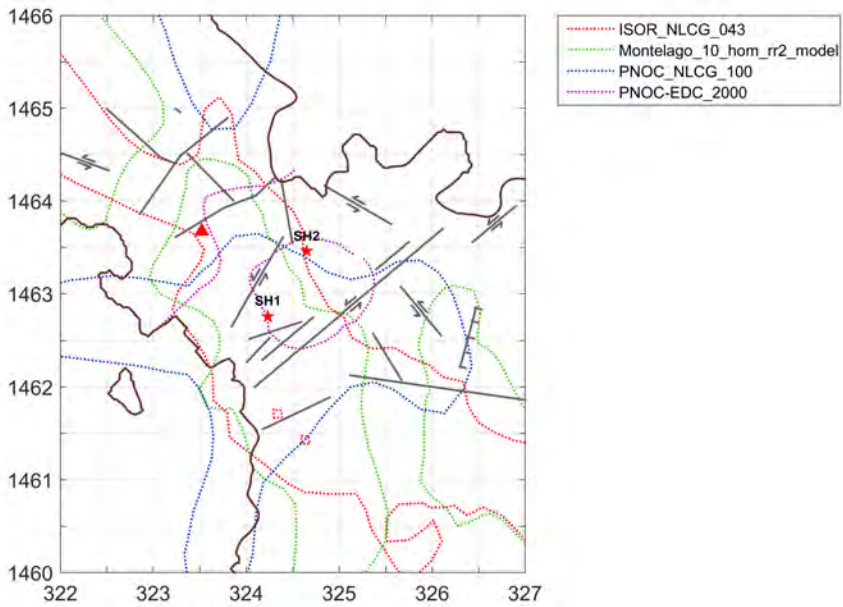
6.6.3 Geothermal interpretation of the 3-D inversion models

It is commonly assumed in the geothermal industry that the 10 Ωm iso-resistivity contour gives the best representation of the resistivity anomalies of the inversion models supposedly related to the geothermal reservoir. As discussed in Section 6.6.2, an analysis of the robustness of inversion models determines whether or not a certain structure is reliably determined and may therefore be interpreted as reflecting a geothermal up-flow area. Using a predefined iso-resistivity contour to determine the dimensions of a geothermal reservoir is, as illustrated by the differences between ModEM-10-mod and WSINV-10-mod, not an accurate technique. Nevertheless, the 10 and 50 Ωm iso-resistivity contours at an elevation of -500 and -1,000 m amsl. respectively, of all magnetotelluric inversion models as well as the interpolated 1-D resistivity models as reported by *Maneja et al.* [2000] are plotted for illustrative purposes in Figure 6.35.

The 10 Ωm iso-resistivity contour at an elevation of -500 m amsl., highlighting the more conductive areas possibly related to the clay cap, as shown in Figure 6.35(a), shows a complex structure. In this Figure, all four models have their 10 Ωm iso-resistivity contour roughly around the center of the survey area near well SH-1, with higher resistivities towards the center of the model. Where the 1-D model has a single anomaly, the 3-D models show more varia-



(a)



(b)

Figure 6.35: See next page for the caption of this Figure.

Figure 6.35: Iso-resistivity contours of the resistivity models of the Montelago geothermal prospect of (a) the 10 Ωm contour at an elevation of -500 m amsl. and (b) the 50 Ωm contour at an elevation of -1,000 m amsl. For reference, the coast line as well as the location of the faults, Mount Montelago (red triangle), and the two exploration wells, SH-1 and SH-2, are shown as well. In this Figure “ISOR_NLCG_043” is ModEM-10-mod (this study), “Montelago_10_hom_rr2_model” is WSINV-10-mod [Árnason and Hersir, 2014], “PNOC_NLCG_100” is PNOC-10-mod (this study), and “PNOC-EDC_2000” is the interpolated 1-D model of the 2000 MT data [Maneja *et al.*, 2000].

tion. The three 3-D inversion models suffer from highly conductive artefacts on the edges of the survey area, especially visible in the PNOC-10-mod model.

The resistive anomalies are more clearly highlighted by the 50 Ωm iso-resistivity contour at an elevation of -1,000 m as shown in Figure 6.35(b). The three 3-D inversion models all show a resistive anomaly located at the south side of the survey area with well SH-1 located in the center of the anomalies. The resistive anomaly identified by the interpolated 1-D modelling of the 2000 magnetotelluric data is positioned more towards the center of the survey area.

As can be observed in the resistivity maps and structural metrics maps of the resistivity models presented in Sections 6.5.3 and 6.6.2, some of the structures present in the resistivity models and structural metrics are coinciding with the mapped faults. This is for example illustrated by the structural metric maps north of Mount Montelago as well as around the SW-NE striking strike-slip fault south of the exploration wells, see Figures 6.32 and 6.33. It is also possible to interpret this strike-slip fault in the intersecting resistivity cross-sections of the two 3-D inversion models of the 2014 magnetotelluric data [Hersir *et al.*, 2014]. These observations indicate a certain degree of fault control of the geothermal prospect. This finding is confirmed by the structural geology data in the prospected area.

The conceptual model as formulated by *PT LAPI ITB* [2014] is compared to the resistivity cross-sections of the 3-D inversion models and the resistivity anomalies present in the maps of the 3-D inversion models, see Figure 6.36. The inferred up-flow area below the Pungao Hot Spring (PHS in Figure 6.36) and the corresponding iso-therms can be recognized in the resistivity structure in both the ModEM-10-mod model and, to a lesser extend, the WSINV-10-mod model. The strike-slip fault connecting the Buloc-Buloc bay hot spring

(BHS) and the resistivity cross-sections is not recognized in the resistivity cross-sections at the corresponding location, although a very shallow relatively resistive anomaly is present at both locations. The other, not presented resistivity cross-sections intersecting the Buloc-Buloc bay hot spring have similar characteristics. Therefore, it is likely that the Buloc-Buloc bay hot spring is not directly related to the geothermal reservoir. The Pungao Fault, oriented roughly north-south towards well SH-2, on the other hand, can be recognized in the two resistivity cross-sections by the shallow resistive anomaly at the location of well SH-2. The resistivity cross-sections and the 50 Ωm contours of the various inversion models indicate that the two wells, SH-1 in the center and SH-2 along the northern margin intersecting a fault, are located within the resistive anomaly resolved by all models discussed here.

While drilling into the SW-NE striking strike-slip fault south of the exploration wells, it was discovered that the temperature is decreasing at greater depths. It can be speculated that this temperature decrease is caused by a connection with permeable sedimentary layers transporting cooler waters from the mountain range along the western shore of Mindoro Island. The resistivity models all show an increasing conductivity below depths of approximately 2,500 m, somewhat shallower in ModEM-10-mod and somewhat deeper in WS-INV-10-mod. Despite that the decrease in resistivity itself is a result of the starting model, the location of this boundary can be interpreted as the top of a porous sedimentary sequence, providing the geothermal system with cooler water. This hydraulic short-circuiting is younger than the volcanic activity in the area and is possibly a forecast for the future temperatures present in the Montelago geothermal system.

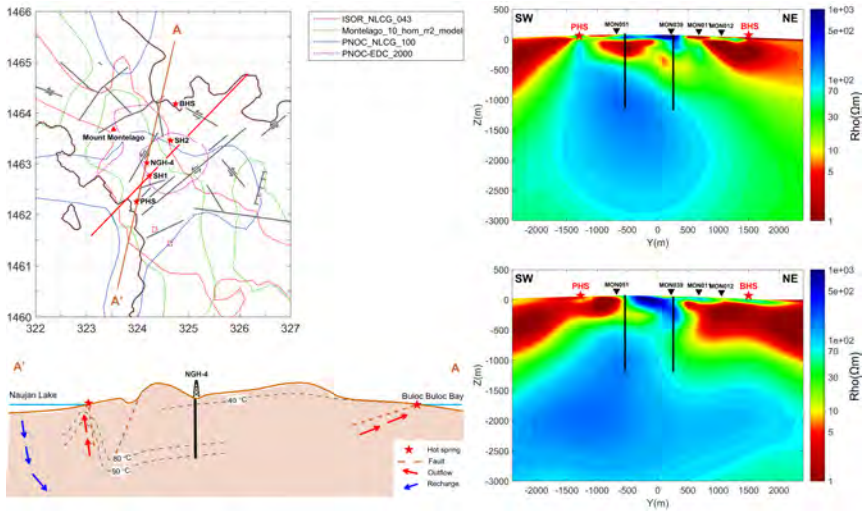


Figure 6.36: Left upper corner: The 50 Ωm iso-resistivity contour at an elevation of -1,000 m amsl. as shown in Figure 6.35(b) with the location of the conceptual cross-section (brown), the coast line, Mount Montelago (red triangle), wells SH-1, SH-2 and NGH-4 (red stars), the Pungao hot spring (PHS) and Buloc-Buloc bay hot spring (BHS), and the faults. Left lower corner: not to scale cross-section of the conceptual model discussed in Section 6.3. The cross-section indicates inferred outflow areas, faults and recharge of the geothermal system. Inferred isotherms are also given in the cross-section. Right upper corner: Resistivity cross-section at $X = 300$ m of ModEM-10-mod. Right lower corner: Resistivity cross-section at $X = 300$ m of WSINV-10-mod. In the two resistivity cross-sections the locations of the wells, hot springs and magnetotelluric stations are given.

6.7 Conclusions

Three different sets of electromagnetic exploration data for the Montelago geothermal prospect were evaluated and inverted in one, two or three dimensions using either WingLink, WSINV3DMT or ModEM software codes.

Near-field data were measured in the CSMT survey, leading to a spurious resistivity model in earlier work [Tolentino *et al.*, 2012]. The near-field data were removed and the erroneous phase data repaired. After running 1-D and 2-D inversions using this re-processed data set, with the majority of the stations having a maximum period of 0.1 to 0.5 seconds, the resulting resistivity models have a shallow penetration depth and are unable to give a well resolved resis-

tivity structure of the subsurface. Nevertheless, the TM-mode 2-D inversion model indicates a resistive anomaly in the south of the project area beneath a conductive layer. Where the shallow conductive layer does not correspond to the 3-D inversion models of the magnetotelluric data, the location of the resistive anomaly does coincide with the 3-D inversion models.

The 2000 magnetotelluric data are digitized and a 3-D inversion model is created of the off-diagonal components of the magnetotelluric transfer function. This model covers only the most central part of the survey area, but is largely in accordance with the other 3-D inversion models available. Due to the limited station data coverage, edge effects of the inversion are present within the geothermal area of interest.

The horizontal components of the magnetotelluric transfer function of the 2014 magnetotelluric data are 3-D inverted using WSINV3DMT and Mod-EM. Although clearly different in detail, the main resistivity structures are recognized in both resistivity models. This resemblance is confirmed by analysing a set of structural metrics of the two inversion models. Generally, the similarities in the center of the inversion models are the largest, while at the model edges more differences are observed.

Not all the structural metrics are equally effective when it comes to the geological interpretation of the resistivity models. It appears that the gradient, the cross gradient and the gradient difference are useful tools to assess the validity of a resistivity structure in a 3-D resistivity model. In the case of the Montelago geothermal prospect, the structural metrics are used to accurately define the boundaries of the main resistivity structures in the research area. Based on the locations of the boundaries of the resistivity structures defined by the structural metrics, the faults and geothermal manifestations in the area, targets for exploration wells can be defined.

In the case of the Montelago geothermal prospect, the locations of the exploration wells drilled were validated using the structural metrics. Based on the structural metrics, the location selected for slim hole SH-1 is well chosen, while the location of slim hole SH-2 can be motivated by combining the

resistivity models and structural metrics with the faults in the area. The Pungao hot spring can be related to the 3-D resistivity models, inferring that this geothermal manifestation is directly connected to the geothermal system.

On basis of differences between PNOC-10-mod, WSINV-10-mod and ModEM-10-mod it can be concluded that for a successful exploration magnetotelluric survey a few data points should be positioned outside the area of interest to eliminate model induced resistivity artefacts close to the area of interest. In the case of Montelago, a 500 m spacing between the magnetotelluric stations is sufficient, while a slightly larger spacing can be used on the edges. For 3-D modelling it would be interesting to investigate the effects of including the vertical magnetic transfer function in the inversion on the accuracy of the inversion models.

The resistivity model of the subsurface of the Montelago geothermal prospect can best be described by a three-layer model. A shallow thin conductive layer and a thicker resistive layer of altered volcanic strata overlying a more conductive base, probably a porous sedimentary sequence. The resistive layer shows up-flow structures in all resistivity models which are interpreted to be related to the geothermal prospect and the faults in the project area.

Although a classic clay alteration resistivity profile is present, the actual temperatures are not matching with the clay alteration mineralogy found in the exploration wells. Consequently it can be concluded that the clay alteration of the Montelago geothermal system is the product of a paleo hydrothermal system. The system might be additionally cooled down by cold water transported into the geothermal system via porous sedimentary layers connected with the mountain range along the western shore of Mindoro Island. As it is assumed that the geothermal system is still heated from below, a plutonic play type geothermal system is still considered to accurately describe the Montelago geothermal prospect.



7

Discussion and conclusions

7.1 Introduction

In the preceding Chapters of this dissertation a variety of geothermal exploration related electromagnetic problems have been discussed. These problems include magnetotelluric data processing, inversion and interpretation, distributed over several geothermal projects. In the following the common denominator of the electromagnetic problems considered in relation to these geothermal projects is discussed. Based on these findings, an approach is formulated which should lead to a successful magnetotelluric survey in regions with high levels of cultural noise and aiming at the exploration of conduction-dominated play type geothermal systems.

7.1.1 The common thread

Interest in geothermal energy as an alternative energy source continues to increase around the globe. Although the geothermal industry is over a century old, it is immature in terms of codes of practice and standardization. Commercially viable power producing geothermal projects are rarely realized outside traditionally successful areas with convection-dominated geothermal play types, such as tectonically active areas with increased surface heat flow and geothermal surface manifestations. For geothermal energy to develop into a serious alternative energy source, it is necessary that geothermal projects are successfully realized in settings with a higher risk profile like industrialized or urbanized areas, conduction-dominated geothermal play types, as well as blind systems in a convection-dominated geothermal play type environment. When it comes to geophysical prospecting using electromagnetic methods, often a decisive part of the geothermal exploration, the conditions of at least three subjects within these methods need to be improved considerably.

- 1 Performing successful magnetotelluric surveys in areas with high levels of cultural electromagnetic noise. Being an active method, conducting a seismic survey that delivers good quality data is, in contrast to a magnetotelluric survey, often possible in regions with high levels of cultural

electromagnetic noise. Seismic surveying is mainly useful when resolving the layering and faulting of the geological formations in the subsurface of sedimentary basins. In the assessment of geothermal prospects in any geological environment determining reservoir properties, such as temperature, and porosity and permeability, is the target of the surface exploration. Consequently, seismic surveying is not always an effective method for geothermal surface exploration and carrying out a magnetotelluric survey is desirable to determine the geothermal reservoir properties. Although sophisticated processing methods that deal with noisy magnetotelluric data exist, acquiring good quality magnetotelluric data is still challenging in areas with high levels of cultural electromagnetic noise.

- 2 Conducting a meaningful magnetotelluric survey in sedimentary basins with little conductivity contrasts. This problem is partially covered by studies investigating the possibilities of joint interpretation and/or joint inversion of resistivity and seismic data, revealing lithological units as well as reservoir properties. However, as seismic data are not available everywhere and new seismic surveys are often too expensive to carry out for geothermal developers, deriving the geological structures of a geothermal prospect in these settings remains challenging when only the acquisition of magnetotelluric data is possible for a geothermal project.
- 3 Interpreting the resistivity response of geothermal systems which do not match the generally applied volcanic play type conceptual models based on clay alteration minerals and an upflow zone. Although a general awareness does exist that such simplified models cannot be applied to non-volcanic systems, a broadly accepted and well-known alternative approach is not available. By adopting a subdivision of geothermal systems by its dominant heat transfer regime and geological setting and conceptualizing the resistivity response of these systems, a starting point is created for the formulation of a more realistic basis for the interpretation of resistivity models of different geothermal systems.

In Sections 7.2 and 7.3 the results of Chapters 4 to 6 are discussed within the perspective of these three subjects. Following, in Section 7.4 the consequences for the conceptual models of the case studies discussed in this dissertation are translated to the interpretation and the accuracy of the inverted resistivity models as presented in Chapters 5 and 6.

Two debates within resistivity modelling approaches are currently heating up the geothermal world. The first debate, on how to correct for static shift when inverting 2-D and 3-D magnetotelluric data, is discussed in Section 7.3. Is it favourable to utilize TEM measurements for the corrections and invert the corrected measurements or does the inversion “automatically” perform the correction? The second debate handles the preferable dimensionality, either interpolated 1-D or 3-D, of the inverted resistivity model to represent the geothermal reservoir. This is discussed in Section 7.4.

This Chapter finalizes with the Sections 7.6 and 7.7, discussing the most important conclusions of the research conducted and analyzed in this dissertation as well as introducing some suggestions for future work.

7.2 Noisy magnetotelluric data, field procedure or processing?

In Chapter 4: “Quality Index pre-sorting”, a novel pre-sorting processing approach is introduced to reprocess a magnetotelluric data set, acquired in Turkey using different instruments and processing codes. By applying Quality Index pre-sorting and a processing algorithm developed in Matlab on this magnetotelluric data set, a comprehensive set of magnetotelluric transfer functions of reasonable quality was obtained. However, not at every frequency the poor quality data points could be smoothed towards the general trend of the specific magnetotelluric transfer function.

Two strategies are available when it comes to obtaining acceptable quality magnetotelluric data in settings where high levels of cultural electromagnetic noise are expected:

- 1 Following an accurate field procedure when recording magnetotelluric data, and
- 2 applying several processing routines and strategies to the recorded magnetotelluric data.

7.2.1 Field procedure

Obviously, when measuring in areas with a large abundance of possible electromagnetic noise sources or a high potential for galvanic distortion, such as a rugged topography or a very resistive top soil, it makes sense to maximize the effort to determine the best recording locations of the magnetotelluric stations. Although this seems a reasonable strategy, in reality this is often not the case in commercial projects, especially when avoiding electromagnetic noise sources. A similar statement can be made for the location of the remote reference station.

Another factor affecting the quality of the magnetotelluric measurements is the accuracy of the station layout. Accurate positioning of all sensors as well as running resistivity checks on the electrodes are crucial for acquiring good quality magnetotelluric measurements. Again, as a result of poor layout gear or a poorly committed field crew, this is not always the case during commercial surveys.

In the following a short recipe for good practice magnetotelluric surveying, assuming proper functioning magnetotelluric equipment, is given. When following this recipe for any magnetotelluric survey consistently, the maximum possible data quality in a survey area can be achieved.

- Perform a desktop study to determine the initial locations of the magnetotelluric stations. Pay close attention to the topography and the locations of possible electromagnetic noise sources such as (refrigerators, TV's and air-conditioning in) houses, industrial activity, power lines and roads. Choose several alternative locations for the remote reference station to test in the field. As a low contact resistance between surface and electrodes is crucial for magnetotelluric measurements, use the desktop

study to gain knowledge on the composition of the topsoil present in the survey area. When a high contact resistance is expected, think of strategies to improve conductivity between electrode and surface.

- Before starting the field measurements, scout the selected remote reference locations and test the quality of the measurement. Spending a few days obtaining the optimal remote reference station is perhaps the most efficient way of improving the survey results. The most important criterion for the remote reference station is the quality of the recorded horizontal magnetic field. Using a continuously recording reference station of proven data quality located far away from the survey area, is an effective strategy to remove electromagnetic noise recorded at a local station.
- If possible, physically scout the stations locations before the magnetotelluric measurements start. Alternatively, inspect the surroundings of a station location and estimate the expected quality of the magnetotelluric measurements before installing the station at the site. When the expected data quality is poor, try to reposition the station to a location where an acceptable data quality can be achieved.
- When installing the magnetotelluric station, work accurately and improvise. Improvising implies that when the station is for example positioned on a slope, the station can be rotated to minimize the effects of the slope on the measurements. An accurate installation of a survey site is achieved by consistently following the prescribed layout procedure for every single station¹. Working systematically ensures consistent measurements and minimizes the chances of layout errors. After installation, run a short test to check if the data quality is sufficient, if not, recording settings might need to be changed or the station layout requires tweaking.
- Before retrieving the station, quickly quality check the collected data. This can be done either by looking at the number of bad recordings, the

¹All institutes carrying out magnetotelluric surveys use a slightly different layout procedure to install a magnetotelluric station in the field. It would go too far to describe them here, however, examples can be found in the manuals of the instrumentation. Additionally, the more practical sides of a magnetotelluric survey, such as the usage of batteries and compasses, the importance of a data storage procedure, and maintaining the electrodes, will not be discussed here.

recorded raw time-series or performing a quick magnetotelluric transfer function estimation². When data quality is insufficient, determine if directly repeating the measurement is useful.

- When the magnetotelluric survey has to be carried out in an area with a high level of electromagnetic noise, it is worthwhile to time the survey in accordance with the forecast of the maximum magnitude of the magnetic activity (the forecast of the AP index³). At days with a high AP index the likelihood of recording good quality magnetotelluric data is significantly higher.

7.2.2 Data processing

Even when the above strategy is followed, poor quality data can be recorded. Especially in regions where cultural electromagnetic noise sources are abundant and the recording of poor quality magnetotelluric data cannot be avoided, additional data processing strategies might improve the quality of the estimated magnetotelluric transfer functions. Using Quality Index pre-sorting as introduced in Chapter 4 can be one of those processing strategies.

Although related to the data acquisition phase of a magnetotelluric survey, sampling rate and penetration depth affect the processing results as described in the following. In geothermal exploration it is generally not necessary to achieve good resolution at depths greater than approximately ten kilometres. Depending on the geothermal play type, a penetration depth of two to seven kilometres is often sufficient.

When measuring at a sampling rate of 1 s, a recording time of thirty minutes up to two hours of good data is sufficient to achieve a penetration depth of two kilometres in a subsurface with a bulk resistivity of 1 to 5 Ωm ⁴. However, in processing routines, data samples are generally stacked and averaged to decrease the computation time of the Fourier transform. When the

²This last option can be done using proprietary commercial software on magnetotelluric time-series recorded for up to approximately 24 hours.

³The AP index is the derivative from the Kpindex and defined as its 24-hour maximum. The Kp index is a standardized measure of the magnetic activity of the Earth's magnetic field.

⁴It is assumed here that at least 20 samples are necessary for a representative data collection.

data in the example above are stacked in windows of for example 16 samples, the minimum measurement time to achieve a similar result would be 8 to 32 hours. When recording or processing data, the choice of both sampling rate during data acquisition and window length during data processing affect the processing results as well as the penetration depth achieved.

Besides adjusting recording and processing settings, there are a variety of processing routines and strategies available for the processing of acquired magnetotelluric data. Quality Index pre-sorting is just one of them. Processing strategies can be divided into three stages.

- 1 The transformation of the data from the time to the frequency domain. As discussed above, sampling rate and window length play a key role in this process. Furthermore, several approaches are available to compute the Fourier transform numerically, leading to slightly different results.
- 2 Pre-sorting processing approaches. As explained in Chapter 4, pre-sorting processing is applied to the magnetotelluric data in the frequency domain, before the estimation of the magnetotelluric transfer function. Pre-sorting approaches are well suited for detecting and eliminating those recordings showing a clear mismatch with the general properties of the recorded data. The exact choice of the criteria of the parameters for pre-sorting remains a matter of interpretation, as different sources of electromagnetic noise are expressed differently in the magnetotelluric data.
- 3 Estimation of the magnetotelluric transfer function. Currently, robust processing is the standard approach for the estimation of the magnetotelluric transfer function. However, several robust processing approaches are available, each performing differently on individual magnetotelluric data sets. Again, the choice for the robust processing algorithm should be determined by its strengths in combination with the properties of the magnetotelluric data to be processed.

All commonly used processing approaches are based on statistics. The evaluation of the distributions of the Fourier coefficients of the electromagnetic fields or of the residuals of the estimation of the magnetotelluric transfer func-

tion is an informative source for the quality of the processed magnetotelluric data. To obtain the best possible result when dealing with noisy magnetotelluric data, the results of at least a few available approaches at each of these three stages should be explored.

Ideally, the processing code used in this dissertation can be expanded by incorporating a few more pre-sorting and alternative robust processing approaches. In that case one can run all robust processing approaches on a few test stations and apply the best performing routine to process the time series of the entire magnetotelluric data set. This also offers a large number of opportunities for the analysis of the reliability of the magnetotelluric transfer function. It is for example possible to assess the reliability of trends observed in the estimated magnetotelluric transfer functions.

Defining a quantitative measure of data quality as proposed in Chapter 4 is a sound, efficient method to apply during magnetotelluric data processing. However, to increase its effectiveness the Quality Index pre-sorting processing routine can be improved. One possible way to achieve this is by replacing the least-squares transfer function estimation by a robust estimation including its error estimates and residuals. Another improvement can be achieved by incorporating the remote reference magnetic channels into the Quality Index pre-sorting algorithm. Instead of masking and excluding the data points with a low QI value, the selected (or all) data points might be weighted based on their respective QI values. This would prevent information to be entirely deleted, while minimizing the effect of outliers. Furthermore it would be interesting to investigate if the Quality Index pre-sorting can be expanded into a general measure of quality for an estimated magnetotelluric transfer function, providing an indication if improvement based on pre-sorting methods is feasible.

7.3 Resistivity modelling of geothermal systems

Two sets of electromagnetic data for geothermal exploration are inverted and modelled in this dissertation and compared to resistivity models using different inversion codes, see Chapters 5 and 6. Using structural metrics it is shown that

although the respective inversions are different, the same dominant, large scale resistivity structures and trends are resolved by the different inversion of the same magnetotelluric data sets. Two different inversion strategies are followed for the two geothermal projects:

- 1 The Turkish magnetotelluric data set is inverted using an initial model comprising both topography and bathymetry. The inverted data are not corrected for static shift and the horizontal components of the magnetotelluric impedance are inverted. Two inversion codes are used: Mack3D and ModEM.
- 2 The magnetotelluric data set from Montelago is inverted using an initial model with a flat earth and bathymetry. The inverted data is corrected for static shift using TEM and the horizontal components of the magnetotelluric impedance are inverted. Two inversion codes are used: WSINV3DMT and ModEM.

The set of structural metrics used for the quantitative comparison of the different resistivity models proved to be an effective tool to analyse the robustness of the resistive structures in the models. In the case of Montelago for example, the structural metrics are used to constrain the boundaries of the inferred geothermal reservoir. In fact, the structural metric analyzing only a single model, the magnitude of the model gradient, could also be utilized to assess the reliability of the resistivity structures resolved by that single inversion model.

7.3.1 Resistivity model of the Çanakkale magnetotelluric survey

An important difference between the two resistivity models of the Turkish magnetotelluric data is that the ModEM_10_Tur model comprises 54 instead of 51 stations. The data quality of the three added stations however is poor, as is the fit between observed and modelled data of the phases of the magnetotelluric transfer function. Despite their poor data quality, the model responses of these three stations are consistent with the resistivity model.

Another difference can be found in the preference of the Mack3D_10_Tur model to resolve horizontally elongated resistivity structures, while the ModEM_10_Tur model shows a preference for horizontally rounded resistivity structures. Considering the layered geology of the survey area, elongated resistivity structures might be more realistic.

The resistivity structures of the Mack3D_10_Tur model are significantly smoother compared to the resistivity structures of the ModEM_10_Tur model. This is especially clear when comparing the near surface resistivity anomalies of both models. This difference is most likely a result of the regularization parameter settings and could not be thoroughly tested as a result of the limited computing time available. Consequently, it is worthwhile to examine this further by running a few more models testing a variety of inversion settings.

Both models support a three layer model comprising a thin shallow relatively resistive layer, overlaying a thick conductive layer, and a relatively resistive basement. This interpretation of the resistivity model is supported by the analysis of the structural metrics and matches the geological structures in the survey area.

Another indication of the accuracy of both inversion models is the very good fit between modelled and observed data. The 3-D inversion models did not correct for static shift effects in the magnetotelluric data. About 15% of the magnetotelluric stations show some degree of static shift, which is not accounted for by the inversion. Consequently, it can be argued that in this case the static shift effects should have been removed prior to inversion of the data.

7.3.2 Resistivity model of the Montelago geothermal prospect

In the case of the Montelago geothermal prospect, the similarities between the two 3-D inversion models of the 2014 magnetotelluric data are apparent. Both resistivity models show a similar resistivity structure which is supported by the structural metrics. Similar as for Western Turkey, a three layer model is the best representation of the resistivity models. This model comprises a shallow heterogeneous predominantly conductive layer, underlain by a thick resistive layer and a less resistivity basement.

Utilizing the structural metrics, the boundaries of the main resistive anomalies related to the geothermal prospect are constrained. Furthermore, the locations of the boundaries of the resistivity structures as defined by the structural metrics, the faults and geothermal manifestations in the area are used to validate the planned locations for the two exploration wells in the area.

In both resistivity models of the Montelago geothermal prospect, the magnetotelluric data are static shift corrected before inversion. Topography is included into the models after inversion. Studying the misfit between observed and modelled data, it can be observed that this strategy did not induce any unwanted resistivity anomalies into the 3-D inversion models. Despite this observation, it would be interesting to examine the differences between the current 3-D resistivity models of the 2014 magnetotelluric static shift corrected data and a 3-D inversion resistivity model of uncorrected magnetotelluric data with an initial model including both topography and bathymetry.

7.4 Interpretation of resistivity models

When it comes to the geological interpretation, the two resistivity models presented in this dissertation are of a different geothermal play type. Where both projects fall within the convection-dominated geothermal systems, the geothermal project in Turkey is best described by an extensional domain geothermal play type while the Montelago geothermal prospect fits within the plutonic geothermal play types.

7.4.1 Interpretation of the Çanakkale resistivity models

The resistivity model of the geothermal project in Western Turkey reveals a thick conductive layer below the shallow resistive thin sedimentary sequences. Depending on the location, this layer extends to depths of 1,000 to 2,000 m. Both layers are overlying a resistive base. The thick conductive layer consists of volcanics while the base layer comprises an ophiolite overlying a limestone sequence. This limestone is targeted as the geothermal reservoir. This interpretation has recently been validated by two wells drilled into the geothermal prospect. These wells penetrated the inferred geothermal reservoir at

a depth of approximately 2,500 m bsl. where a temperature of 120 °C was measured. Additionally, the graben system filled with sediments is recognized in the Mack_10_Tur inversion models and validated by the east-west striking faults in the area.

As the temperatures are expected to be below 200 °C, clay alteration mineralogy will not be the sole contributor to the resistivity of the subsurface. Consequently, it is anticipated that the porosity and permeability contribute significantly to the resistivity of the subsurface for this geothermal project.

7.4.2 Interpretation of the Montelago resistivity models

The situation at Montelago is more complex when it comes to the geological interpretation of the resistivity models. Since the volcanic activity which formed the local geology is no longer active, it is decided to categorize this geothermal system as a plutonic geothermal play type.

The resistivity structures imaged by the two inversion codes as well as the expected temperatures in the subsurface, indicate that the resistivity structure of the subsurface in Montelago is largely controlled by alteration mineralogy of the paleo volcanic system. Geological surveying as well as the two exploration wells indicated the presence of clay alteration minerals in a composition related to a temperature regime of 200 to 250 °C, a strong indication that the conductive shallow subsurface is related to former high temperature volcanic activity. As temperatures at these depths are significantly lower and volcanic activity is no longer present, the high temperatures related to a clay alteration mineralogy causing an increased resistivity are also not present. This is confirmed by the temperature measured in the exploration wells.

It is concluded that the observed resistivity structures are a remnant temperature imprint. Since the resistive structure below the shallow conductive layer is characterized by lateral resistivity variations, it is assumed that the current temperature and porosity and permeability distribution is not laterally homogeneous within this layer. A theory might be that the areas with decreased resistivity values are related to increased porosity and permeability. Or, in other words, fracture driven fluid flow, providing the geothermal system

with its hot fluids. The location and orientation of these zones coincide with the mapped faults in the survey area, which is supported by the analysis of the structural metrics.

As at greater depths lower temperatures are measured, it is assumed that cool waters enter the geothermal system through sedimentary layers locally situated below the thermal anomaly and hydraulically connected to the mountain range along the western shore of Mindoro Island. This implies that the geothermal system is currently not in equilibrium and will probably cool down further. It is inferred that the heat source of the Montelago geothermal prospect is currently situated below or within the sedimentary sequence.

7.5 Application of the magnetotelluric method in the Netherlands

In order to carry out a successful magnetotelluric study in the Netherlands, two challenges have to be dealt with. First, it is difficult for the magnetotelluric method to resolve a resistive structure beneath a conductive geological structure. This is the case in the Netherlands when targeting the carboniferous limestones as a geothermal reservoir. Second, the levels of cultural electromagnetic noise in the Netherlands are high.

A initial strategy to deal with both challenges simultaneously is to measure for several days. By measuring for very long periods, it becomes possible to resolve deep resistors in a conductive setting. Furthermore, the long sounding period increases the number of data points at shorter periods, probably enhancing the total number of good quality data points. Another approach to limit the influence of cultural electromagnetic noise is to utilize the magnetic fields of a second remote reference station. Logically, regions which are especially noisy, such as the west of the country, should be avoided whenever possible.

Given the geology of the Netherlands, the resistivity of the subsurface is mainly controlled by porosity and permeability, either in geological formations or in faults and fractures. Consequently, when deploying magnetotellurics for geothermal exploration, these properties should be targeted.

To set up a successful magnetotelluric survey in the Netherlands, a forward modelling study should be carried out to investigate the sounding period necessary to resolve the deep limestone structures inferred to be geothermal reservoirs, including the difference between porous and impermeable limestone. Using the results of these models, a magnetotelluric survey can be designed specifically targeting karstified limestone sequences.

7.6 Conclusions

By using Quality Index pre-sorting during the reprocessing of magnetotelluric data, noisy magnetotelluric data can be identified and removed from the recorded data. The effectiveness of this processing tool is demonstrated on a magnetotelluric data set for geothermal exploration acquired in Çanakkale province, Western Turkey.

When acquiring data in regions with high levels of cultural electromagnetic noise, it is important to realize that before experimenting with all kinds of sophisticated processing applications, accurate and clever data acquisition procedures will ensure maximum magnetotelluric data quality.

Inversion modelling of resistivity data using different inversion codes, notably ModEM, WSINV3DMT and Mack3D, but similar inversion strategies, results in comparable resistivity models. It is therefore recommended to use two different 3-D inversion codes on a magnetotelluric data set to reliably interpret the resistivity structures in the model in the geological context of the research area. The existing strategy to test various initial models is best maintained.

The various resistivity models generated by the three inversion codes resolve the same large scale resistivity structures, but find different resistivity model solutions for the shallow subsurface. These conclusions are similar for the inverted data sets of the geothermal project in Çanakkale province and for the Montelago geothermal prospect.

Quantitative analysis of multiple inversion models of the same data sets is possible by utilizing structural metrics derived from joint inversion applica-

tions. As illustrated in this dissertation, the structural metrics highlight comparable resistivity structures in different inversion models of the same survey area.

The effectiveness of using structural metrics for model analysis is demonstrated on the two geothermal projects discussed earlier. Especially the model gradient and the cross product are effective tools for the analysis of the robustness of the resistivity structures in inversion models. As shown in this dissertation the structural metrics can be applied to constrain the boundaries of the resistivity structures in the model or, by combining the results with other geological data, to determine well locations for exploration drilling.

The resistivity models of the geothermal project in Çanakkale indicate a layered structure in a graben system. The geothermal system itself is categorized as an extensional domain type geothermal play. The conductive layer is related to volcanics whereas the resistive basement comprises an ophiolitic sequence overlying the geothermal reservoir consisting of a limestone sequence.

Since for the geothermal project in Çanakkale the reservoir and the overlying layer have a similar resistive response, it must be stressed that interpreting this model as a conductive cap and resistive reservoir will lead to drilling the ophiolite instead of the limestone.

The Montelago geothermal prospect is characterized by paleo volcanic activity and therefore categorized as a plutonic geothermal play type. The volcanic activity left a temperature imprint of alteration mineralogy on the resistivity model, overestimating the actual temperatures present in the subsurface. Consequently, this interpretation does not reflect the actual situation, and another interpretation is required. A more accurate interpretation is a fracture controlled geothermal system heated by remnant heat of the paleo volcanic system and cooled down from below. The fractures can be identified by the relatively conductive zones in the resistive layer directly beneath the shallow subsurface with a very low resistivity.

The 3-D inversion of the two-component 2000 magnetotelluric data shows comparable resistivity structures as the two 3-D inversion models of the 2014 magnetotelluric data. Although the survey covered a too small area and too

little data to obtain a full resistivity model of the research area, the resulting resistivity model appears to correct for possible static shift effects in the data. Due to the limited data coverage, inversion model artefacts are present within the area of interest.

Based on the two cases above, it can be stated that a simple model solely utilizing the resistivity response of clay alteration mineralogy is, in a non-volcanic play type geothermal system, seldom the right approach to interpret the resistivity model. These two examples reflect that all other information available, particularly the geological, geochemical and geophysical surface exploration data, should be used during interpretation.

7.7 Future work

Regarding the Quality Index pre-sorting and the processing algorithm it is incorporated in, improvements can be made on both the pre-sorting approach as well as on the magnetotelluric transfer function estimation. The Quality Index pre-sorting can be extended by utilizing the remote reference magnetic channels as well as using another method to estimate the magnetotelluric transfer function and its error and residuals at this stage.

The processing algorithm estimating the transfer function can be optimized by incorporating alternative robust processing approaches, such that for each magnetotelluric data set, the optimal processing code can be selected.

Not all possibilities for the inversion of the magnetotelluric data sets are explored in this dissertation. Notably, for the Turkish magnetotelluric data, experimenting with other regularization settings might improve the inversion results of ModEM as well as the understanding of the resistivity structure of the shallow subsurface. Another interesting experiment is to investigate if inversion of the same data set using a coarser grid will lead to similar results.

Regarding the Montelago geothermal prospect, it is useful to run a 3-D inversion with ModEM including topography using the 2014 magnetotelluric data without static shift correction. This is an effective way to test if the resistivity structures resolved by the 3-D inversion will be similar and if running

a simultaneous TEM survey is indeed necessary in this kind of terrain. The inversion of the 2000 magnetotelluric data indicates that this might not be necessary.

Additionally, testing the structural metrics on inversion models using the same inversion code but different initial models, for example a 10 Ωm and a 100 Ωm homogeneous model, might deliver interesting results.

Bibliography

- Abdul Azeez, K., and T. Harinarayana (2007), Magnetotelluric evidence of potential geothermal resource in puga, ladakh, nw himalaya, *Current Science*, 93(3), 323–329.
- Apuada, N., F. Maneja, and J. Catane (1989), Resistivity survey at montelago geothermal prospect, mindoro, southwestern luzon, *Tech. rep.*, PNOC EDC.
- Arango, C., A. Marcuello, J. Ledo, and P. Queralt (2009), 3d magnetotelluric characterization of the geothermal anomaly in the llucmajor aquifer system (majorca, spain), *Journal of Applied Geophysics*, 68, 479–488.
- Archie, G. (1942), The electrical resistivity log as an aid in determining some reservoir characteristics, *Trans. AIME* 146, p. 54–67.
- Árnason, K. (1989), Central loop transient electromagnetic soundings over a horizontally layered earth, *Report OS-89032/JHD-06*, Orkustofnun; national energy authority geothermal division, Reykjavik.
- Árnason, K. (2015), The static shift problem in mt soundings, in *Proceedings World Geothermal Congress 2015*, Melbourne, Australia.

- Árnason, K., and G. Hersir (2014), 3d inversion of mt data from montelago on mindoro island, philippines, *Tech. rep.*, Iceland Geosurvey.
- Árnason, K., H. Eysteinnsson, and G. Páll Hersir (2010), Joint 1d inversion of tem and mt data and 3d inversion of mt data in the hengill area, sw iceland, *Geothermics*, 39, 13–34.
- Asnin, S. N. (2014), Geochemical survey of montelago geothermal area, Master's thesis, Institut Teknologi Bandung.
- Axelsson, G. (2013), Conceptual models of geothermal systems - introduction, Short Course V on Conceptual Modelling of Geothermal Systems, organized by UNU-GTP and LaGeo, in Santa Tecla, El Salvador.
- Beccalotto, L., and C. Jenny (2004), Geology and correlation of the engine zone: A rhopode fragment in nw turkey?, *Turkish Journal of Earth Sciences*, 13, 145–176.
- Benavente, O., L. Urzua, C. Malate, J. Catane, I. Bogie, B. Lovelock, and G. Ussher (2014), Montelago geothermal project; resource assessment review, *Tech. rep.*, Jacobs.
- Bertani, R. (2015), Geothermal power generation in the world 2010-2014 update report, in *Proceedings World Geothermal Congress 2015*, Melbourne, Australia.
- Bibby, H., T. Caldwell, F. Davey, and T. Webb (1995), Geophysical evidence on the structure of the taupo volcanic zone and its hydrothermal circulation, *Journal of Volcanology and Geothermal Researc*, 68, 29–58.
- Bonté, D., J.-D. van Wees, and J. Verweij (2012), Subsurface temperature of the onshore netherlands: new temperature dataset and modelling, *Netherlands Journal of Geosciences*, 91(4), 491–515.
- Bujakowski, W., A. Barbacki, B. Czerwińska, L. Pająk, M. Pussak, M. Stefaniuk, and Z. Trzeńiowski (2010), Integrated seismic and magnetotelluric

- exploration of the skierniewice, poland, geothermal test site, *Geothermics*, 39, 78–93.
- Cagniard, L. (1953), Basic theory of the magnetotelluric method of geophysical prospecting, *Geophysics*, 18, 605–635.
- Chave, A. (2014), A maximum likelihood estimator for magnetotelluric data, in *Extended Abstract, 22nd EM Induction Workshop*, Weimar, Germany.
- Chave, A., and A. Jones (2012), *The Magnetotelluric Method, Theory and Practice*, Cambridge University Press.
- Chave, A., and D. Thomson (1989), Sine comments on magnetotelluric response function estimation, *Journal of Geophysical Research*, 94, 14 215–14 225.
- Chave, A., and D. Thomson (2004), Bounded influence estimation of magnetotelluric response functions, *Geophysics Journal International*, 157, 988–1006.
- Chave, A., D. Thomson, and M. Ander (1987), On the robust estimation of power spectra, coherences, and transfer functions, *Journal of Geophysical Research*, 92(B1), 633–648.
- Chen, J., B. Heincke, M. Jegen, and M. Moorkamp (2012), Using empirical mode decomposition to process marine magnetotelluric data, *Geophysical Journal International*, 190, 293–309.
- Clemente, V. (1979), Philippine italian technical cooperation on geothermics, stage ii; annex 7: Preliminary assessment of montelago (*orientalmindoro*), *Tech. rep.*, Bureau of Energy Development and ELC-Electroconsult.
- Clemente, V. (1982), A preliminary assessment of the montelago geothermal prospect, *Tech. rep.*, PNOC EDC.

- Cumming, W. (2009), Geothermal resource conceptual models using surface exploration data, in *Proceedings Thirty-Fourth Workshop on Geothermal Reservoir Engineering*, Stanford University, Stanford, California.
- Cumming, W., and R. Mackie (2010), Resistivity imaging of geothermal resources using 1d,2d and 3d mt inversion and tdem static shift correction illustrated by a glass mountain case history, in *Proceedings World Geothermal Congress 2010*, Bali, Indonesia.
- deGroot Hedlin, C. (1991), Removal of static shift in two dimensions by regularized inversion, *Geophysics*, 56(12), 2102–2106.
- Del Rosario Jr., R., M. Pastor, and R. Malapitan (2005), Controlled source magnetotelluric (csmt) survey of malabuyoc thermal prospect, malabuyoc/alegria, cebu, philippines, in *Proceedings World Geothermal Congress 2005*, Antalya, Turkey.
- Delfin, F., and M. Zaide-Delfin (1989), Geology of the montelago geothermal prospect, mindoro, southwestern luzon, *Tech. rep.*, PNOC EDC.
- Delhaye, R., A. Jones, V. Rath, D. Reay, A. Smyth, and the Iretherm Team (), The iretherm project: Magnetotelluric assessment of sedimentary basins in northern ireland as possible geothermal aquifers, in *Proceedings World Geothermal Congress 2015*, Melbourne, Australia.
- Dickson, M., and M. Fanelli (2004), What is geothermal energy?, online.
- Didana, Y., S. Thiel, and H. Graham (), Magnetotelluric characterization of the habanero geothermal eggs project: Initial results on fluid injection monitoring, in *Proceedings World Geothermal Congress 2015*, Melbourne, Australia.
- Egbert, G., and J. Booker (1986), Robust estimation of geomagnetic transfer functions, *Geophysical Journal of the Royal Astronomical Society*, 87, 173–194.
- Egbert, G., and A. Kelbert (2012), Computational recipes for electromagnetic inverse problems, *Geophysical Journal International*, 189, 251–267.

- Erdogdu, E. (2009), A snapshot of geothermal energy potential and utilization in turkey, *Renewable and Sustainable Energy Reviews*, 13, 2535–2543.
- Flóvenz, O., E. Spangenberg, J. Kulenkampff, K. Árnason, R. Karlsdóttir, and E. Huenges (2005), The role of electrical interface conduction in geothermal exploration, in *Proceedings World Geothermal Congress 2005*, Antalya, Turkey.
- Fridleifsson, G. O., B. Pálsson, A. Albertsson, B. Stefánsson, E. Gunnlaugsson, J. Ketilsson, and T. Gíslason (2015), Iddp-1 drilled into magma - world's first magma-egs system created, in *Proceedings World Geothermal Congress 2015*, Melbourne, Australia.
- Fronza, A., M. Marasigan, and V. Lazarro (2015), Geothermal development in the philippines: The country update, in *Proceedings World Geothermal Congress*, Melbourne, Australia.
- Gallardo, L., and M. Meju (2011), Structure-coupled multiphysics imaging in geophysical sciences, *Reviews of Geophysics*, 49, rG1003.
- Gamble, T., W. Goubau, and J. Clarke (1979), Magnetotellurics with a remote reference, *Geophysics*, 44, 53–68.
- Garcia, X., and A. Jones (2008), Robust processing of magnetotelluric data in the amt dead band using the continuous wavelet transform, *Geophysics*, 73(6), F223–F234.
- Geiermann, J., and E. Schill (2010), 2-d magnetotellurics at the geothermal site at soultz-sous-forêts: Resistivity distribution to about 3000m depth, *Comptes Rendus Geoscience*, 342, 587–599.
- GEOSYSTEM SRL (2008), *WinGLink User's Guide*, GEOSYSTEM SRL, Milan.
- Gianni Volpi, G., A. Manzella, and A. Fiordelisi (2003), Investigation of geothermal structures by magnetotellurics (mt): an example from the mt. amiata area, italy, *Geothermics*, 32, 131–145.

- Goldstein, B., et al. (2011), *IPCC Special Report on Renewable Energy Sources and Climate Change Mitigation*, chap. Geothermal Energy. In, Cambridge University Press, Cambridge, United Kingdom and New York, NY, USA.
- Grant, M., and P. Bixley (1982), *Geothermal Reservoir Engineering - Second Edition*, Academic Press.
- Hadamard, J. (1902), Sur les problèmes aux dérivés partielles et leur signification physique, *Princeton University Bulletin*, pp. 49–52.
- Hamza, V., R. Cardoso, and C. Ponte Neto (2008), Spherical harmonic analysis of earth's conductive heat flow, *International Journal of Earth Sciences*, 97(2), 205–226.
- Heijnen, N., A. Ashat, K. v. d. Hoorn, W. v. Leeuwen, M. Muller, N. Suryantini, and M. v. Bergen (2013), Montelago geothermal prospect. phase 1: Review of subsurface data and resource assessment, *Tech. rep.*, IF Technology bv.
- Heise, W., G. Caldwell, B. H.M., and B. S.C. (2008), Three-dimensional modelling of magnetotelluric data from the rotokawa geothermal field, taupo volcanic zone, new zealand, *Geophysical Journal International*, 173, 740–750.
- Hersir, G., K. Árnason, and A. Vilhjálmsson (2013), 3d inversion of magnetotelluric (mt) resistivity data from krýsuvík high temperature geothermal area in sw iceland, in *PROCEEDINGS, Thirty-Eighth Workshop on Geothermal Reservoir Engineering*, Stanford University, Stanford, California.
- Hersir, G., K. Árnason, and A. Vilhjálmsson (2014), Resistivity survey in montelago on mindoro island, philippines; data acquisition, processing and 1d inversion, *Tech. rep.*, Iceland Geosurvey.
- IEA (2014), Key world energy statistics, *Tech. rep.*, International Energy Agency.
- IFC (2013), Success of geothermal wells: A global study, *Tech. rep.*, International Finance Corporation.

- Jiracek, G. (1990), Near-surface and topographic distortions in electromagnetic induction, *Surveys in Geophysics*, 11, 163–203.
- Jones, A., A. Chave, G. Egbert, D. Auld, and K. Bahr (1989), A comparison of techniques for magnetotelluric response function estimation, *Journal of Geophysical Research*, 94(B10), 14,201–14,213.
- Junge, A. (1996), Characterization of and correction for cultural noise, *Surveys in Geophysics*, 17, 361–391.
- Larsen, J., R. Mackie, A. Manzella, A. Fiordelisi, and S. Rieven (1996), Robust smooth magnetotelluric transfer functions, *Geophysical Journal International*, 124, 801–819.
- Layugan, D., D. Rigor Jr., N. Apuada, C. Los Baños, and R. Olivar (2005), Magnetotelluric (mt) resistivity surveys in various geothermal systems in central philippines, in *Proceedings World Geothermal Congress 2005*, Antalya, Turkey.
- Ledo, J. (2005), 2-d versus 3-d magnetotelluric data interpretation, *Surveys in Geophysics*, 26, 511–543.
- Ledo, J., P. Queralt, A. Martí, and A. G. Jones (2002), Two-dimensional interpretation of three-dimensional magnetotelluric data: an example of limitations and resolution, *Geophysical Journal International*, 150, 127–139.
- Ledru, P., and L. Guillou Frottier (2010), *Geothermal Energy Systems*, chap. Reservoir Definition, Wiley-VCH.
- Leynes, R., and J. Rosell (1997), Microtectonic study and stratigraphic review of the montelago geothermal prospect, northeastern mindoro, *Tech. rep.*, PNOC EDC.
- Leynes, R., and D. Sanchez (1998), Geological and geochemical evaluation of the montelago geothermal prospect, oriental mindoro, philippines, in *GEOCON 1998 - 11th Annual Convention of the Geological Society of the Philippines*, edited by G. S. of the Philippines, pp. 150–162.

- Lovelock, B., and A. Lafrades (2011), Assessment of the montelago prospect, philippines, *Tech. rep.*, SKM.
- Mackie, R., and M. Watts (2012), Detectability of 3-d sulphide targets with afmag, in *SEG Technical Program Expanded Abstracts*, pp. 1–4.
- Maneja, F., N. Apuada, and D. Rigor Jr. (2000), Magnetotelluric survey of the montelago geothermal prospect, northeastern mindoro, philippines, *Tech. rep.*, PNOC EDC.
- Manzella, A., V. Spichak, P. Pushkarev, D. Sileva, B. Oskooi, G. Ruggieri, and Y. Sizov (2006), Deep fluid circulation in the travale geothermal area and its relation with tectonic structure investigated by a magnetotelluric survey, *Proceedings, 31st Workshop on Geothermal Reservoir Engineering*, Stanford University, Stanford, California.
- Mertoglu, O., S. Simsek, and B. N. (2015), Geothermal country update report of turkey (2010-2015), in *Proceedings World Geothermal Congress*, Melbourne, Australia.
- Moeck, I. (2013), Classification of geothermal plays according to geological habitats, in *IGA Academy Report; Geothermal Exploration Best Practices – Geology, Exploration Drilling, Geochemistry, Geophysics*, vol. 1, edited by R. Bracke, C. Harvey, and H. Rueter, IGA Service GmbH, Bochum, Germany.
- Moeck, I. (2014), Catalog of geothermal play types based on geological controls, *Renewable and Sustainable Energy Reviews*, 37, 867–882.
- Muñoz, G. (2014), Exploring for geothermal resources with electromagnetic methods, *Surveys in Geophysics*, 35, 101–122.
- Muñoz, G., K. Bauer, I. Moeck, A. Schulze, and O. Ritter (2010), Exploring the großschönebeck (germany) geothermal site using a statistical joint interpretation of magnetotelluric and seismic topography models, *Geothermics*, 39, 35–45.

- Newman, G., E. Gasperikova, G. Hoversten, and P. Wannamaker (2008), Three-dimensional magnetotelluric characterization of the coso geothermal field, *Geothermics*, 37, 369–399.
- Parker, R. (1980), The inverse problem of electromagnetic induction: Existence and construction of solutions based on incomplete data, *Journal of Geophysical Research*, 85(B8), 4421–4428.
- Parker, R., and J. Booker (1996), Optimal one-dimensional inversion and bounding of magnetotelluric apparent resistivity and phase measurements, *Physics of the Earth and Planetary Interiors*, 98, 269–282.
- Parker, R., and K. Whaler (1981), Numerical methods for establishing solutions to the inverse problem of electromagnetic induction, *Journal of Geophysical Research*, 86, 269–282.
- Pastana de Lugão, P., E. LaTerra, B. Kriegshäuser, and S. Fontes (2002), Magnetotelluric studies of the caldas novas geothermal reservoir, brazil, *Journal of Applied Geophysics*, 49, 33–46.
- Pellerin, L., J. Johnston, and G. Hohmann (1996), A numerical evaluation of electromagnetic methods in geothermal exploration, *Geophysics*, 61(1), 121–130.
- Phoenix Geophysics (2005), *Data Processing User Guide*, Phoenix Geophysics.
- PNOC EDC (1989a), Exploration and evaluation of the montelago geothermal prospect, oriental mindoro, *Tech. rep.*, PNOC EDC.
- PNOC EDC (1989b), Results thermal gradient drillings, naujan geothermal project, montelago, oriental mindoro, *Tech. rep.*, PNOC EDC.
- PT LAPI ITB (2014), Monte carlo volumetric assessment and p90 study for montelago geothermal concession mindoro philippines, *Tech. rep.*, PT LAPI ITB.

- Ramos, M. (1989), Geochemical assessment of the montelago geothermal prospect, *Tech. rep.*, PNOC EDC.
- Regandara, R. (2014), Geological structure and permeable zone potential in the montelago geothermal prospect, mindoro island, philippines, Master's thesis, Institut Teknologi Bandung.
- Rikitake, T. (1948), Note on the electromagnetic induction within the earth, *Bull. Earthq. Res. Inst., Univ. Tokyo*, 24, 1–9.
- Rodi, W., and R. Mackie (2001), Nonlinear conjugate gradients algorithm for 2-d magnetotelluric inversion, *Geophysics*, 66(1), 174–187.
- Rojas, F. (2015), Montelago project quantifies potential of 40 mw through initial drilling, website.
- Rosenkjaer, G., E. Gasperikova, G. Newman, and K. Árnason (2015), Comparison of 3d mt inversions for geothermal exploration: Case studies for krafla and hengill geothermal systems in iceland, *Geothermics*, 57, 258–274.
- Sasaki, Y., and M. Meju (2006), Three-dimensional joint inversion for magnetotelluric resistivity and static shift distributions in complex media, *Journal of Geophysical Research*, 111(B05101).
- Serpen, U., N. Aksoy, T. Öngür, and E. Didem Korkmaz (2009), Geothermal energy in turkey: 2008 update, *Geothermics*, 38, 227–237.
- Sigurgeirsson, M., H. Helgadóttir, S. Jónsson, and T. Egilson (2015), Drilling of slimholes sh-01 and sh-02 from surface down to 1250 and 1200 m montelago in mindoro - philippines, *Tech. rep.*, Icelandic GeoSurvey.
- Sigússon, B., and A. Uihlein (2015), 2014 jrc geothermal energy status report, *Tech. rep.*, European Commission, Joint Research Centre.
- Simpson, F., and K. Bahr (2005), *Practical Magnetotellurics*, Cambridge University Press.

- Siripunvaraporn, W. (2012), Three-dimensional magnetotelluric inversion: An introductory guide for developers and users, *Surveys in Geophysics*, 33, 5–27.
- Siripunvaraporn, W., G. Egbert, Y. Lenbury, and M. Uyeshima (2005), Three-dimensional magnetotelluric inversion: data-space method, *Physics of the Earth and Planetary Interiors*, 150, 3–14.
- Spichak, V. (2009), Electromagnetic sounding of geothermal zones, *Journal of Applied Geophysics*, 68(4), 459–478.
- Spichak, V., and O. Zakharova (2015), *Electromagnetic Geothermometry: theory, modeling, practice*, Elsevier Science.
- Spies, B. (1989), Depth of investigation in electromagnetic sounding methods, *Geophysics*, 54, 872–888.
- Stefansson, V. (2005), World geothermal assessment, in *Proceedings World Geothermal Congress 2005*.
- Sternberg, B., J. Washburne, and L. Pellerin (1988), Correction for the static shift in magnetotellurics using transient electromagnetic soundings, *Geophysics*, 53, 1459–1468.
- Szarka, L. (1988), Geophysical aspects of man-made electromagnetic noise in the earth - a review, *Surveys in Geophysics*, 9, 287–318.
- Tikhonov, A. (1950), On determining electrical characteristics of the deep layers of the earth's crust, *Doklady*, 73, 295–297.
- Tolentino, B., R. Poblete, and N. Apuada (2011), Reassessment of montelago geothermal resource, *Tech. rep.*, FEDS Energy Resources and Development Services Inc.
- Tolentino, B., N. Apuada, and R. Poblete (2012), Results of csmt survey in montelago geothermal prospect, *Tech. rep.*, FEDS Energy Resources and Development Services Inc.

- Uchida, T., Y. Song, T. Lee, Y. Mitsuhashi, S. Lim, and S. Lee (2005), Magnetotelluric survey in an extremely noisy environment at the pohang low-enthalpy geothermal area, korea, in *Proceedings World Geothermal Congress 2005*, Antalya, Turkey.
- van Heekeren, V., and G. Bakema (2015), The netherlands country update on geothermal energy, in *Proceedings World Geothermal Congress*, Melbourne, Australia.
- van Leeuwen, W., K. Marnette, R. Schotting, and M. Muller (2015), A geothermal exploration mt data set and its 3-d inversion using two different codes: an example from western turkey, in *Proceedings World Geothermal Congress 2015*, Melbourne, Australia.
- van Leeuwen, W., Suryantini, and G. Hersir (2016), Quantitative comparison of two 3-d resistivity models of the montelago geothermal prospect, in *PROCEEDINGS, 5th ITB International Geothermal Workshop 2016*, Institut Teknologi Bandung, Bandung, Indonesia.
- Wannamaker, P. (1997), Tensor csamt survey over the sulphur springs thermal area, valles caldera, new mexico, u.s.a., part i: Implications for structure of the western caldera, *Geophysics*, NO. 2 (1997); P. ,10 FIGS, 62(2), 451–465.
- Wannamaker, P., G. Hohmann, and S. Ward (1984), Magnetotelluric responses of three-dimensional bodies in layered earths, *Geophysics*, 49(9), 1517–1533.
- Wannamaker, P., R. P.E., D. W.M., J. McCulloch, and N. K. (2005), Magnetotelluric surveying and monitoring at the coso geothermal area, california, in support of the enhanced geothermal systems concept: Survey parameters, initial results, in *Proceedings World Geothermal Congress 2005*, Antalya, Turkey.
- Weckmann, U., A. Magunia, and O. Ritter (2005), Effective noise separation for magnetotelluric single site data processing using a frequency domain selection scheme, *Geophysics Journal International*, 161, 635–652.

- Wibobo, H. (2014a), Magnetic acquisition in montelago geothermal prospect, *Tech. rep.*, Institut Teknologi Bandung.
- Wibobo, H. (2014b), Gravity acquisition in montelago geothermal prospect, philippines, *Tech. rep.*, Institut Teknologi Bandung.
- Williams, C., M. Reed, and A. A.F. (2011), Updating the classification of geothermal resources, in *Proceedings 36th workshop on geothermal reservoir engineering*, Stanford, CA: Stanford University.
- Younger, P. (2014), Missing a trick in geothermal exploration, commentary in *Nature Geoscience*.



Appendices

Structural metrics for the quantitative comparison of resistivity inversion models

The bulk of the resistivity structures in the 3-D inversion models are related to geological structures, particularly those anomalies consistent between various inversion models of the same magnetotelluric data. However, some of the features may be artefacts introduced by the inversions. As the solution of a 3-D inversion is non-unique, an anomaly appearing in two different inversions is reassuring. Those resistivity structures that do not appear in multiple inversion models of the same magnetotelluric data created by different inversion codes, might be introduced by the code and not related to geological structures. By quantitatively analysing and comparing these 3-D inversion models, the actual structures and artefacts can be distinguished from one another, increasing the validity of the interpretation of the models. This quantitative comparison between 3-D inversion models can be done using the set of structural metrics introduced here. These structural metrics are considered to identify those resistivity structures required by the magnetotelluric data to obtain the optimal

fit between observed and modelled data. The robust and required resistivity structures appearing in both models might then be regarded as related to geological structures and consequently suitable for the geothermal interpretation of the resistivity models.

The structural metrics used in this Section are usually applied to compare different geophysical models before joint inversion and are described in, for example, the review article by *Gallardo and Meju* [2011]. Some of these metrics are also used in a slightly modified version proposed by *Rosenkjaer et al.* [2015] to compare electromagnetic inversion models resulting from different inversion codes. The metrics described below are based on the gradient, cross product and Laplace operators. The structural metrics used to verify the resistivity structures in the model are:

- **The magnitude (or norm) of the model gradient** $\|\nabla m\|$, which maps the magnitude of the change in resistivity from cell to cell. Since the model gradient at a certain location in the model is a vector, its magnitude is used for graphical illustration:

$$\|\nabla m\| = \sqrt{\left(\frac{\partial \bar{m}}{\partial x}\right)^2 + \left(\frac{\partial \bar{m}}{\partial y}\right)^2 + \left(\frac{\partial \bar{m}}{\partial z}\right)^2}. \quad (\text{A.1})$$

Here \bar{m} is the three-dimensional resistivity model containing the electrical resistivity in Ω_m at locations x, y, z .

- **The gradient difference** $\delta\bar{\varphi}$, which is computed by computing the difference between the normalized model gradients of the two resistivity models considered. The gradient difference metric linearly assesses the structural similarities between two models [*Gallardo and Meju*, 2011].

$$\delta\bar{\varphi} = \frac{\nabla\bar{m}_1}{\|\nabla m_1\|} - \frac{\nabla\bar{m}_2}{\|\nabla m_2\|}. \quad (\text{A.2})$$

As Equation A.2 is a vector at location x, y, z , its norm is used for graphical illustration. The norm of the gradient difference $\delta\bar{\varphi}$ is computed in a similar fashion as Equation A.1.

- **The cross gradient $\bar{\tau}$** , which is the cross product of the two model gradients, delivers a direct comparison between the two resistivity models [Gallardo and Meju, 2011; Rosenkjaer et al., 2015]. Again, as the cross gradient is a vector at model location x, y, z , the norm of the cross gradient is used to present the result graphically:

$$\bar{\tau} = \nabla m_1 \times \nabla m_2. \quad (\text{A.3})$$

The structural metrics of synthetic resistivity data of two different layered resistivity models (see Figures A.1 and A.2) and a resistivity model containing “circular” resistivity features (see Figure A.3) were computed to guide the interpretation of the structural metrics of the resistivity inversion models based on actual magnetotelluric data.

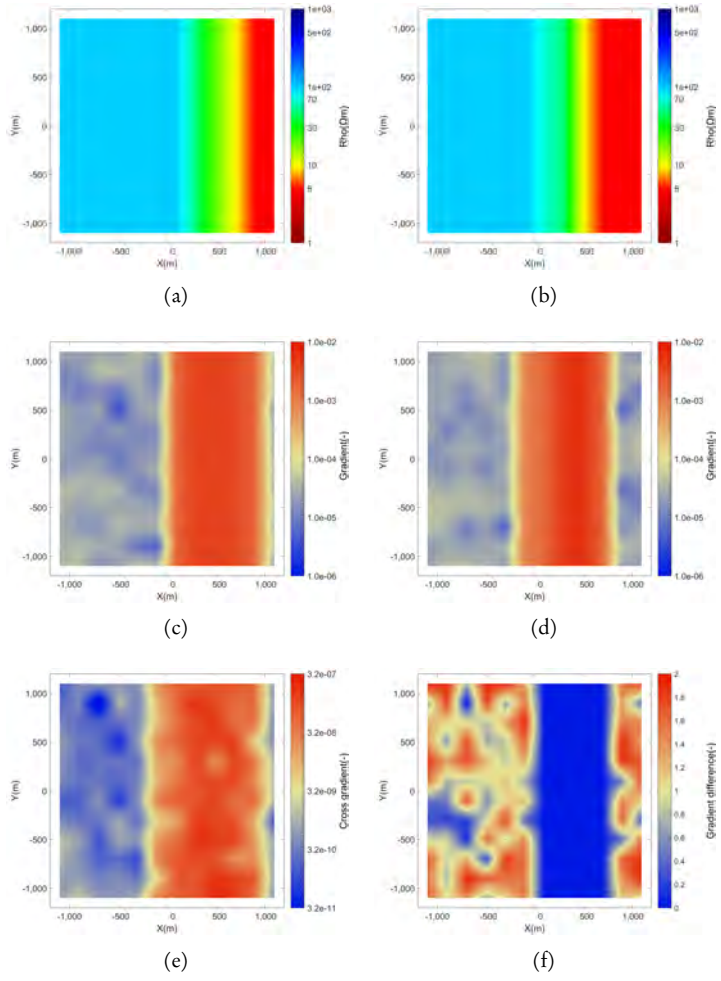


Figure A.1: Synthetic model of two slightly different three-layer resistivity models, model 1 A.1(a) and model 2 A.1(b), as well as the structural metrics of these two models. Resistivities are given in Ωm . Norm of the model gradient of A.1(c) model 1 and respectively of A.1(d) model 2. Here, red colors indicate a change in resistivity, while blue colors indicate regions with a *stable* resistivity structure. A.1(e) shows the norm of the cross product of the two synthetic models. A.1(f) shows the difference between the normalized model gradients of the two synthetic models.

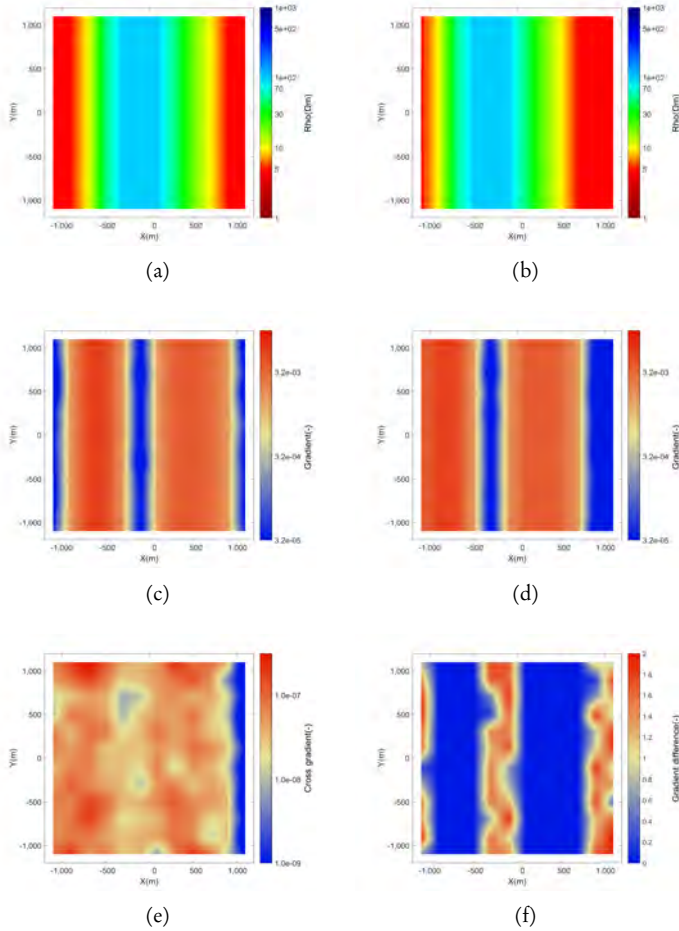


Figure A.2: Synthetic model of two slightly different three-layer resistivity models, model 1 A.2(a) and model 2 A.2(b), as well as the structural metrics of these two models. Resistivities are given in Ωm . Norm of the model gradient of A.2(c) model 1 and respectively of A.2(d) model 2. Here, red colors indicate a change in resistivity, while blue colors indicate regions with a *stable* resistivity structure. A.2(e) shows the norm of the cross product of the two synthetic models. A.2(f) shows the difference between the normalized model gradients of the two synthetic models.

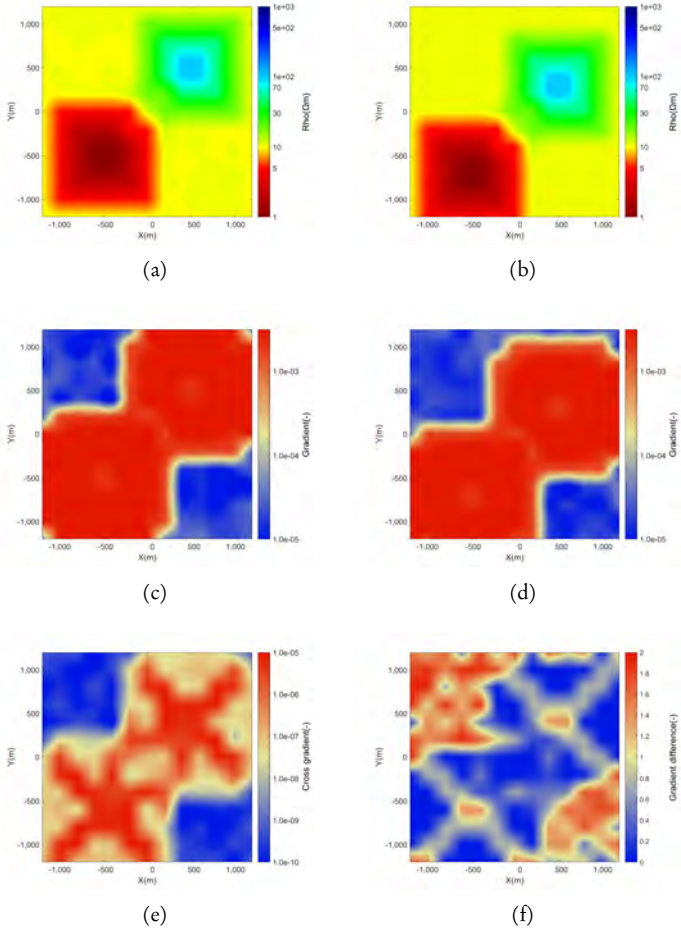


Figure A.3: Synthetic model of two slightly different resistivity models, model 1 A.3(a) and model 2 A.3(b), as well as the structural metrics of these two models. Resistivities are given in Ωm . Norm of the model gradient of A.3(c) model 1 and respectively of A.3(d) model 2. Here, red colors indicate a change in resistivity, while blue colors indicate regions with a *stable* resistivity structure. A.3(e) shows the norm of the cross product of the two synthetic models. A.3(f) shows the difference between the normalized model gradients of the two synthetic models.

Structural metrics of the 3-D inversion models presented in Chapter 5

In this Appendix the structural metrics of the resistivity maps and resistivity cross-sections as presented in Chapter 5: “Comparison and interpretation of two 3-D inversion models” are presented. The structural metrics calculated are introduced in Appendix A: “Structural metrics”.

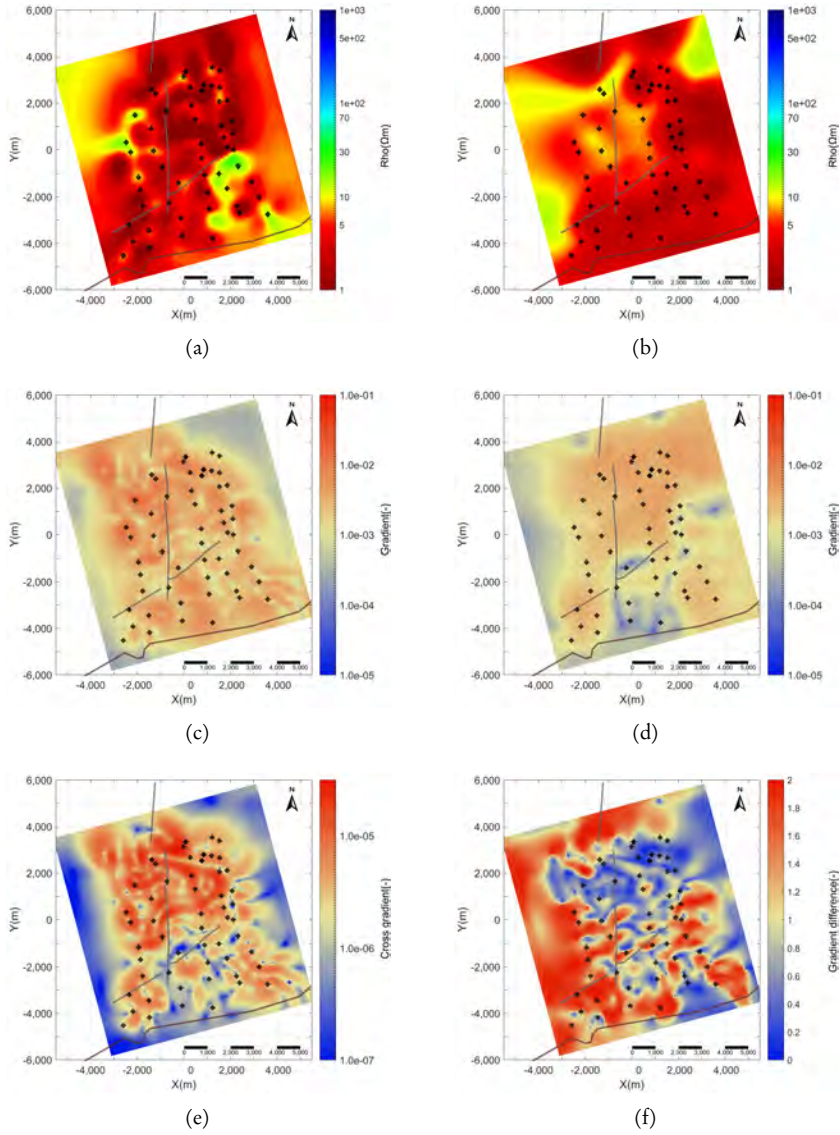


Figure B.1: Resistivity maps at -500 m elevation from (a) ModEM_10_Tur and (b) Mack_10_Tur. Norm of the resistivity gradient at -500 m elevation from (c) ModEM_10_Tur and (d) Mack_10_Tur. (e) The cross gradient of the two resistivity models at -500 m elevation. (f) Normalized difference of the difference between the model gradients. Magnetotelluric stations (diamonds), main faults (grey solid lines) and the coast line (brown solid line) are shown as well in all maps. Resistivity in Ωm .

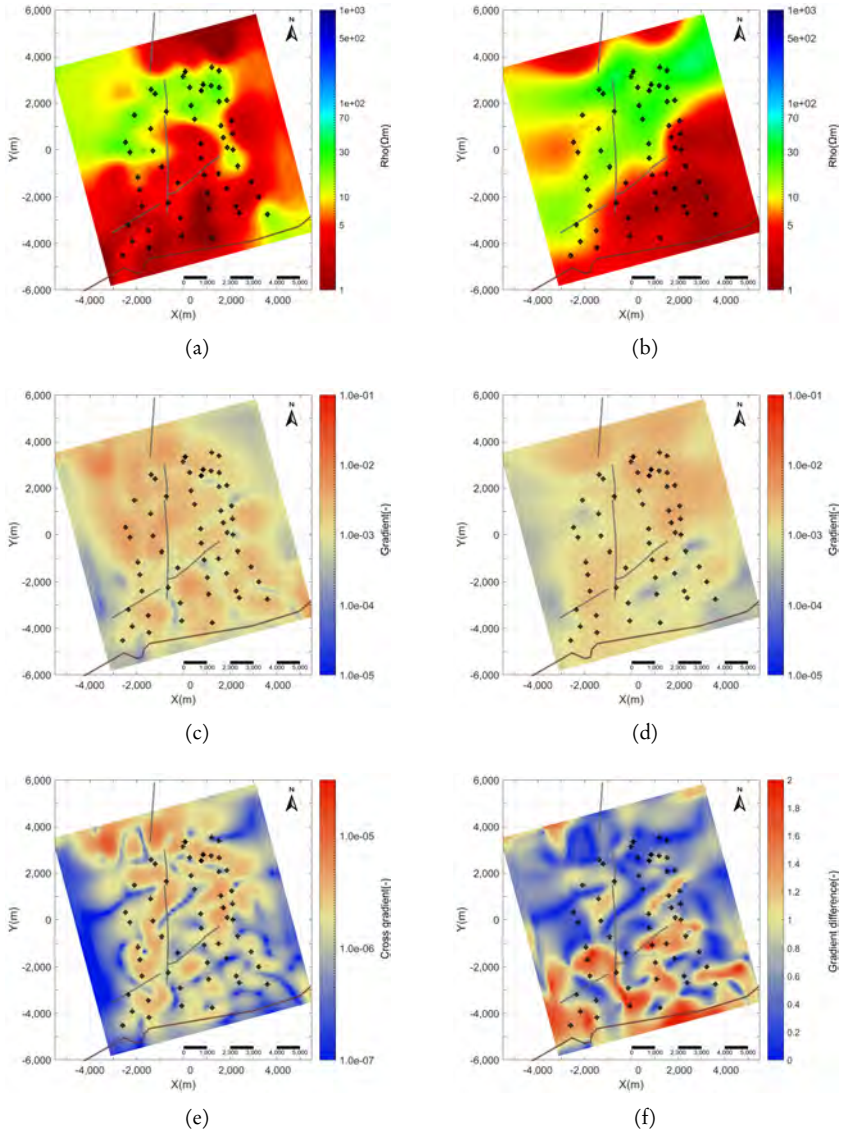


Figure B.2: Resistivity maps at -1,000 m elevation from (a) ModEM_10_Tur and (b) Mack_10_Tur. Norm of the resistivity gradient at -1,000 m elevation from (c) ModEM_10_Tur and (d) Mack_10_Tur. (e) The cross gradient of the two resistivity models at -1,000 m elevation. (f) Normalized difference of the difference between the model gradients. Magnetotelluric stations (diamonds), main faults (grey solid lines) and the coast line (brown solid line) are shown as well in all maps. Resistivity in Ωm .

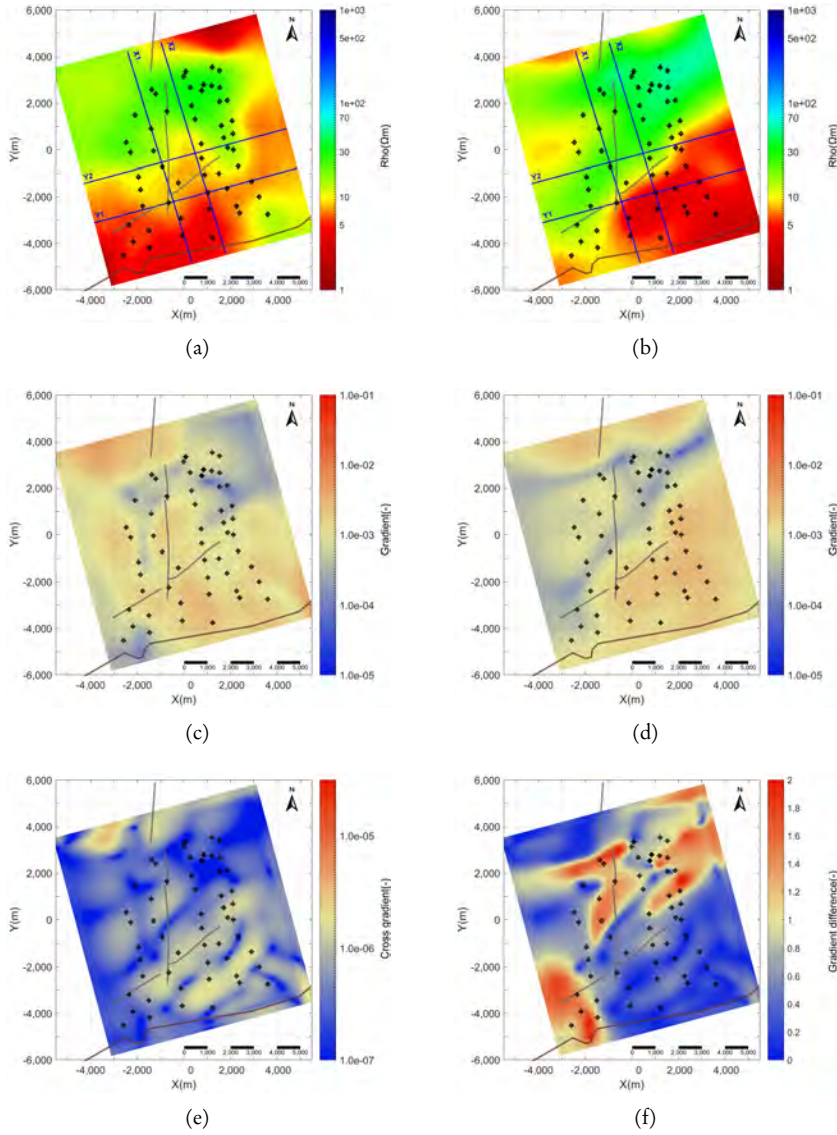


Figure B.3: Resistivity maps at -1,500 m elevation from (a) ModEM_10_Tur and (b) Mack_10_Tur. In these two maps, the locations of the profiles of the cross-sections shown in Figures B.4 to B.7 are given. Norm of the resistivity gradient at -1,500 m elevation from (c) ModEM_10_Tur and (d) Mack_10_Tur. (e) The cross gradient of the two resistivity models at -1,500 m elevation. (f) Normalized difference of the difference between the model gradients. Magnetotelluric stations (diamonds), main faults (grey solid lines) and the coast line (brown solid line) are shown as well in all maps. Resistivity in Ωm .

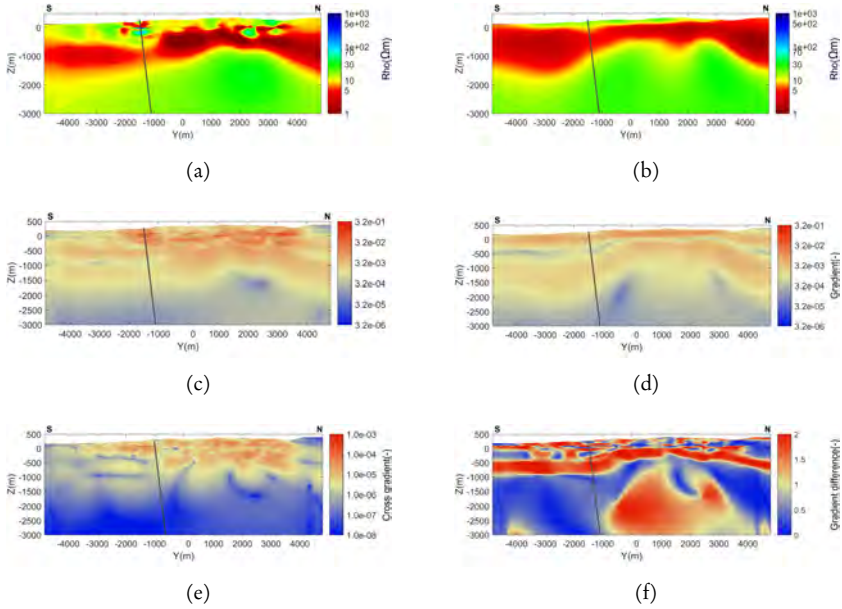


Figure B.4: Resistivity cross-sections of the two models of profile X1 at model coordinate $X = 1187.5$ m and its structural metrics. (a) Resistivity cross-section of ModEM_10_Tur. (b) Resistivity cross-section of Mack_10_Tur. (c) Model gradient of ModEM_10_Tur. (d) Model gradient of Mack_10_Tur. (e) The cross gradient of the two resistivity models for cross-section X1. (f) Normalized difference of the difference between the model gradients. Main fault (grey line) is shown in all cross-sections. Resistivity in Ωm .

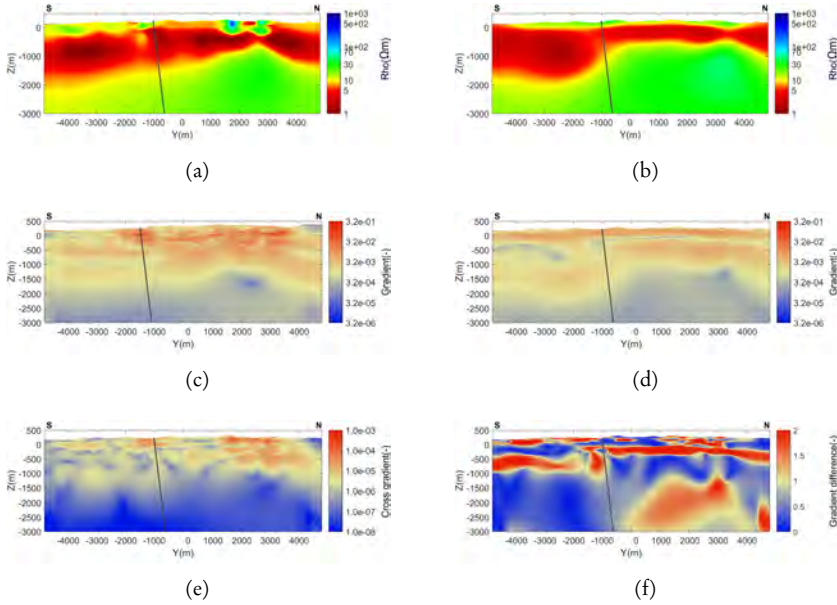


Figure B.5: Resistivity cross-sections of the two models of profile X2 at model coordinate $X = 312.5$ m and its structural metrics. (a) Resistivity cross-section of ModEM_10_Tur. (b) Resistivity cross-section of Mack_10_Tur. (c) Model gradient of ModEM_10_Tur. (d) Model gradient of Mack_10_Tur. (e) The cross gradient of the two resistivity models for cross-section X2. (f) Normalized difference of the difference between the model gradients. Main fault (grey line) is shown in all cross-sections. Resistivity in Ωm .

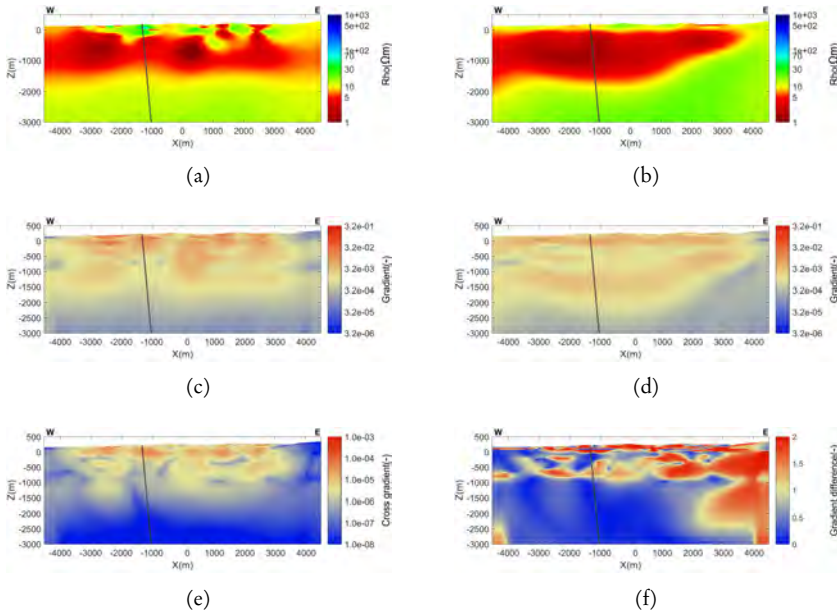


Figure B.6: Resistivity cross-sections of the two models of profile Y1 at model coordinate $Y = 2000$ m and its structural metrics. (a) Resistivity cross-section of ModEM_10_Tur. (b) Resistivity cross-section of Mack_10_Tur. (c) Model gradient of ModEM_10_Tur. (d) Model gradient of Mack_10_Tur. (e) The cross gradient of the two resistivity models for cross-section Y1. (f) Normalized difference of the difference between the model gradients. Main fault (grey line) is shown in all cross-sections. Resistivity in Ωm .

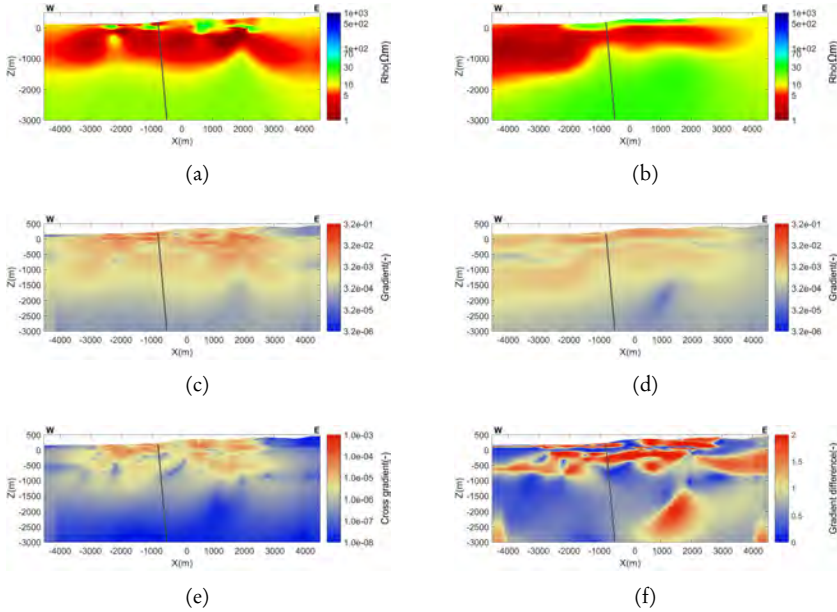


Figure B.7: Resistivity cross-sections of the two models of profile Y2 at model coordinate $Y = -500$ m and its structural metrics. (a) Resistivity cross-section of ModEM_10_Tur. (b) Resistivity cross-section of Mack_10_Tur. (c) Model gradient of ModEM_10_Tur. (d) Model gradient of Mack_10_Tur. (e) The cross gradient of the two resistivity models for cross-section Y2. (f) Normalized difference of the difference between the model gradients. Main fault (grey line) is shown in all cross-sections. Resistivity in Ωm .

Samenvatting

Geothermie

Geothermische energie is een vorm van duurzame energie die wordt gewonnen voor het opwekken van elektriciteit of direct gebruik in de vorm van warmte. In deze thesis wordt met geothermische energie alleen die in de aarde aanwezige warmte bedoeld, die, in potentie door de mens kan worden gewonnen.

De belangrijkste bron van geothermische energie is de warmteproductie in de mantel van de aarde en in de aardkern. De geothermische energie wordt opgeslagen in de aardkorst in gesteente en/of water. Het gebruik van de in de aardkorst opgeslagen warmte staat bekend als geothermische energieproductie. Ingeschat wordt dat de mensheid voor ten minste 80,000 jaar gebruik kan maken van deze duurzame energiebron. Bij deze inschatting is uitgegaan van de winbare thermische energie aanwezig in de bovenste drie kilometer van de aardkorst en bij een verwacht wereldwijd energieverbruik van 500 EJ per jaar. Dit is een conservatieve aanname aangezien in werkelijkheid verscheidene geothermische systemen zich op een aanzienlijk grotere diepte bevinden.

Een geothermisch systeem is hier gedefinieerd als: “iedere lokale geologische setting waar een gedeelte van de in de aarde aanwezige geothermische

energie gewonnen kan worden door natuurlijke of kunstmatige circulatie van vloeistof naar een punt van gebruik.” De lokale geologische omstandigheden en de energievraag van de gebruikers zijn bepalend voor de temperatuur die gewonnen kan worden uit een geothermisch systeem en de uiteindelijke toepassing (warmtewinning of elektriciteitsproductie). Wereldwijd wordt geothermische warmte gewonnen in gebieden met een divers geologisch karakter. Hierbij kan gedacht worden aan vulkanisch actieve gebieden zoals IJsland en Indonesië en spreidingsgebieden zoals Turkije waar temperaturen vaak hoog genoeg zijn voor elektriciteitsproductie. Hiernaast wordt er ook geothermische warmte gewonnen voor elektriciteits- of warmteproductie in tektonisch stabiele bekkens met een lagere temperatuur zoals Nederland, Duitsland en Frankrijk.

Een gebruikelijke benadering om tot de optimale strategie voor de exploratie en ontwikkeling van een geothermisch systeem te komen, is het systeem te beschrijven in een conceptueel model. Het conceptuele model is de geologische beschrijving van het geothermische systeem en bestaat uit de kwalitatieve beschrijving van ten minste drie onderdelen: 1. De warmtebron die het geothermische systeem (voortdurend) van warmte voorziet. 2. Het geothermische reservoir dat de winbare geothermische energie bevat. 3. De afsluitende lagen die de geothermische energie in het reservoir houden. Het conceptuele model van een geothermisch systeem wordt gemaakt op basis van de op dat moment beschikbare exploratiegegevens.

Een vaak gebruikte geofysische techniek tijdens de exploratie van met name vulkanische geothermische systemen is de magnetotellurische (MT) methode. Om te onderzoeken of deze passieve elektromagnetische methode ook geschikt is voor geothermische exploratie in Nederland is het uitgangspunt waarmee dit promotieonderzoek is gestart.

Achtergrond en opbouw van het onderzoek

De magnetotellurische methode is een passieve elektromagnetische techniek die de natuurlijke tijd-varianties in de elektrische en magnetische velden van

de aarde meet. De bron van de tijd-variaties in het elektromagnetische veld zijn zonnestormen en wereldwijde bliksemactiviteit tijdens onweersbuien. De diepte tot waarop een MT meting in de ondergrond doordringt hangt af van de duur van de meting en van de gemiddelde elektrische weerstand van de gemeten ondergrond. De elektrische weerstandsstructuur van de ondergrond kan bepaald worden uit de met een aantal aannames afgeleide lineaire relatie tussen de elektrische en magnetische velden van de aarde.

Ondanks dat de MT methode succesvol is toegepast tijdens de exploratie van hoge enthalpie geothermische systemen¹, kan de methode niet zonder meer overal worden ingezet. In gebieden met een hoge bevolkingdichtheid zoals Nederland, heeft de techniek te lijden onder verstoringen van het signaal als gevolg van het grote aantal artificiële elektromagnetische bronnen zoals bijvoorbeeld schrikdraad, de spoorwegen en ondergrondse kabels en leidingen. Naast het minimaliseren van de invloed van deze “culturele elektromagnetische ruis” op het gemeten signaal, is het ook een uitdaging om met de MT methode de structuren in de Nederlandse ondergrond in kaart te brengen. Dit laatste wordt veroorzaakt door de zeer lage elektrische weerstand van de Nederlandse ondergrond en door de naar verwachting kleine elektrische weerstandscontrasten daarin. Om de MT methode in het kader van geothermische exploratie in Nederland succesvol toe te passen, zullen strategieën ontwikkeld moeten worden om deze twee uitdagingen het hoofd te bieden. Met deze vraag, hoe kan de MT methode succesvol worden ingezet voor geothermische exploratie in Nederland, is dit promotieonderzoek aanvankelijk begonnen.

Omdat tijdens dit promotieonderzoek geen MT data gemeten in Nederland beschikbaar waren, of zouden komen, is met de MT data van twee buitenlandse geothermische projecten gewerkt. Het eerste geothermische project is gesitueerd in Turkije in de Provincie Çanakkale en de data van het tweede geothermische project is geacquireerd voor het Montelago geothermische project op het eiland Mindoro in de Filippijnen. Op basis van de in het kader van dit onderzoek gecreëerde elektrische weerstandsmodellen zijn voor

¹In dit geval wordt met hoge enthalpie bedoeld dat er voldoende energie in het geothermische systeem aanwezig is voor directe elektriciteitsproductie.

beide geothermische projecten conceptuele modellen geformuleerd. Hiernaast zijn de MT data gemeten voor de exploratie van het Çanakkale geothermische project gere-processed met een tijdens dit onderzoek ontwikkeld processing algoritme. De ervaring opgedaan tijdens deze twee casestudies is vertaald naar de mogelijkheden van de toepassing van MT voor geothermische exploratie in Nederland.

De magnetotellurische methode

Zoals hierboven beschreven, worden tijdens een MT meting de natuurlijke tijd-varianties in het elektromagnetische veld van de aarde gemeten. Omdat de penetratiediepte van de MT respons afhankelijk is van frequentie, geldt: hoe langer de meting duurt, hoe dieper de penetratiediepte. Een MT station bestaat gewoonlijk uit twee elektrodeparen en drie magnetische inductiespoelen. De elektrodeparen zijn doorgaans noord-zuid en oost-west geïoriënteerd en meten de varianties in het elektrische veld terwijl de magnetische inductiespoelen noord-zuid, oost-west en verticaal gepositioneerd zijn en de varianties in het magnetische veld meten. Met de vergelijkingen van Maxwell als uitgangspunt en gebruik makend van een aantal aannames, kan een lineaire relatie tussen het elektrische en het magnetische veld worden afgeleid. Deze lineaire relatie wordt beschreven door de MT impedantie op basis waarvan de elektrische weerstandsstructuur van de ondergrond kan worden bepaald.

De MT impedantie is een van de frequentie afhankelijke functie, terwijl de MT data in tijd wordt gemeten. Om de MT impedantie te kunnen bepalen worden door middel van een Fourier transformatie de gemeten data van het tijd-domein naar het frequentie-domein omgezet. Vervolgens worden in het frequentie-domein, op basis van bijvoorbeeld statische parameters die elektrische en magnetische velden vergelijken, de datapunten van slechte kwaliteit geëlimineerd. Tenslotte wordt gewoonlijk met een “robuste processing methode” de MT impedantie berekend. Om uiteindelijk de elektrische weerstandsstructuur van de ondergrond te bepalen, moet de resulterende MT respons van frequentie naar diepte geïnverteerd worden.

Een inversie is hier het inschatten van de elektrische weerstand van ondergrond als functie van diepte op basis van de gemeten MT respons als functie van frequentie. Dit wordt gedaan door op de data algoritmes toe te passen die middels een iteratief proces de best passende oplossing tussen het model en de gemeten data berekenen. Het resulterende inversiemodel kan eventueel gestuurd worden door voorafgaand aan de inversie de al bekende informatie over de ondergrond, zoals bekend uit bijvoorbeeld seismiek of boorgatmetingen, te gebruiken.

In dit promotieonderzoek zijn de elektrische weerstandsmodellen gecreëerd met het “ModEM” inversie-algoritme. Hiernaast zijn elektrische weerstandsmodellen gemaakt met “Mack3D” (voor Çanakkale) en “WSINV3DMT” (voor Montelago) geanalyseerd en vergeleken met de met ModEM gegenereerde inversiemodellen. Alledrie de inversie-algoritmes zijn gebaseerd op vergelijkbare theoretische uitgangspunten maar verschillen in de uitwerking daarvan.

Het Çanakkale geothermische project

De data van het in Turkije gesitueerde Çanakkale geothermische project zijn geacquireerd, geprocesseerd en geïnverteerd door twee verschillende aannemers. Omdat de aangeleverde MT data inconsistenties vertonen, zijn de data in dit promotieonderzoek gere-processed, opnieuw geïnverteerd en geïnterpreerd. De voor het processen gebruikte code is ontwikkeld tijdens dit PhD-onderzoek en levert een in kwaliteit verbeterde MT dataset op. De gere-processede data zijn vervolgens geïnverteerd in een 3-D model. Het nieuwe 3-D elektrische weerstandsmodel is tenslotte kwantitatief en kwalitatief vergeleken met het 3-D elektrische weerstandsmodel zoals aangeleverd door de aannemer. Voor de kwantitatieve analyse van de modellen wordt gebruik gemaakt van zogenoemde “structurele metrieken”. Op basis van de elektrische weerstandsmodellen, aangevuld met geochemische en geologische informatie, is een conceptueel model van dit geothermische systeem geformuleerd. Dit conceptuele model is in 2015 gevalideerd nadat twee exploratieputten in het reservoir zijn geboord.

Re-processing van de MT data met Quality Index pre-sorting

Het re-processen van deze MT dataset is uitgevoerd in het frequentie-domein met een nieuw ontwikkeld processing algoritme: Quality Index pre-sorting. Dit algoritme is gebaseerd op een combinatie van statistische parameters die grafisch weergegeven worden en op basis waarvan de kwaliteit van de MT data wordt ingeschat. De gebruikte statistische parameters zijn de bivariante coherentie, de kleinste kwadraten MT impedantie en de ingeschatte fout van deze MT impedantie. De grafische weergave van een combinatie van de gewogen statistische parameters geeft de datapunten met een lage kwaliteit weer, op basis waarvan deze geëlimineerd kunnen worden voordat de MT respons van de stations wordt berekend. De resulterende gere-processerde MT dataset van het Çanakkale geothermische project is samenhangend en is geschikt voor 3-D inversie.

Inversie en analyse van de modellen

Deze gere-processerde MT dataset is, gebruikmakend van het “ModEM” inversie-algoritme, opnieuw geïnverteerd. Hierbij is gekozen voor zo identiek mogelijke inversieparameters als gebruikt bij de inversie met “Mack3D”, uitgevoerd door de aannemer. De aanwezigheid van de Middellandse Zee en de topografie zijn meegenomen in het voor de inversie gebruikte modelgrid. Het in dit onderzoek gemaakte 3-D elektrische weerstandsmodel en het door de aannemer aangeleverde 3-D elektrische weerstandsmodel zijn zowel kwalitatief als kwantitatief met elkaar vergeleken. Naast het gegeven dat in grote lijnen in beide elektrische weerstandsmodellen vergelijkbare dominante structuren worden waargenomen, zijn ook de absolute waarden van de elektrische weerstanden van de twee modellen vergelijkbaar. Aan de andere kant worden duidelijke verschillen in de kleinschalige anomalieën in beide modellen waargenomen.

Voor de kwantitatieve analyse van de twee inversiemodellen is gebruik gemaakt van structurele metrieken. De gradiënten van de twee inversiemodellen, het kruisproduct van de gradiënten (de kruisgradient) van de twee modellen en het verschil tussen de gradiënten (het gradientverschil) van de twee

modellen zijn gebruikt. Uit de kwantitatieve analyse blijkt dat het gradiëntverschil gevoelig is voor de minimale (binnenste) grenzen van vergelijkbare structuren, terwijl de kruisgradient de maximale (buitenste) grenzen van vergelijkbare structuren benadrukt. Aangezien beide inversiemodellen vergelijkbare dominante ondergrondse weerstandsstructuren weergeven en de overeenkomst tussen de gemodelleerde en de gemeten data groot is, zijn beide modellen een betrouwbare weergave van de gemeten MT data.

Het conceptuele model

De elektrische weerstandsmodellen van de ondergrond van het Çanakkale geothermisch project zijn geologisch als volgt geïnterpreteerd. De dominante geologische structuren worden gevormd door een elektrisch geleidende laag van vulkanisch gesteente die bovenop een dikke basislaag met een grotere elektrische weerstand ligt. Deze laag bestaat uit ophiolietcomplex met een kalksteenformatie eronder. Het is de verwachting dat deze kalksteenlaag het geothermisch reservoir vormt. Dit is recent gevalideerd door twee exploratiebooringen die het veronderstelde reservoir gepenetreerd hebben. Hiernaast kan een rand van het graben-achtige systeem, waarin het geothermische systeem zich bevindt, herkend worden in de inversiemodellen op een locatie die overeenkomt met de breuken in het gebied. Het geothermische systeem wordt waarschijnlijk via deze breuken opgewarmd door een magmatisch lichaam dat zich op enige afstand van de projectlocatie bevindt.

Het Montelago geothermische project

Het Montelago geothermische project op het eiland Mindoro in de Filippijnen kent een lange ontwikkelingsgeschiedenis. Hierdoor zijn in een tijdspanne van 25 jaar vier geofysische exploratie-onderzoeken uitgevoerd. De data van de drie meest recente van deze vier onderzoeken zijn kwalitatief de moeite waard om nader te bestuderen. De bestudeerde onderzoeken zijn een 24-station MT sur-

vey uit 2000, een 112-station CSMT² survey uit 2012 en een 54-station gecombineerde TEM³-MT survey uit 2014. De elektromagnetische gegevens van deze drie onderzoeken zijn opnieuw geanalyseerd en geïnverteerd, resulterend in nieuwe 2-D en 3-D inversiemodellen.

Inversie en analyse van de modellen

Uit analyse blijkt dat de CSMT data uit 2012 gemeten voor lange periodes onbetrouwbaar zijn terwijl hetzelfde geldt voor gemeten fasen voor alle periodes. De onbetrouwbare datapunten zijn geëlimineerd en op basis van de opgeschoonde data zijn nieuwe 2-D inversiemodellen gemaakt. De toegevoegde waarde van de nieuwe inversiemodellen is beperkt omdat ze een penetratiediepte van slechts 600 m hebben. Ondanks dat in deze modellen de elektrische weerstand ondiep zeer heterogeen is, is er op diepte een anomalie waar te nemen op een locatie die overeenkomt met de inversiemodellen gemaakt op basis van de MT data uit 2000 en 2014.

De MT data gemeten in 2000 zijn opnieuw geïnverteerd, en waar oorspronkelijk enkel 2-D inversiemodellen zijn gepresenteerd, is nu gekozen voor een 3-D inversie met ModEM. In het modelgrid voor deze inversie zijn de bathymetrie en de topografie meegenomen. Op vergelijkbare locaties als in de oude 2-D elektrische weerstandsmodellen alsmede in de 3-D elektrische weerstandsmodellen op basis van de MT data uit 2014, worden in het resulterende 3-D elektrische weerstandsmodel grootschalige anomalieën waargenomen. Door de kleine databedekking van het onderzoeksgebied zijn in het weerstandsmodel door het algoritme veroorzaakte randeffecten binnen het onderzoeksgebied waar te nemen.

²Controlled-source magnetotellurics: een actieve variant van MT waarbij een generator wordt gebruikt om een elektromagnetisch signaal te genereren. Door het gebruik van een elektromagnetische bron heeft deze techniek een aanzienlijk kleinere penetratiediepte in vergelijking met de MT methode.

³Transient-domain elektromagnetics: een actieve elektromagnetische methode die een 1-D elektrische weerstandsrespons van de ondergrond geeft. TEM wordt vaak gebruikt om verstoringen in de data te corrigeren die onder andere veroorzaakt worden door een onregelmatige topografie. Deze verstoringen zijn ook wel bekend als galvanische vervorming.

Op basis van de MT data uit 2014 is in dit promotieonderzoek een nieuw 3-D inversiemodel gecrëeerd, en vergeleken met het bestaande 3-D elektrische weerstandsmodel op basis van diezelfde data. Voor het nieuwe model is met het ModEM inversie-algorithme gewerkt, terwijl voor het bestaande model WSINV3DMT is gebruikt. Voor de inversie met ModEM is een vergelijkbare inversiestrategie gekozen. Aangezien de gebruikte MT data gecorrigeerd zijn voor galvanische vervormingen, is alleen de bathymetrie meegenomen in het modelgrid. De resulterende inversiemodellen zijn kwalitatief en kwantitatief vergeleken.

Uit de kwalitatieve vergelijking blijkt dat de dominante anomalieën in beide modellen overeenkomen wat betreft lokatie en magnitude. Voor de kwantitatieve vergelijking is opnieuw gebruik gemaakt van structurele metrieken. Dezelfde metrieken als eerder beschreven zijn toegepast op de twee modellen. De kwantitatieve analyse bevestigt de waarnemingen gemaakt tijdens de kwalitatieve analyse. Gesteld kan worden dat de overeenkomsten tussen de modellen zich vooral in het midden van het onderzoeksgebied bevinden, terwijl aan de randen meer verschillen worden waargenomen. Met behulp van de kwantitatieve analyse zijn de randen van de weerstands anomalieën, de breuken en de geothermische manifestaties gekarteerd. Uit de evaluatie van de locaties van twee geplande exploratieboringen blijkt dat beide boringen anomalieën van verschillende signatuur zullen aanboren die mogelijk gerelateerd zijn aan het geothermische reservoir.

Het conceptuele model

Het onderzoeksgebied van het Montelago geothermische project wordt gekarakteriseerd door vulkanische afzettingen en een uitgedoofde vulkaan die ten minste 1 miljoen jaar geleden voor het laatst actief was. In het projectgebied zijn verschillende geothermische manifestaties zoals warme bronnen te vinden. Al het recente oppervlakte-exploratiewerk is uitgevoerd om het conceptuele model te kunnen definiëren alsmede om locaties te bepalen voor exploratieboringen. Op basis van de genoemde studies en recent uitgevoerd geologisch en geochemisch veldwerk is het conceptuele model van Montelago

geothermische project geformuleerd. De bron van geothermische warmte is onbekend, maar waarschijnlijk afkomstig van een diep gelegen magmalichaam, de doorlatendheid van het geothermische reservoir wordt door breuken gecontroleerd en de afsluitende laag bestaat uit gedeeltelijk verweerde vulkanische afzettingen. De reservoirtemperatuur wordt geschat op ten minste 190°C op een diepte van 400 m, waarmee een geschat elektrisch vermogen van 40 MW kan worden opgewekt. In 2014 zijn twee exploratieboringen gedaan die deze temperatuur hebben aangetroffen op een diepte van 1,200 m, terwijl de in het boorgat aanwezige hydrothermale kleimineralen duiden op een hogere temperatuur. Dit betekent dat het vulkanische systeem warmer is geweest en momenteel afkoelt. Op grotere diepte daalt de temperatuur in het boorgat, dit wordt mogelijk veroorzaakt door de instroom van koud water in het reservoir. Dit water zou dan afkomstig moeten zijn uit de bergketen langs de westelijke rand van het eiland. Aangenomen wordt dat het geothermische systeem nog steeds van onderaf opgewarmd wordt door het (afkoelende) magmalichaam.

Conclusies en aanbevelingen

Om het aanvankelijk doel van dit onderzoek niet uit het oog te verliezen kunnen op basis van de twee beschreven geothermische projecten een aantal algemene alsmede voor Nederland specifieke aanbevelingen gedaan worden voor geothermische exploratie met de MT methode.

In het geval van door culturele elektromagnetische ruis verstoorde data kan gesteld worden dat het in acht nemen van een nauwgezette voorbereiding en het volgen van een weldoordachte, precieze veldwerkprocedure de maximaal haalbare kwaliteit van de data in een gegeven gebied garandeert. Hiernaast kan door middel van het testen van en experimenteren met verschillende processing methoden de datakwaliteit verder verbeterd worden. Voor Nederland specifiek geldt hiernaast dat het mogelijk is succes te behalen met de exploratie van diepe potentiële geothermische reservoirs door de oplossing van het inversiemodel te sturen met “a priori” informatie uit de seismiek. Dit zal er voor zorgen dat het inversie-algoritme beter in staat is om de kleine weerstandsverschillen in de Nederlandse ondergrond te onderscheiden.

Ten slotte kunnen op basis van het uitgevoerde onderzoek nog de volgende conclusies en aanbevelingen gegeven worden.

Door gebruik te maken van Quality Index pre-sorting kan MT data van lage kwaliteit worden geïdentificeerd en verwijderd uit een MT dataset. Door Quality Index pre-sorting toe te passen op de MT data gemeten voor het Çanakkale geothermische project is de effectiviteit van deze methode geïllustreerd. Het is de verwachting dat met Quality Index pre-sorting de verstoringen in MT data gemeten in Nederland verwijderd kunnen worden.

Modelresultaten van 3-D inversiemodellen gecreëerd door gebruik te maken van verschillende inversie-algoritmes, maar met identieke inversiestrategieën, zijn in grote lijnen vergelijkbaar. De elektrische weerstandsmodellen lossen dezelfde dominante weerstandsstructuren op, maar kennen met name ondiep en aan de randen van het onderzoeksgebied significante verschillen. Om tot een goede geologische interpretatie en een optimale keuze van putlocaties te komen, wordt het daarom aanbevolen om op basis van één MT dataset ten minste twee 3-D elektrische weerstandsmodellen te genereren, daarbij gebruik makend van twee verschillende inversie-algoritmes.

Door gebruik te maken van structurele metrieken is het mogelijk verschillen tussen twee inversiemodellen kwantitatief te analyseren. Dit is gedemonstreerd door de structurele metrieken toe te passen op de inversiemodellen van de twee hier besproken geothermische projecten, waar ze toegepast worden om de grenzen van de anomalieën en, aangevuld met andere informatie uit oppervlakte-exploratie, boorlocaties te definiëren.

Ten slotte kan gesteld worden dat het direct correleren van de temperatuur in het reservoir en de elektrische weerstand op basis van de hydrothermale kleimineralogie van de ondergrond misleidend kan zijn. Dit is zeker het geval in niet-vulkanische en afkoelende geothermische systemen. De twee bestudeerde projecten illustreren dat naast de geofysische informatie ook de geochemische en geologische oppervlakte-exploratiedata gebruikt moeten worden tijdens de interpretatie van de geologie en de definitie van het conceptuele model.

Summary

Geothermal energy

Geothermal energy is a sustainable energy source which is utilized for electricity production or direct heat applications. In this thesis, geothermal energy is defined as that part of the Earth's heat that can, potentially, be recovered and exploited by man.

Radiogenic heat production in the mantle and crust is the main source of Earth's heat. The Earth's thermal energy is stored in rocks and/or water in the crust. It is the utilization of this thermal energy which is known as geothermal energy production. It is estimated that mankind can utilize this sustainable energy source for some 80,000 years. For this estimation the retrievable thermal energy present in the upper three kilometres of the crust and a projected global energy consumption rate of 500 EJ per year are considered. Since in reality several geothermal systems are present at considerably larger depths, this is a conservative estimate.

In this thesis, a geothermal system is defined as: "any localized geological setting where portions of the Earth's thermal energy may be extracted from natural or artificially induced circulating fluids transported to a point of

use.” The temperature retrieved from a geothermal system as well as the final geothermal application (electricity production or direct heat) depend on the local geological setting and the type of needed. Globally, geothermal heat is exploited in areas with a varying geological character. One can think of volcanically active regions such as Iceland and Indonesia, and tectonically extensional regions such as Turkey, where temperatures are generally high enough for electricity production. Geothermal energy is also produced for direct heat applications or electricity production in tectonically stable basins with lower temperatures, such as in the Netherlands, Germany and France.

The standard approach to achieve the most effective strategy for exploration and development of a geothermal system is to describe the geothermal system in a conceptual model. A conceptual model is the geological description of the geothermal system and comprises the qualitative description of at least three components: 1. The heat source, (continuously) providing the system with geothermal energy. 2. The geothermal reservoir, containing the recoverable geothermal energy of the system. 3. The seal or cap rock, trapping the geothermal energy in the reservoir. The conceptual model of a geothermal system is defined on basis of all available exploration data.

An often applied geophysical method during the surface exploration of especially volcanic geothermal systems is the magnetotelluric (MT) method. This PhD research originated with the initial question if this passive electromagnetic method can successfully be deployed for geothermal exploration in the Netherlands.

Research background and outline

The magnetotelluric method is a passive electromagnetic technique which measures the natural time-variations in the electric and magnetic field of the Earth. Sun storms and global lightning activity during thunder storms are the source of the time-variations in the electromagnetic field. The penetration depth of an MT sounding depends on the duration of the measurement and the bulk

electrical resistivity of the subsurface. A linear relationship, which contains the electrical resistivity structure of the subsurface, between the electric and magnetic fields of the Earth can be derived by making several assumptions.

Despite the successful application of MT during the exploration of high enthalpy geothermal systems¹, it can not simply be deployed everywhere. For example, in regions with a high population density such as the Netherlands, the technique suffers from disturbances caused by the numerous artificial electromagnetic sources such as electric fences, rail roads and buried pipes and cables. Another challenge, aside from minimizing the influence of this so-called “cultural electromagnetic noise” on the MT measurements, is to image the electrical resistivity structure of the Dutch subsurface. This last point is a result of the highly conductive nature of the Dutch subsurface and the expected small electrical resistivity contrasts within it. These two challenges, linked to the question if it is possible to successfully deploy MT for geothermal exploration purposes in the Netherlands, are the starting point of this PhD research.

Since during the course of this PhD research no MT data measured in the Netherlands were, or would become, available, MT data of two geothermal projects located abroad are used. The first geothermal project is located in the Çanakkale Province in Turkey and the data of the second geothermal project are acquired for the Montelago geothermal project, situated on Mindoro Island, Philippines. Based on the, during this research created, electrical resistivity models of both geothermal projects, conceptual models are formulated. Additionally, the MT data from the Çanakkale geothermal project are re-processed using a for this research developed processing routine. The experience gained while conducting these two geothermal case studies is translated to the possibilities of applying MT for geothermal exploration purposes in the Netherlands.

¹In this setting, high enthalpy indicates that the geothermal system contains sufficient energy for direct electricity production.

The magnetotelluric method

As mentioned above, the natural time-variations in the electromagnetic field of the Earth are measured during an MT measurement. The penetration depth of the MT response depends on the frequency: the longer the measurement time, the deeper the penetration depth. An MT station usually consists of two electrode dipoles and three magnetic induction coils. In most cases, the dipoles are oriented north-south and east-west and measure the variations in the electric field, while the magnetic induction coils are positioned north-south, east-west and vertical and measure the variations in the magnetic field. With the Maxwell equations as a starting point and making several assumptions, a linear relationship is derived between the electric and magnetic field. This linear relationship is described by the MT transfer function on basis of which the electrical resistivity structure of the subsurface can be determined.

While the MT data are measured in time, the MT transfer function depends on frequency. To be able to determine the MT transfer function, a Fourier transform is applied to the acquired MT data to transform the data from the time-domain to the frequency domain. Following, in the frequency-domain, the data points with a poor data quality are eliminated on basis of, for example, statistical parameters comparing the electrical and magnetic fields. Subsequently, generally using “robust processing methods”, the MT transfer function is computed. Ultimately, to determine the electrical resistivity structure of the subsurface, the resulting MT response has to be inverted from frequency to depth.

Inversion is the process of estimating the electrical resistivity of the subsurface as a function of depth on basis of the measured MT responses as a function of frequency. This is carried out by applying inversion algorithms to the MT data which use an iterative process to compute the best fitting solution between the model data and the observed data. Optionally, the resulting inversion model can be guided by using the available subsurface information of the subsurface from, for example, well logs or seismics.

In this PhD research 3-D electrical resistivity models are created using the “ModEM” inversion algorithm. Furthermore, electrical resistivity models created using “Mack3D” (for Çanakkale) and “WSINV3DMT” (for Montelago) are analysed and compared with the models generated using ModEM. All three inversion algorithms are based on comparable theoretical starting points, but vary in the elaboration thereof.

The Çanakkale geothermal project

The data of the in Turkey situated Çanakkale geothermal project are acquired, processed and inverted by two different contractors. In this research, the MT data are re-processed and a new inversion model is created, since the delivered MT data show inconsistencies. The processing code used is developed during this PhD research and delivered a qualitatively improved MT data set. Subsequently, the re-processed MT data are inverted to create a new 3-D electrical resistivity model. The new 3-D electrical resistivity model is qualitatively and quantitatively compared to the 3-D electrical resistivity model delivered by the contractor. The quantitative analysis of the models is carried out using so-called structural metrics. On basis of the electrical resistivity models, complemented with geochemical and geological data, a conceptual model of this geothermal system is formulated. After the drilling of two exploration wells, the conceptual model was validated.

Re-processing of MT data using Quality Index pre-sorting

The MT dataset is re-processed in the frequency domain with a newly developed processing algorithm: Quality Index pre-sorting. This algorithm combines and weighs a selection of statistical parameters that are graphically displayed and on basis of which the quality of the MT data is estimated. The statistical parameters used are the bivariate coherence, the least-squares MT transfer function and the error estimate of this MT transfer function. Using the graphical representation of this combination of the weighted statistical parameters, the data points with a poor quality can be observed. Subsequently,

data points with insufficient quality can be eliminated from the data before the MT response is computed. The resulting re-processed MT data set of the Çanakkale geothermal project is consistent and suitable for 3-D inversion.

Inversion and model analysis

The re-processed MT data set is 3-D inverted using the “ModEM” inversion algorithm. The inversion parameters used for this new inversion are chosen as similar as possible to those used for the inversion with “Mack3D”, carried out by the contractor. The bathymetry and conductivity of the Mediterranean Sea as well as the topography are accounted for in the model grid used for inversion. The for this research created 3-D electrical resistivity model and the by the contractor delivered 3-D electrical resistivity model are both qualitatively and quantitatively compared to each other. Besides the fact that the dominant resistivity structures in both inversion models are comparable, also the absolute resistivity values of both models show comparable values. On the other hand, small scale anomalies are clearly different in the two models.

Structural metrics are used for the quantitative analyses of the two inversion models. The structural metrics used are the gradients of the inversion models (the model gradient), the cross product of the two model gradients (the cross gradient), and the difference between the two model gradients (the gradient difference). The qualitative analyses shows that the gradient difference is sensitive to detect the minimal (inner) boundaries of comparable resistivity structures, while the maximum (outer) boundaries are highlighted by the cross gradient. Both inversion models are a reliable representation of the measured MT data as they show comparable dominate subsurface resistivity structures and the fit between the modelled and the observed data is very good.

Conceptual model

The electrical resistivity models of the Çanakkale geothermal project are geologically interpreted as follows. The dominant geological structures consist of a conductive layer of volcanics overlying a thick layer with a higher electrical

resistivity. This thick layer comprises two geological formations: an ophiolite complex overlying a limestone formation. It is expected that this limestone formation is the geothermal reservoir. The conceptual model is recently validated by two exploration wells which drilled the anticipated geothermal reservoir. Additionally, the edge of the graben-like system, in which the geothermal system is located, is observed in the inversion models at a location coinciding with the faults in the research area. The heat source of the geothermal system is probably a magmatic body, located some distance away from the project location.

The Montelago geothermal project

The Montelago geothermal project, Mindoro Island, Philippines, has an extensive development history of roughly 25 years. During this time four geophysical exploration surveys were conducted. The data of the three most recent of these four surveys are qualitatively worth investigating in the context of this thesis. The investigated surveys are a 24 station MT survey from 2000, a 112 station CSMT² survey from 2012 and a 54 station combined TEM³-MT survey from 2014. The electromagnetic data from these three surveys are analysed and inverted, resulting in new 2-D and 3-D inversion models.

Inversion and model analysis

The analysis of the CSMT data from 2012 shows that the data measured at long periods are unreliable, as are all recorded phases. Unreliable data points are eliminated from the data and on basis of the cleaned data new 2-D inversion models are created. Because of the poor data quality and a maximum penetration depth of approximately 600 m, the added value of the new inversion

²Controlled-source magnetotellurics: an active variant of MT during which a source field is induced in the subsurface by a generator. This technique suffers less from cultural electromagnetic noise, but has a considerably smaller penetration depth in comparison to the MT method.

³Transient-domain electromagnetics: an active electromagnetic method measuring the 1-D electrical resistivity response of the subsurface. TEM is often used to correct for distortions in the MT data caused by subsurface heterogeneities and/or topography. These distortions are known as galvanic distortion.

models is limited. Despite the high heterogeneity of the resistivity at shallow depths, the new inversion models show an anomaly at depth at a location coinciding with the inversion models based on MT data from 2000 and 2014.

A new inversion model of the MT data measured in 2000 is created. In contrast to the 2-D inversion models presented originally, this time a 3-D inversion is carried out. The model grid used for the new inversion includes bathymetry and topography. In the 3-D inversion model the dominant resistivity anomalies are observed at similar locations as in the old 2-D electrical resistivity models. Due to the limited data coverage of the survey area, edge effects induced by the inversion algorithm are observed.

During this PhD-research a new 3-D inversion model is created on basis of the MT data measured in 2014. The new inversion model is compared to the existing 3-D electrical resistivity model based on the same data. The new model is created using ModEM, whereas for the existing model WSINV3DMT was used. A comparable inversion strategy is used for both inversions. As the MT data are already corrected for galvanic distortion, only the bathymetry is included into the model grid. The topography is added to the resulting model after inversion for interpretation purposes. The two inversion models are qualitatively and quantitatively compared.

The qualitative comparison shows that the dominant anomalies in both models are comparable with respect to location and magnitude. Again, the quantitative analysis is carried out using structural metrics. The same metrics as used before are also applied to these resistivity models. The quantitative analysis confirms the observations made during the qualitative analysis. It is stated that the similarities between the two models are mainly located in the center of the survey area, while the differences are observed along the boundaries of the survey area. Using the quantitative analysis, the boundaries of the resistivity anomalies, faults and geothermal manifestations could be mapped. Evaluation of the location of the two planned exploration wells indicate that they are expected to penetrate anomalies with different characteristics, both possibly related to the inferred geothermal reservoir.

Conceptual model

The research area of the Montelago geothermal project is characterized by volcanic deposits and by a volcano, that last erupted approximately 1 million years ago. Several geothermal manifestations such as hot springs are present in the project area. All recent surface exploration work is carried out in order to define the conceptual model, as well as to determine the locations of the exploration wells to be drilled. On basis of the aforementioned studies and recently carried out geological and geochemical field work, the conceptual model of the Montelago geothermal project is formulated. The heat source of the geothermal system is unknown, although it is expected that a deep seated magma body is providing the system with geothermal heat. The permeability of the geothermal reservoir is fault controlled and the sealing cap consists of partly eroded volcanic deposits. The reservoir temperature is estimated to be at least 190 °C at a depth of 400 m, with an estimated electrical capacity of 40 MW. In the two exploration wells that were drilled in 2014, this anticipated temperature was recovered at a depth of 1,200 m. However, the clay alteration minerals present in the bore hole indicated higher temperatures. Consequently, it can be stated that the volcanic system used to have a higher temperature in the past and is currently cooling. At greater depths, the temperature in the bore hole decreases. This might be caused by the inflow of cold water into the reservoir. This cold water is probably running off from the mountain range along the western shore of Mindoro Island. It is assumed that the geothermal system is still heated by the magma body.

Conclusions and recommendations

To maintain focus on the the initial purpose of this research, several general recommendations, as well as a few specifically for the Netherlands, are proposed for geothermal exploration with the MT method.

When the MT data are distorted by cultural electromagnetic noise, it is stated that making a meticulous survey preparation and following a sound and

precise field work procedure can ensure maximum data quality in a specific area. Additionally, testing of and experimenting with a range of processing methods can further increase the resulting MT data quality. Specifically for the Netherlands, a successful exploration strategy of deep potential geothermal reservoirs can be achieved when using geological information derived from seismic data as “a priori” information in the inversion model. This approach increases the capability of inversion algorithms to image the small resistivity differences in the Dutch subsurface.

Finally, on basis of the research carried out, the following conclusions and recommendations are formulated.

Low quality data can be identified and eliminated from an MT data set using Quality Index pre-sorting. By applying Quality Index pre-sorting on the MT data of the Çanakkale geothermal project, the effectiveness of this method is illustrated. It is expected that by using Quality Index pre-sorting on MT data measured in the Netherlands, cultural electromagnetic noise effects can be removed from the data.

Model results of 3-D inversion models created by different inversion algorithms, but using identical inversion strategies, are broadly comparable. The electrical resistivity models solve the same dominant resistivity structures, although significant differences are observed at shallow depths and along the boundaries of the survey area. To arrive at a sound geological interpretation and an optimal well targeting, it is advised to create at least two 3-D inversion models of a single MT data set, using different inversion algorithms.

By using structural metrics, it is possible to quantitatively assess the differences between two 3-D inversion models. This is demonstrated by applying structural metrics to the inversion models of the two geothermal projects discussed in this thesis. For these two geothermal projects, structural metrics are used to determine the boundaries of the anomalies and, complemented with other surface exploration information, target the exploration wells.

Finally, it is stated that it can be misleading to directly correlate reservoir temperature to the electrical resistivity of the clay alteration minerals. This is

specifically the case in non-volcanic as well as in cooling geothermal systems. To two studied projects illustrate that besides geophysical information, also geochemical and geological surface exploration must be used during the geological interpretation and the definition of the conceptual model.

Acknowledgements

The start of this PhD research happened rather sudden. It was something I had never imagined doing after I had finished my studies a few years earlier. However, after two years at IF Technology the opportunity to take up a PhD project came up and, convinced that I would always regret not seizing it, I decided to go for it. There are a number of people I would like to thank for making this adventure a success.

In the first place it were my manager at IF Technology Guus Willemsen and my supervisor Ruud Schotting who created this position and always had confidence in me to bring it to a good end. Thanks for offering me the opportunity and the inexhaustible optimism regarding this project you both showed during the past six years. I would like to thank both of them as well as IF Technology for letting me pursue and orchestrate my own research direction.

Although my work at IF Technology and my PhD research collided at times, the experience and knowledge I was gradually building while researching, could often be utilized for commercial IF projects at many exciting places around the world. These projects offered me the possibility to extend my professional network in the geothermal industry, the conversations with these

knowledgeable persons taught me a lot. In this context, I would especially like to mention Gyffi Páll Hersir, Knútur Árnason and Bill Cummings.

Without the data sets from Transmark Renewables and Emerging Power Inc. I would probably still be searching for suitable data and this booklet would probably be non-existent. Needless to say, I am very grateful to Kris Marnette from Transmark as well as to Ton de Wilde and Guido Delgado from Emerging Power for making these data sets available.

I would especially like to thank Mark Muller, who was at all times willing to patiently listen to my struggles and giving me valuable feedback on my work, throughout the course of my PhD. His feedback also greatly improved my written work. The same holds for Michael Becken, the short visits to Münster University were without exception fruitful. The conversations with Mark and the visits to Münster never failed to refuel my tank and boosted my efforts when needed the most.

My colleagues at the "geothermie team" of IF Technology are thanked for their patience and pleasant company during the hours working in the office at IF in Arnhem. Especially the non-PhD related questions and projects were at times a welcome distraction. The printed version of this book was made possible by a gift from IF Technology, many thanks.

The tips and tricks for this thesis' layout came from Ralf Steegs, thanks for that. Thanks as well for my friends for being interested in my work, it kept me motivated. I'd also like to thank my parents and my sister for their support during these six years, it is much appreciated. The long morning walks with Roef helped me relax and find the necessary focus, paw for you. A last word for Suzan, you helped me to persevere at difficult times and even read the entire draft of the document during our holidays. I'm very grateful that you were there these past years.

Curriculum Vitae

Wouter van Leeuwen was born on May 20, 1981 in Eindhoven, the Netherlands. In 2000 he graduated from VWO at the Lorentz Lyceum in Eindhoven. Subsequently he studied earthsciences at Utrecht University, where halfway through his studies he dedicated a of his time to serve on the board of the geological student society UGV. After that he decided to specialize in geophysics and, following an internship at Fugro, obtained his Master of Science degree in 2007. Already before his graduation ceremony, he started as a geophysicist at Gtec with offices in Delft, the Netherlands, and in the area Liège, Belgium. After a year of working as a field geophysicist for Gtec across Europe and in India and Angola, he took on a new job at IF Technology in Arnhem. At IF Technology he worked for two years as geologist/geophysicist on geothermal projects. Subsequently he started this PhD project, which is a cooperation between IF Technology and the Environmental Hydrogeology Group of Utrecht University. During his PhD he organised the first edition of the National Geothermal Congress in 2011 and joined magnetotelluric surveys as a geophysical consultant for geothermal projects in the Philippines, Chili, Indonesia and Turkey. Currently he works as a geophysical consultant for IF Technology.